

INFORMATION TO USERS

This manuscript has been reproduced from the microfilm master. UMI films the text directly from the original or copy submitted. Thus, some thesis and dissertation copies are in typewriter face, while others may be from any type of computer printer.

The quality of this reproduction is dependent upon the quality of the copy submitted. Broken or indistinct print, colored or poor quality illustrations and photographs, print bleedthrough, substandard margins, and improper alignment can adversely affect reproduction.

In the unlikely event that the author did not send UMI a complete manuscript and there are missing pages, these will be noted. Also, if unauthorized copyright material had to be removed, a note will indicate the deletion.

Oversize materials (e.g., maps, drawings, charts) are reproduced by sectioning the original, beginning at the upper left-hand corner and continuing from left to right in equal sections with small overlaps. Each original is also photographed in one exposure and is included in reduced form at the back of the book.

Photographs included in the original manuscript have been reproduced xerographically in this copy. Higher quality 6" x 9" black and white photographic prints are available for any photographs or illustrations appearing in this copy for an additional charge. Contact UMI directly to order.

U·M·I

University Microfilms International
A Bell & Howell Information Company
300 North Zeeb Road, Ann Arbor, MI 48106-1346 USA
313/761-4700 800/521-0600

Order Number 9318105

**An investigation of heat transfer for air flow through low
porosity perforated plates**

Kutscher, Charles Francis, Ph.D.

University of Colorado at Boulder, 1992

Copyright ©1993 by Kutscher, Charles Francis. All rights reserved.

U·M·I
300 N. Zeeb Rd.
Ann Arbor, MI 48106

AN INVESTIGATION OF HEAT TRANSFER
FOR AIR FLOW THROUGH LOW POROSITY
PERFORATED PLATES

by

CHARLES FRANCIS KUTSCHER

B.S., State University of New York at Albany, 1972

M.S., University of Illinois at Urbana-Champaign, 1975

A thesis submitted to the
Faculty of the Graduate School of the
University of Colorado in partial fulfillment
of the requirement for the degree of
Doctor of Philosophy
Department of Mechanical Engineering

1992

This thesis for the Doctor of Philosophy degree by
Charles Francis Kutscher
has been approved for the
Department of Mechanical Engineering

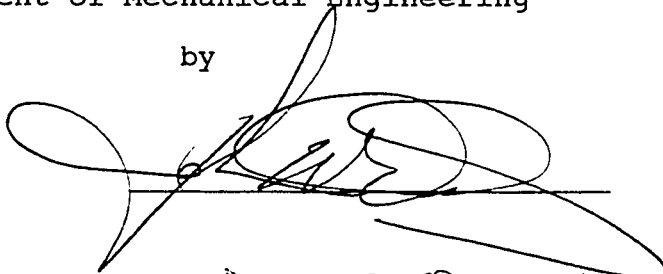
by

John Daily

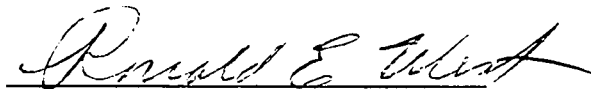
Mel Branch

Ronald West

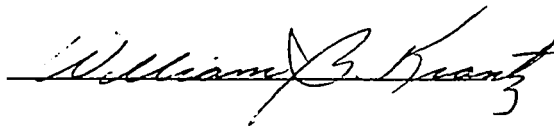
William Krantz



Melvyn C Branch



Ronald E West



William G Krantz

Date Dec 1, 1992

Kutscher, Charles Francis (Ph.D., Mechanical Engineering)
An Investigation of Heat Transfer for Air Flow Through Low
Porosity Perforated Plates

Thesis directed by Professor John W. Daily

Low porosity perforated plates are being used as absorbers for heating ambient air in a new type of unglazed solar collector. This thesis investigates the heat transfer effectiveness for low speed air flow through these plates with and without a crosswind. Heat losses to the wind and pressure drop are also studied. The objectives of this work are to develop a physical understanding of the issues and to provide information which will allow designers to optimize hole size and spacing. The problem is studied analytically, numerically (using the FLUENT program), and experimentally. In order to obtain performance data, a wind tunnel and small solar simulator were designed and built. Experimental data were taken for a range of plate porosities from 0.1% to 5%, hole Reynolds numbers from 100 to 2,000, and wind speeds from 0 to 4 m/s. Correlations were developed for heat exchange effectiveness and pressure drop. Color infrared thermography was used to visualize the heat transfer taking place at the surface.

ACKNOWLEDGMENTS

Because I performed this research while working at the National Renewable Energy Laboratory (NREL), I owe a great deal of thanks to helpful and understanding co-workers. H. Doug Powell, technician, provided assistance and invaluable advice in constructing the experiment. Over the course of the experiment, I was fortunate to have the assistance of a series of dedicated student interns (Mark Lichtwardt, Tom Pettigrew, and Keith Gawlik) who helped with experimental construction and data-taking. Managers Marty Murphy, Terry Penney, and Ren Anderson were understanding of my need to spend time on the research. Craig Christensen, Desikan Bharathan, and many others provided useful technical interaction. Gary Jorgensen gave me excellent advice on software packages. Nancy Greer and the other members of the NREL library staff provided invaluable assistance in my literature searches. I am especially indebted to Bob Hassett of the Department of Energy who provided funding for this research.

In the academic community, I am grateful to the advice I obtained on wind tunnel design from Professors Jane Davidson, Robert Meroney, and others at Colorado State University, from Professor Robert Moffat of Stanford University, and from numerous other generous experts in this field. At the University of Colorado, my committee

members -- Professors Ron West, Bill Krantz, Mel Branch, and Shankar Mahalingam -- were very supportive throughout my dissertation. Also, Frank Kreith gave me some useful prodding which resulted in a more comprehensive thesis than originally intended. A very special thanks to my chief advisor and committee chairman, Professor John Daily, who met with me regularly and helped keep me on track throughout the course of this work.

Finally, I would like to thank my wife, Karen, who was always there to provide emotional support throughout my course work and dissertation, and who made countless sacrifices to allow me to complete my degree.

TABLE OF CONTENTS

CHAPTER		
1.	INTRODUCTION	1
1.0	Background and Objectives	1
1.1	Description of Application	1
1.2	Literature Search	4
1.3	Objectives of Work	6
1.4	Overview of Experimental, Analytical, and Numerical Work	7
1.4.1	Experimental Work	7
1.4.2	Analytical Work	9
1.4.3	Numerical Work	9
2.	ANALYTICAL DEVELOPMENT	11
2.1	Overall Heat Balance	11
2.1.1	Radiation Heat Loss	12
2.1.2	Convection Heat Loss	13
2.2	Laminar Forced Convection	13
2.2.1	Velocity Profile	13
2.2.2	Boundary Layer Thickness	16
2.2.3	Starting Length	17
2.2.4	Temperature Profile	19
2.2.5	Convection Heat Loss	21
2.3	Laminar Free Convection	24
2.3.1	Velocity Profile	24
2.3.2	Convection Heat Loss	27
2.4	Turbulent Forced Convection	28
2.4.1	Wall Turbulence	28
2.4.2	Convective Heat Loss	30
2.5	Collector Efficiency	31
2.5.1	Predictive Model	31
2.5.2	Model Results	32
2.6	Issues and Discussion	35
2.6.1	Pressure Drop Considerations	35
2.6.2	Extension to Discrete Suction	37
2.6.3	3-D and Non-Parallel Flow	38
2.6.4	Free Stream Turbulence	39
2.7	Heat Exchange Effectiveness	40
2.7.1	Previous Work	42
2.7.1.1	Sparrow and Ortiz (1982)	42
2.7.1.2	Kumada, Hirata, and Kasagi (1981)	45
2.7.1.3	Hubbell and Cain (1988)	47
2.7.1.4	Andrews et al.	48
2.8	Integral Solution	50

3. NUMERICAL MODELING	60
3.1 General Approach	60
3.2 Normal Flow Heat Exchange Effectiveness	60
3.2.1 Correlation Development	70
3.2.1.1 Combination of h Values	72
3.2.1.2 Combination of U Values	74
3.2.1.3 Front Surface Heat Transfer	83
3.2.1.4 Hole Heat Transfer	88
3.2.1.5 Back Surface Heat Transfer	96
3.2.1.6 Overall Heat Transfer	100
3.3 Cross-Flow Model	109
4. EXPERIMENTS	114
4.1 Apparatus	114
4.1.1 Test Box	114
4.1.2 Lamp Array Design	116
4.1.3 Wind Tunnel Design	121
4.2 Instrumentation/DAS	135
4.2.1 Data Acquisition System	135
4.2.2 Temperature Measurement	135
4.2.3 Flow Measurement	140
4.2.4 Pressure Measurement	143
4.2.5 Radiation Measurement	144
4.3 Heat Exchange Effectiveness	151
4.3.1 Factorial Experiments	155
4.3.2 Normal Flow Tests	182
4.3.3 Cross-flow Tests	190
4.4 Pressure Drop	213
4.5 Wind Heat Loss	221
5. CONCLUSIONS, SUMMARY, AND FUTURE WORK	228
5.1 Conclusions and Application of Results	228
5.2 Summary	231
5.3 Future Work	233
BIBLIOGRAPHY	236
APPENDIX A. UNCERTAINTY ANALYSIS	240
A.1 Heat Exchange Effectiveness	240
A.2 Pressure Drop	247
APPENDIX B. FLUX DISTRIBUTION MODEL	250

LIST OF FIGURES

1-1.	Unglazed transpired solar collector oriented vertically for building ventilation preheat. Intake air is drawn by the building ventilation fan through the perforated absorber.	3
2-1.	Velocity and thermal boundary layers for laminar forced convection over a flat plate without suction.	15
2-2.	Velocity and thermal boundary layers for laminar forced convection over a flat plate with suction.	15
2-3.	Calculated equivalent convection heat loss length versus suction velocity at various wind speeds.	23
2-4.	Velocity and thermal boundary layers for laminar free convection over a flat plate with suction.	25
2-5.	Predicted thermal performance of a vertical unglazed transpired solar collector as a function of suction velocity, absorber emissivity, and wind speed.	33
2-6.	Impact of heat exchange effectiveness on collector efficiency.	44
2-7.	Comparison of front surface heat transfer coefficient from integral solution and FLUENT simulation, showing that boundary layer equations overpredict heat transfer.	59
3-1.	Plot showing pitch and diameters of all experimental and numerical test plates. . . .	61
3-2.	Grid used for axisymmetric FLUENT model. . .	63
3-3.	Example of streamlines for axisymmetric FLUENT model.	64
3-4.	Color temperature plot for axisymmetric FLUENT model.	65

LIST OF FIGURES (Cont'd)

3-5.	Effectiveness vs. suction flow rate comparing FLUENT predictions and experimental results for two test plates.	68
3-6.	Breakdown of where heat transfer occurs for plate 9.	69
3-7.	Overall heat transfer coefficient based on $T_s - T_{amb}$ from FLUENT simulations of plate 9 and best power law fit.	79
3-8.	Overall heat transfer coefficient based on log mean temperature difference from FLUENT simulations of plate 9 and best power law fit.	80
3-9.	Pitch-based Nusselt number vs. pitch-based Reynolds number for front surface heat transfer.	87
3-10.	Stanton number vs. pitch-based Reynolds number for front surface heat transfer.	88
3-11.	Hole heat transfer correlations from FLUENT and entrance flow correlations.	92
3-12.	Hole heat transfer correlation of FLUENT results using the form of the Sieder-Tate correlation.	93
3-13.	Best fit for Sieder-Tate type of correlation with non-zero intercept.	94
3-14.	Hole heat transfer correlation of FLUENT results using a form similar to the Hausen correlation.	95
3-15.	Hole heat transfer correlation of FLUENT results of the Hausen type but using a best-fit y-intercept.	96
3-16.	Pitch-based Nusselt number vs. pitch-based Reynolds number for FLUENT results for back surface heat transfer.	97
3-17.	Stanton number vs. pitch-based Reynolds number for back surface heat transfer.	98

LIST OF FIGURES (Cont'd)

3-18.	Number of transfer units vs. pitch-based Reynolds number for back surface heat transfer.	99
3-19.	Correlation of overall heat transfer results using the same general form as Andrews, et. al.	105
3-20.	Algebraic equivalent of Andrews type of correlation for overall heat transfer results, but in terms of pitch-based parameters. Note smaller power on pitch-to-diameter ratio.	106
3-21.	Best fit of overall FLUENT heat transfer results using pitch-based parameters.	107
3-22.	NTU vs. pitch-based Reynolds number for overall FLUENT heat transfer results.	108
3-23.	Surface temperature distribution from 3-D plate model.	111
3-24.	Velocity vector plot for 3-D model showing flow through hole.	112
3-25.	Temperature distribution for 3-D model showing thickness of plate boundary layer and heat transfer in hole.	113
4-1.	Fan curve used for wind tunnel.	127
4-2.	Transpired Collector Test Facility showing wind tunnel, test loop, and lamp array.	130
4-3.	Wind tunnel with fan in foreground and lamp array at exit. Wind direction is left to right.	131
4-4.	Wind tunnel flow conditioning box showing honeycomb in foreground and removable screens.	132
4-5.	View of wind tunnel exit showing test plate and lamp array.	133

LIST OF FIGURES (Cont'd)

4-6.	Smoke wire results for 1 m/s wind flow over absorber: a) leading edge boundary layer removal, b) effect of suction mass flow rate = 0.10 kg/m ² -s.	134
4-7.	Photograph of instrument (left) designed to provide transient measurement of net radiation. A typical pyranometer is shown on the right.	148
4-8.	Experimental uncertainty of effectiveness measurement vs. effectiveness for three measurement methods.	153
4-9.	Normal probability plot for factorial experiment.	160
4-10.	Cube plot of measured heat exchange effectiveness values.	161
4-11.	Normal probability plot for heat transfer coefficient.	162
4-12.	Cube plot of measured heat transfer coefficients.	163
4-13.	Effect of plate thickness on heat exchange effectiveness.	166
4-14.	Effect of pitch on heat exchange effectiveness.	167
4-15.	Effect of hole diameter on effectiveness .	168
4-16.	Normal probability plot for investigation of effect of orientation on effectiveness.	172
4-17.	Cube plot of measured effectiveness for investigation of orientation.	173
4-18.	Normal probability plot for investigation of effect of orientation on heat transfer coefficient.	174
4-19.	Cube plot of measured heat transfer coefficients for investigation of orientation.	175

LIST OF FIGURES (Cont'd)

4-20.	Normal probability plot for effect of wind on effectiveness.	178
4-21.	Cube plot of measured effectiveness for investigation of wind speed.	179
4-22.	Normal probability plot for investigation of effect of wind speed on heat transfer coefficient.	180
4-23.	Cube plot of measured heat transfer coefficient for investigation of wind speed.	181
4-24.	Nu_D vs. modified Re_D for vertical test plates.	187
4-25.	Nu_p vs. modified Re_p and curve representing algebraic equivalent of correlation in previous figure.	188
4-26.	Nu_p vs. modified Re_p and best fit curve.	189
4-27.	Heat exchange effectiveness vs. wind speed for plate 5 at $G = .05 \text{ kg}/(\text{m}^2\text{-s})$ in both vertical (upper curve) and horizontal (lower curve) positions.	193
4-28.	Heat exchange effectiveness vs. suction flow rate at 0 and 5 m/s wind speed.	194
4-29.	Infrared image of black matboard absorber in "A" orientation; $G = 0.05 \text{ kg}/\text{m}^2\text{-s}$, wind speed = 0 m/s.	196
4-30.	Infrared image of black matboard absorber in "A" orientation; $G = 0.05 \text{ kg}/\text{m}^2\text{-s}$, wind speed = 1 m/s.	197
4-31.	Infrared image of black matboard absorber in "A" orientation; $G = 0.05 \text{ kg}/\text{m}^2\text{-s}$, wind speed = 2 m/s.	198
4-32.	Infrared image of black matboard absorber in "B" orientation; $G = 0.05 \text{ kg}/\text{m}^2\text{-s}$, wind speed = 0 m/s.	199
4-33.	Infrared image of black matboard absorber in "B" orientation; $G = 0.05 \text{ kg}/\text{m}^2\text{-s}$, wind speed = 1 m/s.	200

LIST OF FIGURES (Concluded)

4-34.	Infrared image of black matboard absorber in "B" orientation; $G = 0.05 \text{ kg/m}^2\text{-s}$, wind speed = 2 m/s.	201
4-35.	Effect of hole orientation on wind test results.	203
4-36.	Nusselt number correlation for vertical test plates at wind speed of 2 m/s.	208
4-37.	Nusselt number for vertical test plates at wind speed of 1 m/s.	209
4-38.	Nusselt number correlation for vertical test plates at wind speed of 4 m/s.	210
4-39.	Universal heat transfer correlation for non-zero wind tests.	213
4-40.	Data and correlation for non-dimensional pressure drop as a function of porosity and Reynolds number.	220
4-41.	Non-dimensional pressure drop vs. wind speed at $G = 0.023 \text{ kg}/(\text{m}^2\text{-s})$ for plate 17.	221
4-42.	Heat loss vs. wind speed for black fabric absorber.	225
4-43.	Collector efficiency vs. wind speed for plate 6.	227
A-1	(Figure 4-8 repeated). Percent uncertainty in effectiveness measurement vs. effectiveness for three different measurement methods -- plate 16.	246
A-2.	Percent uncertainty in non-dimensional pressure drop vs. non-dimensional pressure drop for plate 16.	249
B-1.	Geometry for lamp pointing normal to target.	250
B-2.	Geometry for arbitrary lamp angles.	253

LIST OF TABLES

3-1.	Percentage of heat transfer occurring in different plate regions.	69
3-2.	Geometries of FLUENT plate models.	81
3-3.	Local average heat transfer coefficients for FLUENT simulations.	82
3-4.	Front surface correlations at D = .003175 m	83
3-5.	Front surface correlations at P = .00709 m	83
3-6.	Hole correlations at D = .003175 m	89
3-7.	Hole correlations at P = .00709 m	89
3-8.	Comparison between FLUENT U value results and predicted values from correlations based on those results.	102
4-1.	Original Test Plate Dimensions	156
4-2.	Effectiveness and heat transfer coefficient results for full factorial experiment.	157
4-3.	Effects of each factor in full factorial experiment. To make the terms easier to recognize, this table uses D (instead of B) for diameter, P (instead of A) for pitch, T (instead of C) for thickness, and G (instead of D) for mass flow.	158
4-4.	Effectiveness and heat transfer coefficient results for investigation of orientation.	169
4-5.	Standardized effects for factorial investigation of orientation.	170
4-6.	Effectiveness and heat transfer coefficient results for investigation of wind speed.	176
4-7.	Standardized effects for factorial investigation of wind speed.	177

LIST OF TABLES (Concluded)

4-8.	Experimental heat transfer results for vertical test plates.	184
4-9.	Experimental heat transfer results for vertical plates with cross-flow.	204
4-10.	Coefficients of variation expressed as a percentage for the parameters a, b, and c in the wind run correlations of the form $Nu_p = a(P/D)^b Re_p^c$	208
4-11.	Experimental pressure drop measurements.	215

LIST OF SYMBOLS

- A = area of unit cell on plate less hole area (m^2)
- A' = area of unit cell on plate (m^2)
- A_c = collector area (m^2)
- B_f = transpiration parameter
- B_h = heat-transfer transpiration parameter
- C_p = specific heat at constant pressure (J/kg-K)
- C_f = friction factor
- d = plate thickness (m)
- D = hole diameter (m)
- dA_{surf} = surface element used in lamp analysis (m^2)
- e = absolute error (used in uncertainty analysis)
- F(z) = complex velocity potential
- F_{cg} = collector-to-ground view factor
- F_{cs} = collector-to-sky view factor
- g = acceleration of gravity (m/s^2)
- G = suction mass flow rate (kg/m^2-s)
- I_c = solar insolation incident on the collector (W/m^2)
- h = convective heat transfer coefficient based on
(T_s-T_{amb}) (W/m^2-K)
- h_{in} = enthalpy of inlet air stream (J/kg)
- h_{out} = enthalpy of outlet air stream (J/kg)
- H = pumping head (m)
- k = thermal conductivity (W/m-K)
- K = pressure drop coefficient
- l = channel half-width in integral solution (m)

L_e = equivalent convective heat loss length (m)
 L_s = boundary layer starting length (m)
 \dot{m} = suction mass flow rate (kg/s)
 q'' = net wall radiant heat flux (W/m²)
 Q = volumetric flow rate (m³/s)
 Q_{conv} = collector convective heat loss (W)
 Q_f = heat into suction air stream (W)
 Q_{net} = net radiant heat into surface (W)
 Q_{rad} = collector radiant heat loss (W)
 Q_s = incoming short-wave (lamp) radiation flux (W/m²)
 Q_w = wind heat loss (W)
 R_{in} = incoming long-wave radiation flux (W/m²)

 R_{net} = net long-wave radiation flux on absorber (W/m²)
 T_{amb} = ambient temperature [=T_∞] (K)
 T_{coll} = collector temperature [=T₀] (K)
 T_{gnd} = ground temperature (K)
 T_{out} = collector output temperature (K)
 T_{sky} = sky temperature (K)
 T_s = surface temperature
 T_0 = wall temperature [=T_{coll} and T_s] (K)
 $T_{∞}$ = free stream temperature [=T_{amb}] (K)
 T = local air temperature (K)
 u = velocity parallel to the wall (m/s)
 U = convective heat transfer coefficient based on ΔT_{1m}
(W/m²-K)

U_{∞} = free stream velocity, wind speed (m/s)
 v = velocity normal to the wall (m/s)
 V = far-field approach velocity (m/s)
 v_0 = suction face velocity at wall (m/s)
 W = collector width (m)
 $W(z)$ = complex velocity (m/s)
 x = distance along the wall (m)
 y = distance from the wall (m)

Nu_x = Ux/k or hx/k , Nusselt number
 P = hole pitch, i.e. distance between center of hole and center of next closest hole (m)
 Pr = v/α , Prandtl number
 R = distance between center of hole and stagnation line, or $P/2$ (m)
 Re_x = v_x/v , Reynolds number, where v is relevant velocity scale
 St = $h/\rho v c$, Stanton number, where v is relevant velocity scale
 t = plate thickness (m)
 NTU = UA/mc_p , number of transfer units
 α_c = collector absorptance
 α = thermal diffusivity (m^2/s)
 β = thermal expansion coefficient ($1/K$)
 β_p = pressure parameter
 Δ_{∞} = asymptotic thermal boundary layer thickness (m)

- ΔP = pressure drop (pa)
 ΔT_{lm} = log mean temperature difference (K)
 δ = velocity boundary layer thickness
 δ_t^* = non-dimensional thermal boundary layer thickness
(m)
 δ_{86} = asymptotic velocity boundary layer thickness (m)
 ϵ_c = absorber surface emissivity
 ϵ_{EX} = absorber heat exchange effectiveness
 η = collector efficiency
 θ = angle between lamp centerline and point of
measurement
 κ = angle between lamp-to-surface element line and
surface normal
 Λ_t = Smith-Spalding parameter
 σ = plate porosity, or open area fraction
 σ_{SB} = Stefan-Boltzmann constant = 5.67×10^{-8} W/m²-K
 ν = kinematic viscosity (m²/s)
 ρ = density (kg/m³)
 τ_0 = wall shear stress (N/m²)
 μ = viscosity (kg/m-s)
 ζ = $(1/2)\rho V^2$, non-dimensional pressure drop

Chapter 1. INTRODUCTION

1.0 Background and Objectives

The purposes of this study are to develop practical correlations for heat transfer and pressure drop that can be used by designers of unglazed, transpired solar collectors and to provide insight into the nature of the heat transfer mechanisms involved.

1.1 Description of Application

Solar air collectors are especially efficient when they are used to heat ambient air on a once-through basis, since average absorber temperatures are closer to ambient than for a typical recirculated flow application. A transpired design in which the heated air is drawn through holes or slots in the absorber is well suited to this case because suction can increase heat transfer and also capture much or most of the usual convective heat losses, thereby eliminating the need for a glazing and its associated cost and optical losses. This type of design shows promise for applications such as ventilation preheat, crop drying, and desiccant regeneration. A German patent (Wieneke 1981) describes an unglazed perforated roof absorber for heating ventilation air. Schulz (1988) describes a fabric absorber used in Germany for crop drying. Conserval, Inc., with offices in Toronto and Buffalo, is currently manufacturing and marketing unglazed perforated walls for ventilation

preheat.

Operating parameters for an unglazed transpired collector will depend on the application. Typical face velocities might range from 0.01 m/sec for desiccant regeneration to 0.05 m/sec for preheating ventilation air. A schematic showing a perforated absorber used for ventilation preheat is given in **Figure 1-1**. In this case a building ventilation fan draws outside air uniformly through the vertical absorber and up a plenum between the absorber and the south wall of the building.

A number of studies have been done on transpired, air-heating, solar collectors utilizing porous absorbers. However, almost all of these were glazed units incorporating a thick matrix absorber to heat recirculated air. This dissertation addresses research needs associated with the design and performance prediction of potentially low-cost, high-efficiency, unglazed collectors utilizing a thin, transpired absorber in once-through air-heating systems.

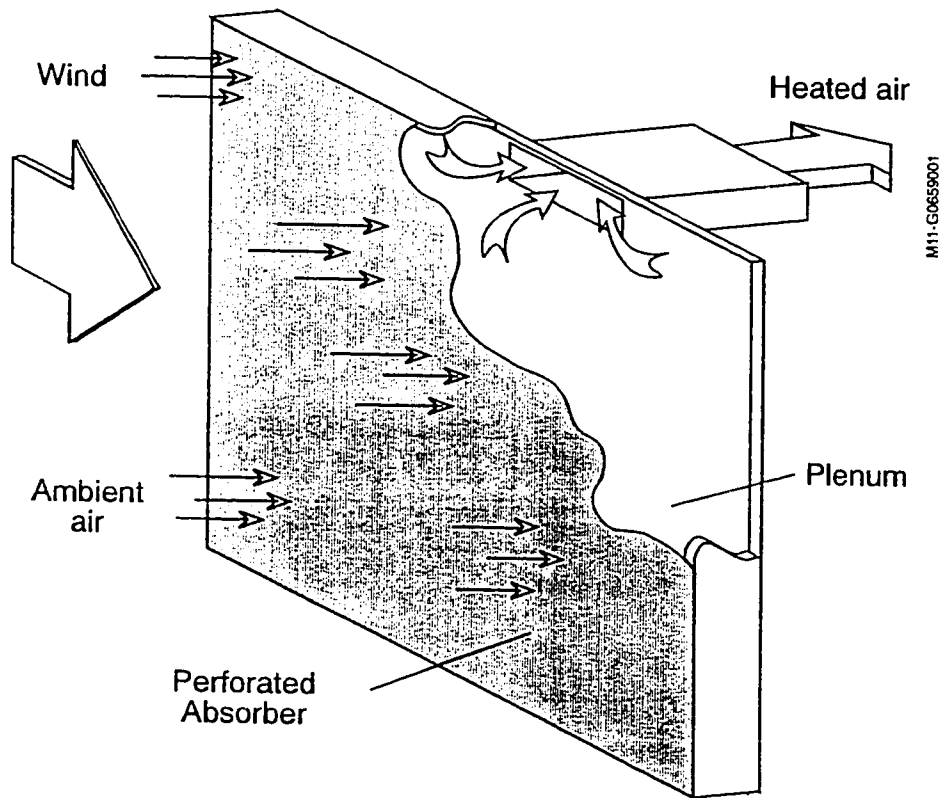


Figure 1-1. Unglazed transpired solar collector oriented vertically for building ventilation preheat. Intake air is drawn by the building ventilation fan through the perforated absorber.

1.2 Literature Search

Information is needed on the heat transfer from a heated perforated plate to both the suction air passing through it as well as to any wind or free convection flow over it. Fluid dynamics and heat transfer for boundary layer flow parallel to porous surfaces have been studied analytically and experimentally. These studies have been motivated by several real applications. Suction (fluid from the boundary layer drawn through the porous wall) has been used to reduce aerodynamic drag on air foils by maintaining laminar flow. Injection (flow injected through the porous wall into the boundary layer) has been used to keep the surfaces of turbine blades and rocket nozzles relatively cool in the presence of hot gases by blowing the boundary layer off the surface. For these applications the emphasis was on the fluid dynamics for the suction case and the heat transfer for the injection case. Heat transfer with suction - the unglazed transpired collector case - is a combination that has not received much attention.

While most of the aerospace literature has focused on the effects of suction on the reduction of drag coefficient, some research on parallel plate heat exchangers has examined heat transfer to air passing normal to a perforated plate. However, this research has been aimed at higher porosity plates than would be suitable for the application studied here. Research on low porosity

plates had been done in conjunction with film cooling applications which are at higher suction flow rates than those of interest here.

Computer searches were done on a large number of engineering data bases using the following key words: suction, transpiration, heat transfer, perforated plate, orifice plate, heat exchanger, boundary layer control. The literature search revealed a considerable amount of information in the aerospace literature on external flow over a suction surface and some information in the heat exchanger literature on heat transfer for flow through a plate. When areas still in need of research were identified, authors of papers in these areas were contacted to verify that this information was not available. In addition, an ASME conference paper was prepared (with two co-authors) providing an overview of the theory of heat loss for transpired collectors and listing research issues, and this was sent out to twenty reviewers in addition to the usual ASME peer review process. Twelve responses were obtained.

1.3 Objectives of Work

This study has primary and secondary objectives as follows:

1) The primary objective is to develop heat exchange effectiveness results for staggered-hole perforated plates in the range of sizes and for the range of flow rates typical for unglazed transpired solar collector applications and to develop an understanding of the heat transfer mechanisms involved.

2) A secondary objective is to obtain some preliminary results for wind heat loss in order to compare with theory previously published by Kutscher, Christensen, and Barker (1991a) and to form the basis for future studies.

The bulk of this report covers the primary objective. This study covers a range of porosities from 0.1% to 5% over a range of hole Reynolds numbers from 50 to 2,000. This is done experimentally and via a numerical model. Visualization of the heat transfer on the surface of the plate is done with IR thermography.

The heat exchange effectiveness (ratio of suction air temperature rise to maximum possible temperature rise) of a transpired absorber will affect its efficiency. If the effectiveness is poor, the surface temperature will be considerably above the delivered air temperature. This will cause higher radiation heat losses to the environment. Considerable performance penalties are incurred if the

effectiveness drops below about 0.70. In determining the hole size and spacing for a transpired absorber, the designer must consider the fan power, uniformity of flow, occurrence of local outflow, and heat exchange effectiveness for the particular delivered temperature required. The current literature does not allow a design engineer to confidently predict heat exchange effectiveness in the low porosity, low Reynolds number ranges of interest.

The problem of normal flow is well-defined and lends itself to two-dimensional analysis. Although transpired collectors will often be subject to winds that cause the flow not to be normal, the no-wind condition is likely to be a worst case in terms of heat exchange effectiveness and is thus suitable for design purposes. Nevertheless, this report includes the effects of cross-wind.

1.4 Overview of Experimental, Analytical, and Numerical Work

1.4.1 Experimental Work

A number of different means for determining the heat exchange effectiveness were identified and compared. These included naphthalene sublimation and three types of heat transfer experiments: transient temperature, energy source measurement, and direct delta T measurements. It was

decided to use heat transfer methods as these deal directly with the problem of interest. All three heat transfer methods were used. Because the transient method displayed less repeatability than the other two methods, and because it does not easily lend itself to cross-flow, it was used only to provide a general confirmation of results obtained using the other two methods. The direct measurement of delta T proved the most accurate method for obtaining heat exchange effectiveness, while an energy balance method combining energy source measurement and delta T measurement was needed to determine wind losses.

After considering various options, it was decided to use a lamp array as an energy source for heating the test plates. In order to determine the effects of cross-winds, a 0-10 m/s open circuit wind tunnel was built. Measurements were taken by an HP 75000 VXI data acquisition system controlled by an IBM PC-AT. Absolute temperatures were measured with 10,000 ohm YSI precision interchangeable thermistors; delta T's were also measured with 30 gauge type T (copper-constantan) thermocouples arranged in a differencing circuit. Suction flow rate was determined by a calibrated Meriam 0-43 CFM laminar flow element and a calibrated MKS capacitance pressure transducer. Wind speed was measured both by hot wire anemometers and pitot tubes. Radiation was measured by the combination of a calibrated Kipp & Zonen CM-11 pyranometer (incoming short wave) and a

calibrated Eppley pyrgeometer (net long wave) as well as by an instrument specifically designed for this study.

1.4.2 Analytical Work

Wind and natural convection heat losses were computed by solving the Navier-Stokes equation for the asymptotic region of the homogeneous suction case, and then integrating the resulting velocity and temperature profiles. To analytically investigate heat exchange effectiveness for normal flow, an integral solution for an idealized case was attempted. This involved solving the problem of slot flow and then applying a Mangler transformation to convert the result to axisymmetric flow through a hole.

1.4.3 Numerical Work

The problem of normal flow through a heated perforated plate can be solved numerically using either a stream function-vorticity approach or direct solution of the Navier Stokes equation in primitive variables (u,v,P). Because neither approach involves any new numerical developments, a commercial code (FLUENT) was employed. This code uses a finite volume version of the direct solution approach and can readily provide pressure drop as well as velocity and temperature profiles.

Visualization of flow normal to perforated plates done by Sparrow showed each hole lies at the center of a hexagonal-shaped unit cell. To numerically model this in two dimensions, the hexagonal unit cell was approximated by a circle, and the flow was modeled in FLUENT as axisymmetric. A non-uniform grid was used with fine mesh size nearest the plate (in the axial direction) and nearest the hole (in the radial direction).

Near the end of this study, a new version of FLUENT (Version 4.11) and accompanying pre-processor (PreBFC) became available which enabled the use of boundary-fitted coordinates. This allowed development of a three-dimensional model of the front surface of the plate with good grid definition around and in the hole. Preliminary results from this model are also included.

Chapter 2. ANALYTICAL DEVELOPMENT

This chapter provides an overview of the heat loss theory, covering both convective and radiative heat loss, and then discusses heat exchange effectiveness. The discussion of collector modeling and heat loss is taken from Kutscher, Christensen, and Barker (1991a), a paper which was presented at the ASME Solar Energy Conference in March 1991. Most of the references obtained in the literature are referred to in this section.

2.1 Overall Heat Balance

The overall heat balance on an unglazed transpired collector is:

$$\rho c_p v_0 A_c \epsilon_{HX} (T_s - T_{amb}) = I_c A_c \alpha_c - Q_{rad} - Q_{conv} \quad (2-1)$$

where ρ is the air density in kg/m^3 , c_p is the constant pressure specific heat in J/kg-K , v_0 is the suction face velocity in m/s , A_c is the collector area in m^2 , ϵ_{HX} is the heat exchange effectiveness (ratio of suction air temperature rise to maximum possible temperature rise), T_s is the surface temperature in K , T_{amb} is the ambient temperature in K , I_c is the solar radiation incident on the collector in W/m^2 , α_c is the collector absorptance, Q_{rad} is the collector radiant heat loss in W , and Q_{conv} is the collector convective heat loss in W .

The left-hand side of this equation represents the

useful energy collected. The first term on the right-hand side is the solar energy absorbed by the absorber and is straightforward to calculate. Note that I_c is the total radiation striking the absorber including direct, diffuse, and reflected. The second and third terms are, respectively, the losses to the environment via radiation and convection. The two most significant unknown terms are the convective heat loss term and the heat exchange effectiveness. The latter determines the surface temperature which, in turn, affects the radiative heat loss.

2.1.1 Radiation Heat Loss

Radiation loss occurs both to the sky and to the ground with the view factors depending on the tilt of the absorber. (It is assumed that the wall behind the collector plenum is adiabatic and at a temperature close to the absorber temperature so that radiation loss to this wall is negligible.) Assuming the absorber is gray and diffuse, the radiant heat loss is:

$$Q_{\text{rad}} = \epsilon_c \sigma_{\text{SB}} A_c (T_{\text{coll}}^4 - F_{\text{cs}} T_{\text{sky}}^4 - F_{\text{cg}} T_{\text{gnd}}^4) \quad (2-2)$$

where ϵ_c is the absorber surface emissivity, σ_{SB} is the Stefan-Boltzmann constant, and T_{coll} , T_{gnd} , and T_{sky} are the collector, ground, and sky temperatures, respectively, in K.

2.1.2 Convection Heat Loss

Convective heat loss from the surface will depend to a certain extent on the nature of the surface. A surface with homogeneous suction (versus suction at discrete holes or slots) has the simplest wall boundary condition and can be analyzed in a straightforward manner. This type of surface is analyzed followed by a discussion of how the results might be extrapolated to a surface with discrete suction. There is a considerable amount of information in the literature on velocity profiles and, to a lesser extent, temperature profiles for homogeneous suction surfaces. This work is reviewed and applied to the problem of convective heat losses for collector applications. The analysis will be further simplified by considering the local free stream flow to be parallel to the surface.

2.2 Laminar Forced Convection

2.2.1 Velocity Profile

For a non-porous plate subjected to a laminar parallel wind, the velocity boundary layer grows as $x^{1/2}$ (see **Figure 2-1**). The Reynolds number also increases as $x^{1/2}$, and transition to turbulent flow will eventually occur. Once the boundary layer becomes turbulent it grows much more rapidly, increasing as $x^{4/5}$ instead of $x^{1/2}$ (Bejan 1984).

The effect of homogeneous wall suction on the velocity and thermal boundary layers is shown in **Figure 2-2**. Using scaling arguments, one can argue that for sufficiently large x , $\partial u/\partial x$ goes to zero (since the denominator becomes large). Thus $u = u(y)$ only and, by continuity, $\partial v/\partial y = 0$. Since $v = -v_0$ everywhere along the wall, one must have for sufficiently large x that $v = -v_0$ everywhere in the flow field. The x -momentum equation becomes linear:

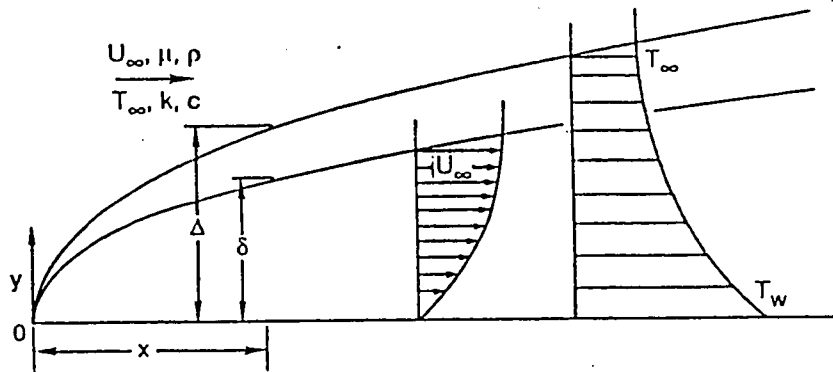
$$-v_0 \frac{du}{dy} = \nu \frac{d^2u}{dy^2} \quad (2-3)$$

where ν is the kinematic viscosity in m^2/s .

This equation is directly integrable. Integrating it twice and applying the boundary conditions that $u = 0$ at the wall and $u = U_\infty$ at infinity, one obtains the following solution:

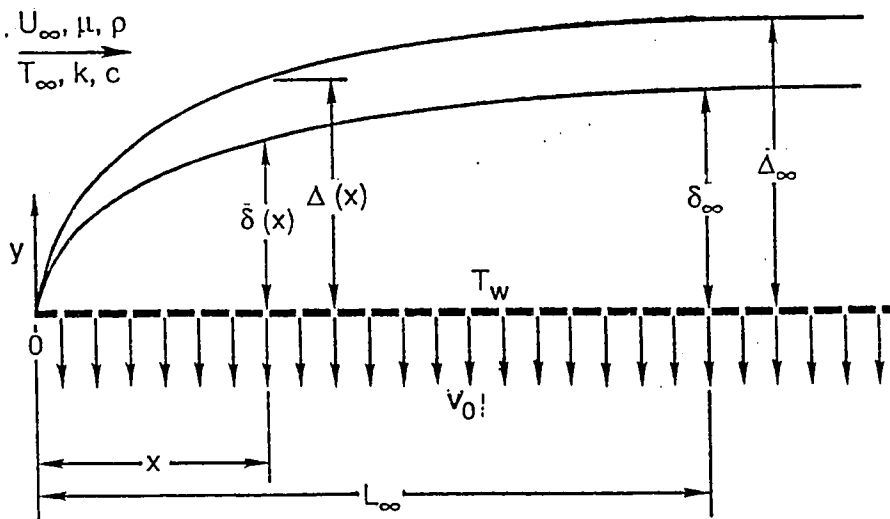
$$u = U_\infty (1 - e^{-\frac{v_0 y}{\nu}}) \quad (2-4)$$

Note that this is an exact solution to the Navier-Stokes equation, and boundary layer approximations are not needed.



BA-G0677003

Figure 2-1. Velocity and thermal boundary layers for laminar forced convection over a flat plate without suction.



BA-G0677002

Figure 2-2. Velocity and thermal boundary layers for laminar forced convection over a flat plate with suction.

2.2.2 Boundary Layer Thickness

Often the boundary layer thickness is defined as that value of y for which the horizontal velocity is 99% of the free stream value, and this is usually written as δ_{99} . The selection of 99% is completely arbitrary, however, and for reasons which will be explained later, it is more convenient to use a definition based on 86% of the free stream value. Putting δ_{86} in place of y in equation (2-4) and setting $u = .86 U_{\infty}$, one can solve for δ_{86} to obtain:

$$\delta_{86} = 2.0 \frac{v}{V_0} \quad (2-5)$$

Unlike the no-suction profile, the boundary layer thickness for suction is a constant independent of distance along the plate, and it does not depend on the free stream velocity. This solution is not valid for the starting length in which du/dx and dv/dy are not zero, but is approached asymptotically and so is called the asymptotic solution. For a typical ventilation suction velocity of .05 m/s, the velocity boundary layer thickness is only 0.6 mm.

As with the case of the no-suction profile, the asymptotic suction profile will be stable only for Reynolds numbers (based on boundary layer thickness) below a certain critical value. Schlichting (1979) points out that suction provides a great deal of stability to flow over a flat

plate, raising the critical Reynolds number by a factor of 130. Because the boundary layer thickness is constant in the asymptotic region, the Reynolds number based on boundary layer thickness will no longer increase. If the flow is laminar and the Reynolds number is below 70,000, transition to turbulence on a smooth plate with uniform suction will not occur, no matter how long the plate.

Schlichting also shows that when the starting length is taken into account, the minimum suction velocity for stability is:

$$v_0 = 1.2 \times 10^{-4} U_\infty \quad (2-6)$$

For practical wind velocities, this is much less than the suction velocities expected for typical unglazed transpired collector applications.

2.2.3 Starting Length

The above results for an asymptotic boundary layer will only apply after a certain starting length. Arpaci and Larsen (1984) give an integral solution from which one can obtain this length. By substituting a parabolic velocity profile which meets the boundary conditions into the integral boundary layer momentum equation, they find that the asymptotic thickness consistent with the assumed profile must be $2\nu/v_0$, or δ_{86} . (This is why the 86%

definition was chosen earlier rather than the more typical 99% value.) Writing the integral boundary layer momentum equation in terms of δ_{86} , and integrating across the boundary layer, Arpaci and Larsen obtain:

$$-\ln\left(1 - \frac{\delta}{\delta_{86}}\right) - \frac{\delta}{\delta_{86}} = \frac{15}{2} \frac{v_0 x}{U_\infty \delta_{86}} \quad (2-7)$$

where δ is the velocity boundary layer thickness.

If one defines a starting length L_s to be that distance along the plate at which the velocity boundary layer thickness is 99% of δ_{86} , one can obtain the following starting length from the integral solution:

$$L_s = .96 \frac{U_\infty v}{v_0^2} \approx \frac{U_\infty v}{v_0^2} \quad (2-8)$$

As one would expect, the starting length becomes infinite as the suction velocity goes to zero. It is worthwhile to note here that, based on a series solution of Iglisch (1949), Schlichting (1979) reports a starting length of $4U_\infty v/v_0^2$. However, Maddaeus and Shanebrook (1983) point out that a number of experimental studies contradict Iglisch and show starting lengths to be in the range of $0.5 U_\infty v/v_0^2$ to $U_\infty v/v_0^2$. Thus the approximate result for a 99% starting length presented here seems reasonable.

Assuming a maximum wind speed of 10 m/s, a typical ventilation suction velocity of .05 m/s, and an average

temperature of 30°C for which $v = 15.7 \times 10^{-6}$, the starting length is 6 cm.

2.2.4 Temperature Profile

Next consider the energy equation. Analogous to the case of the momentum equation, for constant suction velocity there exists at sufficiently large x an asymptotic region where heat convected through the porous plate by suction is exactly balanced by heat conducted from the plate out into the fluid. In this region, the energy equation simplifies and becomes linear:

$$-v_0 \frac{\partial T}{\partial y} = \alpha \frac{\partial^2 T}{\partial y^2} \quad (2-9)$$

where T is the local temperature in K in the boundary layer and α is the thermal diffusivity in m^2/s .

For a constant heat flux plate, the boundary conditions are: At $y = 0$, $dT/dy = -q''/k$; at $y = \infty$, $T = T_\infty$, where k is the thermal conductivity in $W/m-K$, T_∞ is the free-stream temperature in K, and q'' is the net radiant heat flux, which in the case of a transpired absorber is the difference between the absorbed solar flux and the radiation heat loss. Integrating and applying the boundary conditions one obtains:

$$T = T_{\infty} + \frac{q''}{\rho c_p v_0} e^{-\frac{\rho c_p v_0 y}{k}} \quad (2-10)$$

Setting $y = 0$ and rearranging terms, yields:

$$\rho c_p v_0 (T_0 - T_{\infty}) = q'' \quad (2-11)$$

Since T_{coll} equals T_0 for a homogeneous suction plate, equation (2-11) states that in the asymptotic region all of the net heat flux from the wall goes into the suction fluid. Note that because the wall temperature in the asymptotic region of a constant heat flux wall is constant, the result is exactly the same as for an isothermal wall. This can be shown by using the isothermal boundary condition (at $y = 0$, $T = T_0$) in place of the wall heat flux boundary condition and solving as above.

Defining $\Delta_{.86}$ as the value of y at which $(T - T_0) = .86(T_{\infty} - T_0)$, combining equations (2-10) and (2-11) one obtains:

$$\Delta_{.86} = 2.0 \frac{\alpha}{v_0} = \frac{\delta_{.86}}{\text{Pr}} \quad (2-12)$$

where Pr is the Prandtl number, ν/α . So the asymptotic thermal boundary layer thickness is constant and is thicker than the velocity boundary layer thickness by a factor of $1/\text{Pr} = 1.4$ for air.

2.2.5 Convection Heat Loss

These results are now applied to an unglazed transpired solar collector. In the asymptotic region the thermal boundary layer thickness is constant because there is no net flux of heat into the boundary layer. All the heat conducted into the boundary layer is removed convectively by the suction air. In the starting length, on the other hand, the velocity and thermal boundary layers grow because there is a net flux of momentum and heat into the free stream. The total amount of heat lost from the plate into the boundary layer along the starting length will be the same as the heat carried off by the air flowing off the far end of the plate, as can be seen by a simple energy balance on the boundary layer. To determine the amount of this heat loss, one can either integrate (over x) the net heat flux over the starting length or integrate (over y) the heat flux leaving the far end of the plate.

Since the velocity and temperature profiles in the asymptotic region are known, performing the second integration is straightforward. The energy per unit plate width leaving the far end of the plate is:

$$\frac{Q_{\text{conv}}}{W} = \int_0^{\infty} \rho c_p u(y) [T(y) - T_{\infty}] dy \quad (2-13)$$

where W is the collector width in meters.

It is convenient to define an equivalent convection heat loss length, L_e , to be the length of plate which

multiplied by the net radiant heat flux equals the convective heat losses per unit width off the end of the plate. Substituting equations (2-4) and (2-10) into equation (2-13) and performing the integration yields:

$$L_e = \frac{Q_{conv}}{Wq''} = \frac{U_a}{v_o^2} \left[\frac{v}{Pr + Pr^2} \right] \quad (2-14)$$

or,

$$L_e \approx \frac{L_s}{Pr + Pr^2} \quad (2-15)$$

Figure 2-3 shows equivalent convective loss lengths for air flow at various wind speeds and suction velocities.

For a wind speed of 10 m/s, a suction velocity of .05 m/s, and an average temperature of 30°C, for which $Pr = .71$, the equivalent length would be only 5 cm. Thus the convective heat losses are equivalent to the net solar energy on a 5 cm wide strip of collector and would be negligible for a large collector.

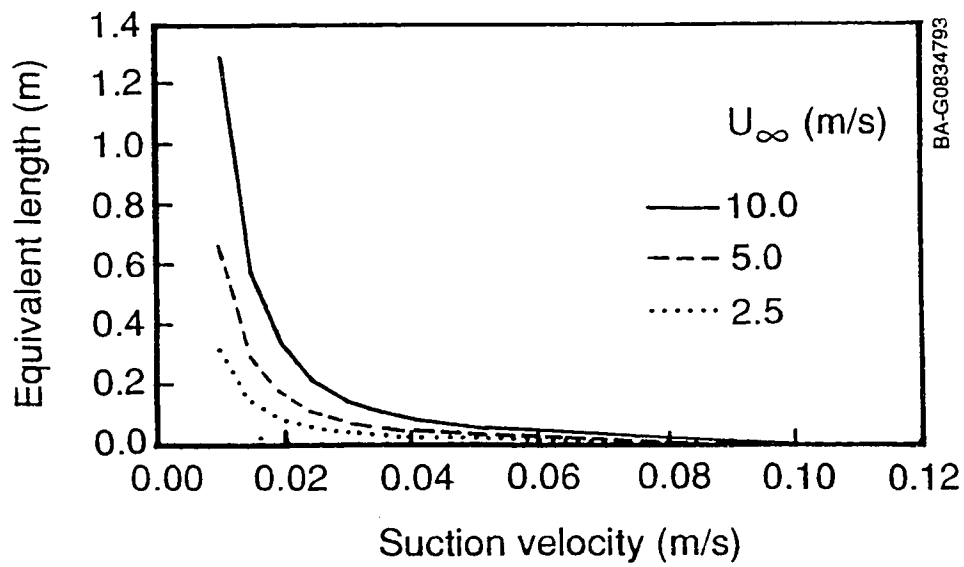


Figure 2-3. Calculated equivalent convection heat loss length versus suction velocity at various wind speeds.

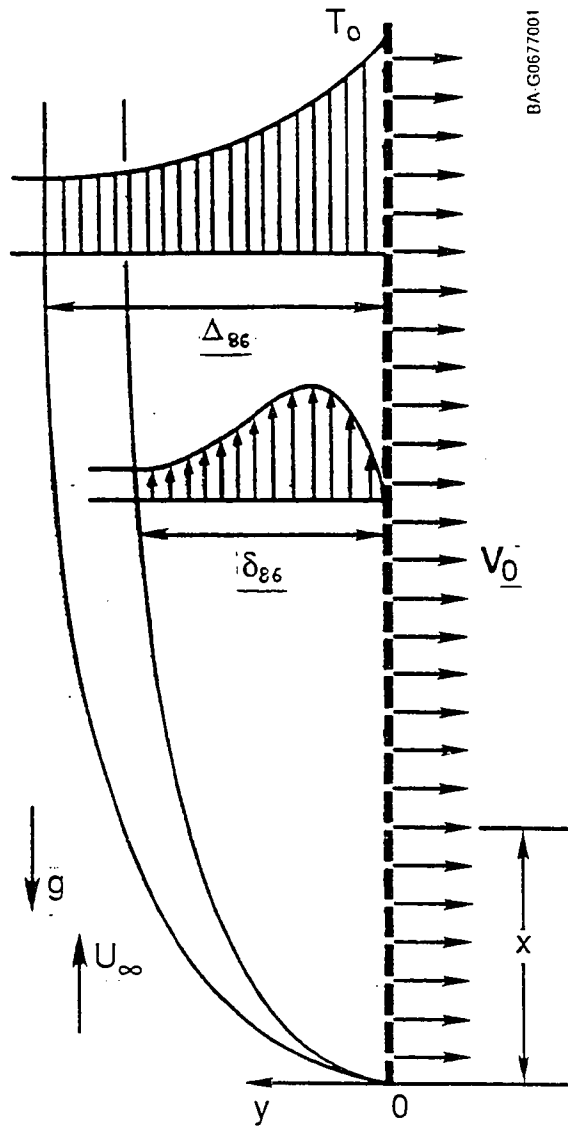
2.3 Laminar Free Convection

2.3.1 Velocity Profile

Up to this point only forced convection has been discussed. Heat loss will also occur by natural convection, and one might expect that this could be an especially important term when there is no wind. The theory for natural convection for a vertical collector (see **Figure 2-4**) is presented in this section. The governing equations are the same as before, but now the x-momentum equation contains a buoyancy term.

A scale analysis (Bejan 1984) indicates that the thermal and velocity boundary layers for a non-porous wall grow as $x^{1/5}$ for a constant heat flux wall. As was the case for forced convection, transition to turbulence will eventually occur, in this case when the Rayleigh number ($Ra = g\beta[T_s - T_\infty]L^3/\nu$, where T_s is the surface temperature, g is the gravitational acceleration in m/s^2 , and β is the thermal expansion coefficient in K^{-1}) exceeds a value of about 10^9 .

In the case of suction, one follows exactly the same reasoning as for the forced convection case. At a sufficiently great distance up the wall, one expects an asymptotic solution in which u is a function of y only and $v = -v_0$ everywhere. The x-momentum equation is linear:



BA.G067001

Figure 2-4. Velocity and thermal boundary layers for laminar free convection over a flat plate with suction.

$$-v_0 \frac{du}{dy} = \beta g (T - T_\infty) + \nu \frac{d^2u}{dy^2} \quad (2-16)$$

The boundary conditions are: At $y = 0$, $u = 0$ and $dT/dy = -q''/k$ (constant heat flux wall); at $y = \infty$, $u = 0$ and $T = T_\infty$.

The energy equation and its boundary conditions are exactly the same as for the forced convection case. Thus the temperature profile is the same as for forced convection, and the wall temperature is again constant in the asymptotic region. Because the temperature profile is the same as for the forced convection case, so is the thermal boundary layer thickness.

To obtain the velocity profile the temperature profile is substituted into the x-momentum equation and integrated to obtain (Arpaci and Larsen 1984):

$$u = \frac{\beta g \alpha^2 q''}{v_0^3 k (Pr - 1)} \left(e^{-\frac{1}{Pr} \frac{v_0 y}{\alpha}} - e^{-\frac{v_0 y}{\alpha}} \right) \quad (2-17)$$

The velocity boundary layer thickness is constant in the asymptotic region (although it cannot be defined in the same way as in the forced convection case). One can determine the distance from the wall at which the maximum velocity occurs by differentiating equation (2-17) and setting it to zero, thus obtaining:

$$y = \frac{\alpha}{v_0} \frac{\text{Pr} \ln(\text{Pr})}{\text{Pr}-1} \quad (2-18)$$

Substituting equation (2-18) back into (2-17), yields for the maximum velocity:

$$u_{\max} = \frac{\beta g \alpha^2 q''}{v_0^3 k (\text{Pr}-1)} \left(e^{-\frac{\ln \text{Pr}}{\text{Pr}-1}} - e^{-\frac{\text{Pr} \ln(\text{Pr})}{\text{Pr}-1}} \right) \quad (2-19)$$

For air at 30°C, a suction velocity of 0.05 m/s, and a heat flux of 1000 W/m², the maximum free convection velocity is only 0.002m/s and occurs at a distance of 3.8 X 10⁻⁴m from the wall.

2.3.2 Convection Heat Loss

Using the known solutions for the velocity and temperature profiles in the asymptotic region, one can now integrate to determine the convective heat loss as was done for the forced convection case and obtain the equivalent convection heat loss length as:

$$L_e = \frac{Q_{\text{conv}}}{W q''} = \frac{\beta g \alpha^3 q''}{v_0^5 k (\text{Pr}-1)} \left(\frac{\text{Pr}}{\text{Pr}+1} - \frac{1}{2} \right) \quad (2-20)$$

For a suction velocity of $v_0 = 0.05$ m/s, a heat flux of 1000 W/m², and properties of air at 30C, the thermal equivalent plate length for convective heat loss is 1.3x10⁻⁵m. Thus for typical suction rates that would be

used for ventilation preheat, end heat loss due to natural convection is negligible. This is because even though the asymptotic thermal boundary layer thickness and temperature profile are the same as for the forced convection case, the velocities caused by natural convection are much lower than for typical forced convection conditions as shown in the previous section. This greatly limits the heat loss over the wall edge.

2.4 Turbulent Forced Convection

2.4.1 Wall Turbulence

In the application of a transpired solar collector, the flow may be turbulent due to imperfect wall conditions (edge effects, discrete suction holes, surface roughness, corrugations, etc.).

Considerable research on transpired flat plates with wall turbulence was done at Stanford (Moffat and Kays 1984). Their experiments looked at the effects of pressure gradient, roughness, and surface curvature on heat transfer from a constant temperature wall with suction or injection. By writing the momentum and energy boundary layer equations in integral form (which is valid for both laminar and turbulent boundary layers), they show that in the asymptotic region the skin friction coefficient (C_f) and Stanton number (St) become simply:

$$\frac{C_f}{2} = St = \frac{v_0}{U_\infty} \quad (2-21)$$

The latter part of this equation is equivalent to the earlier statement that all of the net wall heat flux goes into the suction fluid. Thus an asymptotic boundary layer has been reached when the above conditions are met.

Distinctions between laminar and turbulent asymptotic layers are described by Dutton (1958). Dutton tested both nylon fabric and a perforated plate and found that the turbulent boundary layer reaches a constant thickness for suction ratios, v_0/U_∞ , greater than .0073, although it appears from his graphs that an asymptotic turbulent state might have eventually been reached at greater distances down the plate for lower suction rates. Dutton found that the inner part of the turbulent boundary layer resembled the laminar asymptotic profile, and, when v_0/u_∞ reached .01, the entire boundary layer achieved the laminar asymptotic shape. Moffat and Kays (1984) indicate that for suction rates of v_0/u_∞ greater than .004, the turbulent boundary layer reverts to an asymptotic laminar boundary layer. It would appear that whether the asymptotic boundary layer is laminar or turbulent depends not only on the suction rate, but on the surface condition and the upstream history. Thus a boundary layer which has not transitioned might reach a stable laminar asymptotic state, whereas one that

has become turbulent before suction is applied could have an asymptotic turbulent profile and require greater suction to relaminarize.

2.4.2 Convective Heat Loss

As is the case with any turbulent flow problem, one must rely on empirical data. Verrolet, et al. (1972) report experimental velocity and temperature profiles for a range of suction rates. Unfortunately, the highest ratio of suction to free stream velocity tested was only 0.003. (For a typical ventilation application, this ratio would be 0.020 for a 2.5 m/s wind.) Even for this suction ratio, the thermal boundary layer had not quite become asymptotic at the point where temperatures were measured.

Nevertheless, to get a rough estimate of convective heat losses these experimental profiles were used in numerically performing the same type of integration as for the laminar cases. The result showed convective heat loss for the turbulent boundary layer about an order of magnitude larger than for the laminar asymptotic boundary layer. At the higher suction ratios of interest here, one would expect this difference to be considerably less. Data covering the solar collector operational regime are needed to provide a better estimation of convective heat loss.

The preceding discussion applies to forced convection. Although discrete suction sites or surface roughness could

theoretically cause turbulence in a transpired free convection situation, the velocities along the wall and convective heat losses are so small for the laminar case that one would expect the larger heat losses for the turbulent case to also be negligible. In fact, for the air temperature rise typical of a ventilation preheat application, it can be shown that even a non-transpired collector would have a small free convection heat loss. In any case, no empirical velocity and temperature profile data could be found in the literature for turbulent asymptotic free convection boundary layers with either homogeneous or discrete suction. Such data could be useful for studying transpired collectors working at higher temperatures.

2.5 Collector Efficiency

2.5.1 Predictive Model

Based on the previous analysis, one can assume that natural convection heat losses are negligible. For forced convection with high suction ratios one can also assume an asymptotic laminar boundary layer. Hence, from equations (2-11) and (2-14) the convective heat loss term can be expressed as:

$$Q_{\text{conv}} = 0.82 \left(\frac{U_{\infty} v}{v_o^2} \right) W [\rho c_p v_o (T_{\text{coll}} - T_{\text{amb}})] \quad (2-22)$$

Having determined approximate expressions for the convective and radiative heat losses, the solution for the collector efficiency can now be completed, provided that the heat exchange effectiveness for the air flow through the absorber is known. (For a homogeneous suction absorber such as a fabric, this can be taken as close to one.) Substituting the relationships for Q_{rad} , and Q_{conv} into equation (2-1) one is left with one equation in one unknown, T_{coll} . This nonlinear equation is iterated to find T_{coll} . Once T_{coll} is known, the collector efficiency is given as:

$$\eta = \frac{\rho c_p v_o e_{\text{HX}} (T_{\text{coll}} - T_{\text{amb}})}{I_c} \quad (2-23)$$

2.5.2 Model Results

The simple model allows one to investigate various performance sensitivities. Figure 2-5 shows predicted thermal performance for a vertical unglazed transpired solar collector with unit heat exchange effectiveness as a function of suction velocity for wind speeds of 0 and 5 m/s and absorber emissivities of 0.9 and 0.2. Assumptions are a collector size of 3 m x 3 m, $T_{\text{amb}} = 10^\circ\text{C}$, $T_{\text{sky}} = T_{\text{amb}} - 15^\circ\text{C}$,

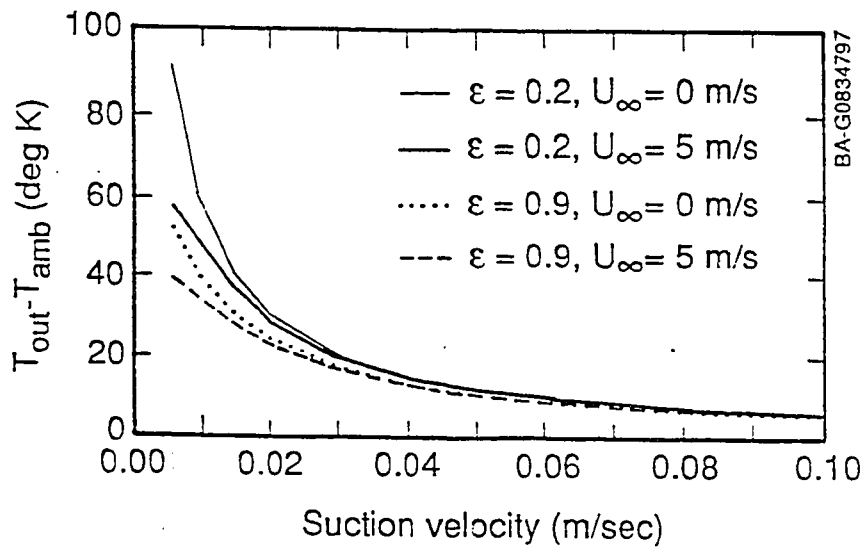
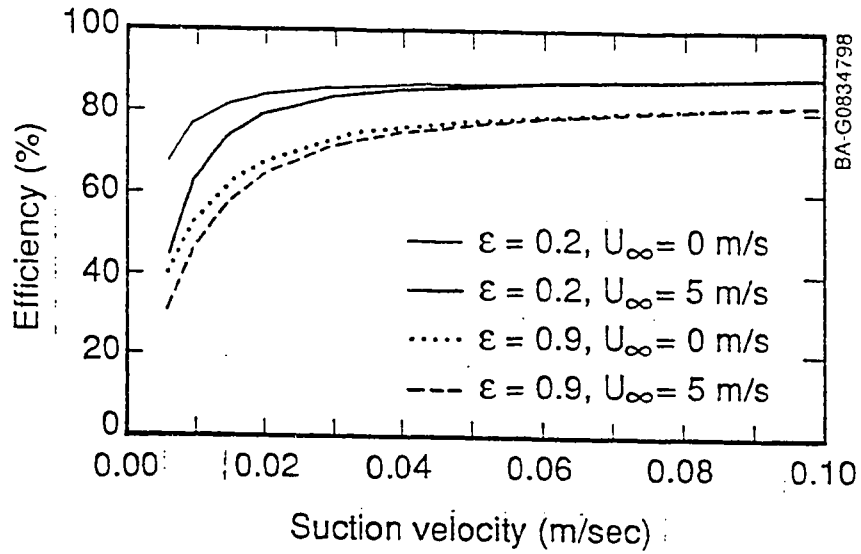


Figure 2-5. Predicted thermal performance of a vertical unglazed transpired solar collector as a function of suction velocity, absorber emissivity, and wind speed.

$T_{\text{gnd}} = T_{\text{amb}}$, and $I_c = 700 \text{ W/m}^2$ and a heat exchange effectiveness of one. The efficiency of the unglazed transpired solar collector is influenced by the fact that radiation losses are directly to ambient but there is no glazing optical penalty. For suction velocities greater than 0.05 m/s , efficiencies are nearly constant and independent of wind speed. As suction velocity decreases, the effect of wind speed on collector efficiency increases, especially for the low emissivity absorber. The benefits due to the low emissivity absorber generally increase as the suction velocity decreases. For once-through applications, the collector inlet temperature equals the ambient temperature. Therefore, $T_{\text{out}} - T_{\text{amb}}$ indicates the collector temperature rise and, indirectly, the delivered air temperature. Except at lower suction velocities, the effect of absorber emissivity on efficiency is more important than the effect on delivered air temperature.

For a typical ventilation preheat suction velocity of 0.05 m/s , the collector temperature rise is approximately $12 \text{ }^\circ\text{C}$ regardless of absorber emissivity, and efficiencies are approximately 78% and 84% for absorber emissivities of 0.9 and 0.2, respectively.

Because of the importance of radiation heat loss, as the ambient temperature drops so does the surface temperature, and thus efficiency increases with decreasing

ambient temperature. This effect is of course true for any solar collector, but is especially so for this one. Chau and Henderson (1977) and others have noted the magnitude of this effect for matrix absorbers.

2.6 Issues and Discussion

This section briefly discusses a number of issues related to the above analysis. The major issue which this dissertation addresses, namely the determination of heat exchange effectiveness for a discrete hole absorber, is discussed separately in Section 2.7

2.6.1 Pressure Drop Considerations

For a transpired collector one needs a sufficiently high pressure drop across the absorber to provide reasonably uniform flow. Typical rules of thumb used for header sizing would dictate a ΔP across a transpired wall on the order of 10 times the ΔP in the plenum behind the wall. Also, researchers in the area of boundary layer control for wings noted the importance of maintaining sufficient pressure drop across the surface to prevent any localized outflow. To prevent any local outflow on a transpired wall, the ΔP must also be high enough to overcome local negative pressure coefficients.

For wall applications the effect of flow around the building is important. Low pressures will occur on the

leeward face of a building and anywhere where the flow separates or velocities are high such as at edges and corners. Davenport and Lui (1982) report mean local pressure coefficients on a smooth building wall as low as -1.2, while Murakami (1990) reports local values as low as -2.0. In addition Arens and Williams (1977) point out that local pressures can drop much further due to the effects of surface irregularities such as casements. In the case of a transpired wall, if corrugations are used in the absorber to provide structural rigidity, local outflow could occur if the wall does not have a sufficient ΔP to overcome the low local pressures just downwind of ridges.

For a perforated metal plate, the pressure drop is roughly proportional to the square of the velocity, and the open area ratio, or porosity, is the most important design parameter (Gregory 1961). Porosities of about 1 percent should provide sufficient pressure drop. Clearly, however, one does not want to use a higher ΔP than absolutely needed or fan power would be wasted. For a 1% porosity, in a transpired wall, at a flow rate of 0.05 m/s, a ΔP of 50 Pa would provide positive suction over an entire smooth wall in wind speeds as high as 10 m/s. Assuming a fan efficiency of 20%, this corresponds to a power requirement of 16W/m². For a wall operating at an efficiency of 80% with an average solar flux of 500W/m², the fan power represents about 4% of the average energy collected. Thus

it appears that pressure drop requirements are reasonable. The results of detailed testing on perforated plates to obtain an accurate correlation for pressure drop as a function of porosity and hole Reynolds number are given in Chapter 4.

2.6.2 Extension to Discrete Suction

As stated earlier, this theory is valid for perfectly homogeneous suction. According to Wuest (1968) suction can be considered homogeneous if the spacing between pores is less than the boundary layer thickness, a criterion not met for typical solar collector applications. Aeronautics researchers (Lachmann 1961) found that suction through discrete holes can actually cause transition to turbulence by bending vorticity lines which run parallel to the plate and perpendicular to the flow. The resulting vortex stretching and bending results in streamwise vorticity which can precipitate transition to turbulence. The asymptotic boundary layer will still have a constant average thickness whether it is laminar or turbulent, but its local thickness will vary at each point depending on the point's distance from suction sites. Thus a perforated plate can be expected to have an asymptotic boundary layer with a dimpled shape.

Dutton (1960) found that for a perforated plate, when the suction rate was sufficient to produce a laminar

asymptotic layer, the average thickness of this layer was the same as one would expect if the same total mass influx were uniformly distributed. In addition, he obtained approximately the same turbulent boundary layer thicknesses for a nylon fabric surface as for a perforated plate. However, these data were for higher free stream velocities and closer hole spacings than might be encountered for transpired absorber applications. Thus more research is needed to determine how well the simple theory applies to this new application.

2.6.3 3-D and Non-Parallel Flow

The previous derivation for convective heat losses assumes that the boundary layer is parallel to the absorber and convects heat over only one edge. Sparrow, Ramsey, and Mass (1979) show that for wind impinging on the collector at large attack angles, a stagnation area will be created and 3-dimensional flow can occur off many edges, thereby increasing the loss above what was assumed. Thus the above value must be multiplied by a correction which will depend on wind direction. However, for large building wall applications, it is reasonable to assume that the local wind is in a direction parallel to the wall.

2.6.4 Free Stream Turbulence

An additional issue not addressed by the basic theory is the impact of free stream turbulence. With the high mean velocities encountered for airplane wings, the turbulent velocity fluctuations of the atmosphere are usually neglected in studies of wing boundary layer control. However, in tests of conventional flat plate collectors in actual wind conditions, some researchers have found that heat loss coefficients can increase several fold due to the free stream turbulence in the wind.

Test, Lessman, and Johary (1981) found that in outdoor testing of a flat plate with an attack angle to the wind of 40° , the curve of heat loss coefficient versus distance along the plate was similar in shape to what one would expect for a laminar boundary layer, but the heat loss coefficient was about twice as large. The higher values than one would expect based on low-turbulence wind tunnel tests corresponded to the higher turbulence intensities experienced outdoors. Significantly, free stream turbulence increased the heat loss without causing transition of the laminar boundary layer.

In a later study, McCormick, Test, and Lessmann (1984) created turbulence intensities higher than typical outdoor values by using a set of horizontal slats in a wind tunnel. They found that the turbulence increased the velocity gradient at the wall and thickened the boundary layer. At

the highest turbulence intensities (on the order of 30%) the boundary layer behaved as if it were turbulent, but the velocity profiles differed from what one expects from a classic turbulent boundary layer resulting from wall friction. Free stream turbulence could increase the heat loss from a transpired wall as it does for a non-transpired wall. All tests done in this study were with a laminar flow stream; however, tests run with a tripped boundary layer and outdoor testing indicate that for a transpired collector free stream turbulence does not appear to have a major effect. More work on this is planned for the future.

2.7 Heat Exchange Effectiveness

Because the radiation heat loss is based on surface temperature, T_{coll} , one needs to relate this to the outlet temperature. For an absorber with homogeneous suction, these temperatures are the same. Surfaces such as a porous concrete or a finely woven fabric will approach this situation. However, for a surface such as a perforated metal plate, the outlet air temperature will be below the surface temperature. One can relate T_{out} and T_{coll} via a heat exchange effectiveness:

$$\epsilon_{HX} = \frac{T_{out} - T_{amb}}{T_{coll} - T_{amb}} \quad (2-24)$$

The impact of heat exchange effectiveness on collector efficiency is shown in **Figure 2-6**. Note that efficiency is degraded for heat exchange effectiveness values less than about 70%.

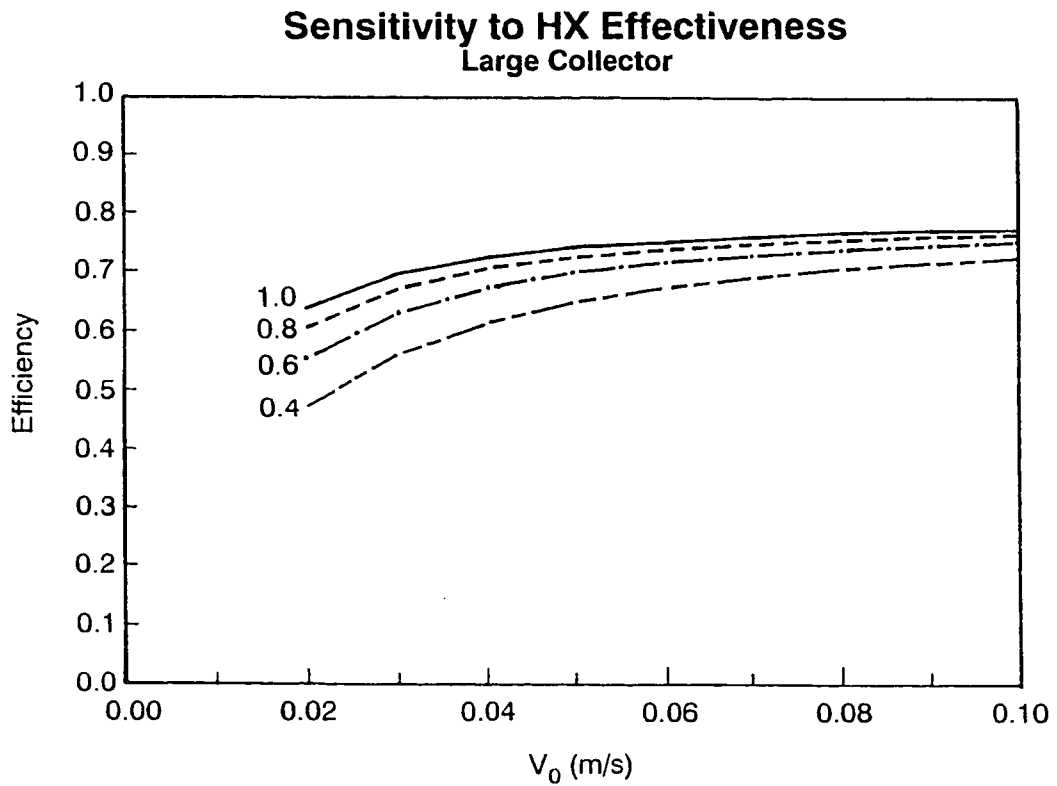


Figure 2-6. Impact of heat exchange effectiveness on collector efficiency.

2.7.1 Previous Work

2.7.1.1 Sparrow and Ortiz (1982)

The first focused work on heat transfer to normal flow through a perforated plate was that of Sparrow and Ortiz (1982), which was mentioned in the background section. They first performed flow visualization on a perforated plate using an oil-lampblack mixture to show that for a staggered hole array (i.e. holes on equilateral triangular centers) unit hexagonal cells are formed with the edges of each hexagon representing adiabatic boundaries and dividing streamlines. To perform their experiment, they milled out a hexagonal unit cell surrounding a hole in the center of a perforated aluminum plate containing 19 holes. They then filled this area with naphthalene and used a metal sleeve within the hole to protect the edge of the naphthalene. The plate was then weighed on a balance readable to 0.1 mg. Air was then drawn through the plate for a period of time sufficient to provide a loss of at least 13 mg of naphthalene due to sublimation, and the plate was reweighed after the experiment.

Knowing the mass of naphthalene sublimated and the densities of naphthalene vapor at the surface and at infinity (taken as zero), the Sherwood number can be computed. The Sherwood number is exactly analogous to the Nusselt number, while the Schmidt number (2.5 for

naphthalene) is analogous to the Prandtl number. Extrapolation of the results to air is made by assuming a Prandtl dependence of $Pr^{1/3}$.

Sparrow and Ortiz performed their experiment for a Reynolds number range of 2,000 to 20,000. Unfortunately, they covered only two closely spaced values of hole pitch-to-diameter, 2.0 and 2.5 representing porosities of 14 and 22%, whereas porosities of 2% or less are of interest here. (Pitch is the distance between the center of a hole and the center of the next closest hole.) Also, only front surface heat transfer was covered.

In examining the Sparrow and Ortiz correlation for front surface heat transfer, it would appear dangerous to extrapolate it to low porosities. The correlations obtained for the two P/D ratios (where P is pitch and D is hole diameter, both in meters) were as follows:

$$Nu_p = 1.78Re^{0.476}, \quad P/D=2.0 \quad (2-25)$$

$$Nu_p = 1.62Re^{0.476}, \quad P/D=2.5 \quad (2-26)$$

where Nu_p is a Nusselt number based on hole pitch, or hP/k .

Note that the characteristic length chosen for the Nusselt number is the pitch, while the length chosen for the Reynolds number is hole diameter. They tried other length scales to collapse all of the data onto one curve and settled on the following correlation:

$$\text{Nu}_{L^*} = 0.881 \text{Re}^{0.476} \text{Pr}^{1/3} \quad (2-27)$$

where $L^* = A/P$ and A is the surface area of a unit cell in m^2 .

Although this provided a good fit, there is no clear physical reason for choosing these length scales. In addition, the two P/D values did not differ very much to begin with, and there is more than one way the data could be collapsed. For example, if one bases both the Nusselt and Reynolds numbers on the pitch, the two correlations would be as follows:

$$\text{Nu}_p = 2.64 \text{Re}_p^{.476}, \quad P/D = 2.0 \quad (2-28)$$

$$\text{Nu}_p = 2.69 \text{Re}_p^{.476}, \quad P/D = 2.5 \quad (2-29)$$

Thus a single correlation based on pitch only with a coefficient of 2.66 or 2.67 would agree with the separate correlations to within about 1%.

It is interesting to note that for laminar stagnation flows, heat transfer coefficients typically vary as the inverse square root of a characteristic length, e.g. the radius of a cylinder or sphere (Kays and Crawford 1980). Sparrow, Tao, and Radtke (1983) show naphthalene sublimation results for a flat plate with parallel slots and give a correlation for the heat transfer coefficient which varies inversely with the square root of spacing

between slots (i.e., pitch) in the limit of zero porosity. However, the Sparrow and Ortiz heat transfer coefficient for holes varies roughly with $D^{-.476}P^{-.048}$ (i.e. very little pitch dependence) in the low porosity limit.

Rewriting the Sparrow and Ortiz hole correlation using pitch as the characteristic length scale for both Nu and Re gives a dependence on the inverse square of pitch in the low porosity limit. However, the flow patterns near holes are certainly different from those near slots, and the effect of the flow accelerating toward and turning into the holes makes this problem significantly different from a classic stagnation flow problem. Without data over a wide range of P/D, one cannot be confident with either Sparrow's correlation or a modification of it. The author spoke with E. M. Sparrow, and he agreed that his results should not be extrapolated to low porosities and indicated that experimental work is needed to cover that range.

2.7.1.2 Kumada, Hirata, and Kasagi (1981)

This study determined local heat transfer coefficients for full-coverage film cooling of a curved perforated plate for application to turbine blades. Although film cooling involves injection, this study examined not only heat transfer coefficients on the film-cooled side but on the back, or suction side, as well. Naphthalene sublimation was also used here, but in this case the entire perforated

plate was made out of naphthalene and the mass loss was determined from electronic micrometer depth measurements instead of weight measurements. This allowed measurement of local values of heat transfer coefficient on the suction side near holes.

Only one plate was studied: $P/D = 5$ with holes slanted at 30° and with a naphthalene depth of 4 mm. The free stream velocity parallel to the plate on the film-cooled side was 20 m/s and hole Reynolds numbers were also high, the minimum being 5,000. They showed that most of the heat transfer occurs near the hole. This is very different from typical stagnation flows in which the heat transfer coefficient is relatively constant in the stagnation region (Kays and Crawford 1980). The flow behaves quite differently from a stagnation flow once it approaches a hole and rapidly accelerates.

The average Stanton number on the back side was correlated as:

$$\overline{St}_B = 9.47 \times 10^{-3} Re_D^{-1/3} \quad (2-30)$$

where

$$\overline{St}_B = \overline{h} / (\rho v_0 c_p) \quad (2-31)$$

and

$$Re_D = v_0 D / \nu$$

(2-32)

Note that this corresponds to a dependence of h on suction velocity to the $2/3$ power in contrast with Sparrow and Ortiz who give an exponent of .476.

2.7.1.3 Hubbell and Cain (1988)

This was an experimental and analytical study of perforated plate heat exchangers. Single blow transient tests were done. A step decrease was made in the inlet air temperature, and the decay of outlet temperature was measured. Hole size, porosity and plate thickness were varied. Porosities tested ranged from 9% to 24.5%. Hole Reynolds numbers (defined as in Sparrow's case) were in the range of 4 to 666.

In order to analytically predict performance, the heat transfer at each plate was divided into three segments: front surface, hole, and back surface. Hubbell and Cain could not find a correlation for front surface heat transfer on a perforated plate (Hubbell indicated in a telephone conversation that they were unaware of Sparrow's work), and so they used a correlation for stagnation flow over a cylinder. They then assumed that the heat transfer on the back surface was the same as on the front surface. For the hole they used two laminar flow models: developing velocity profile in a pipe and fully developed parabolic velocity profile.

Their model considerably overpredicted the experimental data. The authors believed this was due to flow separation in the holes decreasing the hole heat transfer. As will be shown in the numerical modeling results later, using the same heat transfer coefficient on the back of the plate as on the front would cause an overestimation of back surface heat transfer. In addition, use of a correlation for stagnation flow over a cylinder for the front surface is not accurate. Finally, the interactions of the various parallel plates were not considered.

Their correlations for NTU showed that the Reynolds number exponent varied with the porosity, ranging from -.372 for a 9% open area plate to -.569 for a 24.5% porosity plate. This could be because surface flow and hole flow have different Reynolds numbers dependencies and/or because of the multiple plate geometry. Although the latter problem is not of interest here, the former also exists in the case of transpired absorbers and might make it difficult to find a one-term correlation which describes perforated plate heat transfer for a range of hole sizes and spacings.

2.7.1.4 Andrews et al.

Andrews, et. al., 1987 and Andrews, et. al., 1989 conducted a series of overall heat transfer tests on

perforated plates to develop a correlation useful for film cooling applications. All plates tested were 6.35 mm thick and had a square array of holes. A wide range of hole diameters and spacings was tested. The range of suction mass flow rate was from 0.1 to 1.7 kg/m²-s. Thus the case studied here differs in that the plates are thinner, the holes are in a close-packed array, and the suction mass flow rates are an order of magnitude lower, which results in a laminar flow regime and heat exchange effectiveness values close to one.

Andrews, et. al conducted transient cool-down tests on horizontal 152 mm square Nimonic 75 perforated plates. An overall heat transfer coefficient based on the difference between plate and approach temperature was directly inferred from the slope of the log temperature curve. Evidently, no correction for radiation heat loss from the plate was made. The best fit obtained for all of their data was:

$$\text{Nu}_p = 2.44 \left(\frac{P}{D} \right)^{-1.43} \text{Re}_D^{0.57} \text{Pr}^{0.33} \quad (2-33)$$

which is said to cover $500 < \text{Re}_D < 43,000$, $1.9 < P/D < 22$, and $0.8 < t/D < 9.9$.

2.8 Integral Solution

For perpendicular flow through a perforated plate, one expects most of the heat transfer to occur on the front surface. Direct solution of the Navier-Stokes equation is not possible due to the non-linearities. It makes sense to next look at the boundary layer equations. A similarity solution is, unfortunately, not possible because the flow domain is finite. The next best analytical approach is an integral solution of the boundary layer equations. Based on flow visualization by Sparrow, for flow through a perforated plate with a staggered array of holes, each hole is surrounded by a hexagonal flow tube. One can approximate this hexagonal tube with a circular tube of the same cross-sectional area, thus allowing a two-dimensional axisymmetric model.

Solving the axisymmetric integral boundary layer equations proves difficult. However, one can solve the analogous two-dimensional case, and then perform a Mangler transformation to get the axisymmetric solution. The far-field flow can be obtained from the inviscid solution to this problem. Although a solution via Schwarz-Christoffel transformation exists for flow through a finite slot on an infinite plate (Currie, 1972, pp. 125-131), the result is an implicit expression for the complex potential which unfortunately cannot be solved explicitly for the flow field. Also, the case of interest here differs in that the

approaching flow is confined. A solution is available for two-dimensional channel flow into a sink. For the plates of interest, porosities are very low, so assuming an infinitesimally small slit is not necessarily a bad approximation.

Using this as the far field flow, the Spalding-Smith method (based on the Thwaites method) was used for solution of the thermal boundary layer thickness. Having obtained the slit solution, the Mangler transformation was applied to get the thermal boundary layer thickness around the hole.

This solution is now discussed in detail. First, the two-dimensional case of flow toward an infinitesimal slot is solved. From Currie, the complex potential for a line sink in a channel is:

$$F(z) = -\frac{m}{\pi} \ln\left(\sinh \frac{\pi z}{2l}\right) \quad (2-34)$$

where the channel width is $2l$. The total fluid entering the sink is $m = 4lV$, where V is the approaching far-field velocity. Thus,

$$F(z) = -\frac{4lV}{\pi} \ln\left(\sinh \frac{\pi z}{2l}\right) \quad (2-35)$$

For an integral solution on the plate, one is interested in the velocity component parallel to the plate, or perpendicular to the channel. The complex velocity is

$$W(z) = u - iv = \frac{dF}{dz} \quad (2-36)$$

Differentiating $F(z)$, yields

$$W(z) = -2V \coth \frac{\pi z}{2l} \quad (2-37)$$

Now

$$\begin{aligned} \coth z &= \frac{\sinh 2x - i \sin 2y}{\cosh 2x - \cos 2y} \\ &= \frac{\sinh 2x}{\cosh 2x - \cos 2y} - i \frac{\sin 2y}{\cosh 2x - \cos 2y} \end{aligned} \quad (2-38)$$

Of interest is the velocity component parallel to the plate, i.e., the v velocity, or $-\text{Im}[W(z)]$. So,

$$\begin{aligned} v &= -\text{Im}(-2V \coth \frac{\pi z}{2l}) \\ &= -2V \frac{\sin \frac{\pi y}{l}}{\cosh \frac{\pi x}{l} - \cos \frac{\pi y}{l}} \end{aligned} \quad (2-39)$$

For a thin boundary layer, the v velocity near the plate is found by taking the limit of v as x approaches zero,

$$\lim_{x \rightarrow 0} v = -2V \sin \frac{\frac{\pi y}{l}}{1 - \cos \frac{\pi y}{l}} = -2V \cot \frac{\pi y}{2l} \quad (2-40)$$

Switching coordinates and now taking x as the direction parallel to the plate and u as the local velocity in the x -direction, the inviscid velocity parallel to the plate outside the boundary layer is:

$$u(x) = 2V \cot \frac{\pi x}{2l} \quad (2-41)$$

Smith and Spalding (1958) extended the Thwaites method of integral boundary layer solution to thermal boundary layers. The conduction boundary layer thickness is:

$$\delta_t = \frac{k(T_s - T_\infty)}{q''} \quad (2-42)$$

A dimensionless parameter, Λ_t , is formed analogous to the pressure gradient parameter, Λ_x :

$$\Lambda_t = \frac{\delta_t^2}{\nu} \frac{dU_\infty}{dx} \quad (2-43)$$

where U_∞ is the external inviscid flow. One then needs a correlation of the form:

$$U_{\infty} \frac{d}{dx} \left[\frac{-\Lambda_t}{dU_{\infty}/dx} \right] = F_t(\Lambda_t, Pr) \quad (2-44)$$

Smith and Spalding fit the function F_t as:

$$F_t = a(Pr) - b(Pr)\Lambda_t \quad (2-45)$$

with $a=9.072Pr^{-.70}$ and $b=2.95Pr^{.07}$.

For air with $Pr=.72$, $a=11.42$ and $b=2.88$. One thus has for the thermal boundary layer thickness,

$$\delta_t^2 = \frac{av}{U_{\infty}^b} \int_0^x U_{\infty}^{b-1} dx \quad (2-46)$$

Now in this coordinate system, $x=0$ at the center of the slot. But in this case $U_{\infty}(x)$ becomes infinite as x goes to zero. So a Galilean transformation is applied to coordinate $x'=1-x$ and the integration is performed from 0 (where $x=1$, or the start of the boundary layer) to x' at the edge of the hole. In terms of x' , U_{∞} is:

$$U_{\infty}(x') = 2V \cot \left[\frac{\pi}{2l} (1-x') \right] = 2V \tan \frac{\pi x'}{2l} \quad (2-47)$$

Plugging this into the equation for boundary layer thickness, yields:

$$\delta_t^2(x') = 11.42v \frac{1}{(2V \tan \frac{\pi x'}{2l})^{2.88}} \int_0^{x'} (2V \tan \frac{\pi x'}{2l})^{1.88} dx'' \quad (2-48)$$

This gives the thermal boundary layer thickness as a function of the distance from the stagnation line toward the slot. To solve the slot problem, this can be numerically integrated. However, since it is an approximate solution anyway, a further approximation is made, namely, take $2.88 \approx 3$ and $1.88 \approx 2$ so that the equation can be integrated analytically. Thus,

$$\delta_t^2(x') \approx \frac{11.42v}{(2V \tan \frac{\pi x'}{2l})^3} \int_0^{x'} (2V \tan \frac{\pi x'}{2l})^2 dx'' \quad (2-49)$$

Solving this one obtains

$$\delta_t^*(x^*) \approx \frac{1.91}{\sqrt{\frac{Vl}{v}}} \left[\frac{1}{\tan^2 \frac{\pi x^*}{2l}} - \frac{\frac{\pi x^*}{2l}}{\tan^3 \frac{\pi x^*}{2l}} \right]^{0.5} \quad (2-50)$$

where $x^* = x'/l$ and $\delta_t^* = \delta_t/l$ and x^* goes from 0 at the stagnation line to $1 - D/(2l)$ at the hole edge.

To obtain the axisymmetric solution, the Mangler transformation is applied to the 2-D case. Following the notation used by Panton (1984) and using a hat on variables to indicate plane flow and no hat to indicate axisymmetric

flow, the equation for boundary layer thickness for the 2-D case can be re-written as:

$$\delta_t(\hat{x}') \approx 1.91 \sqrt{\frac{vl}{V}} \left[\frac{1}{\tan^2 \frac{\pi \hat{x}'}{2l}} - \frac{\frac{\pi \hat{x}'}{2l}}{\tan^3 \frac{\pi \hat{x}'}{2l}} \right]^{0.5} \quad (2-51)$$

To perform the Mangler transformation, this is first transformed back to the unprimed coordinate system with $x=0$ at the center of the hole (i.e., the line of axisymmetry). Thus performing the Galilean transformation,

$$\hat{x}' = 1 - \hat{x} \quad (2-52)$$

to obtain

$$\delta_t(\hat{x}) \approx 1.91 \sqrt{\frac{vl}{V}} \left[\frac{1}{\tan^2 \left(\frac{\pi}{2} - \frac{\pi \hat{x}}{2l} \right)} - \frac{\frac{\pi}{2} - \frac{\pi \hat{x}}{2l}}{\tan^3 \left(\frac{\pi}{2} - \frac{\pi \hat{x}}{2l} \right)} \right]^{0.5} \quad (2-53)$$

Noting that $\tan(\pi/2 - \theta) = \cot\theta$,

$$\delta_t(\hat{x}) \approx 1.91 \sqrt{\frac{vl}{V}} \left[\frac{1}{\cot^2 \frac{\pi \hat{x}}{2l}} - \frac{\frac{\pi}{2} - \frac{\pi \hat{x}}{2l}}{\cot^3 \frac{\pi \hat{x}}{2l}} \right]^{0.5} \quad (2-54)$$

The Mangler transformation is:

$$\begin{aligned}\hat{x} &= \int_0^x \left(\frac{r_0}{L} \right)^2 dx \\ \hat{y} &= \frac{r_0}{L} y \\ \hat{u} &= u \\ \hat{v} &= \frac{L}{x} \left(v + \frac{y}{x} u \right)\end{aligned}\tag{2-55}$$

For this case $r_0 = x$ and using l in place of the arbitrary reference length L . The transformation equations thus become

$$\begin{aligned}\hat{x} &= \int_0^x \left(\frac{x''}{l} \right)^2 dx'' = \frac{1}{3} \frac{x^3}{l^2} \\ \hat{y} &= \frac{x}{l} y \\ \hat{u} &= u \\ \hat{v} &= \frac{1}{x} \left(v + \frac{y}{x} u \right)\end{aligned}\tag{2-56}$$

Substituting these into the equation for boundary layer thickness, making the additional substitution that $R = 3^{1/3} l$ and non-dimensionalizing based on length R gives the following result:

$$\delta_t^* = \frac{1.101}{\frac{r}{R} \sqrt{\frac{VR}{v}}} \left[\frac{\cot \frac{\pi}{2} \left(\frac{r}{R} \right)^3 + \frac{\pi}{2} \left(\frac{r}{R} \right)^3 - \frac{\pi}{2}}{\cot^3 \frac{\pi}{2} \left(\frac{r}{R} \right)^3} \right]^{0.5}\tag{2-57}$$

where r is distance from the hole in meters and R is the distance from the hole to the stagnation line (edge of flow tube), i.e., the maximum value of r (m).

The local Nusselt number (based on R) is simply the reciprocal of the non-dimensional thermal boundary layer thickness.

This shows the expected result of thinning rapidly as the hole is approached. **Figure 2-7** shows a comparison with numerical modeling results (see Chapter 3) indicating that the integral method predicts too small a boundary layer thickness (and thus too high a heat transfer coefficient) especially near the hole where the flow is turning.

Near the hole and, in general, at the low Reynolds numbers of interest, the boundary layer approximations break down. Also, because the boundary layer is thick, the assumption that the far-field flow parallel to the wall is equal to the limit of the inviscid flow solution at the wall is probably a poor assumption. Thus the integral boundary layer solution for point sinks on a plate does not do a very good job of predicting the low Reynolds number behavior of a plate with finite holes, although it does provide an understanding of the general boundary layer behavior. Although various types of improvements to the integral solution could be attempted, the additional complications they would entail and the availability of a full Navier-Stokes model (discussed in the next chapter) probably do not warrant this.

HEAT TRANSFER COEFFICIENT INTEGRAL SOLUTION VS. FLUENT

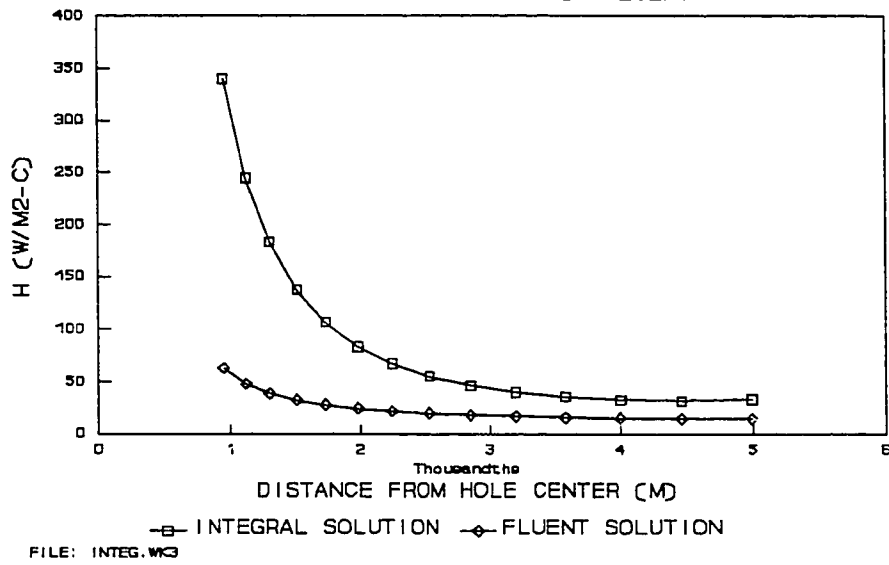


Figure 2-7. Comparison of front surface heat transfer coefficient from integral solution and FLUENT simulation, showing that boundary layer equations overpredict heat transfer.

Chapter 3. NUMERICAL MODELING

3.1 General Approach

A full Navier-Stokes model appears to be the best way to obtain a detailed understanding of the heat transfer mechanisms for flow through perforated plates. Again, for perpendicular flow, one can approximate the flow situation as that of flow through an orifice within a tube. It is interesting to note that although there are published results for modeling flow through orifices in a pipe, there has evidently not been any work on the heat transfer problem of a heated orifice. Also, the model presented here differs somewhat from a heated orifice in a pipe in that the "pipe walls" in this case are a symmetry rather than a no-slip boundary condition.

There are two basic ways to solve the axisymmetric problem: a stream function-vorticity model or direct solution of the Navier-Stokes (and energy) equations in primitive variables. NREL has obtained the FLUENT code which uses the latter method based on a finite volume approach.

3.2 Normal Flow Heat Exchange Effectiveness

A number of perforated plates were modeled using FLUENT. It turns out that in spite of the simplified geometry, this is not an easy problem for FLUENT, because

considerable detail is needed near the orifice, while the outlet boundary condition must be set far enough downstream to be beyond the downstream recirculation zone. Even using a variable grid, the number of nodes required is close to 6,000. Figure 3-1 shows the pitch and diameter dimensions of all plates modeled as well as tested. Because of problems obtaining convergence at low porosities, the FLUENT runs are restricted to a high porosity region. Note that two FLUENT models are of plates which were also experimentally tested: plates 5 and 9.

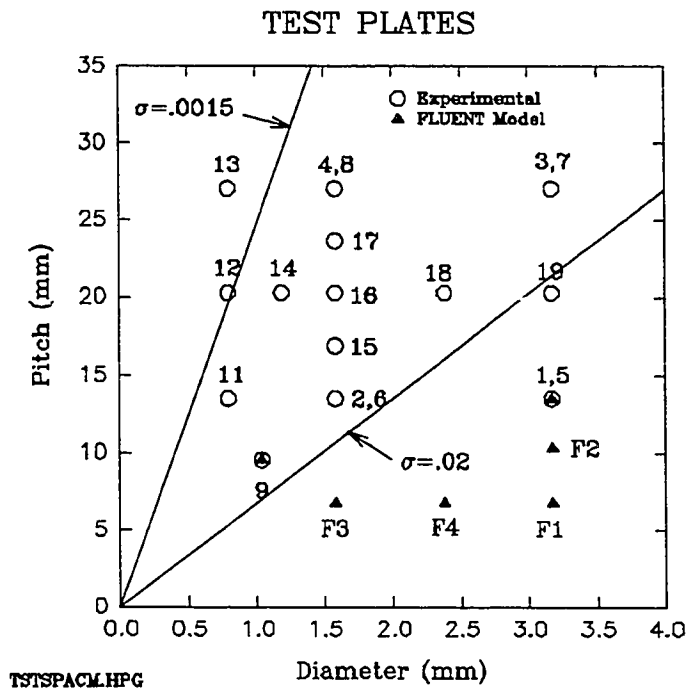


Figure 3-1. Plot showing pitch and diameters of all experimental and numerical test plates.

Figure 3-2 shows the grid used for modeling plate 9. **Figure 3-3** shows a plot of streamlines. (These are magnified plots focussing on the region near the plate. The actual outlet boundary is downstream of the recirculation zone.) **Figure 3-4** is a color plot of temperature. The thermal boundary layer profile on the front of the plate is clearly visible in **Figure 3-4**. Note that the boundary layer is quite thick, although it thins rapidly near the hole due to the acceleration. The overall thickness of the boundary layer and the turning of the flow into the hole suggest why the integral solution, based on the boundary layer equations, does not provide a better prediction of the front surface heat transfer. The jet shooting through the hole results in a recirculation zone on either side. Although the recirculation zone extends far downstream, a region of uniform outlet temperature is reached not very far downstream of the hole.

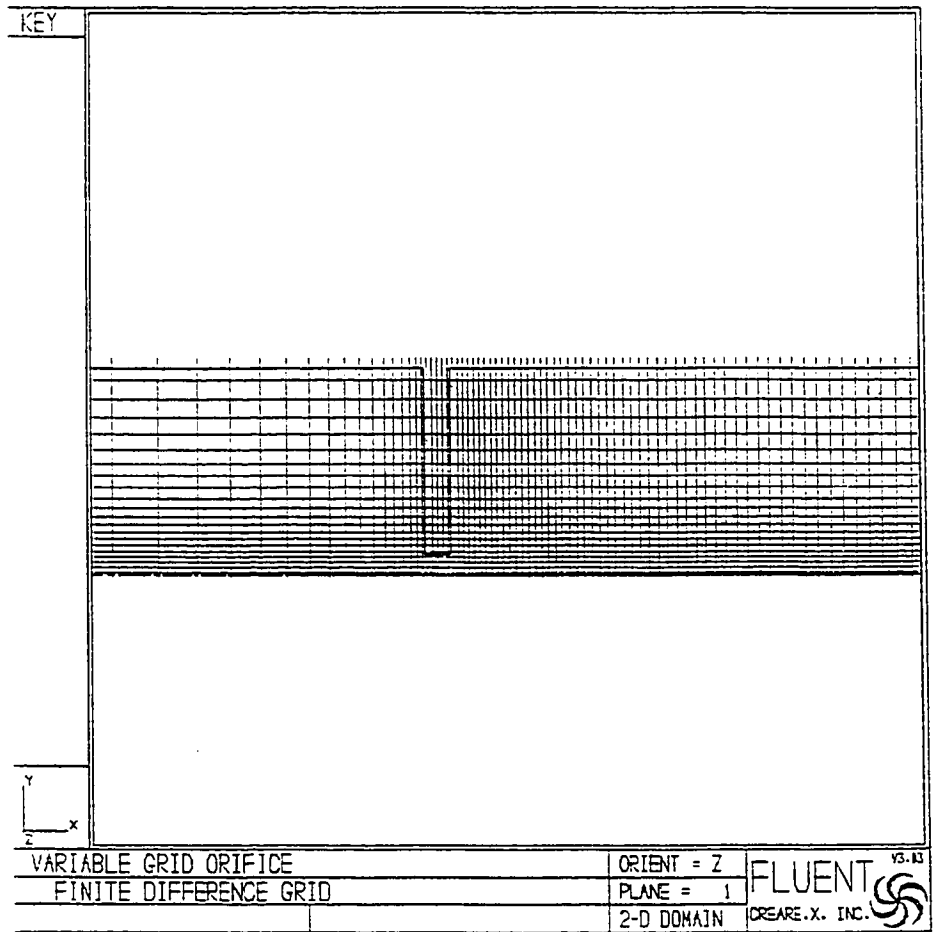


Figure 3-2. Grid used for axisymmetric FLUENT model.

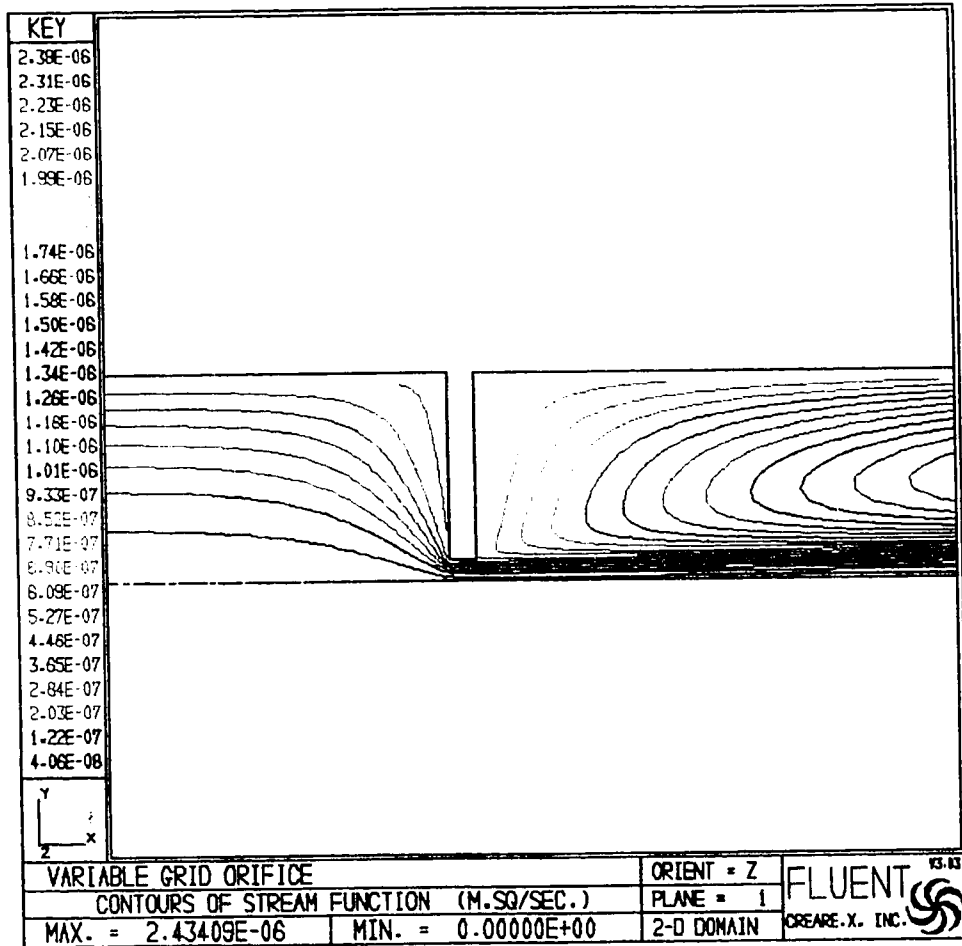


Figure 3-3. Example of streamlines for axisymmetric FLUENT model.

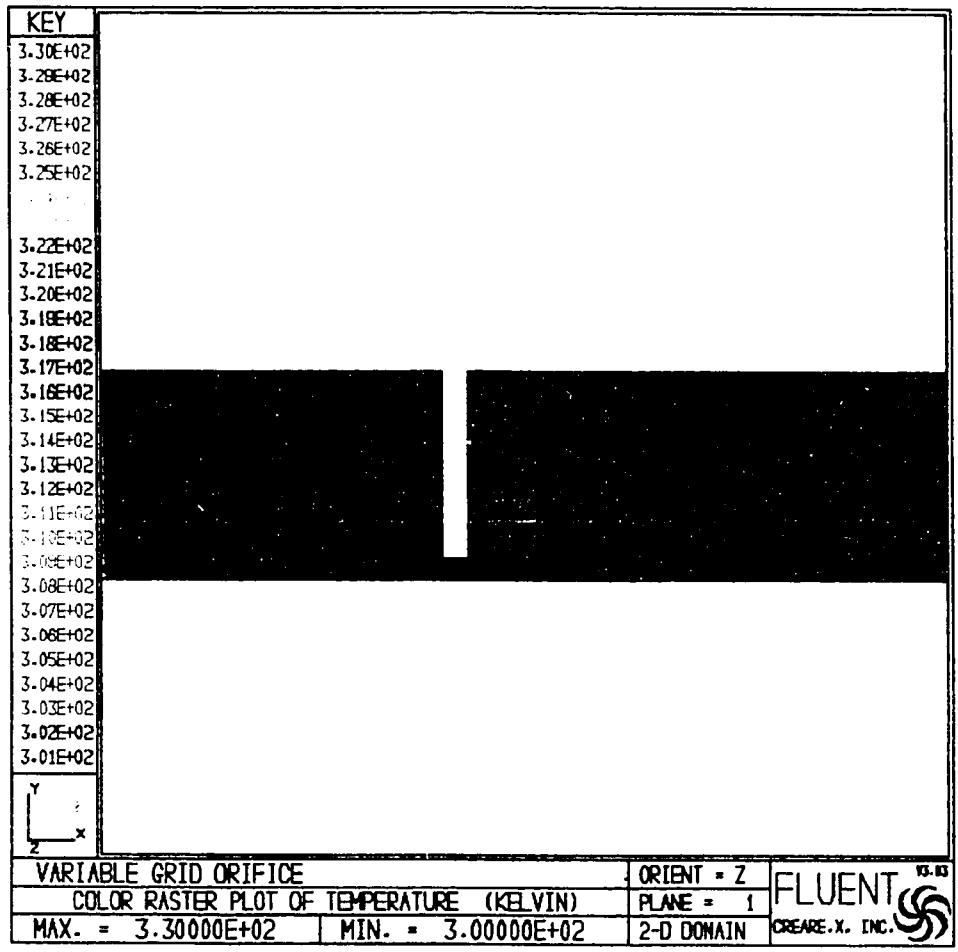


Figure 3-4. Color temperature plot for axisymmetric FLUENT model.

While FLUENT solves the full Navier-Stokes and energy equations, there are still some assumptions and approximations involved. Replacing a hexagonal flow region with a circular one is one approximation. Also, although the flow on the front surface of the plate can be expected to be laminar, the jet transitions to turbulence downstream of the orifice. A laminar model is preferred because it will better handle the boundary layer near the plate than a $k-\epsilon$ turbulence model, but this results in some error. Finally, the axisymmetric model will result in a symmetric eddy or recirculation zone downstream of the plate. The real flow case will not have this symmetry. Unsteady eddies are expected in this region. The model assumptions are most reasonable for the front surface and the hole, but the model cannot be expected to take the place of experimental data.

Figure 3-5 is a comparison between the model and experimental results which are reported in Chapter 4. This figure contains a plot of heat exchange effectiveness versus suction mass flux, G , in $\text{kg}/(\text{m}^2\text{-s})$ for plate 5 (5% porosity) and plate 9 (1% porosity) both from the laboratory and from the FLUENT model. The FLUENT plots are based on discrete points, but only the fitted curves are shown here to avoid confusion with the experimental results shown as data points. Note that while FLUENT under-predicts the effectiveness, it does a better job for the

high porosity plate (plate 5) than for the low porosity plate (plate 9). It is likely that the underprediction of FLUENT is due to the fact that the axisymmetric model does not account for the actual unsteady flow downstream of the plate which could be expected to increase heat transfer coefficients on the back of the plate.

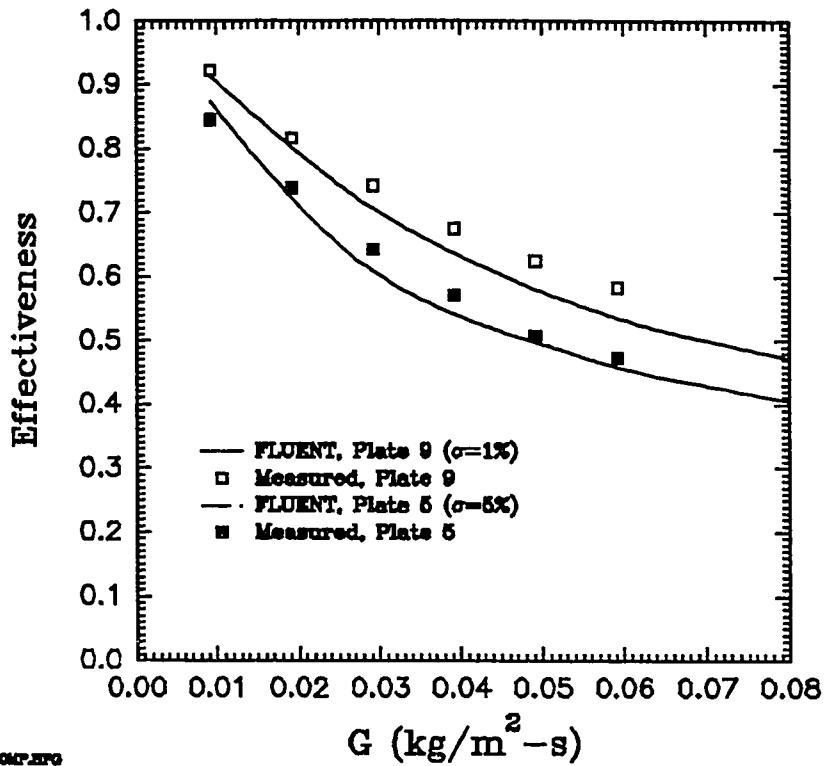


Figure 3-5. Effectiveness vs. suction flow rate comparing FLUENT predictions and experimental results for two test plates.

Figure 3-6 shows the heat transfer predicted by FLUENT for plate 9 at various suction flow rates divided into the three components: front surface, hole, and back surface. These break down as shown in Table 3-1.

FLUENT HEAT TRANSFER PREDICTIONS

PLATE 9

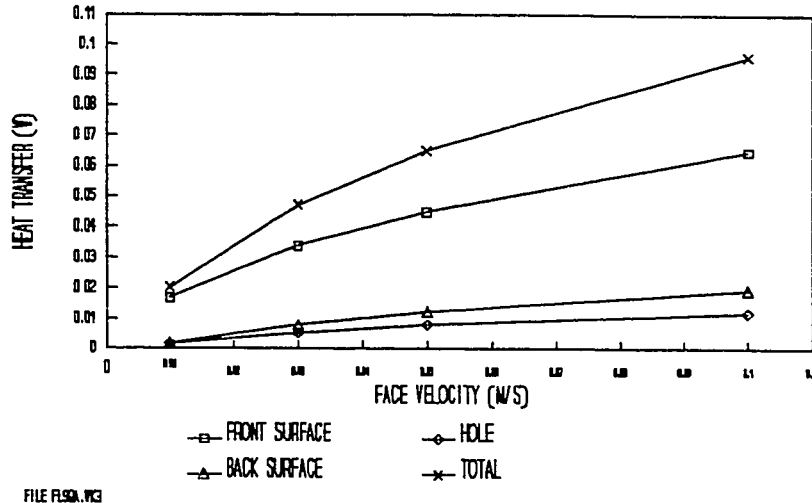


Figure 3-6. Breakdown of where heat transfer occurs for plate 9.

Table 3-1. Percentage of heat transfer occurring in different plate regions.

v_0 (m/s)	Front	Hole	Back
.01	83	8	9
.03	72	11	17
.05	69	12	19
.10	67	13	20

The FLUENT model indicates that the bulk of the heat transfer occurs on the front surface. The proportion of heat transfer on the front surface increases as suction flow rate is reduced. This is because the effectiveness increases, thus increasing the air temperature entering the hole and allowing a smaller ΔT for heat transfer in the

hole or on the back surface. It is perhaps surprising that a significant amount of heat transfer is occurring on the back of the plate. Note that the relative amount of heat transfer on the front versus the back of the plate at a suction flow rate of 0.05 m/s is consistent with the relative thermal boundary layer thicknesses on the front and back shown in **Figure 3-4**.

3.2.1 Correlation Development

Ultimately for purposes of solar collector performance modeling, one needs to know the heat exchange effectiveness. The heat exchange effectiveness can be described in terms of either a heat transfer coefficient, h , based on the difference between the plate surface temperature and the approaching inlet temperature (as done by Andrews, et. al. and Sparrow and Tien), or a heat transfer coefficient, U , based on the log mean temperature difference where h and U are both in W/m^2-K . The effectiveness can be written in terms of these as follows:

$$\epsilon_{HX} = \frac{h}{GC_p} = 1 - e^{-\frac{UA}{\dot{m}C_p}} \quad (3-1)$$

where \dot{m} is the suction mass flow rate.

Thermodynamic considerations require that the heat exchange effectiveness must be in the range of 0 to 1. A value greater than one would mean that the exit air temperature is higher than the plate temperature.

Typically heat transfer coefficients follow a power law relationship for velocity or mass flux. Note that if h has a simple power law relation to G (e.g. $h = KG^5$ where K is a constant of proportionality), as G goes to zero, the effectiveness becomes infinite. (This was not necessarily a problem for Andrews, et. al. or Sparrow and Tien since their data were taken at fairly high suction flow rates corresponding to low effectiveness values.) However, a simple power law correlation for U is entirely consistent with a maximum effectiveness value of one.

Correlations in terms of h would have to be in a form other than a simple power law. One obvious form for h can be derived immediately from the above equation as:

$$h = GC_p (1 - e^{-KG^x}) \quad (3-2)$$

A review of heat transfer correlations in the literature revealed a correlation by Hausen (1943) for thermal entry length heat transfer in a constant temperature pipe which is of a form that can also meet the criterion for effectiveness. In this case, h could be correlated in the following form:

$$h = \frac{GC_p}{1 + K/C_p G^{1-x}} \quad (3-3)$$

For large V , h is then equal to KV^x (where $K=1/K'$) and in the limit of small V , h is GC_p . Thus this form of correlation for h exhibits the right behavior for effectiveness.

Although the goal of this study is to correlate experimental results for overall heat transfer coefficient with sufficient accuracy using simple correlations in the above forms, it is important to recognize that the heat transfer to air flowing through the perforated plate takes place sequentially in three regions: the front surface, the hole, and the back surface. Ideally, if one could obtain heat transfer coefficients for each of these regions, one could combine them into an overall value. To do this, one must first consider how h and U for these different regions combine.

3.2.1.1 Combination of h Values

Consider three heat exchange processes in series, each representing heat exchange between a wall at constant temperature, T_s , and a cooler fluid and each having a heat transfer coefficient, h_i , based on the local difference between the surface temperature and the inlet fluid temperature and corresponding to local area A_i . Finally, consider an overall heat transfer coefficient, h_T , representing the entire set of three exchangers and based

on some arbitrary area A_T . A heat balance gives the following:

$$h_T A_T (T_S - T_1) = h_1 A_1 (T_S - T_1) + h_2 A_2 (T_S - T_2) + h_3 A_3 (T_S - T_3) \quad (3-4)$$

To determine the value of $h_T A_T$ in terms of $h_1 A_1$, $h_2 A_2$, and $h_3 A_3$, one must eliminate T_2 and T_3 in the above equation. An energy balance on the second and third heat exchangers yields:

$$h_1 A_1 (T_S - T_1) = \dot{m} C_p (T_2 - T_1) \quad (3-5)$$

$$h_2 A_2 (T_S - T_2) = \dot{m} C_p (T_3 - T_2) \quad (3-6)$$

Using these equations to eliminate T_2 and T_3 , yields the following for $h_T A_T$:

$$h_T A_T = h_1 A_1 + h_2 A_2 + h_3 A_3 - \frac{h_1 A_1 h_2 A_2}{\dot{m} C_p} - \frac{h_2 A_2 h_3 A_3}{\dot{m} C_p} - \frac{h_1 A_1 h_3 A_3}{\dot{m} C_p} + \frac{h_1 A_1 h_2 A_2 h_3 A_3}{(\dot{m} C_p)^2} \quad (3-7)$$

Thus if one could obtain correlations for each of the three heat exchange segments of the plate, combining them into an overall correlation would result in a fairly complicated result.

3.2.1.2 Combination of U Values

Now consider the U values in the same way. Considering UA as the product of U and its corresponding heat exchange area, one has:

$$U_T A_T \frac{T_4 - T_1}{\ln \frac{T_s - T_1}{T_s - T_4}} = U_1 A_1 \frac{T_2 - T_1}{\ln \frac{T_s - T_1}{T_s - T_2}} + U_2 A_2 \frac{T_3 - T_2}{\ln \frac{T_s - T_2}{T_s - T_3}} + U_3 A_3 \frac{T_4 - T_3}{\ln \frac{T_s - T_3}{T_s - T_4}} \quad (3-8)$$

The goal is to obtain $U_T A_T$ as a function of $U_1 A_1$, $U_2 A_2$, and $U_3 A_3$. Performing energy balances on, respectively, the whole plate, and the three individual sections, yields:

$$U_T A_T \frac{T_4 - T_1}{\ln \frac{T_s - T_1}{T_s - T_4}} = \dot{m} C_p (T_4 - T_1) \quad (3-9)$$

$$U_1 A_1 \frac{T_2 - T_1}{\ln \frac{T_s - T_1}{T_s - T_2}} = \dot{m} C_p (T_2 - T_1) \quad (3-10)$$

$$U_2 A_2 \frac{T_3 - T_2}{\ln \frac{T_s - T_2}{T_s - T_3}} = \dot{m} C_p (T_3 - T_2) \quad (3-11)$$

$$U_3 A_3 \frac{T_4 - T_3}{\ln \frac{T_s - T_3}{T_s - T_4}} = \dot{m} C_p (T_4 - T_3) \quad (3-12)$$

Re-arranging and exponentiating each of these equations gives:

$$\frac{T_s - T_4}{T_s - T_1} = e^{-\frac{U_1 A_1}{\dot{m} C_p}} \quad (3-13)$$

$$\frac{T_s - T_2}{T_s - T_1} = e^{-\frac{U_2 A_2}{\dot{m} C_p}} \quad (3-14)$$

$$\frac{T_s - T_3}{T_s - T_2} = e^{-\frac{U_3 A_3}{\dot{m} C_p}} \quad (3-15)$$

$$\frac{T_s - T_4}{T_s - T_3} = e^{-\frac{U_4 A_4}{\dot{m} C_p}} \quad (3-16)$$

Thus each of these equations represents the fractional decrease in the driving temperature difference between the wall and the bulk fluid temperature for the overall plate and for the three individual sections, respectively. The fractional temperature decrease values simply multiply as:

$$\frac{T_s - T_4}{T_s - T_1} = \frac{T_s - T_2}{T_s - T_1} \times \frac{T_s - T_3}{T_s - T_2} \times \frac{T_s - T_4}{T_s - T_3} \quad (3-17)$$

OR,

$$e^{-\frac{U_1 A_1}{\dot{m} C_p}} = e^{-\frac{U_2 A_2}{\dot{m} C_p}} e^{-\frac{U_3 A_3}{\dot{m} C_p}} e^{-\frac{U_4 A_4}{\dot{m} C_p}} \quad (3-18)$$

Thus taking the log and multiplying through by $-\dot{m} C_p$, yields the simple result:

$$U_T A_T = U_1 A_1 + U_2 A_2 + U_3 A_3 \quad (3-19)$$

Of course this result could also have been obtained by leaving the equations in the original logarithmic form, but the exponential form makes the physical significance, namely the fractional change in the driving temperature difference, clearer.

Thus, unlike the case of a heat transfer coefficient based on inlet temperature difference, if one obtains simple correlations for the heat transfer coefficient based on log mean temperature difference for each of the three sections, they can simply be added to obtain the overall correlation. Of course, there is no guarantee that each value of UA will follow a simple power law in velocity. In particular, the heat transfer occurring in the hole and at the back of the plate are dependent on the temperature and velocity profiles entering these regions. Thus, as will be shown later, the problem of heat transfer in the hole is different from entrance flow in a tube since the entering flow is not purely axial and does not have a uniform profile in either velocity or temperature.

For heat transfer from a constant temperature surface, use of the log mean temperature difference makes sense physically, as can be seen by examining front surface heat transfer as an example. Consider the local heat transfer coefficient, h , for a ring element of plate surface area dA around the hole. The heat convected from this element

heats the air stream, leading to the following energy balance:

$$h(T_s - T) dA = \dot{m} C_p dT \quad (3-20)$$

where T is the local temperature of the air stream. (This "local" temperature is admittedly ill-defined, although it can be thought of as the bulk fluid temperature that would result from heat transfer from all of the plate area at a radius greater than that of the area element ring.) Rearranging,

$$\frac{1}{\dot{m} C_p} \int_0^A h dA' = \int_{T_1}^{T_0} \frac{dT}{T_s - T} \quad (3-21)$$

Defining an average heat transfer coefficient over the surface as

$$\bar{h} = \frac{1}{A} \int_0^A h dA' \quad (3-22)$$

and integrating the right hand side yields:

$$\bar{h} A \frac{T_0 - T_1}{\ln \frac{T_s - T_1}{T_s - T_0}} = \dot{m} C_p (T_0 - T_1) \quad (3-23)$$

Thus defining a local h based on the local temperature difference between the surface and the fluid results in an

overall heat transfer coefficient based on the log mean temperature difference. Since from boundary layer theory, one expects h to vary as a simple power law in velocity, one may also expect the overall coefficient based on log mean temperature difference (which is just the local value integrated over the area) to be a simple power law in velocity as well. Although one cannot make this same conclusion for the hole and back surface heat transfer cases due to their complicated inlet conditions, it is clear that for thin high effectiveness plates, the front surface heat transfer will be the largest term, and so an overall coefficient based on log mean temperature difference may provide an adequate correlation.

Figure 3-7 shows a plot of overall heat transfer coefficient, h , based on $T_s - T_a$ versus suction mass flow rate for plate 9. A best fit power law curve is shown. As discussed earlier, a simple power law fit for h is not consistent with a limiting effectiveness of 1 at zero flow rate, so it is not surprising that a power law fit is not better. **Figure 3-8** shows an overall heat transfer coefficient, U , based on log mean temperature difference versus suction mass flow rate. Note that a simple power law gives an excellent fit for this plate.

In order to investigate the effects of hole diameter and spacing on the local heat transfer coefficients, FLUENT runs were made on five different plates representing three

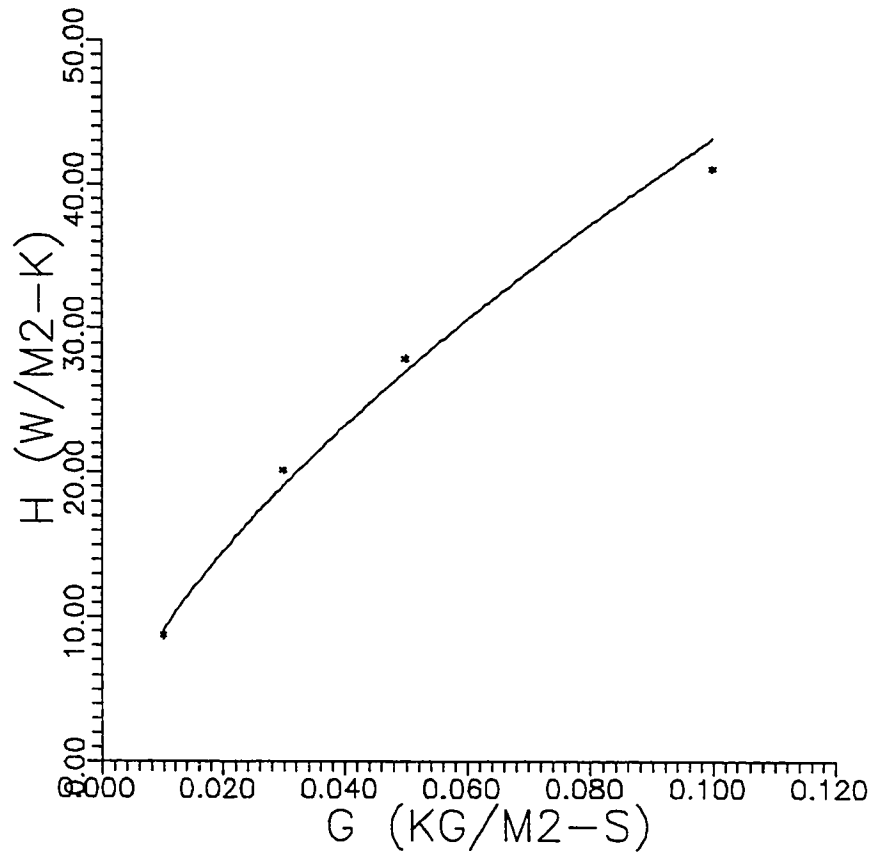


Figure 3-7. Overall heat transfer coefficient based on $T_s - T_{amb}$ from FLUENT simulations of plate 9 and best power law fit.

different pitches at the same diameter and three different diameters at the same pitch. The intention was to get the effects of hole size and pitch without the random variation that one expects with experimental data. Because the FLUENT model will not converge at the lowest porosities investigated experimentally, modeling was performed on

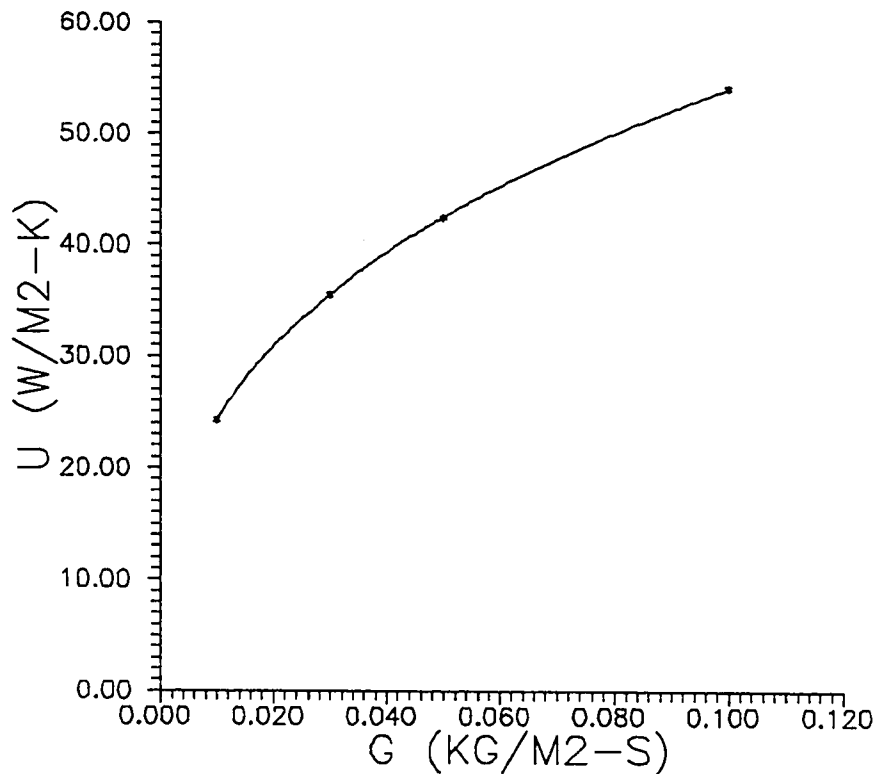


Figure 3-8. Overall heat transfer coefficient based on log mean temperature difference from FLUENT simulations of plate 9 and best power law fit.

several plates not replicated by experiments in addition to test plate 5. Plates represented only by FLUENT models are given the numerical designations F-1, F-2, F-3, and F-4. **Table 3-2** gives the geometries of these plates.

Table 3-2. Geometries of FLUENT plate models.

Plate No.	Pitch (m)	Diameter (m)
F-1	.00709	.003175
F-2	.01080	.003175
F-3	.00709	.001590
F-4	.00709	.002380
5	.01420	.003175

Thus plates F-1, F-2, and 5 represent three different pitches (in ascending order) at the same hole diameter, and plates F-3, F-4, and F-1 represent three different diameters (in ascending order) at the same hole pitch. Plate F-1 is common to both sensitivity runs.

Table 3-3 gives the local average heat transfer coefficients based on log mean temperature difference for all the simulated conditions. (Because of lengthy run times, not all plates were run at all velocities.)

Table 3-3. Local average heat transfer coefficients for FLUENT simulations.

Plate	V (m/s)	P (m)	D (m)	U_f (W/m ² -K)	U_b (W/m ² -K)	$U_{b'}$ (W/m ² -K)
F-1	.01	.00709	.00318	13.8	31.5	12.2
	.02	"	"	18.9	38.3	12.8
	.03	"	"	22.0	41.7	12.2
	.04	"	"	24.5	44.4	12.0
	.05	"	"	26.6	47.0	11.9
	.06	"	"	28.6	49.6	12.0
F-2	.02	.01080	.00318	15.1	44.7	7.4
	.04	"	"	19.6	54.4	8.6
	.05	"	"	21.4	59.2	9.2
F-3	.01	.00709	.00159	15.0	61.7	9.1
	.02	"	"	19.9	73.4	10.2
	.03	"	"	23.0	81.2	11.3
	.04	"	"	25.5	88.2	12.3
	.05	"	"	27.7	94.7	13.2
F-4	.01	.00709	.00238	14.3	42.6	11.5
	.02	"	"	19.3	50.1	11.2
	.03	"	"	22.3	54.4	11.2
	.04	"	"	24.8	58.3	11.6
	.05	"	"	27.0	62.0	12.1
	.06	"	"	28.9	65.7	12.5
F-5	.01	.0142	.00318	10.2	42.5	5.2
	.03	"	"	15.2	57.9	7.0
	.05	"	"	18.7	72.6	8.1
	.06	"	"	20.2	79.3	8.6

Now consider each region separately.

3.2.1.3 Front Surface Heat Transfer

The relevant area for front surface heat transfer is the actual exposed plate area, i.e., the area of a unit cell minus the hole area. In the FLUENT runs the hexagonal unit cell is replaced by a circle of equal area, so the area of interest is the area of this circle minus the cross-sectional hole area. Basing the correlations for front surface heat transfer on this area yields the following correlations for U_f (Tables 3-4 and 3-5):

Table 3-4. Front surface correlations at $D = .003175$ m

Plate No.	Pitch (m)	U_f
F-1	.0071	$88.0 V^{.40}$
F-2	.0108	$69.8 V^{.39}$
5	.0142	$63.6 V^{.41}$

Table 3-5. Front surface correlations at $P = .00709$ m

Plate No.	Diameter (m)	U_f
F-3	.00159	$85.8 V^{.38}$
F-4	.00238	$87.1 V^{.39}$
F-1	.00318	$88.0 V^{.40}$

It is clear in this formulation that not only is the exponent on V quite constant, but there is very little dependence of the coefficient on hole diameter. It is desirable to obtain a correlation of these results in non-dimensional form. The dependence on only pitch suggests that one can relate a pitch-based Nusselt number to a pitch-based Reynolds number as was possible with the data

of Sparrow and Tien. Considering the exponent on Reynolds number as an unknown, b , :

$$\begin{aligned} \text{Nu}_p &= a' \text{Re}_p^b \\ \frac{hP}{k} &= a' \left(\frac{PV}{v} \right)^b \\ h &= a P^{b-1} v^b \end{aligned} \tag{3-24}$$

Taking b as .40 yields an exponent of -.60 for P . A linear regression to obtain a simple power law fit for P from the above table gives an exponent on P of -.47. Since this is not too far from a form that would yield a non-dimensional result, one can proceed to perform a regression to obtain values for the parameters a and b in the above equation and expect a reasonably good fit to the numerical results.

The computer software package, SigmaPlot 5.0, was used to perform non-linear regression of the data points from the five different simulated plates at various suction velocities. (For simple power law fits, one can take the log of both sides of the equation and perform linear regression. However, the non-linear curve fitter allowed for the possibility of geometry-dependent exponents.) The SigmaPlot curve fitter uses the Marquardt-Levenberg algorithm. This is a least squares procedure to minimize the sum of the squares of the differences between the equation values and the data values. The procedure is an

iterative one in which the user must enter initial values for all parameters. (It is possible for different initial conditions to result in convergence to different local minima, but the same results were typically obtained over a wide range of initial conditions.) SigmaPlot allows equations with up to 25 parameters and 10 independent variables and also allows up to 25 constraints. The following correlation was obtained for U:

$$U = 4.57 P^{-.60} V^{.40} \quad (3-25)$$

In non-dimensional form with both Nusselt and Reynolds numbers based on hole pitch, this becomes:

$$Nu_p = 2.37 Re_p^{.40} \quad (3-26)$$

At this point it should be noted that throughout this report, for correlations derived from both numerical and experimental results, fluid properties are based on the inlet (ambient) temperature. An alternative would be to base properties on the average of inlet and outlet bulk air temperature. However, for most applications of transpired collectors, temperature rises are reasonably small (with a correspondingly small effect on dimensionless group correlations), and it was felt that the typical designer would be reluctant to perform iterative calculations that basing properties on average air temperature would

necessitate. All FLUENT-derived correlations are based on an ambient air temperature of 300 K; a surface temperature of 330 K was used for all simulations. Experimental results reported in the next chapter are also based on fluid properties at an ambient temperature of 300 K, which was a typical value near the test plates.

Recall that Sparrow's front surface heat transfer data could also be correlated using only a pitch length scale and that the equation which best described his data was:

$$Nu_p = 2.67 Re_p^{.476} \quad (3-27)$$

The difference in this case (other than that the correlation here is derived from numerical modeling and his from naphthalene sublimation experiments) is that the Reynolds numbers here are much lower, and the Nusselt number used here incorporates a heat transfer coefficient based on log mean temperature difference instead of the difference between surface temperature and the approaching free stream temperature. Using Sparrow's correlation for this case would erroneously predict an exit air temperature higher than the plate temperature.

Figure 3-9 shows how well the FLUENT results for all five plates are fitted by a pitch-based correlation relating Nusselt number to Reynolds number. Figure 3-10 shows Stanton number ($St = U/\rho Vc_p$) versus pitch-based Reynolds number. The Nusselt number correlation can be

converted algebraically to a Stanton number correlation. However, the two figures show the result of a separate regression for each. The correlation which minimizes the sum of the squares of the residuals in each case results in two correlations which are not quite identical algebraically.

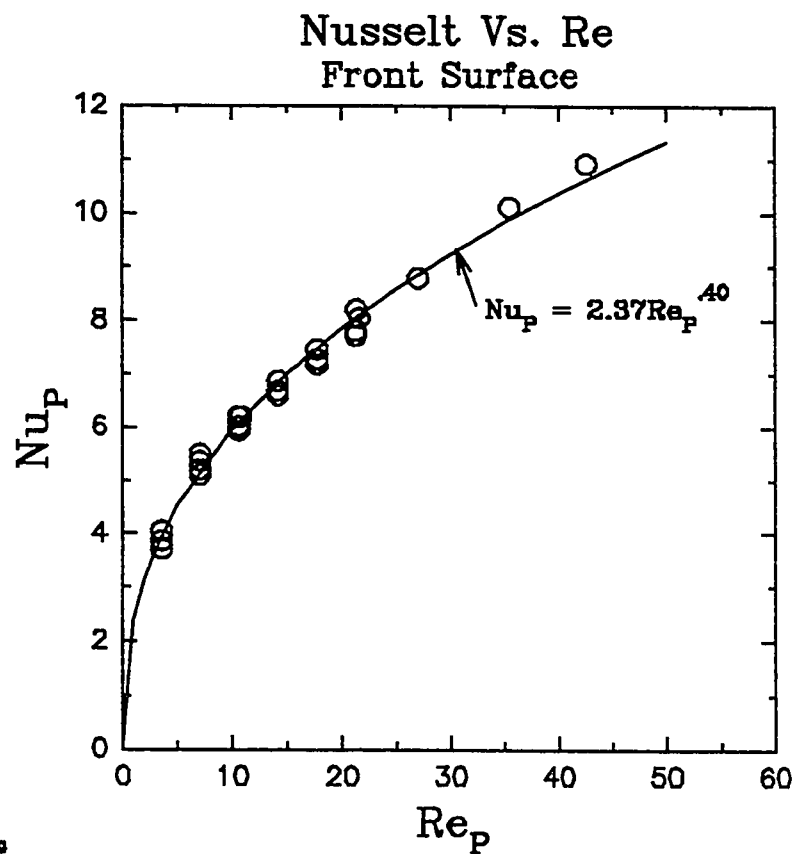


Figure 3-9. Pitch-based Nusselt number vs. pitch-based Reynolds number for front surface heat transfer.

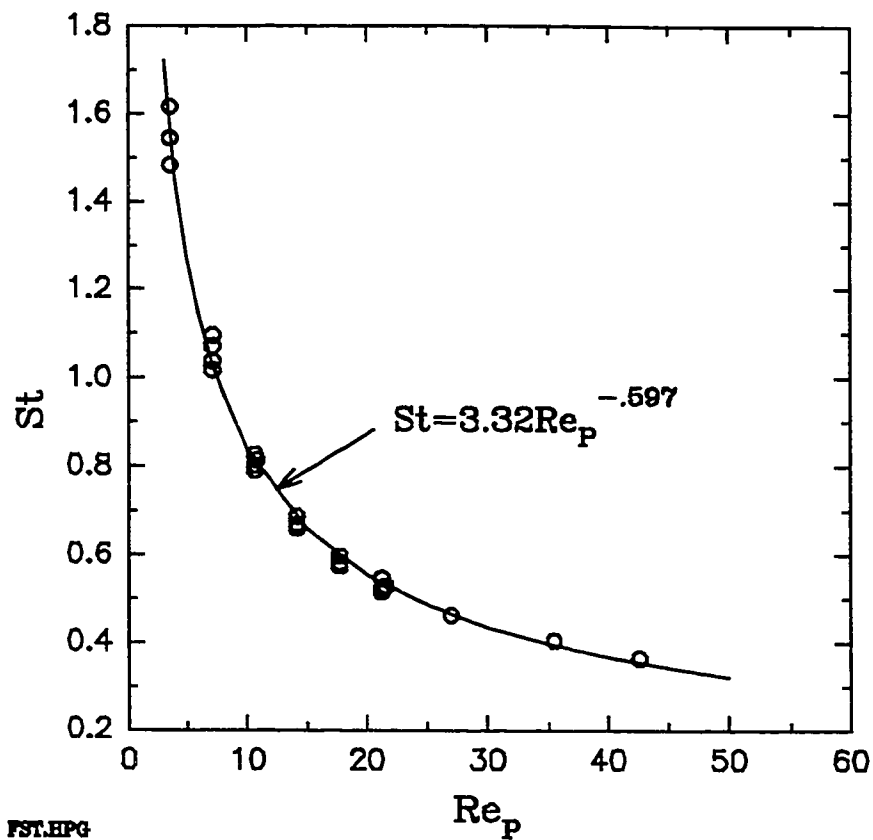


Figure 3-10. Stanton number vs. pitch-based Reynolds number for front surface heat transfer.

3.2.1.4 Hole Heat Transfer

Just as was done for the front surface, consider the local heat transfer coefficients based on the local area for heat transfer in the hole. Again, to ensure that the maximum effectiveness at very low flow rates is one, the coefficients are based on the log mean temperature difference. Simple power law correlations for local U_h are contained in Tables 3-6 and 3-7.

Table 3-6. Hole correlations at $D = .003175$ m

Plate No.	Pitch (m)	U_h (W/m ² -K)
F-1	.0071	110 $v^{.27}$
F-2	.0108	172 $v^{.35}$
5	.0142	253 $v^{.41}$

Table 3-7. Hole correlations at $P = .00709$ m

Plate No.	Diameter (m)	U_h (W/m ² -K)
F-3	.00159	220 $v^{.28}$
F-4	.00238	127 $v^{.24}$
F-1	.00318	110 $v^{.27}$

This situation contrasts considerably with the case of front surface heat transfer. The coefficients appear to be functions of both pitch and diameter. Although the velocity exponent does not vary very much with hole diameter, it does vary with pitch. The apparent poor behavior can be understood by examining the thermal boundary layer. Unlike the entrance flow in a pipe which begins with zero thermal boundary layer thickness, a finite thermal boundary layer already exists in this case as the flow enters the hole. Moreover, this starting thickness is a function of the amount of heat transfer on the front surface. For entrance flow in a pipe, the coefficient on Reynolds number in the correlation depends on hole diameter but the exponent is constant. In this case, the exponent depends mostly on pitch which is the parameter which determines the amount of front surface heat transfer.

Also, although the simple power law fit works well on the front surface, the power law fits shown above for the hole do not fit the numerical model results as well as in the case of the front surface.

Consider the local average heat transfer coefficient, U_h , for the hole, defined such that the total heat transferred from the hole wall to the bulk fluid, Q_h , is:

$$Q_h = U_h A_h \Delta T_{lm} \quad (3-31)$$

where A_h is the surface area of the hole wall in m^2 , and ΔT_{lm} is the log mean temperature difference in K for flow through the hole.

Incropera and DeWitt (1985) give two correlations for heat transfer in the entry region of a pipe. A thermal entry length correlation (i.e. it assumes the velocity profile is already fully developed) attributed to Hausen is:

$$Nu_D = 3.66 + \frac{0.0668 (D/L) Re_D Pr}{1 + 0.04 [(D/L) Re_D Pr]^{2/3}} \quad (3-32)$$

For the combined entry length, the Sieder-Tate correlation is:

$$Nu_D = 1.86 \left(\frac{Re_D Pr}{L/D} \right)^{1/3} \left(\frac{\mu}{\mu_s} \right)^{0.14} \quad (3-33)$$

In each case, $Nu_p = U_h D / k$ and $Re_p = (V/\sigma) D / \nu$ where V/σ is the approaching face velocity in m/s divided by the plate porosity, i.e., the average hole velocity. (Each assumes a heat transfer coefficient based on log mean temperature difference.) μ and μ_s are air viscosities evaluated, respectively, at the mean air temperature (average of inlet and outlet) and the surface temperature.

Figure 3-11 is a plot of U_h values from these two correlations as well as results from FLUENT for plate F-4. For this plate the FLUENT curve follows closely to, but a little below, the Hausen correlation and predicts a considerably lower heat transfer coefficient than the Sieder-Tate correlation. This latter fact is likely due both to the pre-existing thermal boundary layer entering the hole as well as the fact that the flow streamlines are not parallel as they enter the hole.

HOLE HEAT TRANSFER COEFFICIENTS

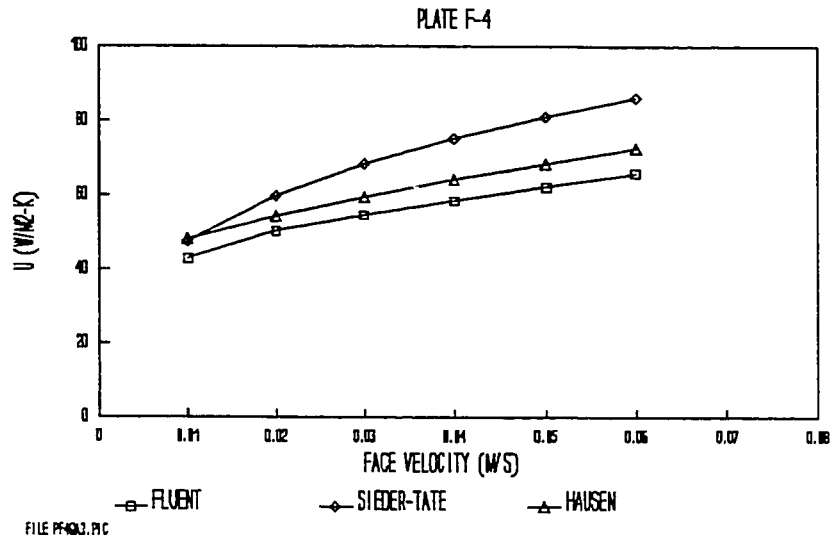


Figure 3-11. Hole heat transfer correlations from FLUENT and entrance flow correlations.

Figure 3-12 is a plot of Nusselt numbers based on hole diameter for a best fit correlation of the form of the Sieder-Tate. Regression analysis showed the best fit is with an exponent of .29 and a coefficient of 1.78.

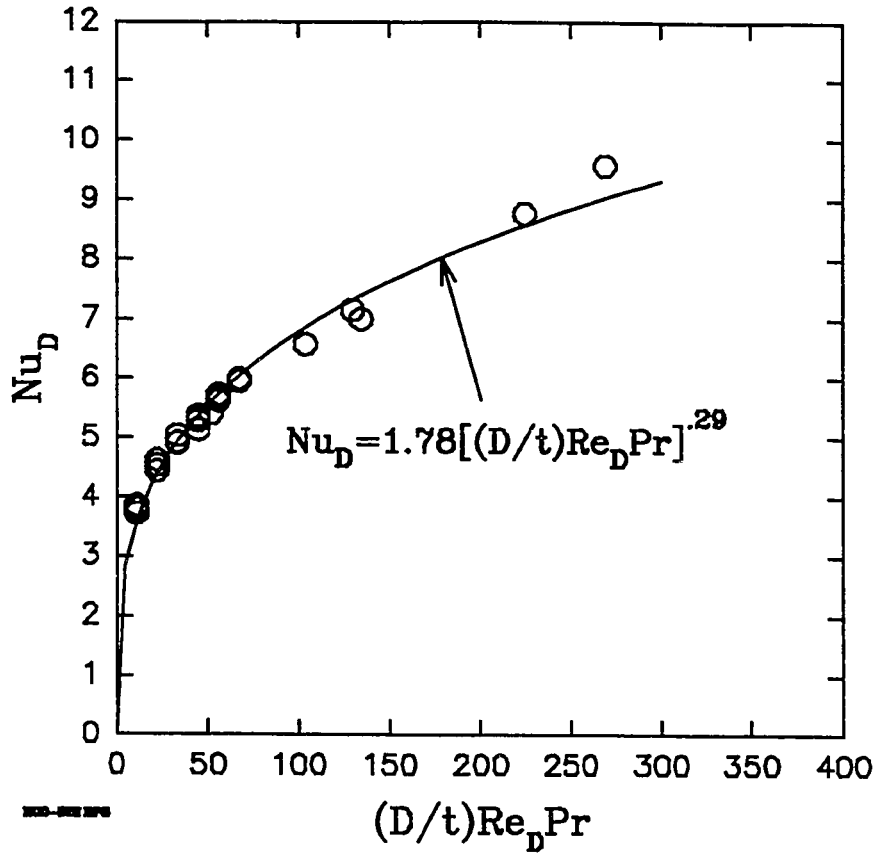


Figure 3-12. Hole heat transfer correlation of FLUENT results using the form of the Sieder-Tate correlation.

Figure 3-13 is a fit which allows for a non-zero y-intercept. Note that the best fit results in a considerably higher exponent in this case.

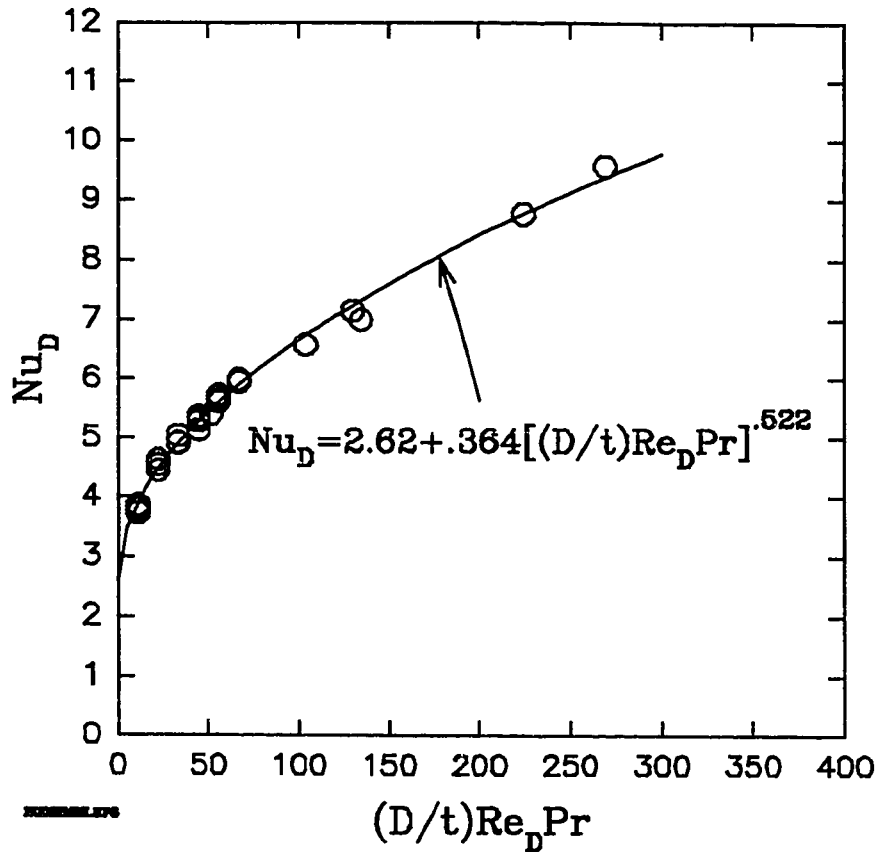


Figure 3-13. Best fit for Sieder-Tate type of correlation with non-zero intercept.

Figure 3-14 uses the form of the Hausen equation, but keeping the minimum Nusselt number at 3.66 and keeping the same exponents on Reynolds number. Finally, Figure 3-15 allows for the minimum Nusselt number to be lower than 3.66.

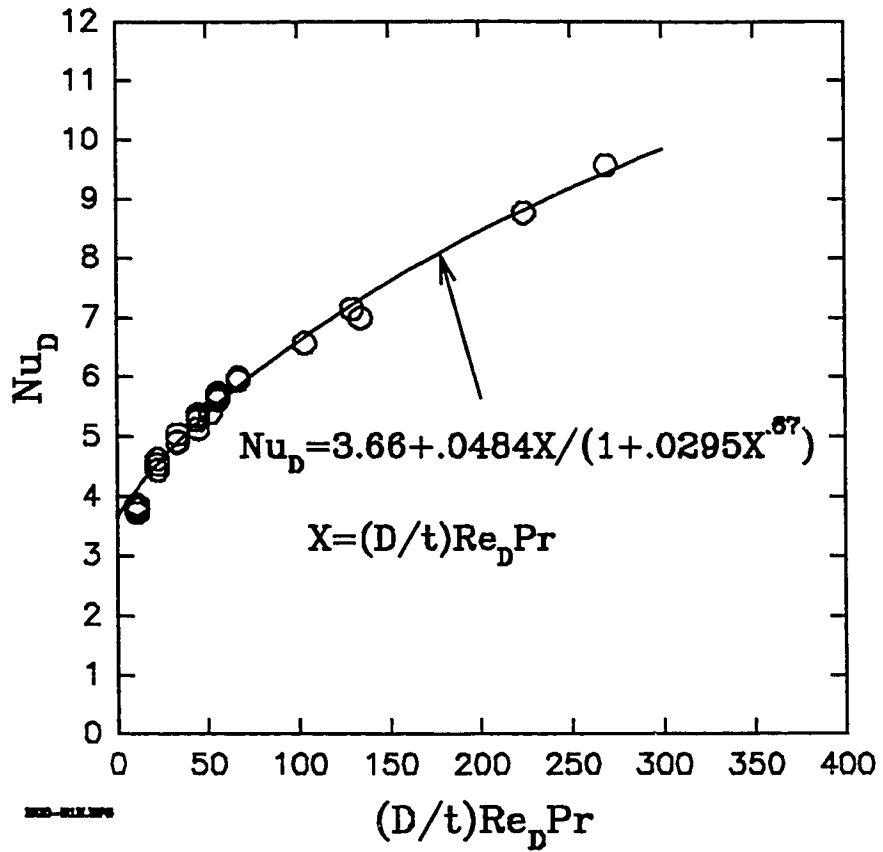


Figure 3-14. Hole heat transfer correlation of FLUENT results using a form similar to the Hausen correlation.

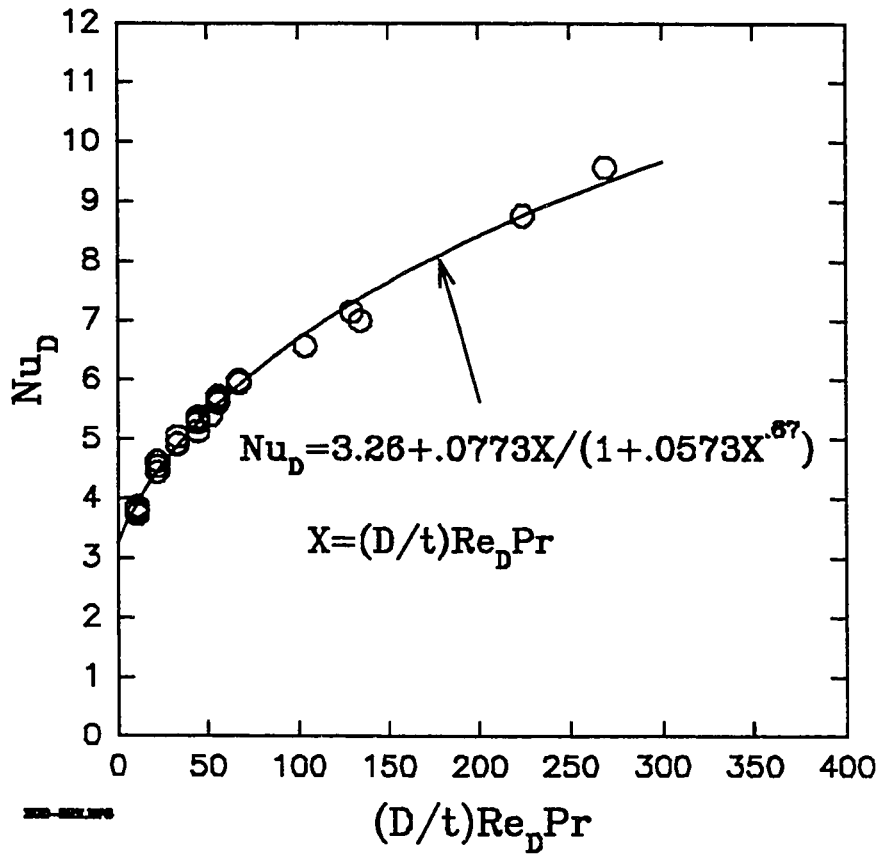


Figure 3-15. Hole heat transfer correlation of FLUENT results of the Hausen type but using a best-fit y-intercept.

3.2.1.5 Back Surface Heat Transfer

One might expect that the back surface heat transfer will have the same length scale as the front surface, namely pitch. Figure 3-16 shows the results in terms of Nu_p vs. Re_p .

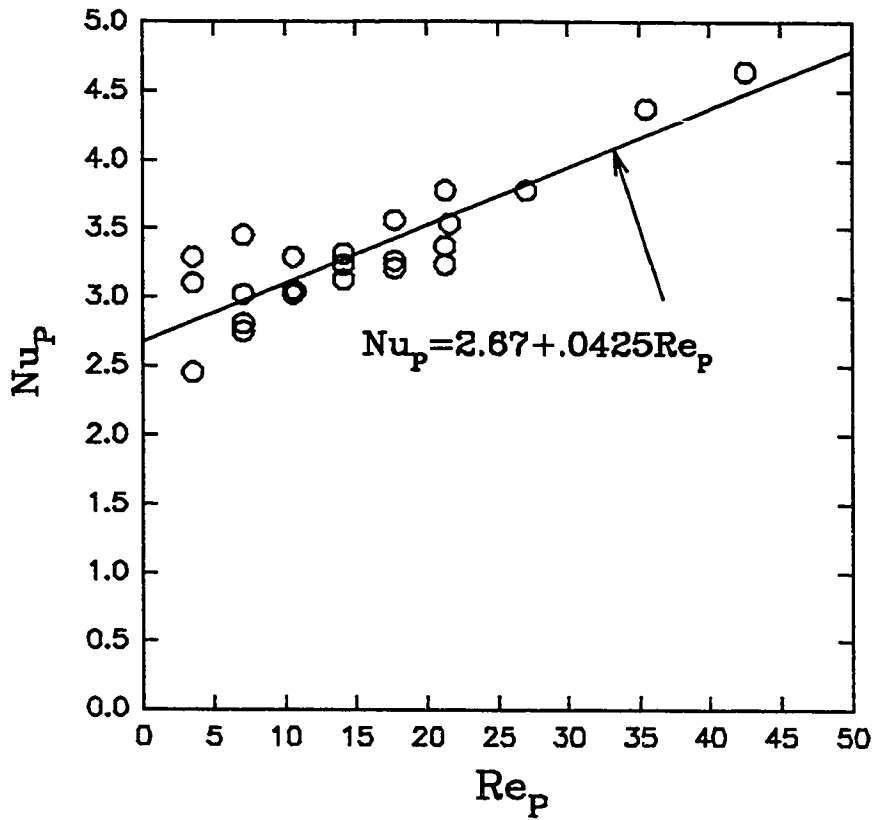


Figure 3-16. Pitch-based Nusselt number vs. pitch-based Reynolds number for FLUENT results for back surface heat transfer.

These data do not collapse as tightly as those of the front surface and the hole. However, the data are much tighter if plotted as Stanton number versus pitch-based Reynolds number as shown in Figure 3-17.

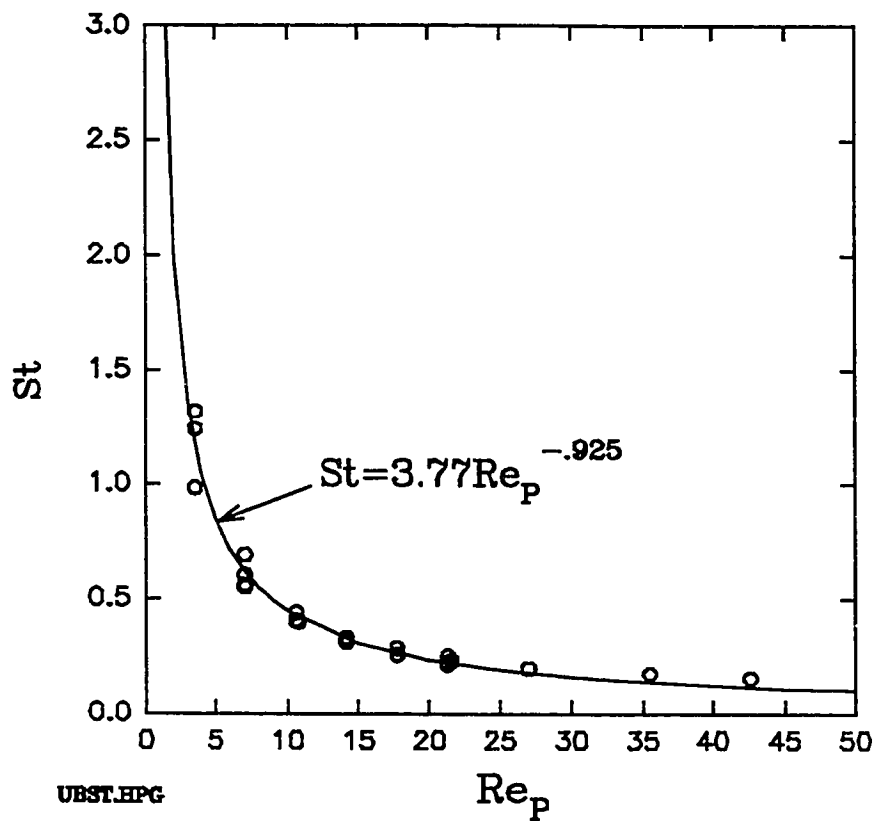


Figure 3-17. Stanton number vs. pitch-based Reynolds number for back surface heat transfer.

Figure 3-18 shows the very similar correlation, NTU vs. pitch-based Reynolds number for the back surface. In basing the heat transfer coefficient on the solid plate surface area (i.e., excluding the hole area), St and NTU are related as:

$$NTU = (1 - \sigma) St$$

Thus, for low porosity plates these two non-dimensional parameters are very close. For the back surface fit the

regression for the NTU fit has a slightly higher R^2 than for the St fit.

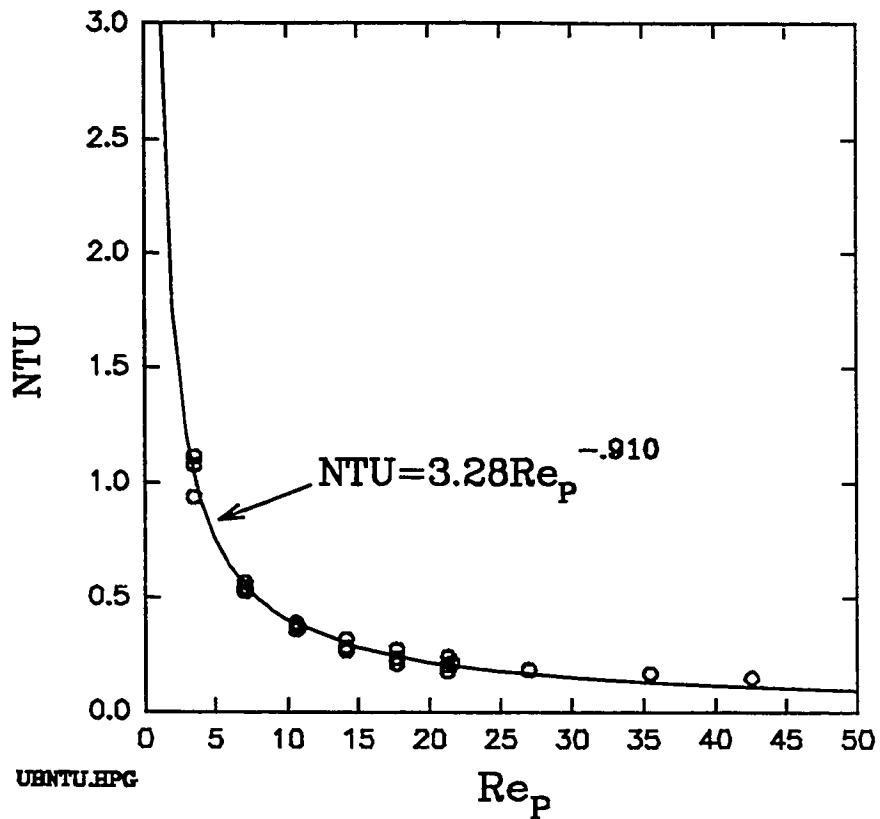


Figure 3-18. Number of transfer units vs. pitch-based Reynolds number for back surface heat transfer.

At this point it should be emphasized that the numerical model used here is laminar and axisymmetric. Although these are probably reasonable assumptions for the front surface and the hole, they may result in unrealistic values for the back surface heat transfer because of

asymmetrical, unsteady flow and because of the jet becoming turbulent downstream.

3.2.1.6 Overall Heat Transfer

Theoretically one could attempt to combine the results from the three regions. The simplest way to do this is to convert each Nusselt or NTU correlation to a correlation for local average heat transfer coefficient, U , multiply each U by its corresponding heat transfer area, and then add these together to obtain an overall UA .

Summarizing, the local average heat transfer coefficients (from the corresponding non-dimensional relationships) are as follows:

Front:

$$U_f = 2.37 k v^{-.40} P^{-.60} V^{.40} \quad (3-34)$$

Hole:

$$U_h = 2.62 k D^{-1} + .364 k Pr^{.522} v^{-.522} D^{.044} t^{-.522} \left(\frac{V}{\sigma}\right)^{.522} \quad (3-35)$$

For the FLUENT models, the porosity, σ , is D^2/P^2 . However, for the actual staggered hole plates, it is $.907 D^2/P^2$.

Back surface:

$$U_b = 3494 v^{.925} P^{-.925} V^{.075} \quad (3-36)$$

Table 3-8 shows a comparison between the results of these correlations and the actual U values, including the total overall U value.

Table 3-8. Comparison between FLUENT U value results and predicted values from correlations based on those results.

V	P	D	SIGMA	FLUENT		MODEL		FLUENT		MODEL		FLUENT	MODEL	U _b	U _a _{total}	MODEL	Δ DIFF.
				U _t	U _i	U _h	U _h	U _b	U _b	U _a _{total}	U _a _{total}						
0.01	0.00709	0.003175	0.200	13.8	14.6	31.5	32.3	12.2	12.2	10.8	10.8	0.00132	0.001315				-0.37
0.02	0.00709	0.003175	0.200	18.9	19.2	38.3	37.0	12.8	12.8	11.4	11.4	0.001607	0.001553				-3.34
0.03	0.00709	0.003175	0.200	22	22.6	41.7	40.6	12.2	12.2	11.7	11.7	0.00174	0.001729				-0.66
0.04	0.00709	0.003175	0.200	24.5	25.4	44.4	43.6	12.0	12.0	12.0	12.0	0.001855	0.001872				0.91
0.05	0.00709	0.003175	0.200	26.6	27.8	47	46.3	11.9	11.9	12.2	12.2	0.00196	0.001996				1.88
0.06	0.00709	0.003175	0.200	28.6	29.9	49.6	48.8	12.0	12.0	12.3	12.3	0.002067	0.002107				1.92
0.02	0.0108	0.003175	0.086	15.1	14.9	44.7	45.4	7.4	7.4	7.7	7.7	0.002591	0.002618				1.03
0.04	0.0108	0.003175	0.086	19.6	19.7	54.4	55.7	8.6	8.6	8.1	8.1	0.003222	0.003216				-0.19
0.05	0.0108	0.003175	0.086	21.4	21.6	59.2	59.9	9.2	9.2	8.2	8.2	0.003499	0.003448				-1.45
0.01	0.00709	0.00159	0.050	15	14.6	61.7	64.6	9.1	9.1	10.8	10.8	0.001393	0.001465				5.20
0.02	0.00709	0.00159	0.050	19.9	19.2	73.4	73.8	10.2	10.2	11.4	11.4	0.001711	0.001735				1.43
0.03	0.00709	0.00159	0.050	23	22.6	81.2	81.0	11.3	11.3	11.7	11.7	0.00193	0.001933				0.131
0.04	0.00709	0.00159	0.050	25.5	25.4	88.2	87.1	12.3	12.3	12.0	12.0	0.002117	0.002094				-1.08
0.05	0.00709	0.00159	0.050	27.7	27.8	94.7	92.5	13.2	13.2	12.2	12.2	0.002285	0.002234				-2.24

V	P	D	SIGMA	FLUENT		MODEL		FLUENT		MODEL		FLUENT		MODEL		% DIFF.
				U _t	U _h	U _t	U _h	U _b	U _h	U _b	U _h	U _b	U _h	U _b	U _h	
0.01	0.00709	0.00238	0.113	14.3	14.6	14.6	43.1	11.5	10.8	0.00141	0.001403	0.00141	0.001403	0.001403	-0.48	
0.02	0.00709	0.00238	0.113	19.3	19.2	50.1	49.3	11.2	11.4	0.001663	0.00166	0.001663	0.00166	0.00166	-0.21	
0.03	0.00709	0.00238	0.113	22.3	22.6	54.4	54.1	11.2	11.7	0.001819	0.001848	0.001819	0.001848	0.001848	1.56	
0.04	0.00709	0.00238	0.113	24.8	25.4	58.3	58.2	11.6	12.0	0.001967	0.002002	0.001967	0.002002	0.002002	1.76	
0.05	0.00709	0.00238	0.113	27	27.8	62	61.8	12.1	12.2	0.002106	0.002135	0.002106	0.002135	0.002135	1.38	
0.06	0.00709	0.00238	0.113	28.9	29.9	65.7	65.1	12.5	12.3	0.00223	0.002254	0.00223	0.002254	0.002254	1.04	
0.01	0.0142	0.003175	0.050	10.2	9.6	42.5	43.6	5.2	5.7	0.00299	0.002996	0.00299	0.002996	0.002996	0.19	
0.03	0.0142	0.003175	0.050	15.2	14.9	57.9	60.6	7.0	6.2	0.004257	0.004137	0.004257	0.004137	0.004137	-2.82	
0.05	0.0142	0.003175	0.050	18.7	18.3	72.6	72.6	8.1	6.4	0.005182	0.004871	0.005182	0.004871	0.004871	-6.00	
0.06	0.0142	0.003175	0.050	20.2	19.7	79.3	77.7	8.6	6.5	0.005589	0.005173	0.005589	0.005173	0.005173	-7.44	

Adding three separate correlations together is clearly not the most desired solution for the designer. Therefore the results were correlated using a form developed by Andrews, et al. They did a correlation of diameter-based Nusselt number vs. the product of powers of pitch-to-diameter ratio and diameter-based Reynolds number. Fitting these results to the same type of correlation, but using a log-mean-temperature basis for Nusselt number, yields:

$$\text{Nu}_D = 9.075 \left(\frac{P}{D} \right)^{-1.384} \text{Re}_D^{.2523} \quad (3-37)$$

A plot of this correlation is shown in Figure 3-19.

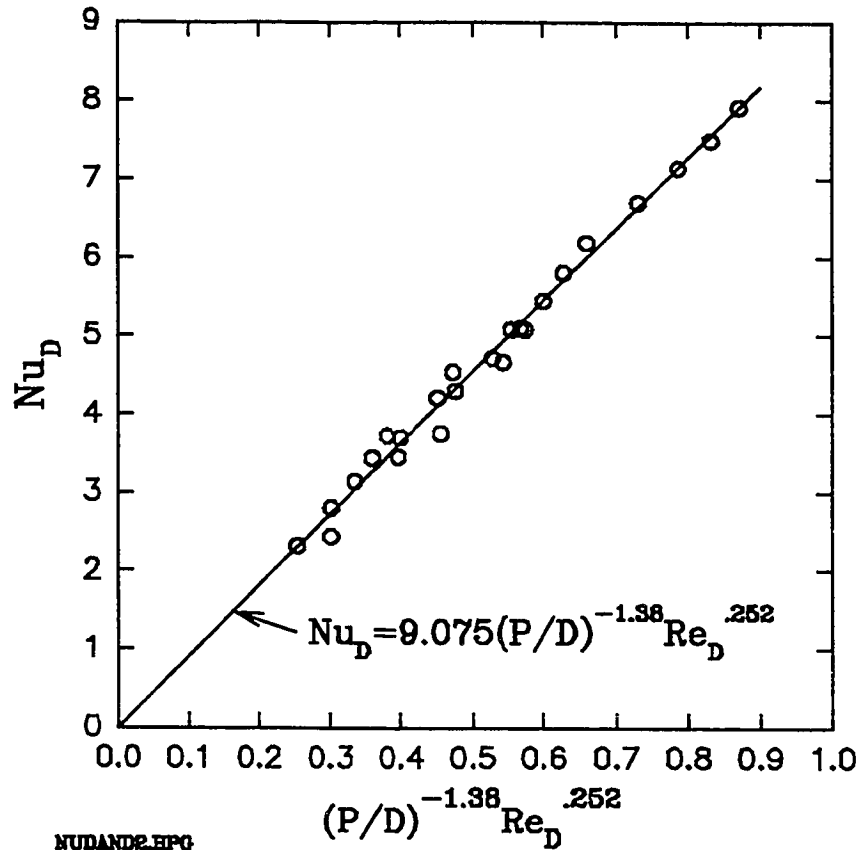


Figure 3-19. Correlation of overall heat transfer results using the same general form as Andrews, et. al.

As discussed earlier, correlations based on Nu_p and Re_p make more physical sense because of the dominance of front surface heat transfer. The above correlation can be written equivalently in terms of these non-dimensional parameters as:

$$Nu_p = 9.075 \left(\frac{P}{D} \right)^{-1.317} Re_p^{.2523} \quad (3-38)$$

Note that if one considers (P/D) as a correction factor, this has a much smaller value in this second correlation. A plot of this correlation is contained in **Figure 3-20**. Note that because the x-axis does not have as large a spread in this case, this correlation does not look quite as good, but it is mathematically equivalent.

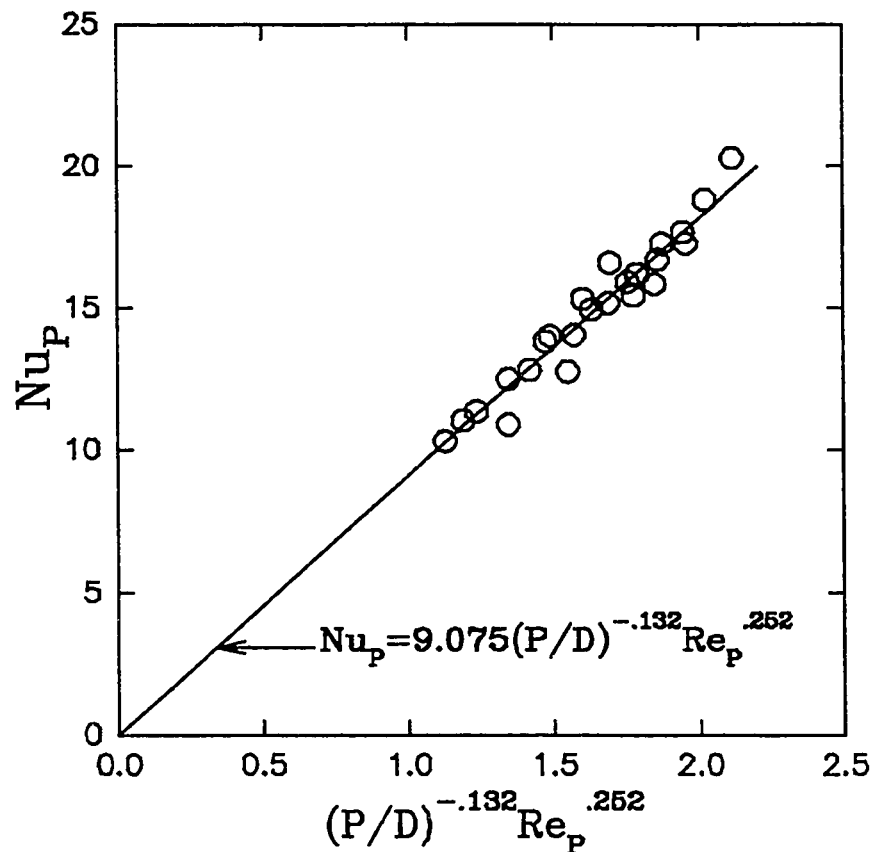


Figure 3-20. Algebraic equivalent of Andrews type of correlation for overall heat transfer results, but in terms of pitch-based parameters. Note smaller power on pitch-to-diameter ratio.

Performing an independent curve fit using the form of the second correlation results in slightly different parameters and yields the following result:

$$Nu_p = 8.676 \left(\frac{P}{D} \right)^{-0.1146} Re_p^{.2618} \quad (3-39)$$

This is plotted in Figure 3-21.

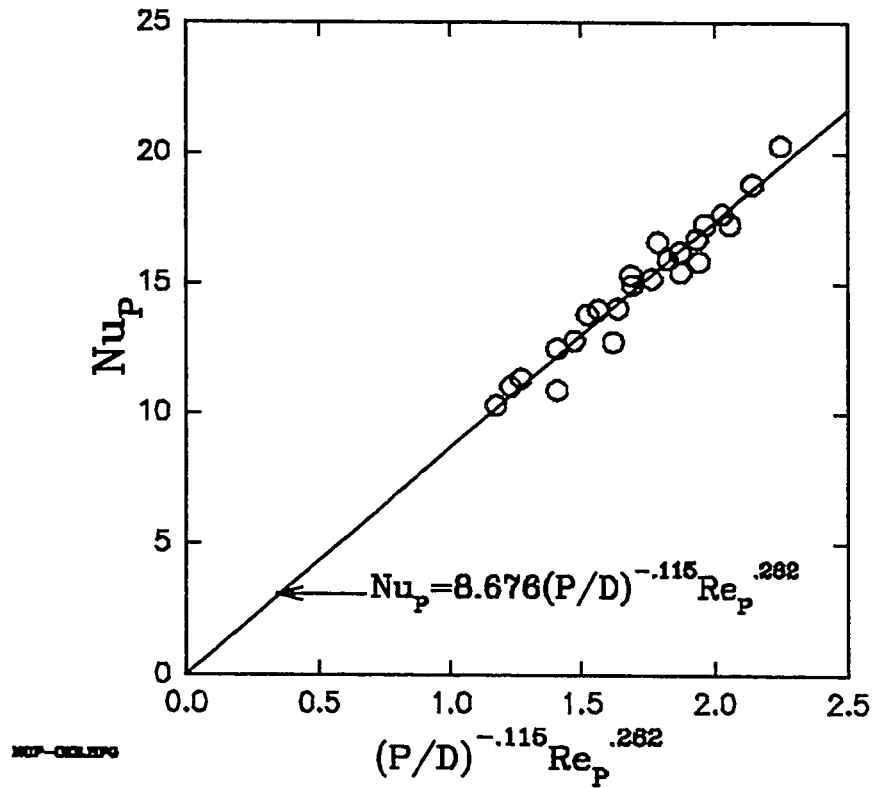


Figure 3-21. Best fit of overall FLUENT heat transfer results using pitch-based parameters.

Finally, based on the success of correlating back surface heat transfer as NTU vs. Re_p , a fit of this type was attempted for the entire plates and yielded:

$$NTU = 9.848Re_p^{-.7518} \quad (3-40)$$

This is plotted in Figure 3-22.

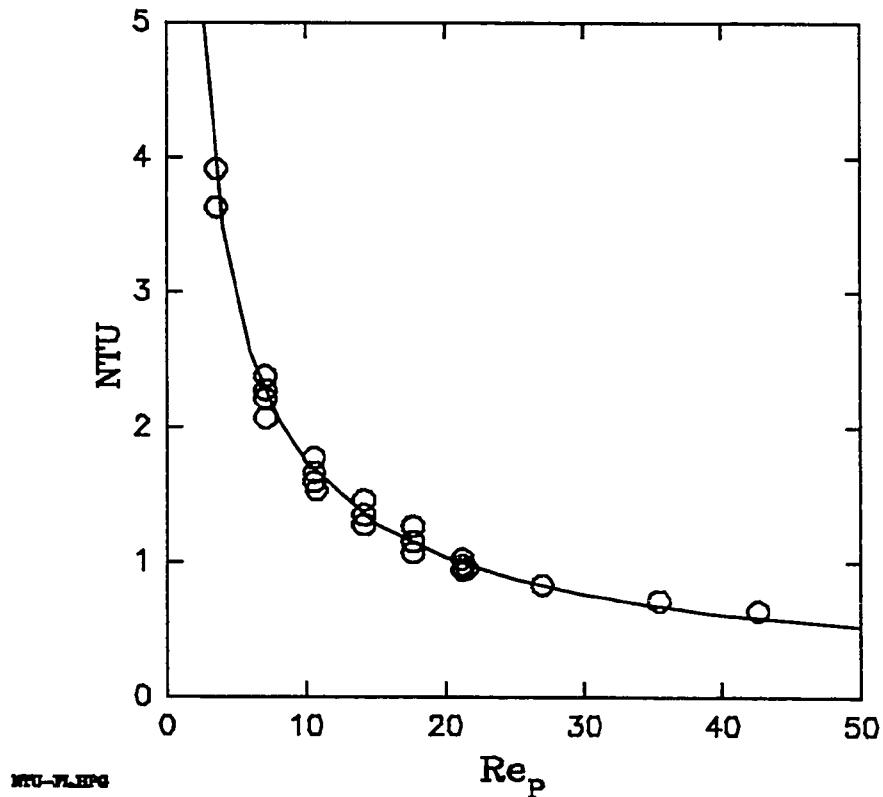


Figure 3-22. NTU vs. pitch-based Reynolds number for overall FLUENT heat transfer results.

Note that although this fit is not bad, there is vertical spread in the data due to the effect of the hole diameter. Using a correction term of $(P/D)^x$ does not work since this

involves P also. (A fit using this term yields a value of 0 for the exponent x .) Attempts to fit the data by defining Re based on $P-D$ instead of P resulted in considerable scatter. Thus the obtained fit may be the best that is possible with a single term correlation of this form.

3.3 Cross-Flow Model

When the effect of a cross wind on the absorber is added to the problem, it ceases to have axisymmetry, and a three-dimensional model is required. In addition, in order to accurately model the edges of the holes, a boundary-fitted coordinates capability is needed. This capability only became available near the end of this study in the form of FLUENT version 4.11 and its companion boundary-fitted coordinates grid generator, PreBFC. A 28,000-node model of plate 5 was set up and run on the 33-Mhz 486 computer on which the NREL copy of FLUENT is licensed. Flow conditions were a 0.03 m/s face velocity and a 2 m/s wind speed with a heat flux of 800 W/m² applied to the plate surface. Convergence on the 486 took over 48 hours, thus making multiple runs impractical. As of this writing, NREL has obtained a new dedicated work station and is in the process of converting to a work station license which will allow extensive 3-D models in the near future.

Although multiple runs have not yet been made and refinements in the grid are still underway, the single run provides useful physical insight into the problem, and some qualitative results will be shown here. To model the flow, a control volume was assumed to be in the asymptotic region of the plate. The control volume includes a half-hole and two quarter-holes with symmetry boundary conditions for the sides in the flow direction and cyclic boundaries for the upstream and downstream edges. The entire plate thickness is modeled, with constant pressure boundary conditions used at the hole exits and free stream wind conditions at the edge of the boundary layer taken as 1 cm above the plate.

Figure 3-23 shows the surface temperature distribution (wind direction is from left to right). In this plot, the surface is reflected across the centerline of the half hole to make it easier to view. **Figure 3-24** is a velocity vector plot showing the separation and recirculation which occurs on the upstream side of the hole passage. **Figure 3-25** shows the temperature distribution in the same plane showing the recirculation region in the hole as well as the thickness of the thermal boundary layer above the plate. The effect of wind on both the surface and the hole can be expected to result in a change in effectiveness as wind is applied. This will be shown in the experimental results covered in the next chapter.

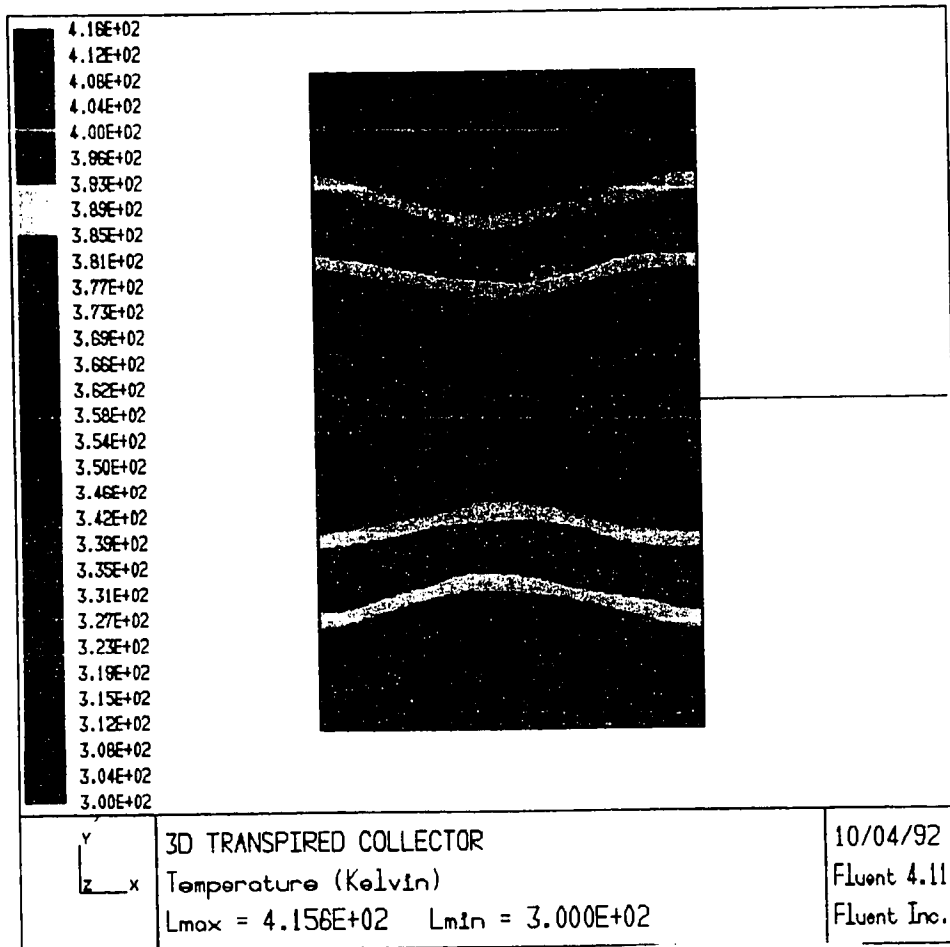


Figure 3-23. Surface temperature distribution from 3-D plate model.

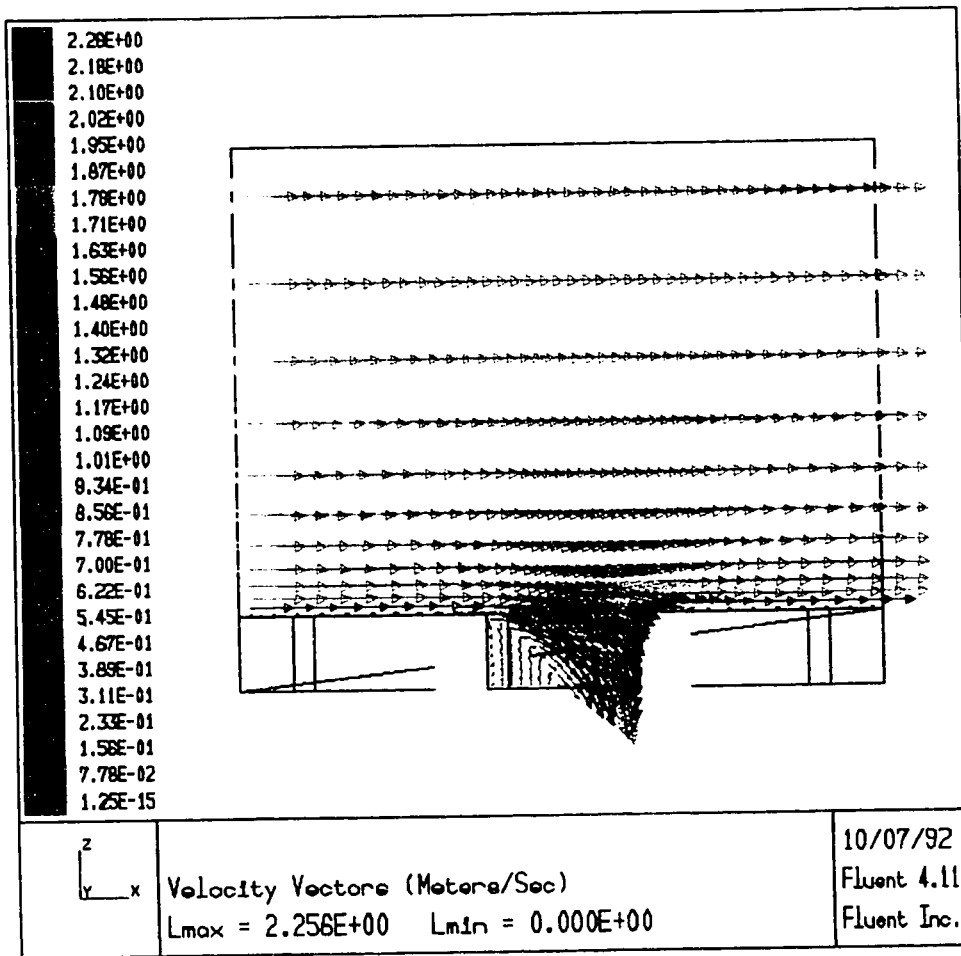


Figure 3-24. Velocity vector plot for 3-D model showing flow through hole.

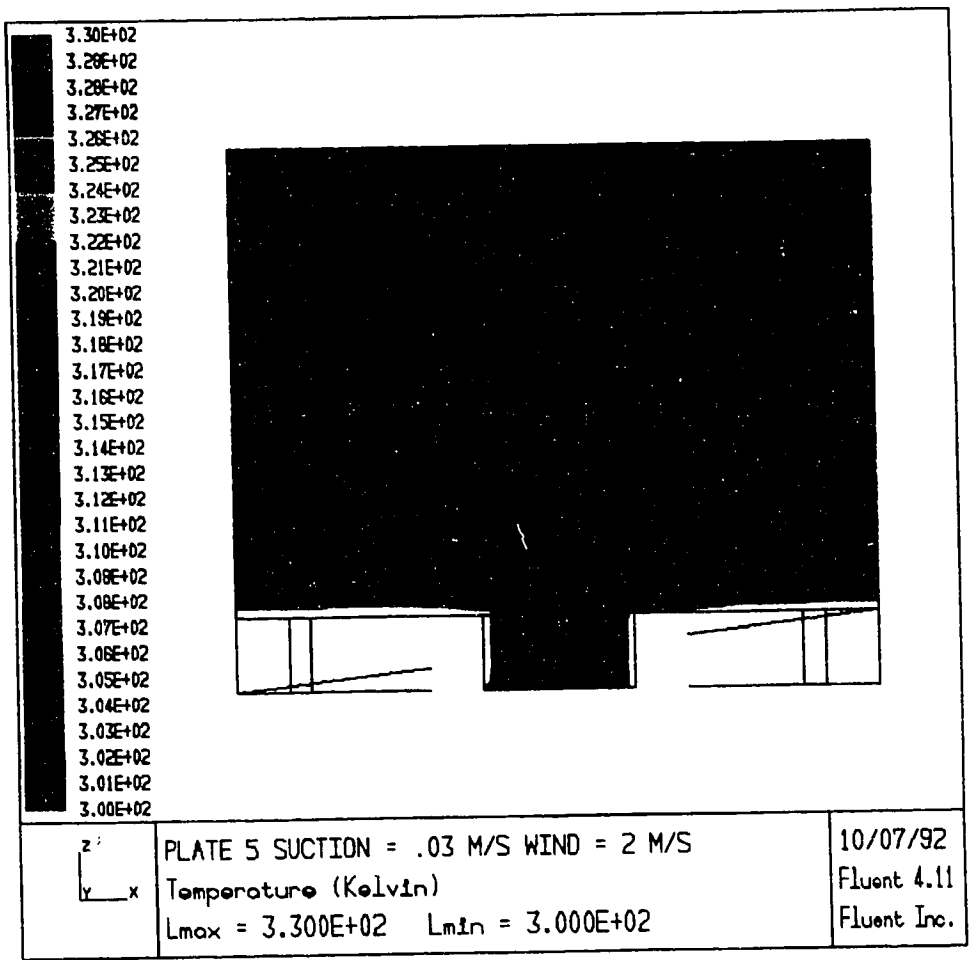


Figure 3-25. Temperature distribution for 3-D model showing thickness of plate boundary layer and heat transfer in hole.

Chapter 4. EXPERIMENTS

4.1 Apparatus

The purpose of the experimental apparatus was to determine the heat transfer characteristics of transpired perforated plate solar absorbers under controlled conditions of heating, ambient temperature, and wind speed. Although outdoor test data had been taken on one test absorber by Kutscher, Christensen, and Barker (1991b), the test conditions were too variable to provide reliable, repeatable data on heat exchange effectiveness and wind heat loss. Accordingly, the Transpired Collector Test Facility (TCTF) was designed and built at NREL. This consists of a 0-10 m/s open circuit wind tunnel, a test box with suction piping, a lamp array to provide uniform heating, and an instrumentation and data acquisition system.

4.1.1 Test Box

It was desired to test plates of sufficient size to cover a range of different wind speeds. Uniform suction theory as described in Chapter 2 indicates that the starting length before establishment of an asymptotic boundary layer can be expressed as:

$$L_s \approx \frac{U_a v}{V_0^2} \quad (4-1)$$

The absorber length needed for the boundary layer to become asymptotic thus depends on the minimum suction velocity and maximum wind velocity of interest. Other experimental constraints include reasonable sizes of the light source and wind tunnel. Using the minimum suction velocity of 0.01 m/s and a maximum wind speed of 10 m/s yields a starting length of 1.59 m which would require both a large tunnel size (as discussed later) and a large light source. By allowing a minimum suction velocity of 0.02 m/s the starting length at a wind velocity of 10 m/s is .48 m. Using a 0.50 m long absorber covers this condition and also allows a suction velocity of 0.01 m/s at a wind speed of 2.5 m/s. (Actual test data for this study were taken at considerably lower wind velocities, namely 0 to 4 m/s to cover the reasonable range of expected conditions.) The width of the absorber was chosen based on typical width-to-length ratios used for boundary layer experiments in the past and by the requirement based on boundary layer thickness of Rotta (1970). It was also desired to maintain a low aspect ratio to minimize the ratio of perimeter to surface area and thus minimize edge conduction losses in normal flow heat exchange effectiveness experiments. A 0.5 m x 0.3 m absorber has the same perimeter as a 0.4 m x 0.4 m absorber and 94% of the surface area.

The test box was constructed of 9.5 mm (3/8") Baltic birch plywood. This plywood has nine plies which contain virtually no voids. The box was screwed and glued together, and the inside joints were sealed with silicone caulk. Two layers of one-inch poly-isocyanurate foam insulation were used to line the box, giving the walls an effective insulation value of R-15. The top lid is essentially a frame which holds the test absorber. Both the top and one long side are removable for instrumentation access. Closed foam weatherstripping is used to seal the edges when the top and side are in place. Duct tape is then used over the outside joints to ensure a leak-free seal. The absorber is mounted on a series of plastic push-pins which provide minimal conduction paths between the absorber and the top frame. Tape is used to cover the gap between the metal absorber and the frame to prevent leakage around the edge of the absorber.

Suction through the box is provided by an Ametek Model No. 116465 0-110 CFM universal AC-DC vacuum motor, and its speed is controlled by a 10 amp variable transformer. Piping and fittings are 5.1 cm (2-in.) CPVC.

4.1.2 Lamp Array Design

It was decided to use a light source to provide uniform heating of the absorber. This provides even heating and is not effected by the presence of holes in the

plate as would be an electric heating arrangement. It also allows for the use of plate boundaries with very low thermal conduction loss. An additional advantage is that it can provide the same heating to a variety of different plate thicknesses and hole geometries, whereas electric heating would require different currents and attachments for each plate and would lead to considerable fabrication costs. Finally, a light source provides a close simulation of solar heating while avoiding the problems associated with using actual sunlight, namely, variable outdoor temperature, wind, and radiation conditions.

A number of light sources were considered. Use of a single lamp with an appropriately designed lens or reflector was considered, but it was difficult to achieve better than a $\pm 10\%$ flux uniformity with such designs. It was decided that an array of lamps would provide the best uniformity. The lamps were only needed as a source of heat, and duplication of the solar spectrum with expensive lamps was not required. Since a black absorber could be used (and is in fact useful for viewing with an infrared camera) there was no inherent advantage of using infrared lamps. Normal lamps which provide both visible light and infrared can be filtered with glass sheets to remove radiation above 3 microns in wavelength and can thus be read by a calibrated solar pyranometer with this same upper wavelength cut-off.

A number of different lamps were tested to determine which lamps provided fairly high flux with considerable amount of visible radiation and with good uniformity. It was found that 300 W GE R-40 indoor reflector flood lamps with a light frost inside coating provided the most uniform light as measured by an Eppley PSP pyranometer. In order to determine the right arrangement of lamps in an array to provide a target uniformity of $\pm 2\%$ with at least 700 W/m^2 , a FORTRAN computer model was written to calculate total flux on the target due to an array of individually aimed lamps.

The target is assumed to lie in the x-y plane, and the lamps can have any location and tilt in a region above the target plane (positive z). The coordinate origin is at the center of the target plane. The program prompts for target dimensions in the x and y directions, the desired size of the grid in the target plane, and the input data file. The input data file contains the three spatial coordinates and the three pointing angles (relative to positive x, y, and z axes) for each lamp.

A distribution curve (in the form of a fitted polynomial) for lamp intensity as a function of angle off the center beam is contained in a subroutine. The program calculates the flux at each grid point for a given lamp and then adds flux contributions from successive lamps. The output is flux in W/m^2 at each grid point in the target

plane as well as simple statistics such as average flux and spread. The flux distribution is also output to a disk file to allow contour plots to be made.

Details of the flux distribution model are given in Appendix B, which contains the following:

- Calculations and algorithms
- A sample lamp intensity curve and a polynomial fit to the curve.
- Program listing (including set-up instructions and other comments)
- Sample input file
- Sample output

The main difficulty in obtaining uniform flux from an array of lamps is that the tails of the intensity distributions from all of the lamps overlap in the center of the target, thereby causing a flux peak in the center. This problem was handled here by aiming all 16 lamps in the same direction (i.e. normal to the target plane), but using a lamp arrangement with a vacated region in the center. This approach tends to waste a fair amount of light energy off the edges of the target, but the power level required was only 4.8 kW, the lamps are inexpensive, and the set-up is simple. The flux uniformity possible from this approach was found to be excellent.

The array of 16 300-watt lamps is divided into two separate sub-arrays of 8 lamps each so that each sub-array

requires only 2.4 kW, which, at 120 V translates into 20 amps of current. This allows the use of two 30-amp circuits. Each sub-array is controlled by a separate 30-amp 0-140 V output variable transformer (Superior Electric Powerstat Model No. 146), and these are kept at identical settings by using two matched Newport (Model No. 201AN-AC5) digital voltmeters readable to ± 0.1 V. The transformers not only allow the lamps to be adjusted to lower settings, but also allow much higher flux levels (exceeding 1200 W/m^2) by applying over-voltage to the 120-V lamps. At 140 V, however, although the lamps put out 70% more visible light, lamp life is only 14% of the rated value of 2,000 hours at 120 V, and so higher settings were only used on occasion to obtain higher delta-T's to increase accuracy at higher suction rates.

Originally, three ordinary window glass sheets were used between the lamps and the absorber. The glass absorbs wavelengths above about 2.8 microns, and thus passes only light wavelengths which can be read by a solar pyranometer. Unfortunately, the window glass sheets heated up considerably, presumably due to absorption bands in the near-infrared (around 1-2 microns) and re-radiated a significant amount of infrared to the absorber. These were replaced with three sheets of low-iron glass which stayed much cooler. A used furnace fan was installed to suck room air through the gap between the two glass sheets closest to

the absorber, and this arrangement kept the temperature of the closest glass sheet to within 5°C of ambient. An additional benefit of the glass sheets is that, like most low-iron glass which is made by passing through rollers, it has a textured surface on one side. This provided some diffusion of the light which further improved flux uniformity. After some trial and error in arranging lamps (since lamp intensities tended to vary from one sample to another), flux variations over the absorber were measured to be less than $\pm 1.5\%$. Infrared thermography confirmed the excellent uniformity of heating.

4.1.3 Wind Tunnel Design

A wind tunnel was needed to investigate the effects of a cross-wind on the heat exchange effectiveness. The tunnel was also needed for research on measuring heat loss to the wind (example results of which are given later). After being unable to obtain wind tunnel time at the University of Colorado, the decision was made to design and build a tunnel at NREL. A number of wind tunnel experts and texts were consulted, and tunnels at both the University of Colorado and Colorado State University were visited.

The tunnel built for these experiments is an open-circuit design with a .362 m x .64 m (14.25 in. x 25 in.) cross-section at the test section. Flow is driven by a

2.36 m³/s (5000 CFM) centrifugal fan controlled by a variable frequency AC drive. To obtain laminar flow, wind tunnel designers usually use a combination of screens, honeycombs, and a contraction. In general, the honeycombs and/or screens are used upstream of the contraction where they create a smaller pressure drop penalty. The contraction in theory increases the mean u velocity without increasing the turbulence velocity, thereby decreasing the turbulence intensity. A contraction adds to the complexity of the design, however, and must be well-shaped to function properly. Because the needed wind tunnel was small, and operating power was not an important consideration, the decision was made to forego the use of a contraction and instead use a high pressure drop centrifugal fan which would allow use of a large amount of flow conditioning via screens and honeycomb.

An important consideration in the design of the tunnel was the desire to be able to observe the test section easily with an infrared camera. Designing a test section on the suction side of the fan would have required the use of expensive observation windows made of crystalline materials which are transparent to IR. A blow-through design was therefore selected in which the test section is located within the inviscid core of the tunnel exit jet.

This design not only allows easy observation with the infrared camera, but it also provides ready access to the

test plates for changing and instrumenting. It also avoids a problem which can occur in closed test sections operating under a vacuum, namely that any small leak results in a jet of air entering the test area. Finally, wall boundary layers in the test section are avoided, and the test article can be adjusted to allow some flexibility in the attack angle to the wind. Use of a blow-through design with the test section downstream of the fan, however, requires considerable flow conditioning to obtain laminar conditions at the exit.

The dimensions of the wind tunnel were determined from the size of the test article. The free jet at the exit of the tunnel is characterized by an undisturbed inviscid core which extends downstream a distance which depends on the dimensions of the tunnel exit. The tunnel was designed so that the test absorbers would fit entirely within this flow.

Although the tunnel has been used in two different orientations to test both horizontal and vertical plates, the tunnel was originally built for a horizontal, face-up absorber, and the following description applies to this orientation. For an upward-facing plate which serves as the extended floor of the tunnel, room air becomes entrained at each side and at the top of the exit jet. Considering first the horizontal direction, the free jet exiting the wind tunnel contains an inviscid core which

extends downstream on the order of 2 to 6 times the width of the exit. In order to be conservative, the factor of two was used to determine the necessary wind tunnel width. In the vertical direction the exit jet behaves like one-half of a jet which is twice the height of the tunnel exit and is symmetric about the floor. Thus the inviscid core extends downstream 4 to 12 times the height of the wind tunnel exit. Based on an absorber which is .3 m (12 in.) wide by .5 m (20 in.) long and allowing for a 10 cm (4 in.) leading edge before the plate, the required wind tunnel exit dimensions were .61 m (24 in.) wide by .3 m (12 in.) high. A .64 m (25 in.) by .362 m (14.25 in.) dimension was used in order to provide some additional margin of safety and to allow easier mating to the selected fan which has a .362 m (14.25 in.) width on the outlet.

The desired wind speed range was 0 to 10 m/s. (As 5 m/s is considered a very high wind for solar collector testing, this was a generous design criterion, and the tunnel was oversized to allow greater flexibility for future applications.) With a known cross-sectional area for the test section, the required fan volumetric flow rate is easily determined to be 2.36 m³/s (5,000 CFM). Selection of a centrifugal fan allows for a high system delta P, which provides good flow conditioning. Standard pressure drop calculations were performed to determine the system head loss curve. For flow conditioning, seven 16-mesh

window screens were used, preceded by a plastic honeycomb. An additional screen was used upstream of the honeycomb to provide relatively uniform flow to the honeycomb. These devices reduce large-scale turbulence to smaller scale turbulence which dies out quickly, and they also provide a uniform velocity profile. The screens have a K factor of about 0.70. According to (Rae and Pope, 1984) this provides sufficient ΔP without causing a reversal of the flow pattern across the screen. The screens are placed 12.7 cm (5 in.) apart, based on a rule-of-thumb of 500 wire diameters to allow turbulence introduced by the wires to die out before the next screen. Each screen is expected to reduce axial turbulence by a factor of $f = 1/(1+K)$.

The plastic honeycomb has a cell size of .64 cm (.25 in.) and a depth of 5.1 cm (2 in.), providing an L/D (ratio of cell length to cell diameter) of 8, within the range of 6-8 typically used for wind tunnel design. It decreases lateral turbulence by a factor of $f = 1/(1+K)^{0.5}$ and also reduces any swirl in the flow. (Plastic was used instead of metal, because the thin metal walls in honeycomb structures tend to bend at the edges and this can introduce turbulence.) Studies of honeycomb/screen combinations have concluded that a honeycomb located upstream of the screens provides the best combination (Loehrke and Nagib 1976). The first downstream screen was placed immediately downstream of the honeycomb to prevent the generation of

turbulence due to shear interactions between the exit jets from the honeycomb cells.

A Unistrut rig was built to stretch the screens prior to gluing them to wooden frames. In order to have the screens extend all the way to the wind tunnel walls, the walls of the flow conditioning section were made out of Gatorfoam, a rigid styrofoam material with a thin cardboard veneer, which can be machined smoothly. A router was used to create grooves for the screen frames to seat in. The external walls of the flow conditioning box are made out of 1.27 cm (1/2 inch) plywood.

Pressure drop calculations included loss terms for the entrance, diffusing section, straight duct, honeycomb, screens, and exit. Since the total head loss is heavily dominated by the multiple screens, tests were run in the lab to measure the K factor of ordinary nylon window screens. The average measured value was about 0.85, compared with a value from the ASHRAE handbook of .57. The larger value was used in the head loss calculations. Total system head loss at 2.36 m³/s (5,000 CFM) was calculated to be 423 Pa (1.7 in. H₂O). To meet this operating point, a backward-inclined centrifugal fan was selected (since backward-inclined blades provide more stable operation) with an H-Q curve which was very steep near the operating point. This means that any variations in head (H) only cause very small changes in flow rate (Q).

The selected fan was Dayton (Grainger) Model No. 3C074A. Its operating curve at 1672 RPM is shown in **Figure 4-1**. This model has a sound rating of 73 dbA, which was considered acceptable. It is belt-driven by a 2.24 kW (3 HP) motor operating off a 3-phase, 230 V power source. A Fincor Model No. 5204P1 adjustable frequency AC motor control is used to control fan speed. This allows the wind tunnel speed to be varied while remaining at the same stable point on the fan curve.

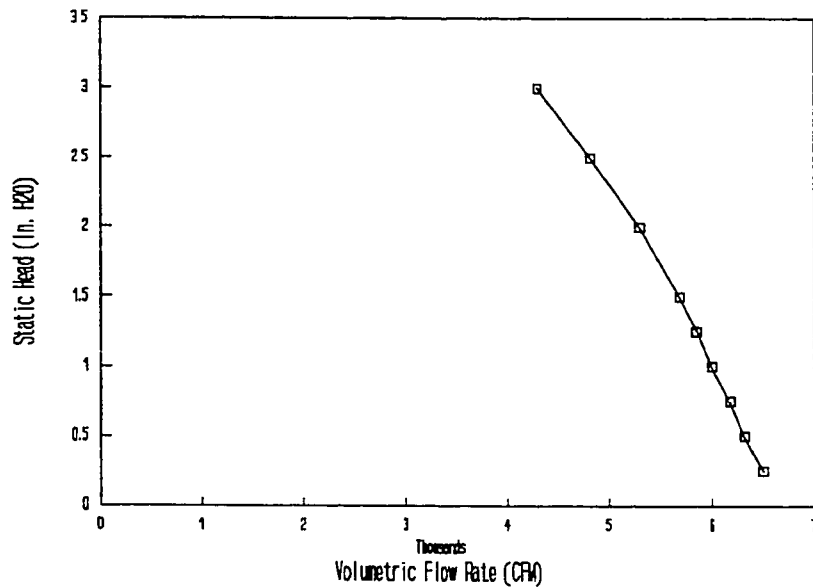


Figure 4-1. Fan curve used for wind tunnel.

Once the fan model was selected, the design of the diffuser section between the fan outlet and the flow conditioning box could be completed. This provides a smooth transition from the fan outlet dimensions of .498 m (19-5/8 in.) vertical by .362 m (14-1/4 in.) horizontal to the flow conditioning box (and test section) dimensions of .362 m (14-1/4") vertical by .635 m (25 in.) horizontal. Due to an original reluctance to operate the fan on its side, this required a contraction in the vertical plane and an expansion in the horizontal plane. (The test section vertical dimension was chosen as exactly .362 m [14-1/4 in.] so that if the fan were later placed on its side, a simpler diffuser with parallel wall and ceiling would suffice. However, when vertical test results were later desired, it was found that the entire tunnel, including the fan, could be rotated onto its side, with the only required modification being setting the fan shaft set screws into the shaft to prevent the fan cage from migrating along the shaft.)

It is important in a diffuser to avoid any flow separation on the walls. According to Rae and Pope (1984), the total angle between opposite walls in an expansion should be less than 7°. A diffuser design angle of 6° was selected, which translated into a 2.87 m (9'5") diffuser length. The diffuser was made out of grade A-C 1.27 cm (1/2 in.) plywood with the A (smoother) side facing inward.

The diffuser is framed by four 2"x2" redwood boards, with the side walls screwed into the redwood. Because of the unusual outflow pattern from a centrifugal fan, there was still the possibility of flow separation. One of the diffuser side walls was made removable so that corrective measures could be taken in case this became a problem. Measurements of wind speed showed a range of 0 to 9.7 m/s, thus allowing winds in excess of 20 mph. Pitot tube traverses show flow uniformity of $\pm 3\%$ over the test section with or without plexiglass side walls in place.

A smoke wire consisting of .25 mm (10-mil) constantan (from a 30-gauge copper-constantan thermocouple pair) coated with Lionel model train oil at low wind speeds and ordinary motor oil at higher speeds and with an applied voltage of 10 V AC is used to visualize flow. The electric resistance heating of the wire causes small beads of oil on the smoke wire to vaporize, thereby serving as a source for streaklines. The resulting streak lines show good laminar flow. **Figure 4-2** shows the experimental apparatus. **Figures 4-3** through **4-5** are photographs showing, respectively, the wind tunnel, flow conditioning box, and test section. **Figures 4-6a** and **b** are streak line photographs showing, respectively, passive wind tunnel boundary layer removal with a sharp leading edge upstream of the test plate and the effect of suction on the test plate. Turbulence intensity was also checked using a TSI

IFA-100 hot wire anemometer system and values of 0.60% to 0.80% were measured. However, examination of the hot wire output with an oscilloscope indicated some electronic noise being picked up, so the above values of turbulence intensity are believed to be conservative.

TRANSPIRED COLLECTOR TEST FACILITY

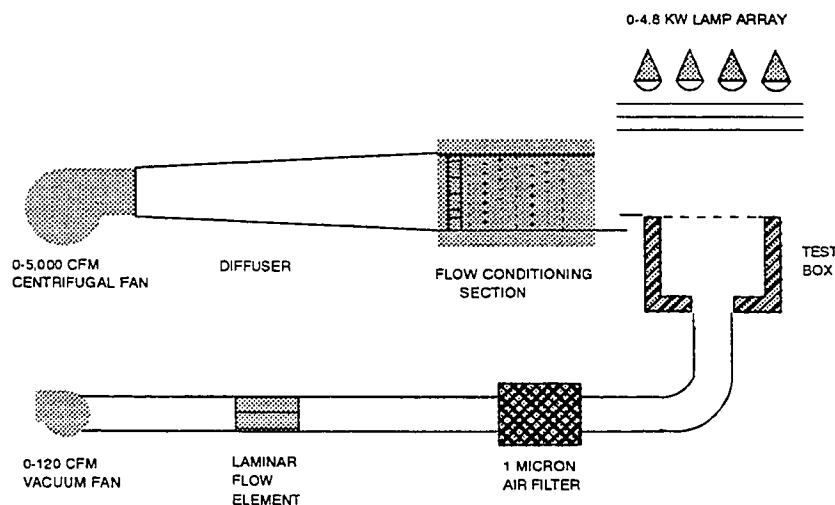


Figure 4-2. Transpired Collector Test Facility showing wind tunnel, test loop, and lamp array.

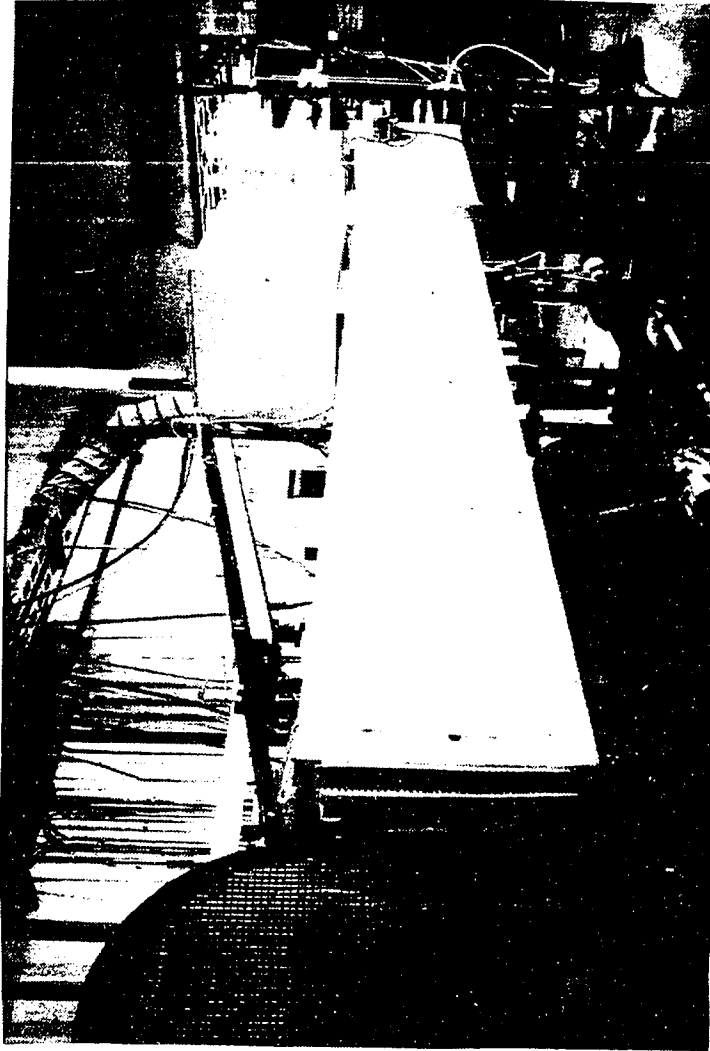


Figure 4-3. Wind tunnel with fan in foreground and lamp array at exit.
Wind direction is left to right.

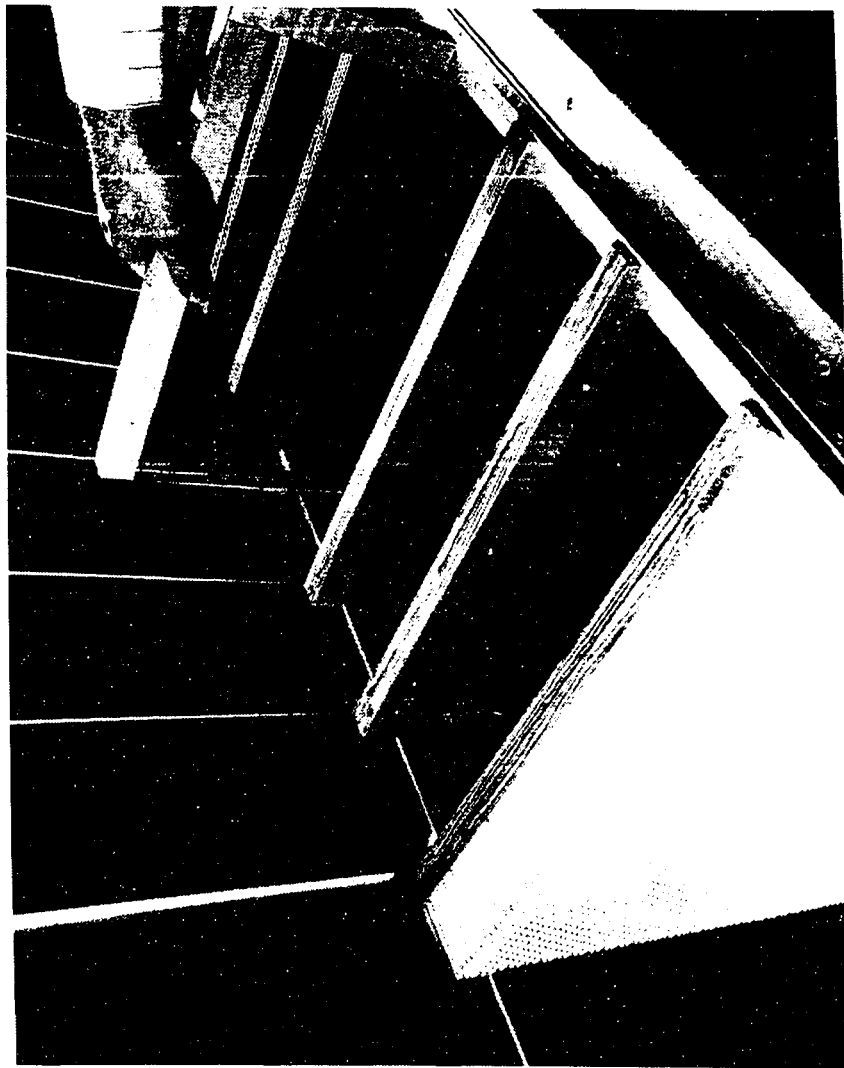


Figure 4-4. Wind tunnel flow conditioning box showing honeycomb in foreground and removable screens.

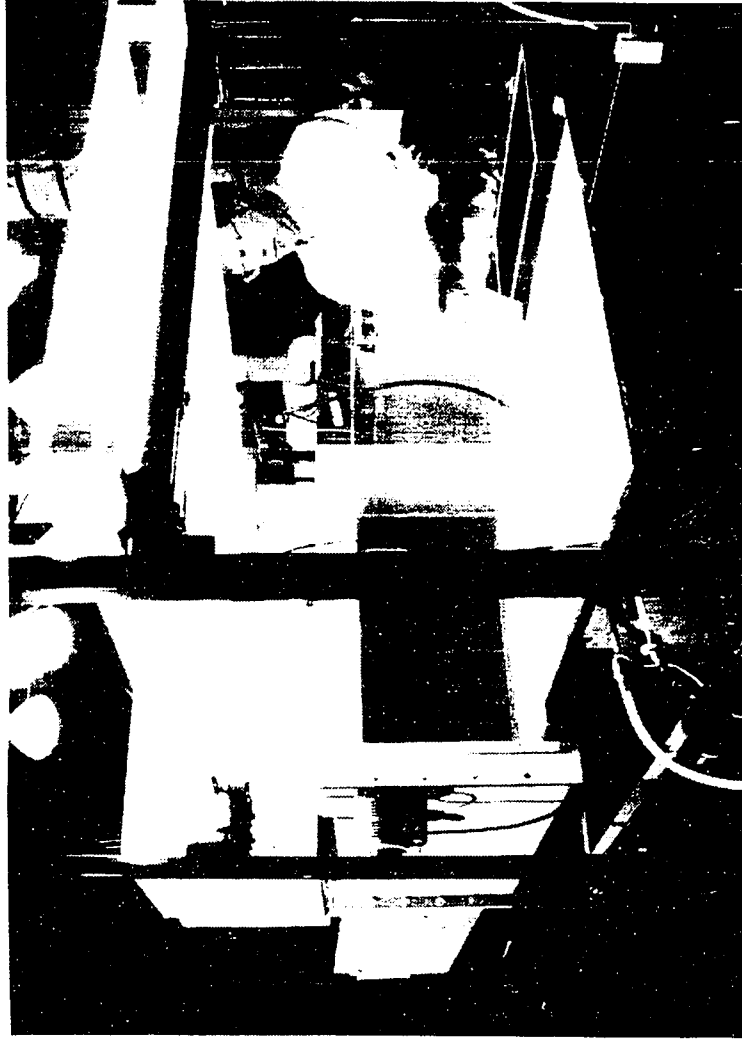


Figure 4-5. View of wind tunnel exit showing test plate and lamp array.

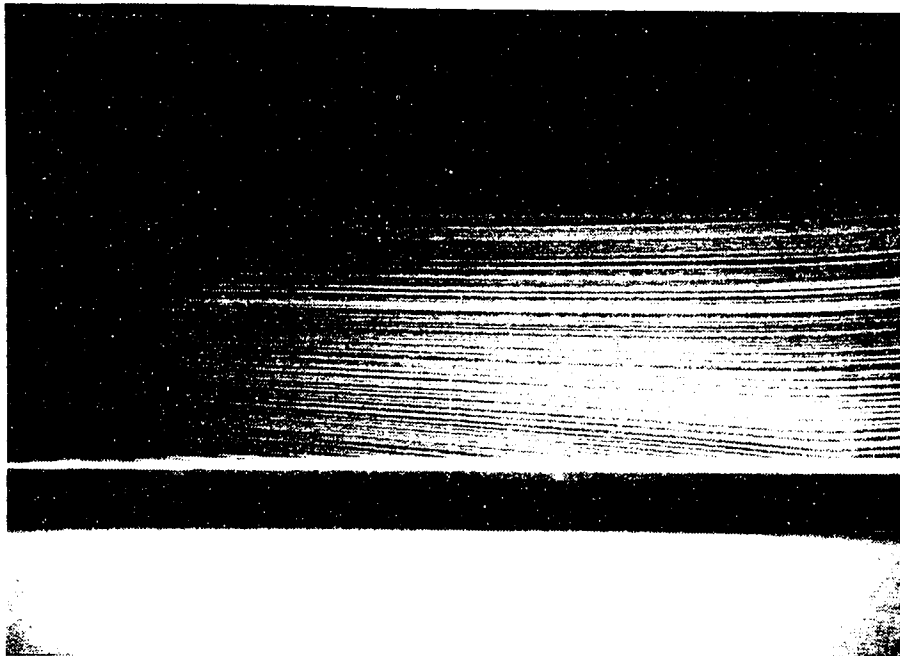
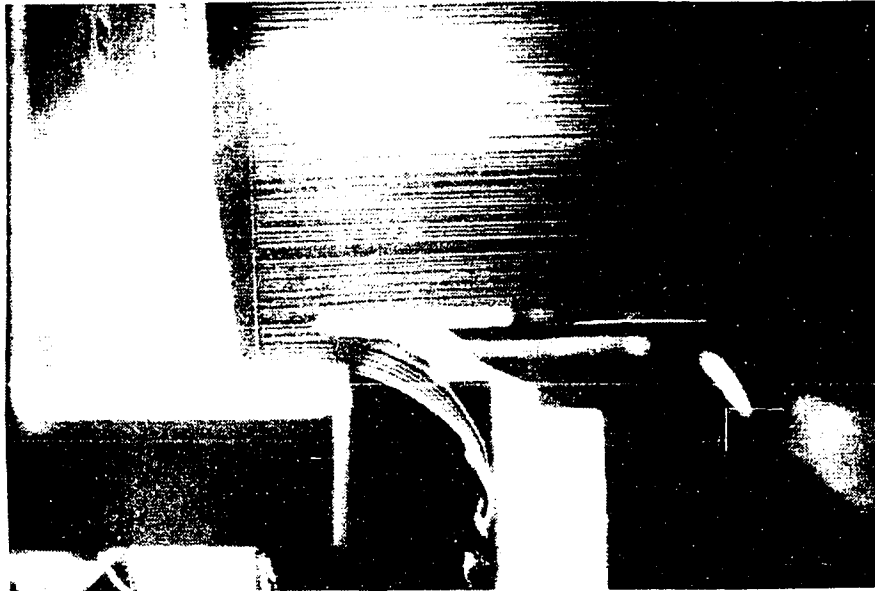


Figure 4-6. Smoke wire results for 1 m/s wind flow over absorber: a) leading edge boundary layer removal, b) effect of suction mass flow rate = $0.10 \text{ kg/m}^2\text{-s}$.

4.2 Instrumentation/DAS

4.2.1 Data Acquisition System

Data acquisition was done using an HP-75000 B-frame VXI bus data acquisition unit, controlled by an IBM PC-AT programmed in HT-Basic (a commercial version of HP-Basic). The HP-75000 consists of an internal HP-1326 5-1/2-digit digital voltmeter and several multiplexer/thermocouple cards. The voltmeter has 1 μV resolution and 5 μV accuracy. Quoted overall data acquisition system accuracy (not including sensors) for measuring temperature is $\pm 0.5^\circ\text{C}$ for type T thermocouples and $\pm 0.1^\circ\text{C}$ for 10,000 ohm thermistors. Experience with this unit would suggest that these accuracy specifications are quite conservative especially for the thermocouples.

4.2.2 Temperature Measurement

Both type T (copper-constantan) thermocouples and YSI 10,000 ohm ($\pm 0.1^\circ\text{C}$ interchangeable) thermistors were used to provide a check. The thermocouples were made from Gordon 30-gauge special calibration ($\pm 0.5^\circ\text{C}$) wire. Dr. Robert Moffat of Stanford University, an expert in the use of thermocouples, has estimated that two-thirds of the wire error results from spool-to-spool variation. Thus all thermocouples were made from the same spool. Also, to avoid errors associated with the data acquisition system

reference junction and to avoid the error associated with two independent voltage measurements, thermocouples were wired in a difference network to measure ΔT directly. The emf from each thermopile was converted to a temperature difference by taking a fourth order NBS polynomial for $E(T)$ which is accurate to $\pm 1 \mu V$ and inverting it in the software with a Newton-Raphson subroutine. In this way, the software temperature conversion has an accuracy of $\pm 0.025^\circ C$.

Because emfs are created throughout the wires in a thermocouple installation, separate calibration of thermocouples was not performed. However, a zero thermopile reading was checked by placing both junctions in a zone box. Thermocouple connectors were kept in a zone box and thermopile ΔT 's were checked against the same ΔT made by separate thermistor measurements.

Where accurate absolute temperature measurements were needed, the YSI thermistors were used. The choice of 10,000 ohms was based on consideration of the temperature range needed and the current sources provided by the HP-75000 to minimize thermistor self-heating error. Using a still air dissipation constant provided by YSI of 1 milliwatt/ $^\circ C$, the largest self heating error to be expected in the experiment was about $0.05^\circ C$. Lead wire was chosen such that its resistance was less than 0.1% of the lowest thermistor resistance expected. Calibration of all thermistors was checked in the NREL Calibrations

Laboratory. Ice bath readings were also taken. Thermistor conversion (from resistance to temperature) was done automatically by built-in "firmware" in the HP-75000. This conversion was checked over the range of interest by comparing it to a software conversion using the Steinhart-Hart equation as well as by direct comparison to the YSI tabulated data, and it was found to be accurate to better than $\pm 0.03^{\circ}\text{C}$.

With sensor and data acquisition errors at a minimum, the major sources of error are associated with installation. Temperature is measured at three basic locations: ambient, plate surface, and plate outlet. The plate surface measurement is made by gluing thermocouples and thermistors to the bottom of the plate using high thermal conductivity epoxy. The bottom of the plate is used to avoid radiation error from the lamps. Position on the plate is not critical, as both finite difference analysis and infrared thermography indicated that the aluminum plates are isothermal to within less than 0.05°C between adjacent holes. For normal flow tests, the plates were virtually isothermal except for about a 1 cm border along the edges. To minimize thermal conduction loss along the sensor leads, the leads were also glued to the bottom of the plate using high thermal conductivity epoxy for a distance of more than 10 cm. This installation method was compared to other means such as mounting the sensor in high

conductivity silicone paste and covering with copper electrode tape, and the difference was less than 0.05°C.

The ambient temperature probe containing both a thermocouple and a thermistor was provided with two concentric, radiation shields and aspirated with enough suction flow to level out the temperature reading. Outlet temperature is measured 10 cm below the plate by an array of nine exposed junction 30-gauge type T thermocouples connected in parallel and wired in a thermopile circuit with the ambient thermocouple and by a radiation-shielded, aspirated thermistor probe located 7.5 cm below the plate.

The bottoms of the test plates are unpainted aluminum, as is the pressure drop plate inside the test box, and the walls of the test box are covered with low emissivity aluminum tape so that the outlet air sensors are surrounded by a low emissivity environment. With these precautions taken and with the low temperature differences involved, radiation error is small. Nevertheless, the outlet thermistor is shielded because of its greater exposed sensor area. Rather than using conventional aspiration which would disturb the flow inside the test box, a new probe was developed consisting of a cone-shaped shield filled with a fiberglass matrix. Air is aspirated at a flow rate of $3.93 \times 10^{-5} \text{ m}^3/\text{s}$ (5 SCFH) through a small hole at the apex of the cone and is drawn through the matrix in which the thermistor is embedded. This provides a radiant

environment for the thermistor that is close to the air temperature. The small aspiration rate (which also serves to mix the air) was determined experimentally by increasing the suction rate until no further temperature change occurred. The aspirated air is returned to the air stream below the box exit but before the flowmeter so that the total flow rate across the test plate is properly recorded.

For normal flow experiments, the ambient probe position was adjusted to sample the air as close to the plate as possible without getting into the warmer thermal boundary layer. This usually meant taking a reading a few centimeters above the plate. When taking cross-flow data, the probe was located just above the leading edge (used to remove the boundary layer from the bottom of the wind tunnel). The probe location was also tested at the downstream side of the leading edge to make sure that any temperature rise due to heat transfer from the leading edge was negligible. In both the normal flow and crossflow cases, the ambient probe was located near a region of the plate away from the surface temperature measurement so that the flow would not be disturbed at that location. The outlet probe location was found to be relatively insensitive to depth inside the plenum box, but was located directly under the surface temperature measurement. A compartment made from reflective matboard was used to isolate the air stream in which the outlet air temperature

was read to avoid influence of the boundary layers on the inside walls of the test box.

4.2.3 Flow measurement

Several flowmeters were tried. Originally, orifices were used. A major problem was that because of the dependence of pressure on the square of velocity, it required several orifice plates to cover the flow range desired. This meant that some inevitable discontinuity in the data occurred when changing plates and the changeover was inconvenient. More importantly, ISO accuracy and conversion specifications do not cover orifices as small as the ones needed. An available turbine meter was calibrated and installed, but did not provide a smooth plot of absorber pressure drop versus suction rate, and was very non-linear at the low end of the range. Such meters are also subject to decalibration as the bearing wears with time. Calibrated rotameters were considered, but these typically have low accuracy when used near the minimum of their range, and they do not typically provide output that can be read by a computer and averaged. They also incur very high pressure drops. Vortex shedding meters were not available for the low air flow rates used in this experiment. Mass flow meters (which measure the temperature rise across a heated element) did not provide the high accuracy ($\pm 1\%$ of reading) desired.

What was needed was a flowmeter that could provide high accuracy (i.e., 1 percent of reading, not of full scale) over a wide flow range, would not easily decalibrate, and could be read by the data acquisition system. The only flowmeter that could be found meeting these specifications was a laminar flow element. Accordingly, a 0-.020 m³/s (0-43) CFM Meriam laminar flow element was purchased and mounted inside 5.1 cm (2") PVC pipe. Straight pipe sections of 24 pipe diameters were used on both the upstream and downstream sides. The laminar flow element was calibrated at the Colorado Engineering Experiment Station, Inc. (CEESI) with the inlet and outlet pipes in place and was found to agree with the Meriam factory calibration curve to within 0.5% over the full flow range. The pressure drop across the flowmeter was read using a $\pm 0.5\%$ of reading MKS capacitance pressure transducer (see next section).

Laminar flow elements have two potential disadvantages: they exact a high pressure drop (typically 2,000 Pa [8 in. H₂O] at maximum rated flow), and their small passages can eventually clog if they are exposed to very dirty air. In this experiment, the suction fan could provide over 25,000 Pa (100 in. H₂O) pressure drop, and fan power was not an issue as it might be in an industrial process. Although the laboratory air is reasonably clean, a 1 micron Fram automotive air filter was placed inside a

specially built plexiglas housing and installed upstream of the laminar flow element.

Typical flow rates through the test box ranged from 1.65×10^{-3} to 1.65×10^{-2} m³/s (3.5 to 35 CFM). In order to ensure that the laminar flow element could read at the lower end of this range with sufficient accuracy, a test was made with a 0 - 3.54×10^{-3} m³/s (0-7.5 CFM) laminar flow element mounted in series with the 0 - .020 m³/s (0-43 CFM) unit. Readings were made over a range of 7.1×10^{-4} to 3.54×10^{-3} m³/s (1.5 to 7.5 CFM), and the two elements agreed to within one percent over this range. This would indicate that with pressure drop measured using the MKS transducer, the installed laminar flow element can provide a useable turndown ratio on the order of 30:1 with $\pm 1\%$ of reading accuracy.

Ultimately, the flow velocity across the test plates is needed. By knowing the overall volumetric flow rate from the laminar flow element, it is a simple matter to calculate the approach velocity for the plate, provided the flow across the plate is uniform. In general the plates tested had very low porosities (5% maximum), and the resulting high pressure drops tended to cause uniform flow. Nevertheless, an additional low porosity perforated plate was placed inside the plenum box to ensure flow uniformity. Flow uniformity across the absorber was checked by observing the surface temperature distribution with an

infrared camera under conditions of uniform flux, and by taking pressure readings at each suction hole. (A manometer was read with one leg at ambient pressure outside the box, and the other leg placed over individual suction holes to measure the local pressure inside the box.) Variations in this pressure difference were found to be less than one percent from hole to hole.

Wind speed measurements were originally taken with a pitot tube with an MKS pressure transducer used to measure the pressure differential (total minus static pressure). A traverse of wind velocities above the test absorber showed uniformity of $\pm 3\%$. Because pitot tubes cannot provide good accuracy below a velocity of about 3 m/s, the wind tunnel fan RPM was separately measured with a Monarch digital tachometer (which utilizes an optical sensor). Plotting fan RPM vs. pitot tube velocity yields an excellent linear fit that passes through the origin. The data acquisition system reads the fan RPM and converts this to wind speed using the slope of this calibration curve. This allows for accurate wind speed measurements below the range of the pitot tube.

4.2.4 Pressure measurement

Absolute pressure at the entrance of the laminar flow element was measured using an MKS 133-133,000 Pa (1-1,000 torr) absolute pressure transducer, rated at $\pm 0.5\%$ of full

scale accuracy. This was factory-calibrated and frequently checked against a mercury barometer. Pressure drop across the laminar flow element was measured using an MKS 0-2490 Pa (0-10 in. H₂O) transducer rated at $\pm 0.5\%$ of reading accuracy and calibrated at CEESI. The transducer was periodically checked against a Meriam 0-2490 Pa (0-10 in. H₂O) inclined manometer, readable to 2.49 Pa (0.01 in.), and agreement was within 0.2%. Pressure drop across the absorber was determined by a Dwyer 0-498 Pa (0-2 in. H₂O) point gauge manometer readable to 2.49 Pa (0.001").

4.2.5 Radiation measurement

Although, as explained in the next section, all heat exchange effectiveness measurements reported in this thesis were determined by direct temperature measurements, net radiation measurements were used in conjunction with an energy balance to serve as an independent check. Also, direct radiation measurement was needed to determine the wind heat losses reported in Section 4.5. Net radiation on the plate was determined by taking separate measurements of short-wave and long-wave radiation. Short wave ($<3\mu$) was measured with an Kipp & Zonen CM-11 pyranometer calibrated to $\pm 3\%$ at the NREL Calibration Laboratory. Long-wave ($>5\mu$) radiation was measured using an Eppley pyrgeometer calibrated at the Eppley factory and rated at $\pm 3\%$ accuracy.

The Kipp & Zonen pyranometer was chosen over the more commonly used Eppley PSP pyranometer because literature showed that it suffers from less falloff in response in the near infrared, where considerable lamp energy is contained. (It was also verified by direct comparison that the Kipp & Zonen reads a radiation value of 5% higher than an Eppley under the lamp array.) It consists of a black sensor located under two glass domes. These domes are essentially opaque to radiation wavelengths greater than 3 μ . Although the tungsten elements in the lamps used to irradiate the absorber are sufficiently hot that they produce essentially no radiation above this wavelength, the glass covers on the lamps get hot and re-radiate energy at longer wavelengths. In order that the lamps do not provide energy to the absorber that cannot be read by the pyranometer, three glass sheets were used to filter out this radiation. The glass sheets themselves get warm, but their temperature is only on the order of 30-35°C, and thus they re-radiate much longer wavelengths that are readily measured by the pyrgeometer. Thus the pyranometer and pyrgeometer are both employed at the absorber position under the glass sheets. The pyranometer measures the short-wave radiation from the lamps which is transmitted through the glass sheets, and the pyrgeometer measures the incoming long-wave radiation from both the warm bottom glass sheet as well as the surrounding laboratory.

One concern in using a combination of pyranometer and pyrgeometer for measuring radiation was that both instruments are designed for outdoor applications. The pyranometer is specifically designed and calibrated to read solar radiation. Although the short wave radiation here was filtered to be less than 2.8μ , the peak of the distribution was considerably to the right of the solar peak. Although the Kipp & Zonen shows better response at these longer wavelengths than an Eppley, it is still not calibrated for this use. The Eppley pyrgeometer, on the other hand, is made to determine nighttime sky temperatures in the absence of short wave radiation. Radiant temperatures were higher here and were measured in the presence of lamp radiation. Although corrections were applied (see Section 4.5), there remained some question regarding application of these devices to this type of experiment.

In order to check the two-component radiation measurement method, a special device was constructed for providing a single, direct measurement of net radiation absorbed by the plate. This consists of a thin aluminum disk painted on one surface with the same flat black paint used on the test absorbers. The edge of the disk is beveled, and it rests on three point contacts such that it is supported on a massive aluminum housing. The housing is aspirated to maintain its temperature at ambient. A 30

gauge type K (chromel-alumel) thermocouple is imbedded in the disk to measure the temperature of the disk as a function of time. A photograph of this device is shown in **Figure 4-7.**

To measure the net radiation, the disk is first placed in a plastic bag and immersed in ice water. After reaching a temperature of 15°C or less, it is removed from the bath and the plastic bag and placed in its supports. The black surface faces the lamp array and is located at the same position as the center of the test absorber. (The absorber is removed to allow the measuring device to be positioned properly.) As the disk heats up, its temperature is recorded at a frequency of at least 10 times per second, until a temperature of 10°C greater than ambient is reached. The aluminum housing is cooled by a suction air stream throughout the duration of the test to maintain its temperature at ambient. The ambient temperature is also recorded during the run.

At any time during the test, the total net heat flux into the disk is proportional to the slope of the temperature vs. time curve. At the precise point in time at which the temperature of the disk is equal to ambient temperature, there is no transfer of heat by either conduction or convection between the disk and the environment, and the increase in temperature of the disk is solely the result of the net radiation heat transfer (both

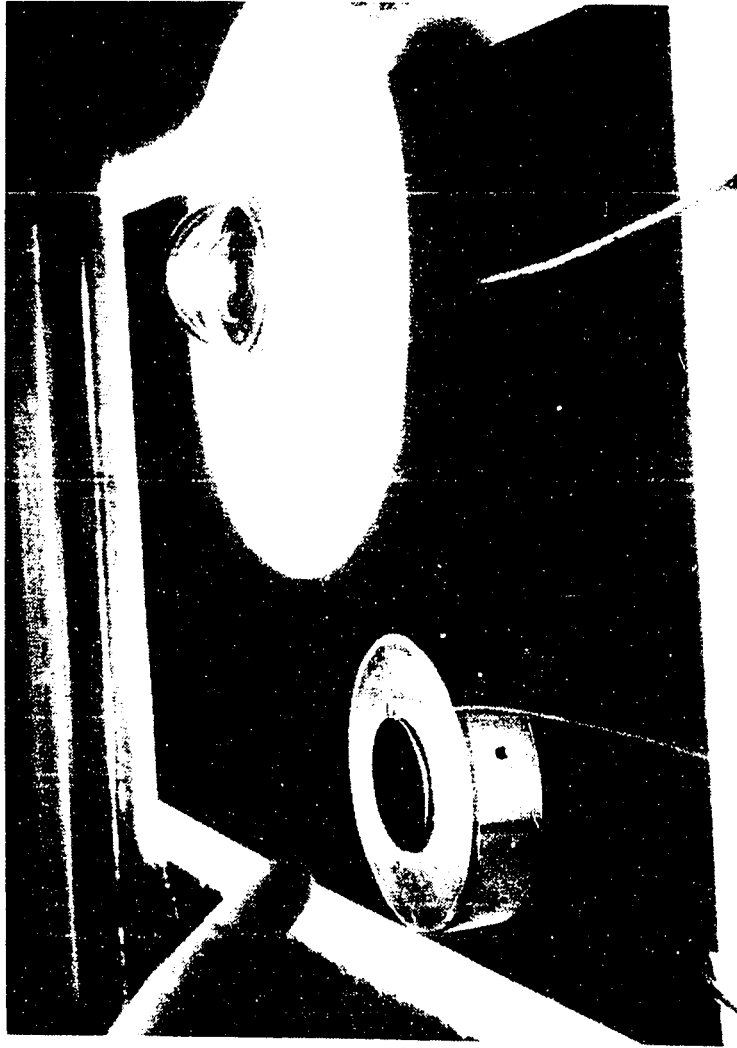


Figure 4-7. Photograph of instrument (left) designed to provide transient measurement of net radiation. A typical pyranometer is shown on the right.

long wave and short wave) with the environment. Thus,

$$Q''(T_{\text{amb}}) = \frac{MC_p \left(\frac{dT}{dt} \right)_{T=T_{\text{amb}}}}{A} \quad (4-2)$$

where $Q''(T_{\text{amb}})$ is the net surface radiant heat flux in W/m^2 , M is the mass of the disk in kg, C_p is the specific heat of the disk in $J/kg-K$, A is the front (painted) surface area of the disk in m^2 . Note that $Q''(T_{\text{amb}})$ is the net radiant heat flux on the absorber when it is at ambient temperature. During a test with an absorber, the absorber will be at a temperature higher than ambient. Thus its emitted radiation will be slightly higher than at ambient and this must be corrected as follows:

$$Q''(T) = Q''(T_{\text{amb}}) + \epsilon \sigma_{\text{SB}} T_{\text{amb}}^4 - \epsilon \sigma_{\text{SB}} T^4 \quad (4-3)$$

where ϵ is the emissivity of the surface.

This method of measurement offers a number of advantages. It does not distinguish between long wave and short wave radiation, and there is no uncertainty regarding any overlap or gap which could occur between two separate measurements. The spectral response of the instrument is exactly the same as that of the test article since it has the same painted surface. (Although the disk could be made of copper or graphite, aluminum was used so that the surface texture would be the same as the test articles.

For a thick layer of paint, however, this is probably not a concern.) No measurement of surface absorptivity is necessary. Although surface emissivity must be measured, it only appears in the term $\epsilon\sigma_{SB}(T_{amb}^4 - T^4)$, which is a small part of the net radiation term.

One disadvantage of this method is that it is more time consuming than the pyranometer/pyrgeometer approach. It also has some uncertainties associated with local variations of ambient temperature in the neighborhood of the disk, lack of perfect isothermality of the disk, etc. The approach used here was to use the pyranometer/pyrgeometer approach after first obtaining good agreement with the transient method.

Initially, three normal window glass sheets were used between the lamp array and the test plates. With this configuration, the net radiation measured by the transient method exceeded that from the pyranometer/pyrgeometer by 16%. Later, the three window glass sheets were replaced by low iron glass sheets, and the transient method then gave a value 3% higher than the pyranometer/pyrgeometer. This difference is well within the expected accuracy of the pyranometer/pyrgeometer and is probably reasonable for the transient device without further refinements. Without detailed spectral measurements, it is difficult to ascertain why better agreement is achieved with the low iron glass sheets than with the normal window glass, but it

must be related to the spectral response characteristics of the pyranometer or pyrgeometer or both. (The low iron glass more closely matches the type of glass used for the domes over the pyranometer sensor.) All net radiation measurements used in this study were done using three low iron glass sheets below the lamp array with a cooling air stream drawn between the two sheets closest to the absorber.

4.3 Heat Exchange Effectiveness

A number of different techniques were considered for measuring heat exchange effectiveness. Naphthalene sublimation was rejected because of the difficulty of using it for thin plates and the problem of Prandtl number extrapolation. Three different heat transfer methods were considered: transient cool-down, energy balance method, and direct delta T measurement. In the transient method, the plate is heated above ambient by the lamp array, and then the lamp radiation is blocked by a shield. The heat transfer coefficient can be determined from the slope of the temperature vs. time curve as the plate cools down. In the energy balance method, the net radiation on the plate is measured, and this is assumed equal to the energy in the airstream.

In the direct temperature measurement method, the effectiveness is simply found from the definition:

$$e = \frac{T_o - T_{amb}}{T_s - T_{amb}} \quad (4-4)$$

where T_o is the outlet air temperature in K.

Figure 4-8 shows a comparison of the estimated experimental uncertainty for all three methods using an effectiveness model based on the final data correlation for zero wind results. (An approximate model used for initial assessment of the three experimental methods yielded similar relative results.) Note that the direct method has good accuracy at high effectiveness values. This is because ΔT 's are high, and so the impact of uncertainties in the temperature measurements is low. At low values of effectiveness, the direct method is poor, although accuracy can be improved by turning the lamp array voltage up and reaching flux values of 1200 W/m² or more. (The curves in **Figure 4-8** are based on a flux of 800 W/m².)

All three methods were tested in the laboratory. In applying the first method, it was found that the uncertainty in measuring slope resulted in less repeatability than desired in measuring effectiveness. The second method suffers from the uncertainty in net radiation measurement. In both of the first two methods, one must essentially estimate and subtract out the radiation heat loss taking place to determine the convective heat loss to the air. At very high effectiveness values, uncertainty

UNCERTAINTY ANALYSIS

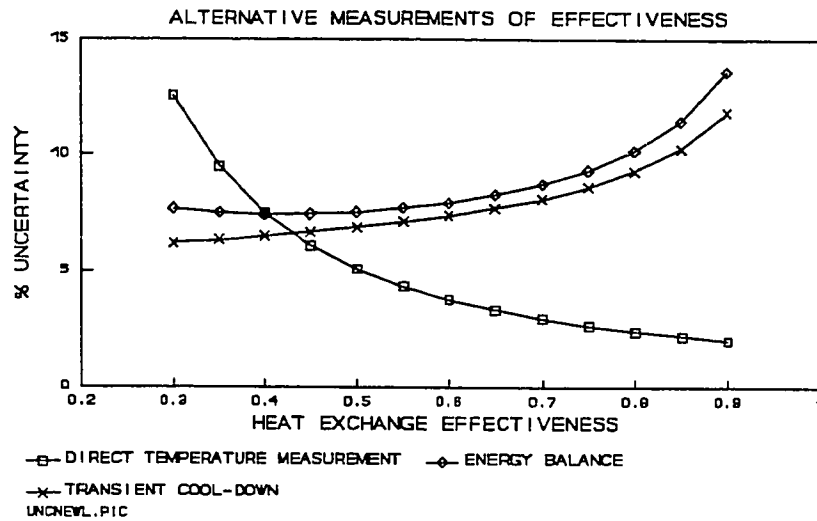


Figure 4-8. Experimental uncertainty of effectiveness measurement vs. effectiveness for three measurement methods.

can become very high as the forced convective heat transfer being measured becomes small compared with the radiation term which must be subtracted out. Thus at the highest effectiveness levels, each of the first two methods can yield effectiveness values exceeding one.

For solar collector applications, high effectiveness values are mostly of interest, and the plates tested ranged in effectiveness from about .40 to about .90. The direct

temperature measurement method has reasonably good accuracy over this region, and it does not yield the unphysical result of an effectiveness that exceeds one. It has the additional advantage that it directly yields the quantity of interest without requiring any conversion. Because of these reasons, as well as the excellent repeatability found in the lab tests, it was chosen as the prime measurement technique, although values from the energy balance method were recorded as well. Measurements of effectiveness with all three methods agreed to within the experimental uncertainty.

The direct temperature method requires measurement of the outlet temperature. As it turns out, this is actually easier to measure accurately than the ambient temperature. The ambient temperature must be measured in all three methods.

One disadvantage of the direct method is that at the low Reynolds numbers encountered, it can take over an hour for a stable, steady-state data point to be obtained, due to the time it takes for the outlet temperature to stabilize. It is thus critical to make data runs in an efficient manner. The major parameters of interest in terms of their impacts on heat exchange effectiveness are the hole pitch, hole diameter, plate thickness, and suction mass flow rate. Also of interest are the effect of wind

speed and the effect of plate orientation. (The two orientations horizontal and vertical were considered here.)

4.3.1 Factorial Experiments

To efficiently determine parameter sensitivities, the experimental work began with a full factorial test of 16 runs covering the three geometry parameters plus suction mass flow rate. Once one of these parameters was found to have a low sensitivity (plate thickness), it was replaced first by wind speed and then by plate orientation in additional factorial runs.

A series of eight original test plates were manufactured to perform the first full-factorial statistical experiment to determine the relative impact of varying hole size, spacing, and plate thickness over the ranges expected for transpired collector applications. See again **Figure 3-1** for a plot of all plate geometries. All plates were made of aluminum and painted on one side with a flat black paint. Holes were then punched on a computer-controlled punching machine. The first eight test plates, numbers 1 through 8 form a square in the test space. (Although they tend toward the high porosity range, this was necessary to meet the manufacturing constraint that hole diameter exceed plate thickness and still allow a 2 to 1 variation of hole diameter and plate thickness.) The plate dimensions are given in **Table 4-1**. The ninth plate

shown is the same geometry used in a large outdoor test wall.

Table 4-1. Original Test Plate Dimensions

Plate No.	Pitch (m)	Diameter (m)	Thickness (m)
1	.01351	.003175	.000794
2	.01351	.001588	.000794
3	.02703	.003175	.000794
4	.02703	.001588	.000794
5	.01351	.003175	.001588
6	.01351	.001588	.001588
7	.02703	.003175	.001588
8	.02703	.001588	.001588
9	.00953	.000991	.000635

Plates 1 through 8 represent a full factorial design. For purposes of the two-level full factorial experiment, data points for two mass flow rates, $G = 0.02$ and 0.06 $\text{kg}/(\text{m}^2\text{-s})$ were included in the analysis. **Table 4-2** gives the results of this full-factorial experiment.

Table 4-2. Effectiveness and heat transfer coefficient results for full factorial experiment.

A Pitch (m)	B Diameter (m)	C Thickness (m)	D Mass Flow (kg/m ² -s)	Effect- iveness	U (W/m ² -K)
.01351	.003175	.000794	.02	.712	26.4
.01351	.003175	.000794	.06	.447	37.7
.01351	.001588	.000794	.02	.736	27.2
.01351	.001588	.000794	.06	.488	41.0
.02703	.003175	.000794	.02	.566	17.0
.02703	.003175	.000794	.06	.350	26.4
.02703	.001588	.000794	.02	.614	19.2
.02703	.001588	.000794	.06	.469	38.4
.01351	.003175	.001588	.02	.739	28.5
.01351	.003175	.001588	.06	.473	40.7
.01351	.001588	.001588	.02	.766	29.6
.01351	.001588	.001588	.06	.529	46.1
.02703	.003175	.001588	.02	.558	16.7
.02703	.003175	.001588	.06	.353	26.6
.02703	.001588	.001588	.02	.637	20.5
.02703	.001588	.001588	.06	.487	40.5

Effects of each factor from an analysis of variance (ANOVA) are contained in Table 4-3.

Table 4-3. Effects of each factor in full factorial experiment. To make the terms easier to recognize, this table uses D (instead of B) for diameter, P (instead of A) for pitch, T (instead of C) for thickness, and G (instead of D) for mass flow.

Factor	Effect Effectiveness	Effect U
P	-.107	-8.99
D	-.066	-5.31
T	.020	1.98
G	-.217	14.00
PxD	-.029	-2.66
PxT	-.011	-1.16
PxG	.038	.59
DxT	-.008	-.74
DxG	-.022	-3.34
TxG	.002	.61
PxDxT	-.004	-.14
PxDxG	-.010	-1.64
PxTxG	-.0005	-.29
DxTxG	-.0005	-.26
PxDxTxG	.0035	.19

Note that since this is a full-factorial experiment, there are not just the effects of each variable but of all of the interactions as well. A positive effect means that an increase in the corresponding factor causes an increase in the response (effectiveness or U). It can be seen from this table that the major effects are (in order of decreasing significance): mass flow, pitch, diameter, and pitch-mass flux interaction.

The results were also analyzed using the computer program "Design-Ease" and the standardized effects given by "Design-Ease" agreed exactly with **Table 4-3**. "Design-Ease" provides a graphical way to determine the important effects. As described in Box, Hunter, and Hunter (1978), a normal probability plot of the effects is very useful for assessing the importance of effects in non-replicated factorials. A normal distribution is a bell-shaped curve of percentage probability versus response value. If one starts at the left end of this curve and plots the cumulative value of the probability versus the response value, one obtains a so-called sigmoid cumulative normal curve. A normal probability plot is one that has the vertical scale adjusted so that this curve becomes a straight line. Thus on a normal probability plot, normally distributed data (i.e., data that are simply the result of random variation about a fixed mean) will lie on a straight line. Any data not falling on this straight line would not be explained by chance occurrence, and are therefore significant.

A plot of normal probability of effects vs. factor effect, from "Design-Ease" is shown in **Figure 4-9**. Again, the most important effects are seen to be D (mass flow rate) and A (pitch). B (diameter) is also quite significant. **Figure 4-10** shows a cube plot summarizing the effectiveness results for the two levels of mass flow rate,

pitch, and diameter. Similarly, Figure 4-11 shows a normal probability plot for heat transfer coefficient, U , and Figure 4-12 shows a cube plot of results for U .

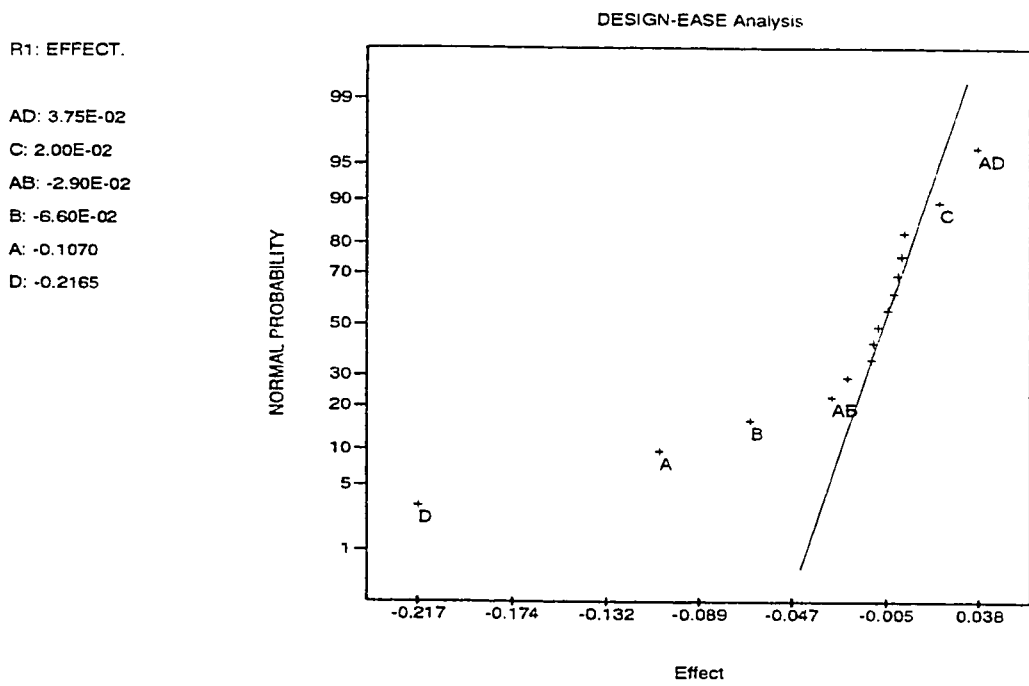


Figure 4-9. Normal probability plot for factorial experiment.

DESIGN-EASE Analysis
 Cube Plot of Actual Values

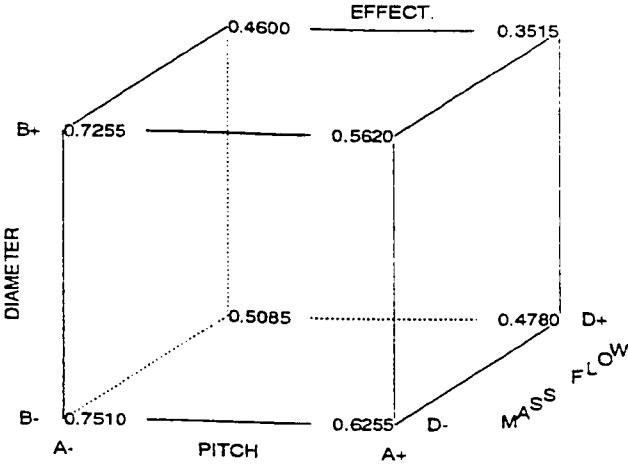


Figure 4-10. Cube plot of measured heat exchange effectiveness values.

R2: U

D: 14.04
C: 1.987
AB: -2.663
BD: -3.337
B: -5.313
A: -8.988

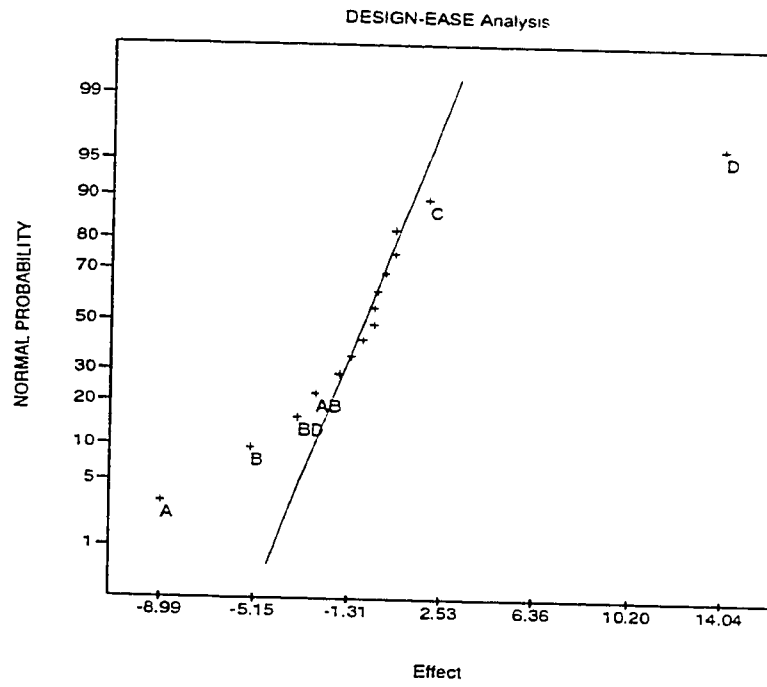


Figure 4-11. Normal probability plot for heat transfer coefficient.

DESIGN-EASE Analysis
 Cube Plot of Actual Values

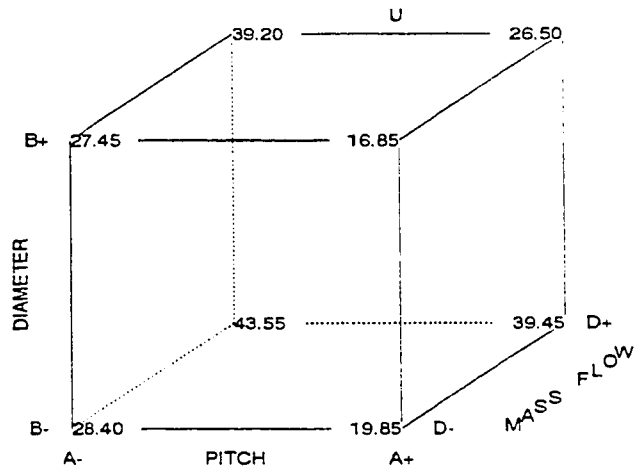


Figure 4-12. Cube plot of measured heat transfer coefficients.

Design-Ease performs an empirical polynomial curve fit of the data for the full factorial experiment accounting for the major effects. The equation obtained is:

$$\varepsilon_{\text{EX}} = 1.15 - 13.5 P - 41.6 D - 8.2 G + 138.8 PG$$

or,

$$U = 27.6 - 665 P + 858 D + 601 G - 101515 DG$$

Note that since there are only two values for each major factor, the equation is linear in these factors. Note also that the cross-interactions between pitch and mass flow rate and diameter and mass flow rate result in cross-product terms in the equations. This equation predicts all 16 data points in the full factorial experiment to within 5% or better.

Of course, the above model is purely deterministic, and it is much more useful to develop a physically-based mechanistic model in terms of non-dimensional parameters. Such a model is not only more physical, but can be extrapolated somewhat outside the range from which it was derived. The development of such a correlation is a major goal of this study.

Because all plates were run over the full range of mass flow rate (which is the most significant effect and which can be varied without fabrication expense), one can see the effect of other parameters by examining each parameter at a time vs. mass flow rate.

Curves of effectiveness vs. G for plates 4 and 8 are shown in Figure 4-13. These plates differ only in thickness -- .794 mm vs. 1.588 mm (1/32 in. vs. 1/16 in.) Over this range there is only a small increase in effectiveness with thickness. (Plates thicker than 1.588 mm [1/16 in.] would likely be too expensive, and plates thinner than .794 mm [1/32 in.] would probably be too flimsy.) The small difference due to plate thickness suggests that not much heat transfer occurs in the holes. This is consistent with the FLUENT results. Not only is the hole surface area limited for these plates, but most of the heat transfer occurs at the start of the hole.

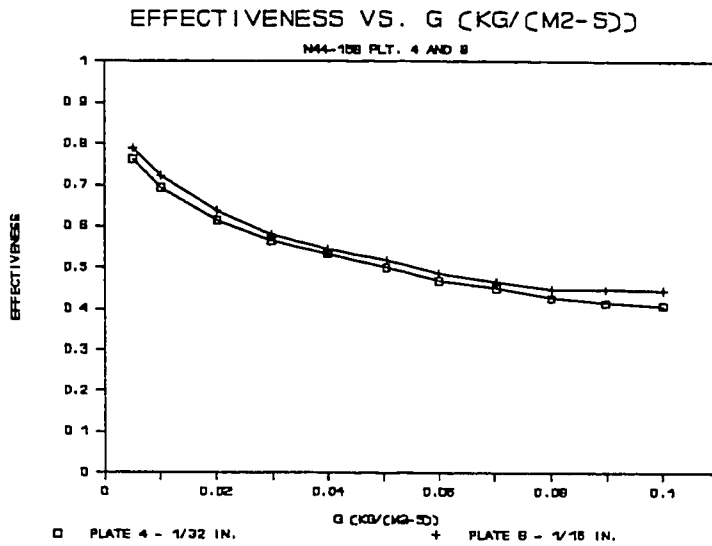


Figure 4-13. Effect of plate thickness on heat exchange effectiveness.

Figure 4-14 shows the effect of hole pitch. Plate 6 with a smaller pitch shows greater effectiveness than plate 8 over the flow rates typically used. This is consistent with the FLUENT result for front surface heat transfer, which dominates the problem, as well as for back surface heat transfer.

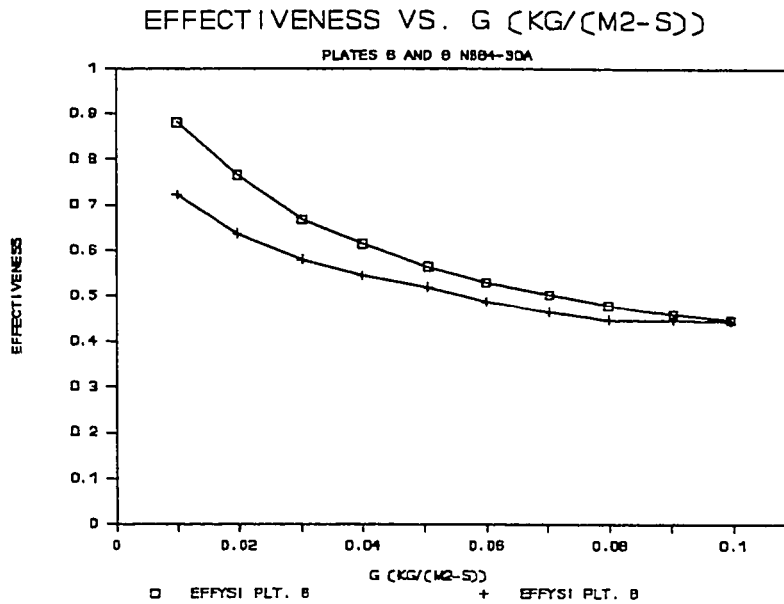


Figure 4-14. Effect of pitch on heat exchange effectiveness.

Figure 4-15 shows the effect of hole diameter. Plate 3 (with a smaller hole diameter) performs better at higher suction rates than plate 4, probably due to the fact that the larger hole does not force flow against the plate as much as in the case of the smaller hole. The smaller hole also allows more front surface heat transfer area at the point where the boundary layer is thinnest.

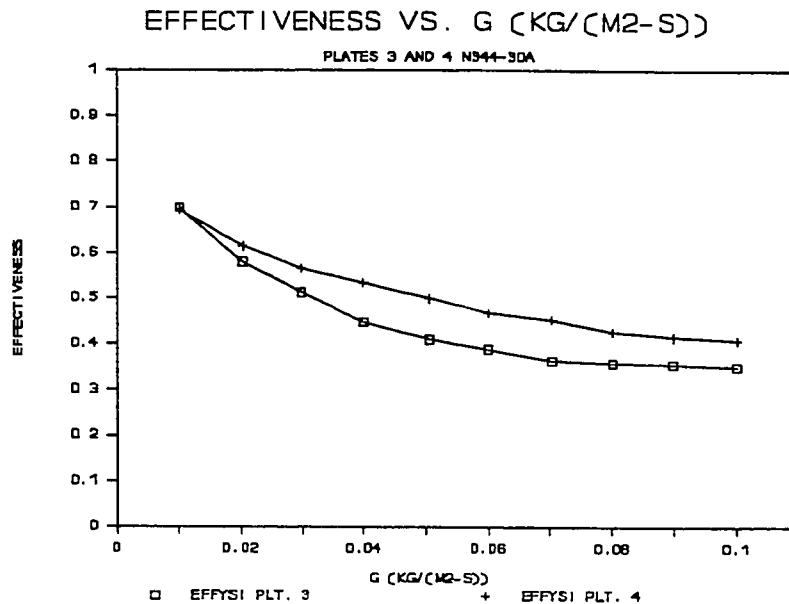


Figure 4-15. Effect of hole diameter on effectiveness

After the original factorial experiment, it was decided to perform additional factorial experiments to determine the importance of collector orientation and wind. Tests were run for plates 1, 2, 3, and 4 in the vertical configuration and compared with the horizontal results. Thus collector orientation replaced plate thickness as a variable. The test results are given in Table 4-4.

Table 4-4. Effectiveness and heat transfer coefficient results for investigation of orientation.

A Pitch (m)	B Diameter (m)	C Orientation	D Mass Flow (kg/m ² -s)	Effect- iveness	U (W/m ² -K)
.01351	.003175	H	.02	.712	26.4
.01351	.003175	H	.06	.447	37.7
.01351	.001588	H	.02	.736	27.2
.01351	.001588	H	.06	.488	41.0
.02703	.003175	H	.02	.566	17.0
.02703	.003175	H	.06	.350	26.4
.02703	.001588	H	.02	.614	19.2
.02703	.001588	H	.06	.469	38.4
.01351	.003175	V	.02	.739	28.5
.01351	.003175	V	.06	.504	44.6
.01351	.001588	V	.02	.767	29.7
.01351	.001588	V	.06	.501	42.5
.02703	.003175	V	.02	.581	17.7
.02703	.003175	V	.06	.390	30.2
.02703	.001588	V	.02	.643	20.8
.02703	.001588	V	.06	.519	44.4

The effects for the various factors computed by Design-Ease (using the symbol O to denote orientation) are as contained in Table 4-5.

Table 4-5. Standardized effects for factorial investigation of orientation.

Factor	Effect Effectiveness	Effect U
P	-.0953	-7.938
D	-.0560	-4.338
O	.0328	3.138
G	-.2113	14.834
PxD	-.0335	-3.538
PxO	.0008	-0.113
PxG	.0423	1.338
DxO	.0020	.238
DxG	-.0155	-2.513
OxG	.0073	1.413
PxDxO	-.0080	-1.013
PxDxG	-.0190	-2.713
PxOxG	.0043	.463
DxOxG	.0065	.563
PxDxOxG	-.0055	-0.888

Again, mass flow rate followed by pitch are the major effects. These are followed by diameter, pitch-mass flow interaction, and orientation. The normal probability plots (Figure 4-16 and 4-18) would suggest that the last two have little statistical significance, although the cube plots in Figures 4-17 and 4-19 show the effectiveness and heat transfer coefficient to be consistently higher for the vertical configuration than for the horizontal configuration. One would expect some improvement for the

vertical configuration due to the tendency for natural convection to increase the heat transfer coefficient over the front surface. The effect of orientation is clearly small, however, indicating that forced convection dominates any natural convection effects.

R1: EFFECT.

C: 3.28E-02
CD: 7.25E-03
AB: -3.35E-02
B: -5.60E-02
A: -9.53E-02
D: -0.2113

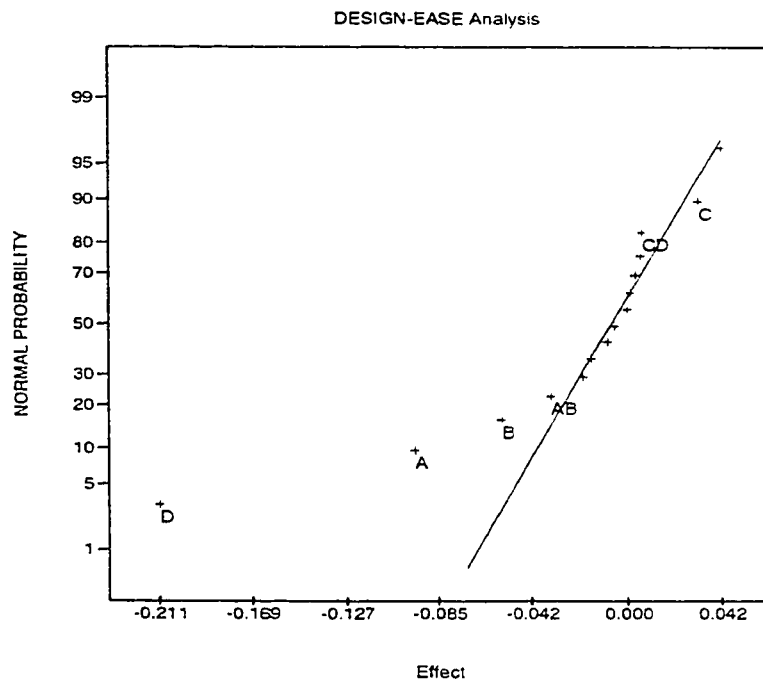


Figure 4-16. Normal probability plot for investigation of effect of orientation on effectiveness.

DESIGN-EASE Analysis
Cube Plot of Actual Values

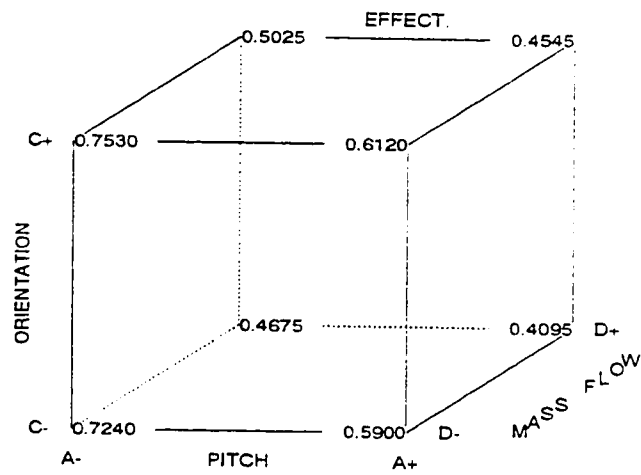


Figure 4-17. Cube plot of measured effectiveness for investigation of orientation.

R2: U
D: 14.84
C: 3.138
A: -7.938

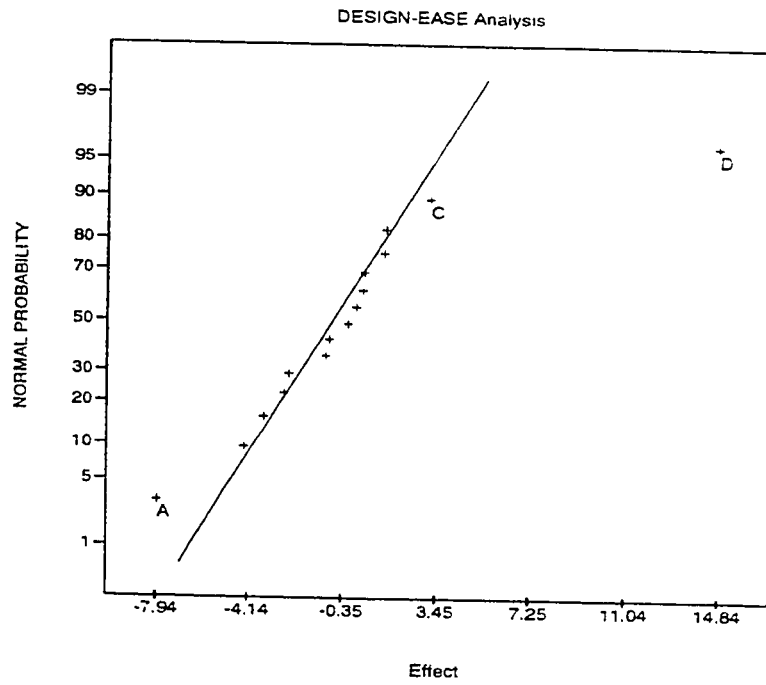


Figure 4-18. Normal probability plot for investigation of effect of orientation on heat transfer coefficient.

DESIGN-EASE Analysis
Cube Plot of Actual Values

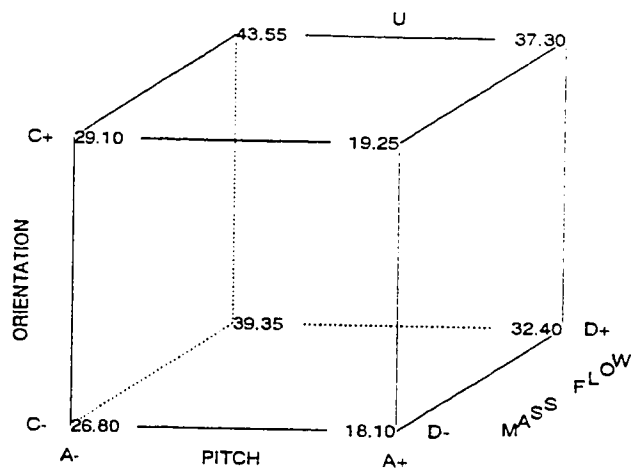


Figure 4-19. Cube plot of measured heat transfer coefficients for investigation of orientation.

The effect of wind was explored for vertical plates, using an additional factorial experiment on plates 1, 2, 3, and 4. As a wind of 3 m/s would be considered a high wind for a solar collector application, the two cases of zero wind and 3 m/s were run. The results are shown in Table 4-6.

Table 4-6. Effectiveness and heat transfer coefficient results for investigation of wind speed.

A Pitch (m)	B Diameter (m)	C Wind Speed (m/s)	D Mass Flow (kg/m ² -s)	Effect- iveness	U (W/m ² -K)
.01351	.003175	0	.02	.739	28.5
.01351	.003175	0	.06	.504	44.6
.01351	.001588	0	.02	.767	29.7
.01351	.001588	0	.06	.501	42.5
.02703	.003175	0	.02	.581	17.7
.02703	.003175	0	.06	.390	30.2
.02703	.001588	0	.02	.643	20.8
.02703	.001588	0	.06	.519	44.4
.01351	.003175	3	.02	.840	38.9
.01351	.003175	3	.06	.625	62.4
.01351	.001588	3	.02	.802	33.0
.01351	.001588	3	.06	.576	52.5
.02703	.003175	3	.02	.678	23.1
.02703	.003175	3	.06	.494	41.7
.02703	.001588	3	.02	.690	23.7
.02703	.001588	3	.06	.529	45.6

The effects for the various factors computed by Design-Ease (using the symbol W to denote wind speed) are given in Table 4-7:

Table 4-7. Standardized effects for factorial investigation of wind speed.

Factor	Effect Effectiveness	Effect U
P	-.1038	-10.60
D	-.0220	-.64
W	.0738	7.81
G	-.2003	18.56
PxD	-.0375	-4.81
PxW	-.0093	-2.56
PxG	.0353	.59
DxW	.0320	3.46
DxG	-.0060	-.89
WxG	.0038	2.31
PxDxW	.0040	-.26
PxDxG	-.0165	-2.72
PxWxG	-.0113	-1.21
DxWxG	.0030	1.06
PxDxWxG	.0080	.89

Again, the major effects are mass flow rate and pitch, followed by wind speed. In this particular series of runs, the effect of diameter was smaller than several two-way interactions. The normal probability plots of **Figures 4-20 and 4-22** also show that the statistically significant effects are mass flow, pitch, and wind speed. **Figures 4-21 and 4-23** are cube plots which clearly show the impact of wind.

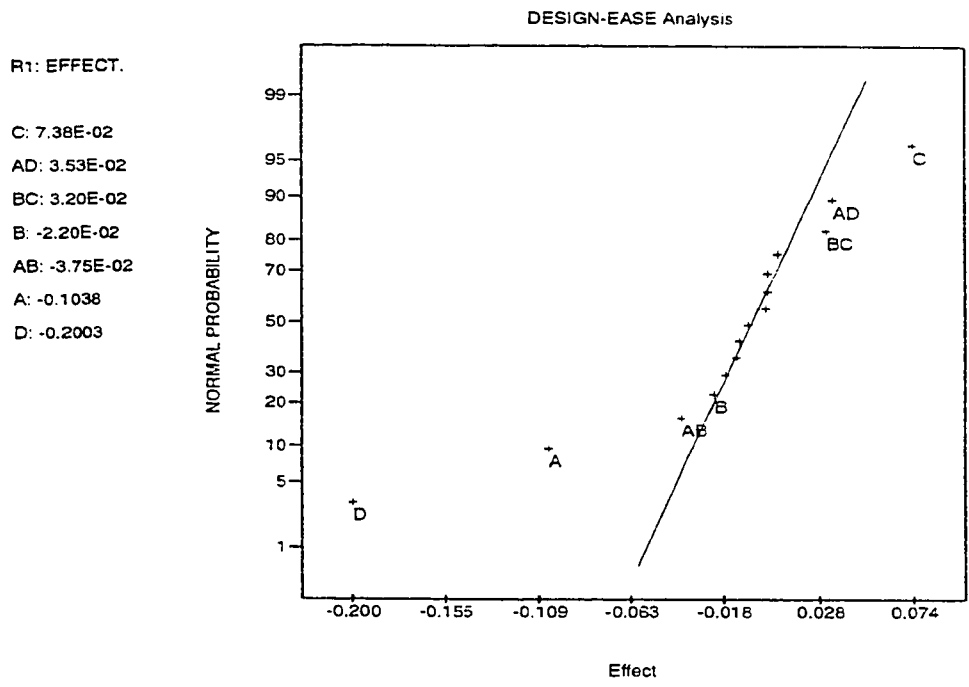


Figure 4-20. Normal probability plot for effect of wind on effectiveness.

DESIGN-EASE Analysis
Cube Plot of Actual Values

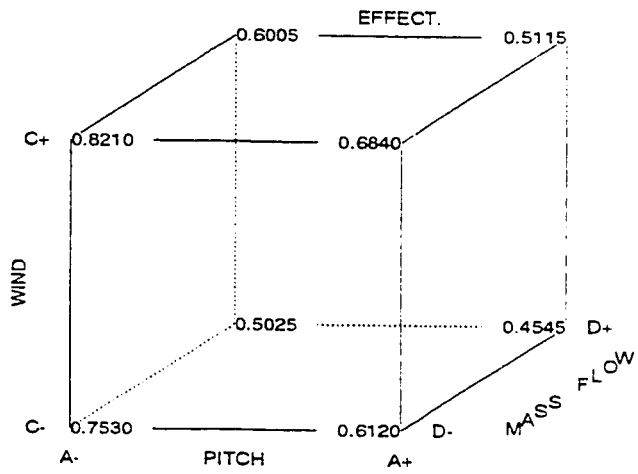


Figure 4-21. Cube plot of measured effectiveness for investigation of wind speed.

R2: U
D: 18.56
C: 7.813
BC: 3.463
B: -0.6375
AB: -4.813
A: -10.61

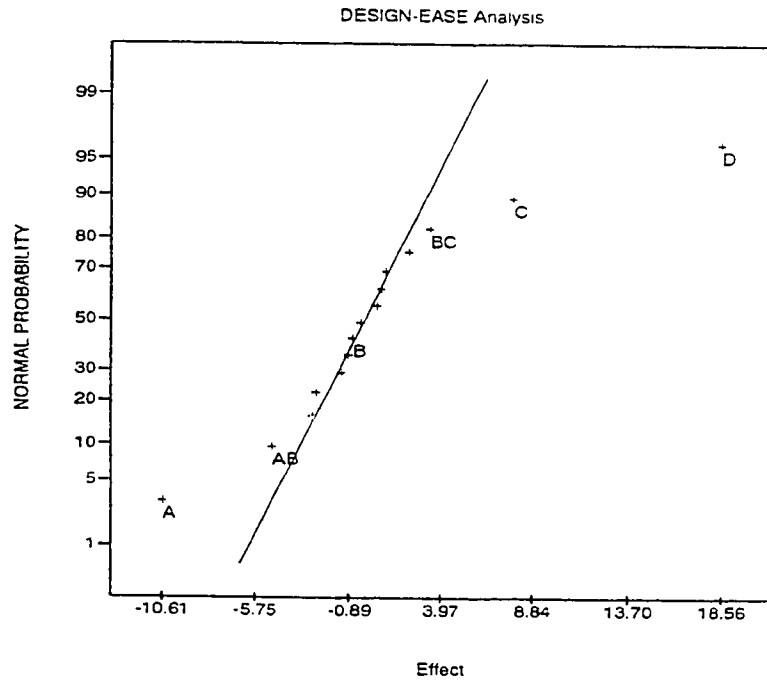


Figure 4-22. Normal probability plot for investigation of effect of wind speed on heat transfer coefficient.

DESIGN-EASE Analysis
Cube Plot of Actual Values

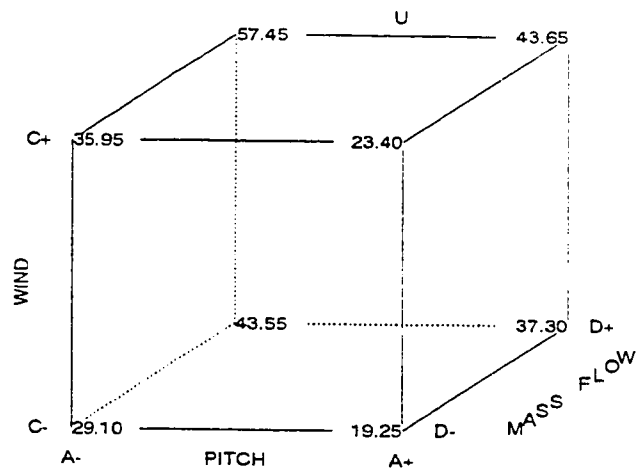


Figure 4-23. Cube plot of measured heat transfer coefficient for investigation of wind speed.

4.3.2 Normal Flow Tests

The overall efficiency of a transpired solar collector is relatively insensitive to variations in heat exchange effectiveness on the order of 5-10%. The factorial runs indicate that a useful predictive correlation must include the effects of mass flow rate and hole pitch. Inclusion of hole diameter effects would also be desirable. A correlation for zero wind would be conservative since wind speed has a positive effect on heat exchange effectiveness. It would in fact be difficult for a designer to determine what average wind speed to use for determining effectiveness. (Nevertheless, the effect of wind on performance is covered later in this chapter.)

To obtain a sufficient range of data to generate correlations, additional plates were fabricated. See again **Figure 3-1** for a plot of hole pitch versus hole diameter with each data point representing a different test plate. The two straight lines represent two values for plate porosity: 2% and .15%. Practical unglazed solar absorbers would be expected to generally fall within this range of porosities.

The computer software package, SigmaPlot 5.0, which was described in Chapter 3, was used to perform non-linear regression of the data points. The original eight test plates, 1 through 8, were tested in a horizontal position. However, since the difference in effectiveness between

horizontal and vertical plates was small, and since the latter is of more practical interest, the detailed testing for correlation development was done on the vertical configuration. In addition, since the factorial runs indicated that thickness was not a very significant parameter, all tests were done using a plate thickness of .794 mm (1/32 in.), which is the size used commercially. **Table 4-8** gives the data obtained for all the vertical test plate runs. (Plate 1 was not included in the detailed tests, since its high porosity was outside the range of interest.)

Table 4-8. Experimental heat transfer results for vertical test plates.

PLATE NO.	g	P	D	Eff.	U	Re _p	Re _b	Nu _y	Nu _b
2	0.00916	0.01351	0.001588	0.883	20.04	6.69	62.79	10.30	1.210
	0.01915	0.01351	0.001588	0.773	28.96	13.99	131.27	14.88	1.748
	0.02920	0.01351	0.001588	0.680	33.93	21.33	200.16	17.43	2.048
	0.04917	0.01351	0.001588	0.548	39.82	35.91	337.05	20.46	2.403
3	0.00922	0.02703	0.003175	0.735	12.49	13.47	126.40	12.83	1.507
	0.01909	0.02703	0.003175	0.621	18.89	27.89	261.72	19.41	2.280
	0.02907	0.02703	0.003175	0.526	22.13	42.47	398.54	22.74	2.672
	0.04920	0.02703	0.003175	0.422	27.50	71.87	674.52	28.26	3.320
4	0.00926	0.02703	0.001588	0.752	13.04	13.53	253.90	13.40	0.787
	0.01924	0.02703	0.001588	0.642	19.96	28.11	527.55	20.52	1.205
	0.02918	0.02703	0.001588	0.576	25.29	42.63	800.10	25.99	1.527
	0.04916	0.02703	0.001588	0.513	35.73	71.82	1347.94	36.72	2.157
11	0.00925	0.01351	0.000794	0.890	20.62	6.76	126.81	10.60	0.622
	0.01913	0.01351	0.000794	0.804	31.49	13.97	262.27	16.18	0.950
	0.02919	0.01351	0.000794	0.726	38.17	21.32	400.19	19.61	1.152
	0.04915	0.01351	0.000794	0.637	50.31	35.90	673.83	25.85	1.518
12	0.00925	0.02027	0.000794	0.813	15.64	10.13	285.33	12.05	0.472
	0.01913	0.02027	0.000794	0.738	25.84	20.96	590.10	19.91	0.780
	0.02919	0.02027	0.000794	0.671	32.72	31.98	900.42	25.22	0.988
	0.04915	0.02027	0.000794	0.583	43.35	53.85	1516.12	33.41	1.308
13	0.00918	0.02703	0.000794	0.810	15.36	13.41	503.42	15.79	0.464
	0.01913	0.02703	0.000794	0.747	26.50	27.95	1049.07	27.23	0.800
	0.02924	0.02703	0.000794	0.692	34.70	42.72	1603.49	35.66	1.047
	0.04925	0.02703	0.000794	0.626	48.81	71.95	2700.81	50.16	1.473

PLATE NO.	G	P	D	Eff.	U	Re _p	Re _b	Nu _p	Nu _b
14	0.00923	0.02027	0.001191	0.824	16.20	10.11	189.71	12.48	0.734
	0.01926	0.02027	0.001191	0.713	24.29	21.10	395.86	18.72	1.100
	0.02917	0.02027	0.001191	0.644	30.43	31.96	599.55	23.46	1.378
	0.04922	0.02027	0.001191	0.565	41.39	53.93	1011.65	31.90	1.875
15	0.00913	0.01689	0.001588	0.851	17.64	8.34	97.79	11.33	1.065
	0.01922	0.01689	0.001588	0.739	26.21	17.55	205.86	16.83	1.582
	0.02916	0.01689	0.001588	0.647	30.82	26.62	312.32	19.80	1.861
	0.04922	0.01689	0.001588	0.524	37.09	44.94	527.18	23.82	2.239
16	0.00919	0.02027	0.001588	0.795	14.75	10.07	141.74	11.37	0.890
	0.01916	0.02027	0.001588	0.698	23.23	20.99	295.51	17.90	1.402
	0.02919	0.02027	0.001588	0.616	28.29	31.98	450.21	21.80	1.708
	0.04927	0.02027	0.001588	0.517	36.31	53.98	759.91	27.98	2.192
17	0.00916	0.02365	0.001588	0.783	14.15	11.71	192.30	12.72	0.854
	0.01926	0.02365	0.001588	0.654	20.67	24.62	404.32	18.58	1.248
	0.02917	0.02365	0.001588	0.583	25.80	37.29	612.37	23.20	1.557
	0.04921	0.02365	0.001588	0.506	35.09	62.90	1033.06	31.55	2.118
18	0.00923	0.02027	0.002381	0.799	15.10	10.11	94.91	11.64	1.367
	0.01923	0.02027	0.002381	0.685	22.65	21.07	197.73	17.46	2.051
	0.02918	0.02027	0.002381	0.599	27.19	31.97	300.04	20.96	2.462
	0.04925	0.02027	0.002381	0.478	32.65	53.96	506.40	25.16	2.956
19	0.00919	0.02027	0.003175	0.788	14.68	10.07	70.87	11.32	1.772
	0.01921	0.02027	0.003175	0.661	21.40	21.05	148.14	16.49	2.584
	0.02918	0.02027	0.003175	0.571	25.43	31.97	225.03	19.60	3.070
	0.04924	0.02027	0.003175	0.457	30.97	53.95	379.72	23.87	3.739

Figure 4-24 shows all of the data points for the vertical plate tests plotted using the same dimensionless parameters as those used by Andrews, et. al., but with the Nusselt number defined in terms of a heat transfer coefficient based on the log mean temperature difference.

The best fit correlation equation is

$$\text{Nu}_D = 2.748 \left(\frac{P}{D} \right)^{-1.208} \text{Re}_D^{.4295} \quad (4-5)$$

This fit has a coefficient of determination, R^2 , of .990. The coefficients of variation of the three parameters are as follows:

leading coefficient: $2.748 \pm 6.8\%$

(P/D) exponent: $-1.208 \pm 1.9\%$

Re_D exponent: $.4295 \pm 3.5\%$

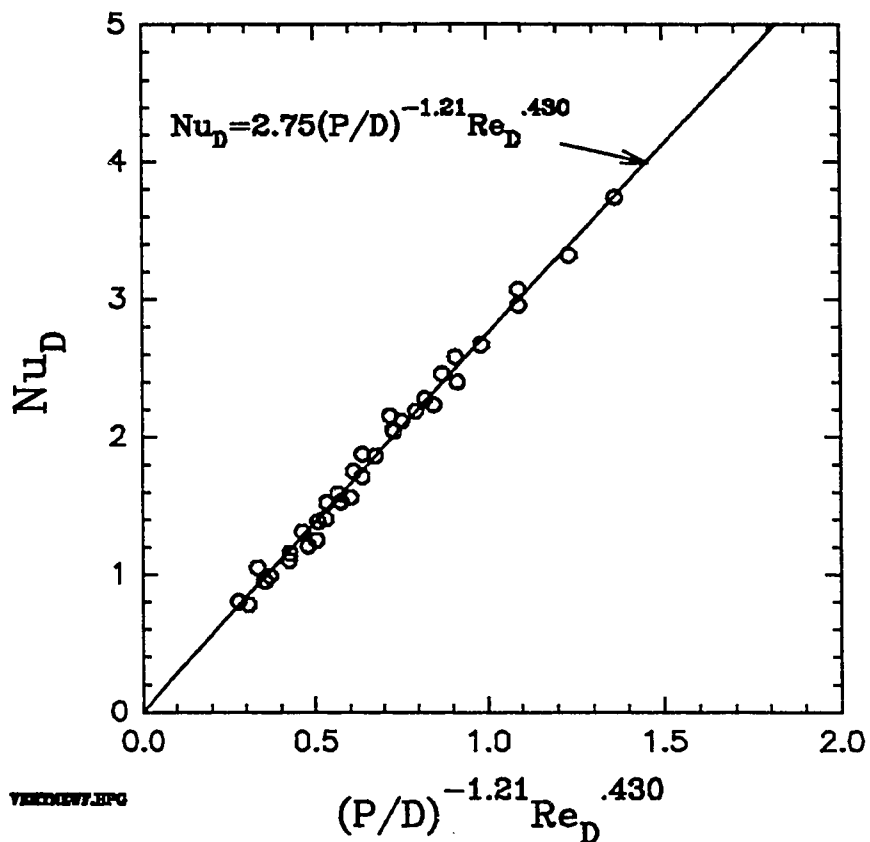


Figure 4-24. Nu_p vs. modified Re_p for vertical test plates.

An algebraically equivalent correlation in terms of pitch-based non-dimensional parameters is:

$$Nu_p = 2.867 \left(\frac{P}{D} \right)^{.2210} Re_p^{.4295} \quad (4-4)$$

Physically, one might prefer a correlation of this type, since it is more physical (in that it has the form one would expect for heat transfer dominated by the front surface). Note that the pitch-to-diameter ratio correction

term is smaller than for the other correlation. This is plotted in Figure 4-25. Note that although it is equivalent to the previous correlation, the data do not appear to cluster as closely when plotted in this way, and, in fact, the coefficient of determination is lower for this fit.

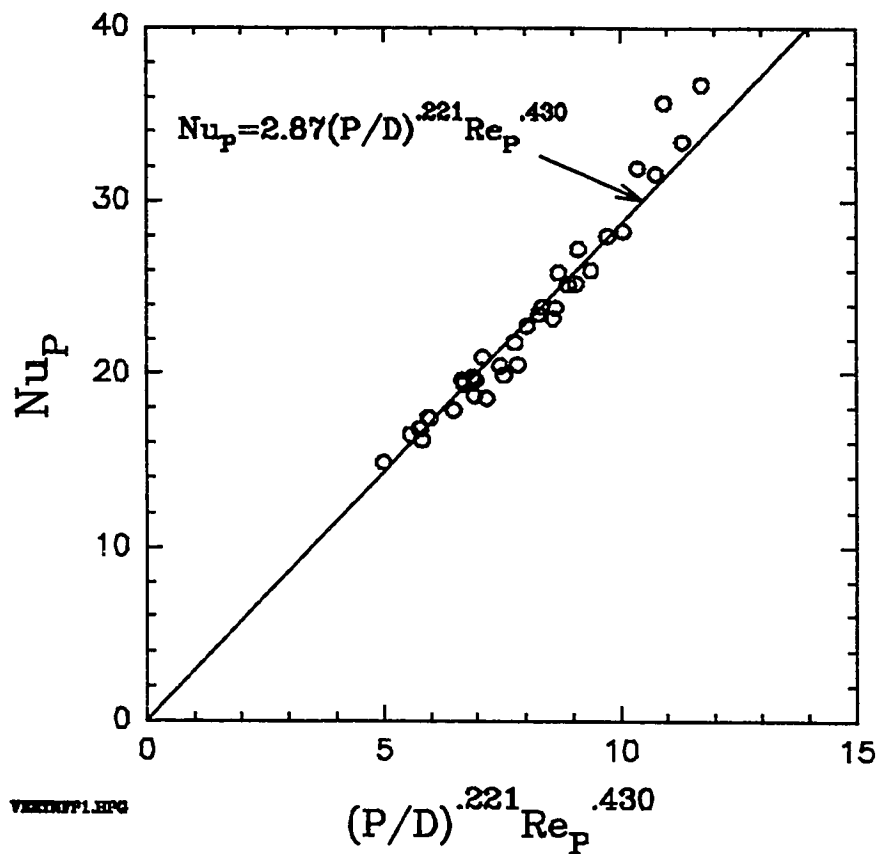


Figure 4-25. Nu_p vs. modified Re_p and curve representing algebraic equivalent of correlation in previous figure.

If a regression is performed directly using a correlation of this form, the parameters are slightly different, and the result is:

$$Nu_p = 2.197 \left(\frac{P}{D} \right)^{.2566} Re_p^{.4780} \quad (4-7)$$

This is plotted in Figure 4-26.

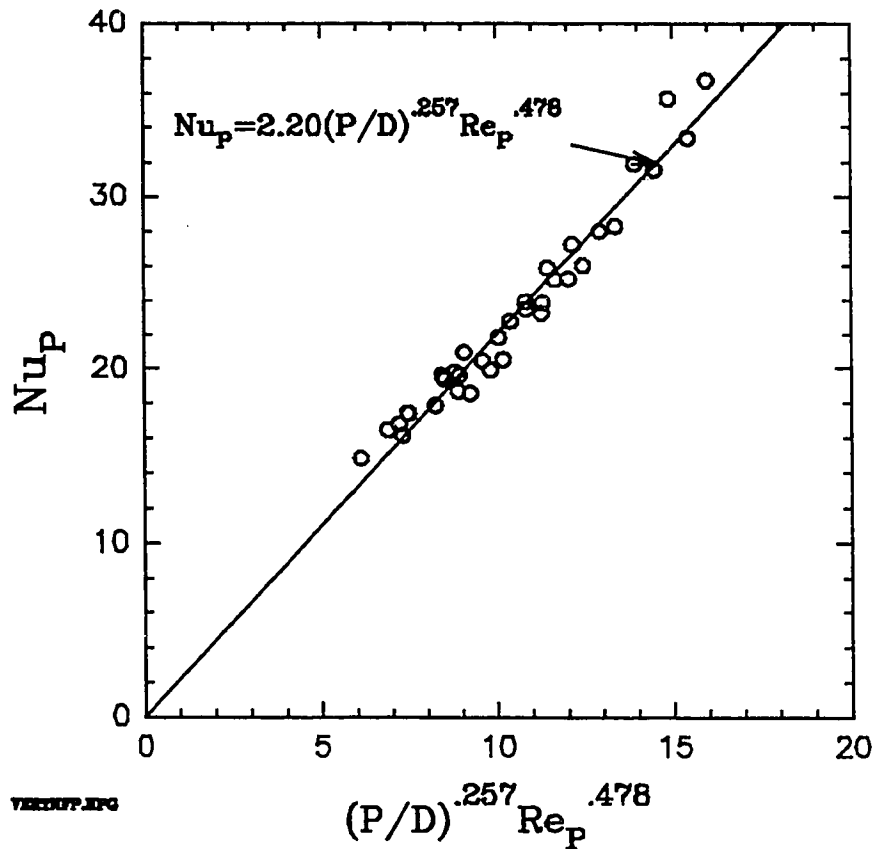


Figure 4-26. Nu_p vs. modified Re_p and best fit curve.

The first correlation shown provides the best fit to the data. It has a coefficient of determination, R^2 , of

.990, compared with an R^2 of .96 for the best fit for a correlation of non-dimensional parameters based on pitch.

4.3.3 Cross-flow Tests

For wind tests, the test box was fitted with a sharp leading edge upstream from the test plate to allow for wind tunnel boundary layer removal and a well defined starting condition. The leading edge was made of a sharpened steel plate and extended out 4 in. (10.2 cm) from the test box. Another 2.375 in. (6.03 cm) of flat surface (covering the side wall and 2 inches of side wall insulation) existed before the opening in the test box. Finally a tape width varying from about .5 in. (1.27 cm) to 1 in. (2.54 cm) existed just upstream from the start of the actual test surface.

Originally, simple passive boundary layer removal was used in which the lower 1 in. (2.54) cm of wind tunnel air was allowed to passively exit the slot under the leading edge. Later, active boundary layer suction was added by means of a small .118 m³/s (250 CFM) centrifugal fan and speed controller. Using the latter device in conjunction with the smoke wire allows very precise adjustment of the suction to ensure that the flow splits exactly at the leading edge. Passive and active boundary layer removal produced very similar heat exchange effectiveness results, but the latter improved repeatability somewhat.

Wind test data were taken under conditions in which the boundary layer could be considered at or very close to asymptotic. Suction mass flow rates were varied from 0.02 kg/(m²-s) to a maximum of 0.07 kg/(m²-s), and the maximum wind speed tested was 4 m/s. The combination of minimum suction flow and maximum wind speed yield a maximum theoretical starting length of approximately 18 cm. This is based on a uniformly homogenous suction surface and also does not account for the fact that a velocity boundary layer has already built up on a flat surface approximately 18-19 cm in length upstream of the absorber.

To test for the impact of downstream location, effectiveness measurements were taken both at the center of the absorber (25 cm downstream from the start of suction) and at a position 42 cm downstream from the start of suction. In each case, the local effectiveness was determined from measurements of the approaching air temperature (measured upstream from the absorber), the local surface temperature, and the local outlet temperature. It was found that the downstream measurement was typically within 5% (and usually much closer) of the center plate measurement. To see if boundary layer build-up on the leading edge was affecting the measurements at all, experiments were conducted in which the test surface was given a positive angle of attack with respect to the wind direction thus causing a favorable pressure gradient

which could be expected to decrease the starting length. This had no discernible effect on either of the effectiveness measurements. Because results at the two locations were close, and because the center location offered advantages such as direct comparison with zero-wind results (the same location and same surface and outlet sensors were used for the no-wind tests) and better isolation from plate edge losses, all of the wind results reported here are for the 25 cm location.

The effects of wind can be seen in **Figures 4-27** and **4-28**. **Figure 4-27** shows the effectiveness of plate 5 at a suction mass flow rate of $0.05 \text{ kg}/(\text{m}^2\text{-s})$ for a range of wind speeds and for both a horizontal and a vertical orientation. The vertical orientation performs slightly better than the horizontal orientation. Note that in both cases, the effect of wind levels off at the higher wind speeds. In actual practice, wind speeds near the wall can be expected to be less than 3 m/s. Nevertheless, the increase in effectiveness for this plate at this suction flow rate is significant. **Figure 4-28** shows effectiveness vs. mass suction flow rate for plate 5 in a horizontal orientation at zero wind and at a wind speed of 5 m/s. The effect of wind is greatest at the higher suction rates (i.e., at the lower effectiveness values).

Summary of Wind Test Results at Fixed G

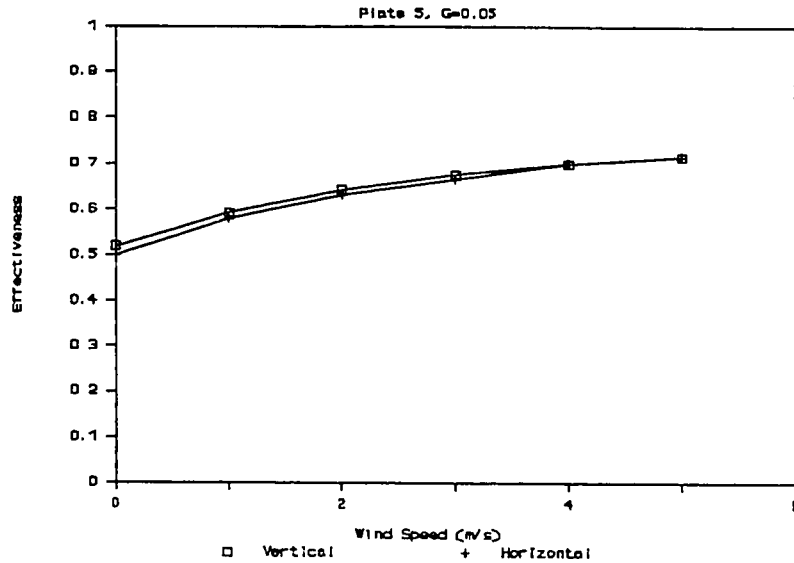


Figure 4-27. Heat exchange effectiveness vs. wind speed for plate 5 at $G = .05 \text{ kg}/(\text{m}^2\text{-s})$ in both vertical (upper curve) and horizontal (lower curve) positions.

For a staggered array of holes on a triangular pitch, it is important to note that the geometry presented to the wind depends on the major direction. Consider orientation "A" as the one in which the distance between holes in the downstream direction is lesser and the "B" direction as the one in which this distance is greater. The previously described tests of plate 5 were taken in the "A"

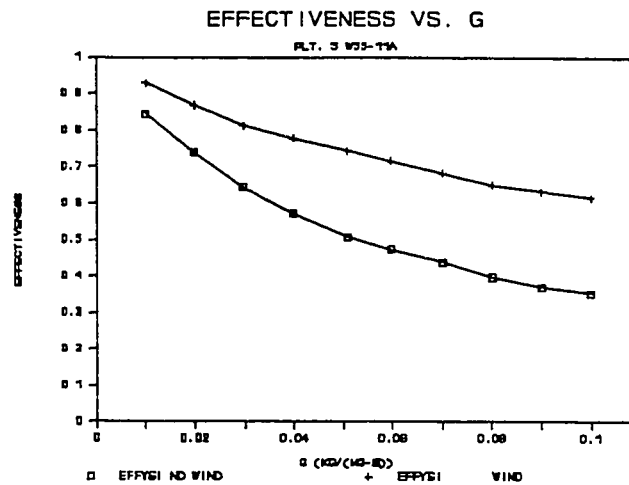


Figure 4-28. Heat exchange effectiveness vs. suction flow rate at 0 and 5 m/s wind speed.

orientation. The effect of orientation can best be seen from infrared thermography images. Absorbers made of black matboard were perforated with the same hole pattern as plate 19 and used for thermal visualization. These absorbers have low thermal conductivity and hence with a constant surface heat flux, variations in local heat transfer coefficient show up as variations in the local temperature.

Figures 4-29 through 4-31 show the surface temperature distribution (red is the highest temperature, blue the coldest) for the "A" orientation with a suction mass flow

rate of $.05 \text{ kg/m}^2\text{-s}$ and wind speeds respectively (from right to left) of 0, 1 and 2 m/s. Note that these pictures were taken for vertical plates and the slight skewing of the patterns at no wind results from natural convection flow. Note also that as the wind comes on, the warm stagnation regions between holes are cooled. This explains why the heat exchange effectiveness increases.

Figures 4-32 through 4-34 show the same suction and wind conditions but for the "B" direction. Note that the downstream banding that occurs in the A direction does not occur in the B direction.

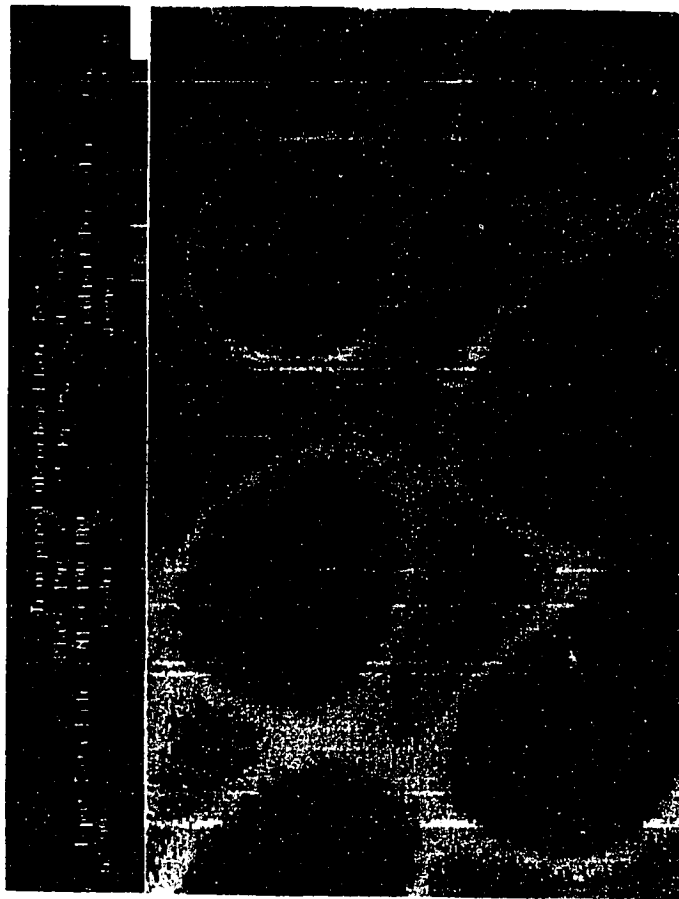


Figure 4-29. Infrared image of black matboard absorber in "A" orientation; $G = 0.05 \text{ kg/m}^2\text{-s}$, wind speed = 0 m/s.

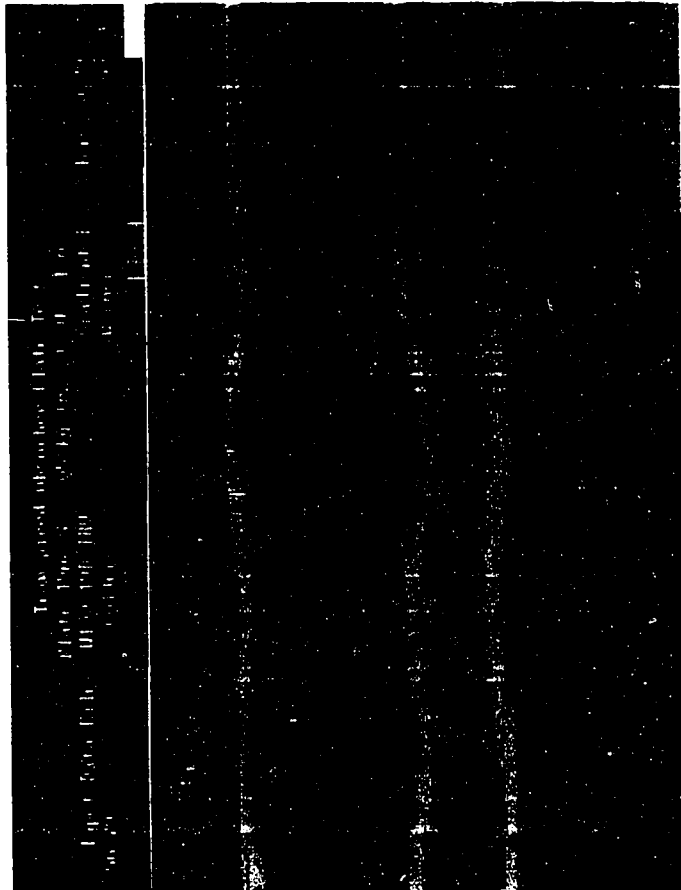


Figure 4-30. Infrared image of black matboard absorber in "A" orientation; $G = 0.05 \text{ kg/m}^2\text{-s}$, wind speed = 1 m/s.

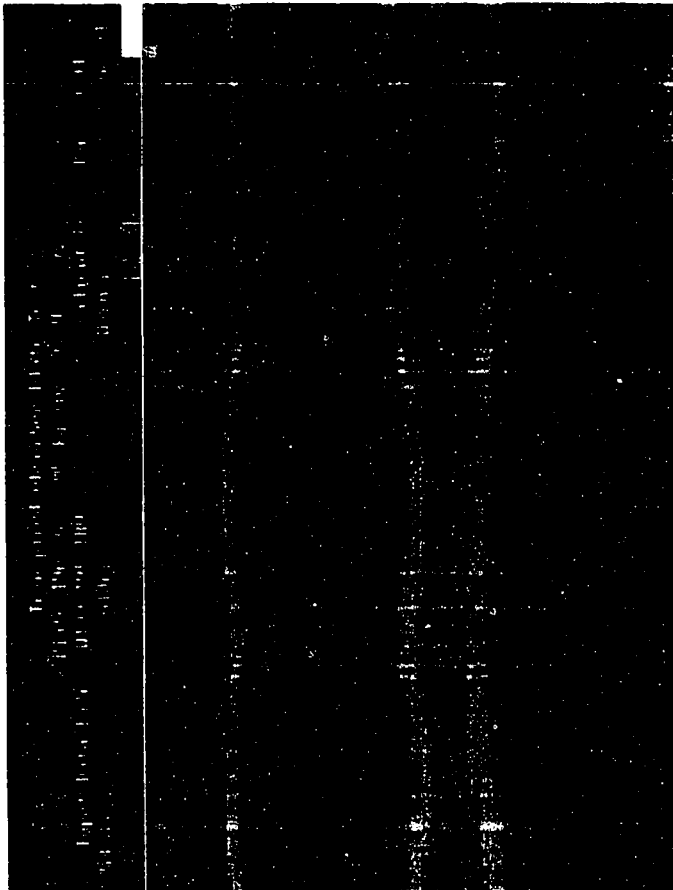


Figure 4-31. Infrared image of black matboard absorber in "A" orientation; $G = 0.05 \text{ kg/m}^2\text{-s}$, wind speed = 2 m/s.

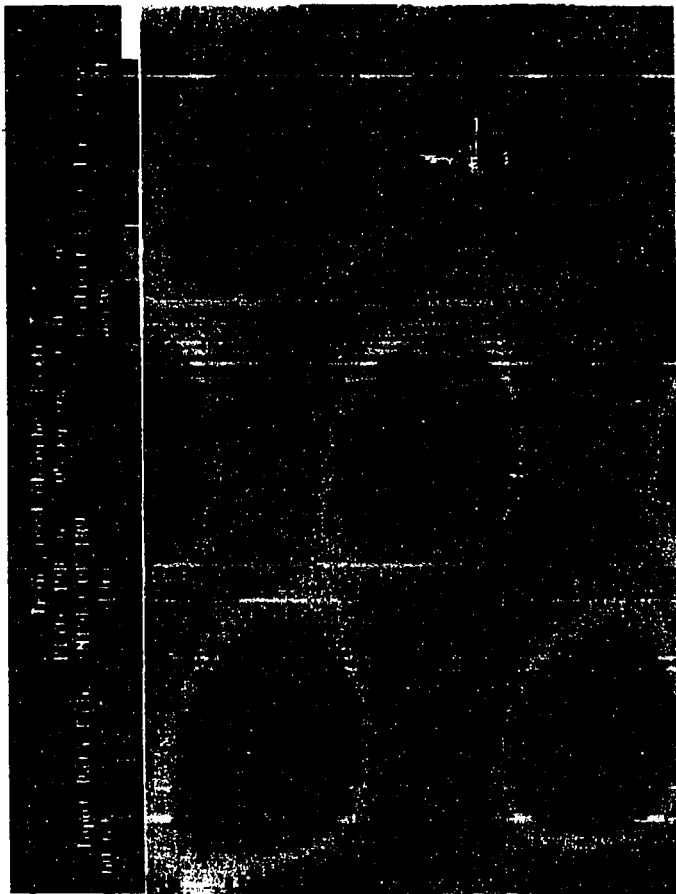


Figure 4-32. Infrared image of black matboard absorber in "B" orientation; $G = 0.05 \text{ kg/m}^2\text{-s}$, wind speed = 0 m/s.

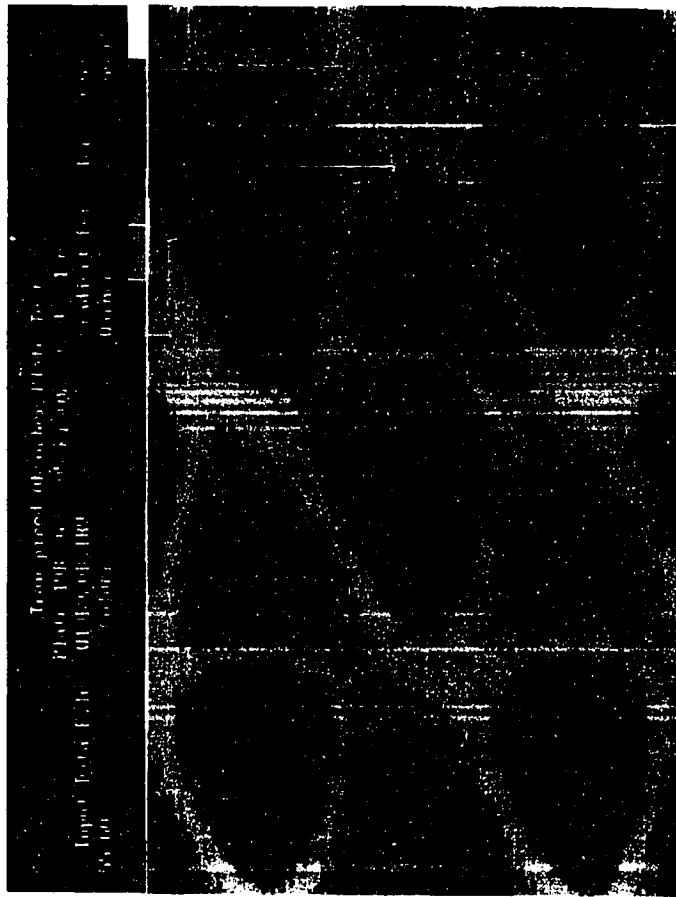


Figure 4-33. Infrared image of black matboard absorber in "B" orientation; $G = 0.05 \text{ kg/m}^2\text{-s}$, wind speed = 1 m/s.

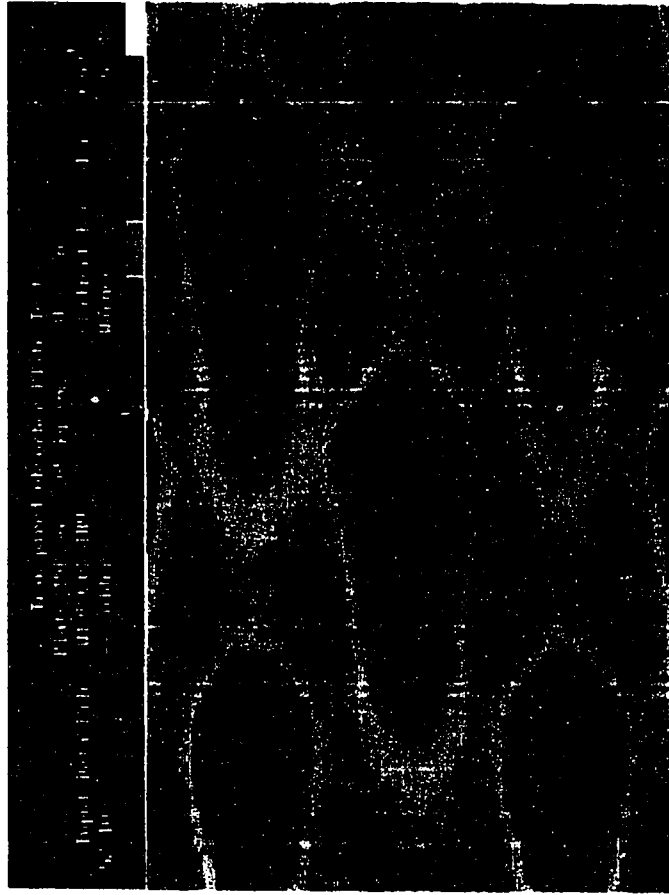


Figure 4-34. Infrared image of black matboard absorber in "B" orientation; $G = .05 \text{ kg/m}^2\text{-s}$, wind speed = 2 m/s.

Tests of two versions of several plates with both the "A" and "B" orientations of holes indicated that the "B" direction has a somewhat higher heat exchange effectiveness than the "A" direction. This is shown in **Figure 4-35** for plate 15. The upper two curves show effectiveness versus wind speed for a suction mass flow rate of $0.02 \text{ kg}/(\text{m}^2\text{-s})$, while the lower curves are for $G = 0.07 \text{ kg}/(\text{m}^2\text{-s})$. At each suction mass flow rate, a higher effectiveness is obtained for the B orientation of holes as compared with the A orientation.

Because the higher performing orientation is of greater interest (one generally wants to maximize heat transfer), tests were run for seven different "B" orientation plates at all permutations of three suction mass flow rates ranging from $G = 0.02$ to $G = 0.07 \text{ kg}/\text{m}^2\text{-s}$ and at least three wind speeds (1, 2, and 4 m/s). (The original factorial test plates were fabricated in the "A" orientation only and thus were not included in these tests.) The results are given in **Table 4-9**.

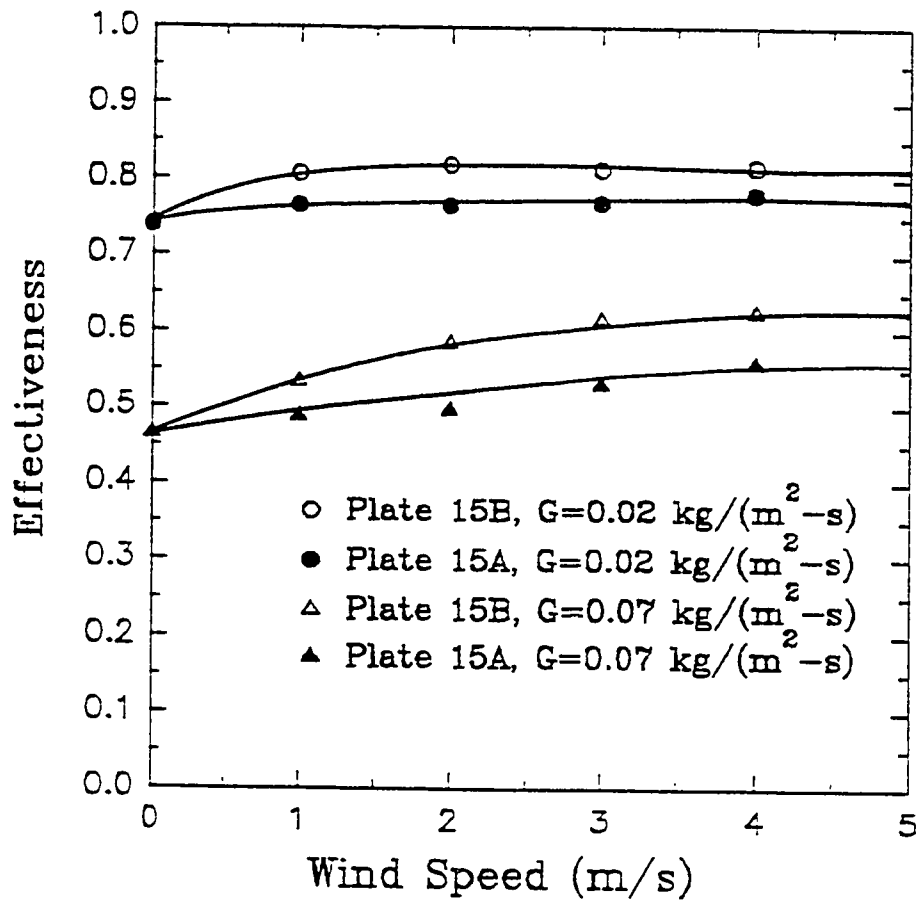


Figure 4-35. Effect of hole orientation on wind test results.

Table 4-9. Experimental heat transfer results for vertical plates with wind.

Plate	Pitch (m)	Diam (m)	Porosity	G (kg/m ² -s)	V (m/s)	U _x (m/s)	Effectiveness	Re _o	Nu _b
11B	0.01351	0.000794	0.00313	0.01921	0.02007	1	0.841	263.3	1.077
11B	0.01351	0.000794	0.00313	0.03915	0.04091	1	0.737	536.6	1.595
11B	0.01351	0.000794	0.00313	0.05921	0.06187	1	0.658	811.5	1.937
11B	0.01351	0.000794	0.00313	0.01914	0.02000	2	0.854	262.3	1.123
11B	0.01351	0.000794	0.00313	0.03913	0.04089	2	0.769	536.3	1.749
11B	0.01351	0.000794	0.00313	0.0592	0.06186	2	0.696	811.4	2.150
11B	0.01351	0.000794	0.00313	0.01916	0.02002	4	0.862	262.6	1.157
11B	0.01351	0.000794	0.00313	0.0392	0.04096	4	0.779	537.3	1.805
11B	0.01351	0.000794	0.00313	0.05927	0.06193	4	0.717	812.3	2.282
12B	0.02027	0.000794	0.00139	0.0192	0.02006	1	0.792	592.1	0.918
12B	0.02027	0.000794	0.00139	0.03933	0.04110	1	0.696	1212.8	1.426
12B	0.02027	0.000794	0.00139	0.05926	0.06192	1	0.627	1827.4	1.779
12B	0.02027	0.000794	0.00139	0.01908	0.01994	2	0.802	588.4	0.941
12B	0.02027	0.000794	0.00139	0.03929	0.04106	2	0.719	1211.6	1.518
12B	0.02027	0.000794	0.00139	0.05927	0.06193	2	0.667	1827.7	1.984
12B	0.02027	0.000794	0.00139	0.01921	0.02007	4	0.8	592.4	0.941
12B	0.02027	0.000794	0.00139	0.03929	0.04106	4	0.727	1211.6	1.553
12B	0.02027	0.000794	0.00139	0.05921	0.06187	4	0.675	1825.8	2.026
13B	0.02703	0.000794	0.00078	0.01926	0.02013	1	0.781	1055.9	0.890
13B	0.02703	0.000794	0.00078	0.03919	0.04095	1	0.715	2148.5	1.497
13B	0.02703	0.000794	0.00078	0.01918	0.02004	2	0.779	1051.5	0.881
13B	0.02703	0.000794	0.00078	0.0392	0.04096	2	0.72	2149.1	1.518
13B	0.02703	0.000794	0.00078	0.01912	0.01998	4	0.786	1048.2	0.897

Plate	Pitch (m)	Diam (m)	Porosity	G (kg/m ² -s)	V (m/s)	U _w (m/s)	Effect-iveness	Re _p	Nu _b
13B	0.02703	0.000794	0.00078	0.03916	0.04092	4	0.729	2146.9	1.556
16B	0.02027	0.001588	0.00557	0.01925	0.02011	1	0.779	296.8	1.777
16B	0.02027	0.001588	0.00557	0.03914	0.04090	1	0.644	603.5	2.472
16B	0.02027	0.001588	0.00557	0.05927	0.06193	1	0.539	913.8	2.806
16B	0.02027	0.001588	0.00557	0.01922	0.02008	2	0.784	296.3	1.801
16B	0.02027	0.001588	0.00557	0.03919	0.04095	2	0.678	604.2	2.715
16B	0.02027	0.001588	0.00557	0.05921	0.06187	2	0.588	912.9	3.210
16B	0.02027	0.001588	0.00557	0.01916	0.02002	4	0.789	295.4	1.823
16B	0.02027	0.001588	0.00557	0.03915	0.04091	4	0.679	603.6	2.720
16B	0.02027	0.001588	0.00557	0.05924	0.06190	4	0.606	913.4	3.374
19B	0.02027	0.003175	0.02226	0.01926	0.02013	1	0.751	148.5	3.329
19B	0.02027	0.003175	0.02226	0.03925	0.04101	1	0.59	302.7	4.351
19B	0.02027	0.003175	0.02226	0.05869	0.06133	1	0.486	452.6	4.857
19B	0.02027	0.003175	0.02226	0.01919	0.02005	2	0.772	148.0	3.527
19B	0.02027	0.003175	0.02226	0.03918	0.04094	2	0.644	302.1	5.031
19B	0.02027	0.003175	0.02226	0.05963	0.06231	2	0.548	459.8	5.887
19B	0.02027	0.003175	0.02226	0.01913	0.01999	4	0.795	147.5	3.769
19B	0.02027	0.003175	0.02226	0.03954	0.04132	4	0.676	304.9	5.541
19B	0.02027	0.003175	0.02226	0.05955	0.06223	4	0.593	459.2	6.656
15B	0.01689	0.001588	0.00802	0.01916	0.02002	1	0.807	205.2	1.932
15B	0.01689	0.001588	0.00802	0.0491	0.05131	1	0.601	525.7	2.765
15B	0.01689	0.001588	0.00802	0.06926	0.07237	1	0.534	741.6	3.242
15B	0.01689	0.001588	0.00802	0.01918	0.02004	2	0.819	205.4	2.009

Plate	Pitch (m)	Diam (m)	Porosity	G (kg/m ² -s)	V (m/s)	U _m (m/s)	Effectiveness	Re _p	Nu _p
15B	0.01689	0.001588	0.00802	0.04911	0.05132	2	0.645	525.8	3.117
15B	0.01689	0.001588	0.00802	0.06928	0.07239	2	0.586	741.8	3.745
15B	0.01689	0.001588	0.00802	0.01912	0.01998	3	0.813	204.7	1.965
15B	0.01689	0.001588	0.00802	0.04908	0.05129	3	0.685	525.5	3.475
15B	0.01689	0.001588	0.00802	0.06922	0.07233	3	0.617	741.2	4.072
15B	0.01689	0.001588	0.00802	0.01906	0.01992	4	0.817	204.1	1.984
15B	0.01689	0.001588	0.00802	0.04918	0.05139	4	0.685	526.6	3.482
15B	0.01689	0.001588	0.00802	0.06913	0.07224	4	0.627	740.2	4.179
17B	0.02365	0.001588	0.00409	0.01918	0.02004	1	0.726	402.5	1.516
17B	0.02365	0.001588	0.00409	0.04924	0.05145	1	0.553	1033.3	2.421
17B	0.02365	0.001588	0.00409	0.0694	0.07252	1	0.492	1456.4	2.870
17B	0.02365	0.001588	0.00409	0.01905	0.01991	2	0.727	399.8	1.510
17B	0.02365	0.001588	0.00409	0.04903	0.05123	2	0.583	1028.9	2.618
17B	0.02365	0.001588	0.00409	0.06946	0.07258	2	0.525	1457.7	3.157
17B	0.02365	0.001588	0.00409	0.04912	0.05133	3	0.593	1030.8	2.696
17B	0.02365	0.001588	0.00409	0.06897	0.07207	3	0.537	1447.4	3.242
17B	0.02365	0.001588	0.00409	0.04912	0.05133	4	0.599	1030.8	2.740
17B	0.02365	0.001588	0.00409	0.06906	0.07216	4	0.544	1449.3	3.311

In seeking correlations for the wind results, it was found that at each individual wind speed, an accurate correlation could be obtained of the form used for zero wind speed.

The following correlations were obtained based on the data from the first five plates listed in the table (plates 15 and 17 were tested after the others and are included in the global correlation given later in this section):

$U_{\infty} = 1 \text{ m/s}$:

$$\text{Nu}_D = 3.967 \left(\frac{P}{D} \right)^{-1.194} \text{Re}_D^{.3992} \quad (4-8)$$

$U_{\infty} = 2 \text{ m/s}$:

$$\text{Nu}_D = 3.614 \left(\frac{P}{D} \right)^{-1.337} \text{Re}_D^{.4867} \quad (4-9)$$

$U_{\infty} = 4 \text{ m/s}$:

$$\text{Nu}_D = 3.920 \left(\frac{P}{D} \right)^{-1.438} \text{Re}_D^{.5225} \quad (4-10)$$

Figures 4-36 through 4-38 show the results for each wind speed. The coefficients of determination, R^2 , for the three wind speeds of 1, 2, and 4 m/s are, respectively, .9908, .9952, and .9954. Denoting the parameters of the fit symbolically as:

$$\text{Nu}_D = a \left(\frac{P}{D} \right)^b \text{Re}_D^c \quad (4-11)$$

the coefficients of variation for each parameter are shown in Table 4-10.

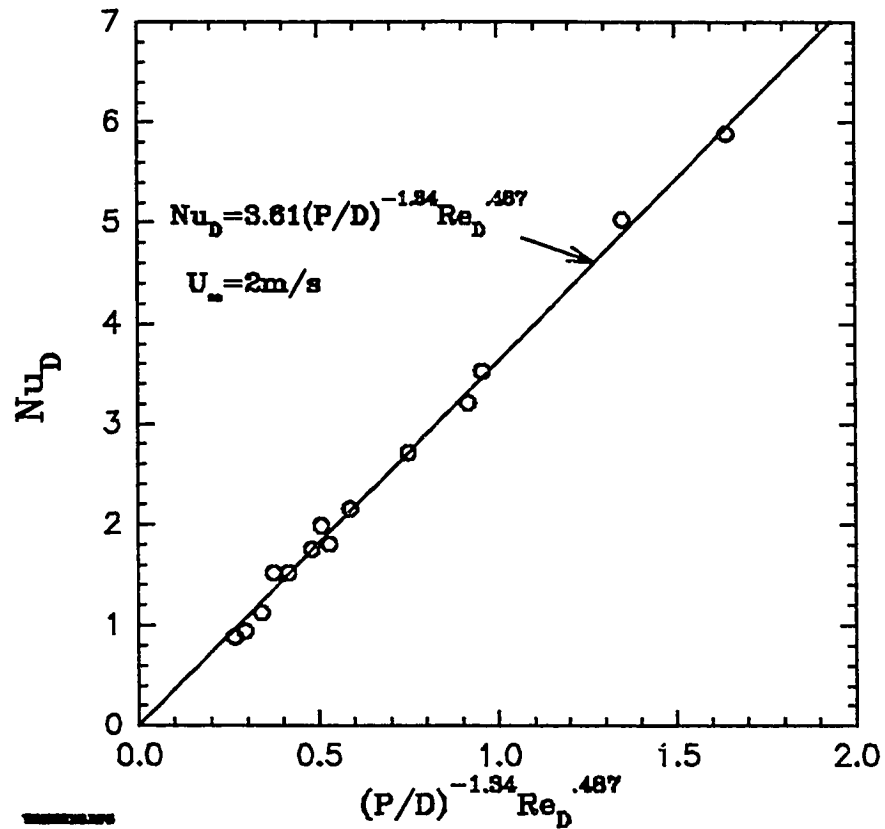


Figure 4-36. Nusselt number correlation for vertical test plates at wind speed of 2 m/s.

Table 4-10. Coefficients of variation expressed as a percentage for the parameters a, b, and c in the wind run correlations of the form $Nu_D = a(P/D)^b Re_D^c$.

U_∞ (m/s)	a	b	c
1	14.6	3.4	8.1
2	11.7	2.4	5.3
4	12.5	2.4	5.2

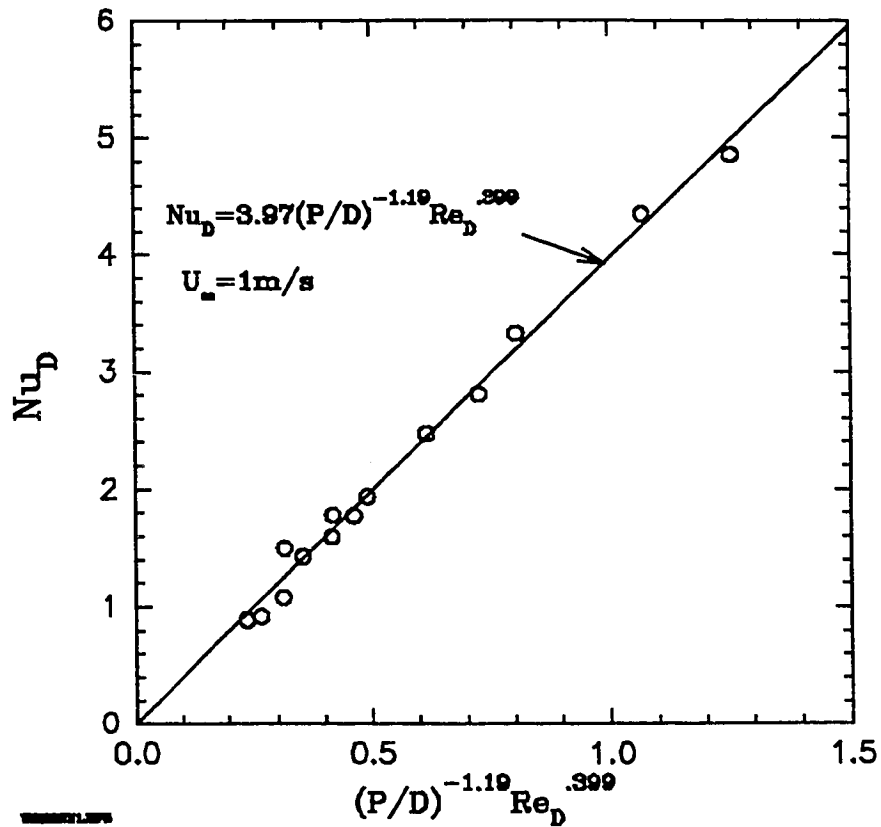


Figure 4-37. Nusselt number for vertical test plates at wind speed of 1 m/s.

Various means were attempted for correlating all of the results into a single equation. The goal is to obtain a non-dimensional correlation that reduces to the zero-wind case at zero wind and is zero at zero suction velocity. It appears reasonable to non-dimensionalize the wind speed by dividing by the suction face velocity, v . This is because the asymptotic thermal boundary layer thickness is proportional to v/V . Consider that the incremental heat transfer above the zero-wind value can be correlated in a

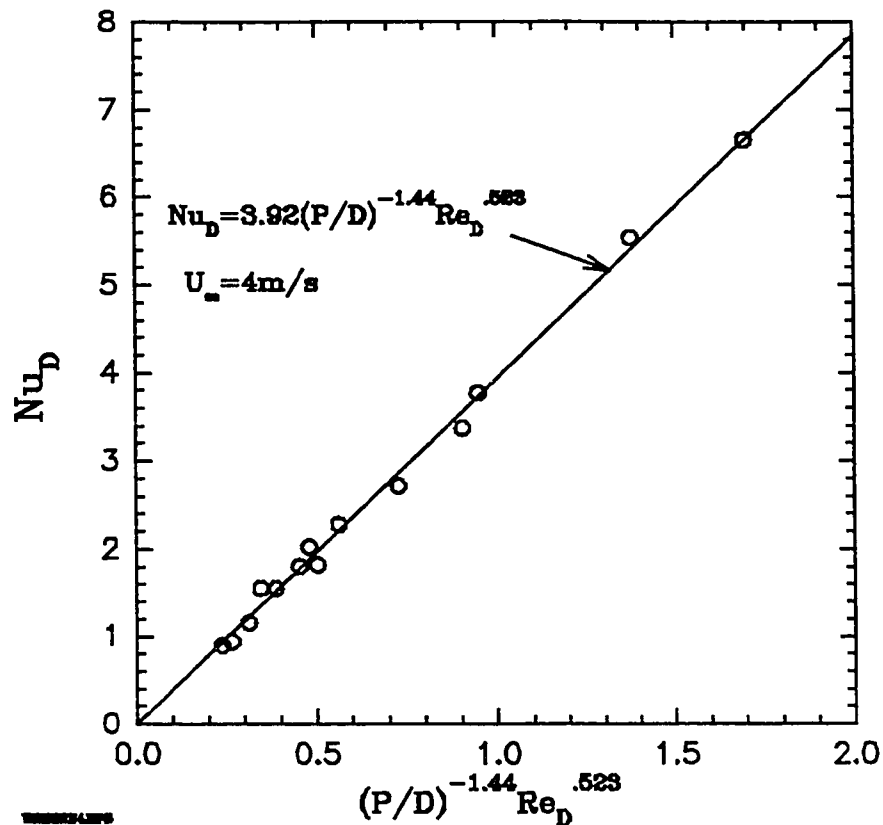


Figure 4-38. Nusselt number correlation for vertical test plates at wind speed of 4 m/s.

form that relates a Nusselt number based on thermal boundary layer thickness to a Reynolds number based on the same length scale (and using wind speed as the velocity scale). Thus,

$$Nu_\delta \sim Re_\delta^x \quad (4-12)$$

Here the Nusselt number is based on an incremental heat transfer coefficient, $U' = U - U_0$, where U_0 is the value at

zero wind and U is the value with non-zero wind. In terms of U' and δ ,

$$\frac{U'\delta}{k} \sim \left(\frac{U_\infty \delta}{v} \right)^x \quad (4-13)$$

Noting that

$$\delta \sim \frac{v}{V} \quad (4-14)$$

the incremental heat transfer coefficient is:

$$U' \sim \frac{k}{v} V \left(\frac{U_\infty}{V} \right)^x \quad (4-15)$$

At this point, note that if the exponent x is less than one, the incremental heat transfer coefficient goes to zero if wind speed or suction velocity go to zero.

Since the zero wind correlation is in the form of a Nusselt number based on hole diameter, it is convenient to multiply both sides of this equation by D/k , obtaining:

$$Nu_D' \sim \sigma Re_D \left(\frac{U_\infty}{V} \right)^x \quad (4-16)$$

and

$$Nu_D = (Nu_D)_0 + Nu_D' \quad (4-17)$$

The wind data were thus fitted to a correlation of the form

$$Nu_D' = a \sigma Re_D \left(\frac{U_\infty}{V} \right)^b \quad (4-18)$$

Regression using SigmaPlot yielded:

$$a = .03048$$

$$b = .4797$$

The coefficients of variation are $\pm 18.3\%$ for a and $\pm 9.3\%$ for b . Thus the wind data are correlated as:

$$Nu_D = 2.748 \left[\left(\frac{P}{D} \right)^{-1.208} Re_D^{.4295} + .01109 \sigma Re_D \left(\frac{U_\infty}{V} \right)^{.4797} \right] \quad (4-19)$$

Note that for laminar flow over a plate, one expects an exponent on the wind speed of $1/2$, and the fitted exponent is close to that. A plot of Nu_D for the non-zero wind data is shown in **Figure 4-39**. When this correlation is used to determine heat exchange effectiveness, all measured heat exchange effectiveness values for the wind runs are predicted to within $\pm 10\%$ (the highest error is 9%). The R^2 value for predicted vs. measured effectiveness for wind runs is $.926$.

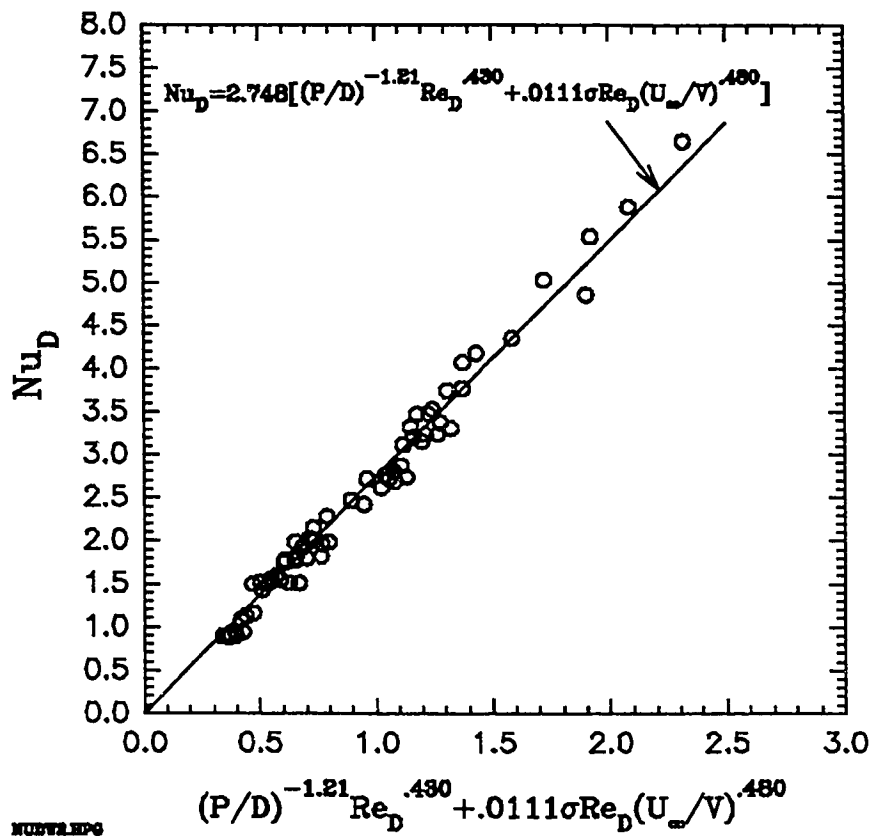


Figure 4-39. Universal heat transfer correlation for non-zero wind tests.

4.4 Pressure Drop

In the design of a transpired collector, it is necessary to know heat exchange effectiveness to determine thermal performance. It is also necessary to predict pressure drop to ensure that it is sufficient to provide good flow uniformity and prevent outflow and in order to minimize fan power. The most complete source that could be found on pressure drop information is the Russian work by

I. E. Idelchik, entitled Handbook of Hydraulic Resistance (Idelchik, 1986).

Data for the Reynolds number (based on hole diameter) range of interest (about 30 to 2,000) are given on page 406 of that book in the form of graphs and tables for a wide porosity range, but are stated as "tentative" for this flow regime. Determining the pressure drop for any given plate requires a complicated series of steps to evaluate various parameters and combine them into a final result.

In order to test the validity of the Idelchik data and to explore the possibility of a simpler correlation, all plates of .794 mm (1/32 in.) thickness were tested at suction mass flow rates from 0.01 to 0.08 kg/m²-s. (Only data points with a minimum pressure drop of 5 Pa were recorded.) Flow rate was measured with the laminar flow element, and pressure drop was recorded by reading a Dwyer point gauge manometer. This manometer has a range of 0-498 pa (0-2 in. of water) and is readable to 2.29 Pa (0.001 inch).

The pressure drop data are given in **Table 4-11**. The mean of the absolute value of the percentage error between the measured value and that calculated from the handbook is 14.6% with the highest error being 44%. Clearly there is room for improvement in predicting the pressure drop for these low porosity plates.

Table 4-11. Experimental pressure drop measurements.

Plate	Pitch (m)	Dia. (m)	σ	G(kg/s-m ²)	Re _p	ΔP (Pa)	ξ
2	0.01351	0.001588	0.01253	0.03076	211.3	5.98	11746
2	0.01351	0.001588	0.01253	0.03987	273.8	9.47	11065
2	0.01351	0.001588	0.01253	0.05017	344.6	13.95	10314
2	0.01351	0.001588	0.01253	0.06015	413.1	19.43	9987
2	0.01351	0.001588	0.01253	0.07050	484.2	26.40	9873
2	0.01351	0.001588	0.01253	0.07982	548.2	32.88	9593
3	0.02703	0.003175	0.01252	0.03061	420.6	5.48	10883
3	0.02703	0.003175	0.01252	0.04029	553.6	9.47	10834
3	0.02703	0.003175	0.01252	0.04979	684.1	14.70	11018
3	0.02703	0.003175	0.01252	0.06056	832.1	21.92	11118
3	0.02703	0.003175	0.01252	0.07056	969.5	30.14	11247
4	0.02703	0.001588	0.00313	0.01007	276.7	8.72	159800
4	0.02703	0.001588	0.00313	0.01504	413.3	18.68	153469
4	0.02703	0.001588	0.00313	0.02014	553.4	32.13	147107
4	0.02703	0.001588	0.00313	0.03097	851.0	72.24	139776
4	0.02703	0.001588	0.00313	0.04013	1102.7	119.32	137520
4	0.02703	0.001588	0.00313	0.05005	1375.3	185.08	137164
4	0.02703	0.001588	0.00313	0.06011	1651.8	269.27	138306
4	0.02703	0.001588	0.00313	0.07100	1951.0	378.88	139504
11	0.01351	0.000794	0.00313	0.01021	140.3	12.45	221262
11	0.01351	0.000794	0.00313	0.01555	213.6	25.91	198325
11	0.01351	0.000794	0.00313	0.02007	275.7	40.85	187839
11	0.01351	0.000794	0.00313	0.02498	343.2	60.28	178770
11	0.01351	0.000794	0.00313	0.03016	414.4	84.94	172731
11	0.01351	0.000794	0.00313	0.03510	482.3	111.84	167726
11	0.01351	0.000794	0.00313	0.04070	559.2	146.22	163384
11	0.01351	0.000794	0.00313	0.05021	689.9	216.96	159259
11	0.01351	0.000794	0.00313	0.06056	832.1	311.62	157337
11	0.01351	0.000794	0.00313	0.06992	960.7	413.00	156416
12	0.02027	0.000794	0.00139	0.01025	316.9	49.57	887263
12	0.02027	0.000794	0.00139	0.01267	391.7	74.48	871581
12	0.02027	0.000794	0.00139	0.01516	468.7	101.38	828153
12	0.02027	0.000794	0.00139	0.01761	544.4	134.51	814052
12	0.02027	0.000794	0.00139	0.02019	624.1	169.39	780099
12	0.02027	0.000794	0.00139	0.02258	698.0	210.24	773632
12	0.02027	0.000794	0.00139	0.02515	777.5	257.07	764439
12	0.02027	0.000794	0.00139	0.02768	855.7	308.38	756259
12	0.02027	0.000794	0.00139	0.03041	940.1	371.65	755361

Plate	Pitch (m)	Dia.(m)	σ	G(kg/s-m ²)	Re _o	ΔP (Pa)	ξ
12	0.02027	0.000794	0.00139	0.03265	1009.3	424.96	749495
13	0.02703	0.000794	0.00078	0.00220	120.9	9.47	3672341
13	0.02703	0.000794	0.00078	0.00402	220.9	26.40	3072571
13	0.02703	0.000794	0.00078	0.00613	336.9	54.55	2724868
13	0.02703	0.000794	0.00078	0.00799	439.1	87.93	2586349
13	0.02703	0.000794	0.00078	0.00994	546.3	130.78	2485901
13	0.02703	0.000794	0.00078	0.01242	682.6	194.30	2365143
13	0.02703	0.000794	0.00078	0.01425	783.1	247.60	2287929
13	0.02703	0.000794	0.00078	0.01637	899.7	320.09	2241257
13	0.02703	0.000794	0.00078	0.01818	999.1	389.09	2207974
13	0.02703	0.000794	0.00078	0.02024	1112.3	473.28	2168939
14	0.02027	0.001191	0.00313	0.01027	211.5	9.47	168697
14	0.02027	0.001191	0.00313	0.01514	311.9	19.93	163281
14	0.02027	0.001191	0.00313	0.02051	422.5	35.37	157826
14	0.02027	0.001191	0.00313	0.02521	519.3	51.81	153162
14	0.02027	0.001191	0.00313	0.03051	628.4	73.48	148248
14	0.02027	0.001191	0.00313	0.04024	828.9	126.29	146453
14	0.02027	0.001191	0.00313	0.05052	1040.6	200.27	147469
14	0.02027	0.001191	0.00313	0.06088	1254.0	297.17	150604
14	0.02027	0.001191	0.00313	0.07068	1455.9	410.01	154033
14	0.02027	0.001191	0.00313	0.07437	1531.9	458.59	155692
15	0.01689	0.001588	0.00801	0.02019	216.7	5.73	26433
15	0.01689	0.001588	0.00801	0.0304	326.3	11.96	24320
15	0.01689	0.001588	0.00801	0.04089	438.9	20.92	23512
15	0.01689	0.001588	0.00801	0.05045	541.5	30.89	22793
15	0.01689	0.001588	0.00801	0.06025	646.7	43.34	22461
15	0.01689	0.001588	0.00801	0.07061	757.9	58.79	22150
16	0.02027	0.001588	0.00556	0.02110	326.1	11.96	50573
16	0.02027	0.001588	0.00556	0.03110	480.7	24.66	48013
16	0.02027	0.001588	0.00556	0.04178	645.8	43.34	46724
16	0.02027	0.001588	0.00556	0.05210	805.3	65.76	45565
16	0.02027	0.001588	0.00556	0.06229	962.8	92.91	45109
16	0.02027	0.001588	0.00556	0.07255	1121.4	124.80	44659
17	0.02365	0.001588	0.00409	0.01038	218.4	5.48	95821
17	0.02365	0.001588	0.00409	0.02010	422.9	19.43	90525
17	0.02365	0.001588	0.00409	0.03031	637.7	42.35	86838
17	0.02365	0.001588	0.00409	0.04069	856.1	73.23	83304
17	0.02365	0.001588	0.00409	0.05011	1054.2	110.10	82510
17	0.02365	0.001588	0.00409	0.06083	1279.8	162.91	82917

Plate	Pitch (m)	Dia.(m)	σ	G(kg/s-m ²)	Re ₀	ΔP (Pa)	ζ
17	0.02365	0.001588	0.00409	0.07051	1483.4	220.20	83433
18	0.02027	0.002413	0.01285	0.04055	412.4	7.97	9126
18	0.02027	0.002413	0.01285	0.05085	517.1	12.70	9241
18	0.02027	0.002413	0.01285	0.06016	611.8	17.93	9329
18	0.02027	0.002413	0.01285	0.07076	719.6	24.91	9372
18	0.02027	0.002413	0.01285	0.07997	813.2	31.88	9389
19	0.02027	0.003175	0.02225	0.06049	467.5	6.48	3347
19	0.02027	0.003175	0.02225	0.07046	544.5	8.72	3323
19	0.02027	0.003175	0.02225	0.07987	617.3	11.46	3401

The non-dimensionalized pressure drop, ζ , is defined as:

$$\zeta \equiv \frac{\Delta P}{\frac{1}{2} \rho V^2} \quad (4-20)$$

where V is the approaching face velocity. According to Idelchik (1986) ζ is a function of porosity, the Reynolds number based on hole diameter, and the friction factor. Since the hole Reynolds numbers for the test plates are less than 2300, the flow is laminar, and the friction factor is just $64/Re_D$. In seeking a simple single-term correlation for ζ , one can thus simply consider products of porosity and Reynolds number to unknown powers. In order not to prejudice the correlation, however, curve fits were done to determine dimensional pressure drop in terms of powers of hole pitch, hole diameter, and approach velocity. The resulting powers were highly consistent with the non-dimensional variables given above.

When fitting the non-dimensional variables, the power on porosity was very close to -2, that is ζ was approximately proportional to $1/\sigma^2$. As shown in Batchelor (1967), the pressure drop across a perforated plate is analogous to a sudden enlargement in a pipe, and the decrease in the Bernoulli constant (i.e. the unrecoverable pressure drop) can be determined in non-dimensional form from conservation of momentum as:

$$\zeta = \left(\frac{1-\sigma}{\sigma}\right)^2 \quad (4-21)$$

Batchelor points out that viscosity is not important unless the holes are very small. Note that for the plates tested here, which have very low porosity,

$$\left(\frac{1-\sigma}{\sigma}\right)^2 \approx \frac{1}{\sigma^2} \quad (4-22)$$

so that it is not surprising that the data show an inverse dependence on the square of the porosity.

Expressing the porosity term in Batchelor's form is consistent with the physics and could be expected to make the correlation more extrapolatable to higher porosities. Because it did not have a negative impact on the accuracy of the fit, this term was used in the correlation. The fact that the curve fitting yields a non-zero exponent on the Reynolds number indicates that the holes are small

enough for viscosity to play a role in the pressure drop. The best fit for the plates tested was:

$$\zeta = 6.818 \left(\frac{1-\sigma}{\sigma} \right)^2 \text{Re}_D^{-.2360} \quad (4-13)$$

When compared with the data, this fit yields an average value for the absolute magnitude of the error equal to 6.5%, but with a few considerably higher errors, the extreme being 26%. The coefficient of determination, R^2 , for the fit is .9992. Thus this simple correlation fits the data better than the much more complicated procedure presented in Idelchik (1986). In fairness to Idelchik, this correlation covers a much smaller range, namely the range suitable for transpired solar collectors. The correlation result together with the data are presented in **Figure 4-40**.

All of the above data were taken in the absence of wind. A few runs were made to test the effect of a cross-flow, and it was found that wind increases the pressure drop a small but significant amount. This can be seen in **Figure 4-41** which shows the increase in pressure drop for plate 17 as a function wind speed. Tests with both the "A" and "B" orientations showed little effect of orientation on pressure drop.

The increase in pressure drop due to wind is not surprising when one considers the flow pattern found from

the three dimensional FLUENT model described in Chapter 3. The separation bubble which occurs in the hole has the effect of decreasing the effective hole size and thereby increasing the magnitude of the sudden enlargement. A detailed study of the effect of wind on pressure drop was beyond the scope of this report but is being pursued as future work.

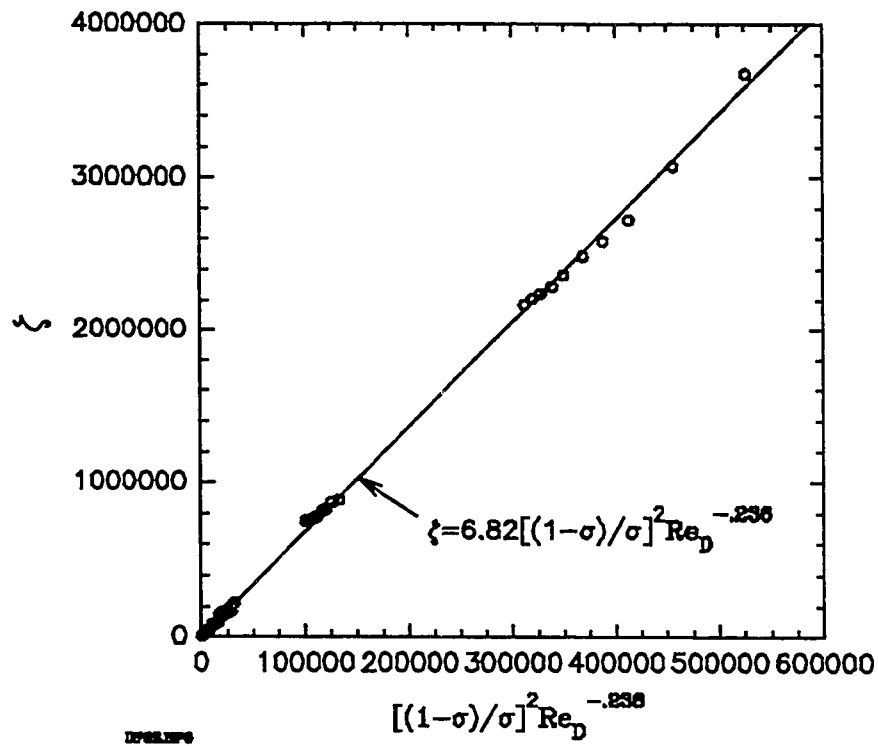


Figure 4-40. Data and correlation for non-dimensional pressure drop as a function of porosity and Reynolds number.

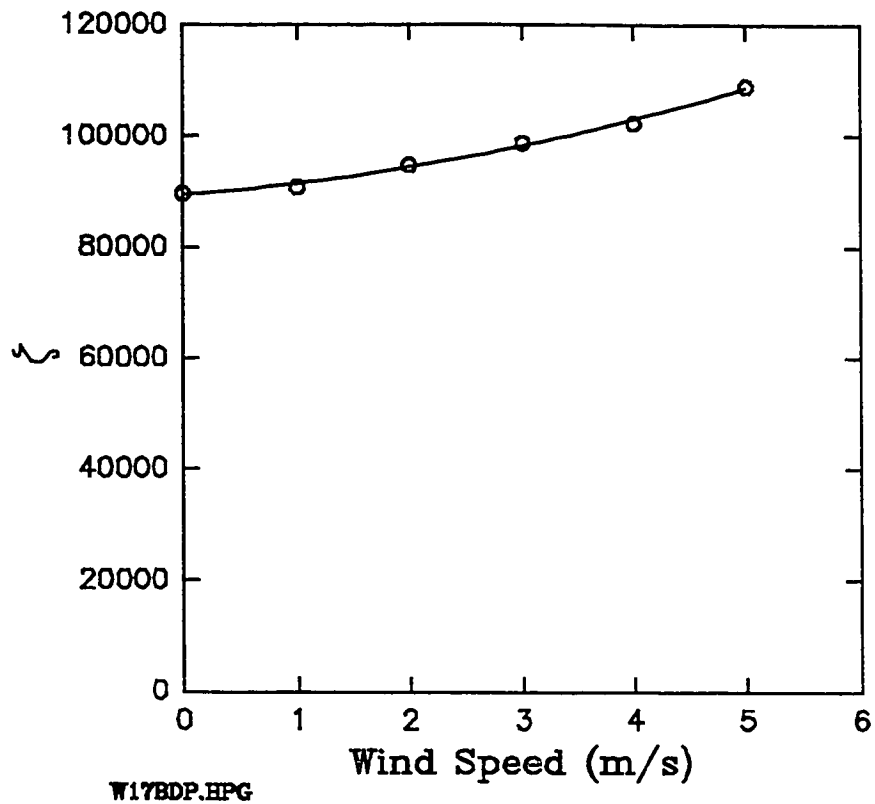


Figure 4-41. Non-dimensional pressure drop vs. wind speed at $G = 0.023 \text{ kg}/(\text{m}^2\text{-s})$ for plate 17.

4.5 Wind Heat Loss

In order to verify the laminar asymptotic boundary layer theory presented in Chapter 2, wind heat loss tests were carried out on an absorber consisting of two layers of black cotton fabric. The purpose of the cotton fabric was to approach the assumption of uniform homogenous suction used in the theoretical development. Fabrics are also low-cost candidate absorber materials for crop drying.

Hemispherical reflectance of the two-layer black fabric was measured as a function of wavelength using a Perkin Elmer Lambda-9 UV-VIS-NIR spectrometer. The resulting curve was weighted by a 2750 K blackbody radiation curve (representing the lamp radiation) in order to generate an average value of reflectance. Absorptivity was determined by subtracting the reflectivity from 100% and was found to be 80%. (Transmissivity was measured at 5%, but was not subtracted out, as transmitted light was assumed to be ultimately captured.) A Gier Dunkle model DB100 infrared reflectometer was used to measure infrared reflectance from which an emissivity of .91 was determined.

The wind heat loss, Q_w , was determined by subtracting the energy picked up by the suction fluid, Q_f , from the net energy absorbed by the surface, Q_{net} with all heat terms in watts.

Thus,

$$Q_w = Q_{net} - Q_f \quad (4-24)$$

where,

$$Q_{net} = \alpha Q_s - \epsilon \sigma_{SB} T_s^4 + \epsilon R_{in} \quad (4-25)$$

and

$$Q_f = \dot{m}(h_{out} - h_{in}) \quad (4-26)$$

where h_{out} and h_{in} are the enthalpies in J/kg of, respectively, the exit air and the inlet air.

As discussed earlier, the incoming lamp radiation, Q_s , is measured with a Kipp & Zonen CM-11 pyranometer. The long-wave incoming radiation, R_{in} is measured by an Eppley pyrgeometer. Although this device has a built-in battery powered compensation circuit to provide an output of R_{in} , users have reported that higher accuracy can be obtained by reading the thermopile voltage corresponding to the net long-wave radiation, R_{net} , and converting this to R_{in} via the following equation:

$$R_{in} = R_{net} + .99 \sigma T_{case}^4 + 3.0 \sigma_{SB} (T_{case}^4 - T_{dome}^4) \quad (4-16)$$

The second term on the right side of the equation is the outgoing radiation with the sensor emissivity taken as .99. The last term is an empirical correction term which compensates for the fact that the glass dome is heated and transfers some radiation to the sensor. A dome thermistor (YSI 44031) measures the dome temperature, T_{dome} , and the black receiver temperature is taken as that of the case, T_{case} which is also measured with a YSI 44031 10,000 ohm thermistor.

The combination of pyranometer and pyrgeometer used to measure net radiant energy into the absorber can be expected to give a result (for this non-solar application) of no better than $\pm 5\%$. Since wind heat loss is determined by subtracting energy collected from the net radiant energy, the error on radiant energy can translate into a

large uncertainty in the wind loss. For example, a value of 100 watts of net radiant energy onto the absorber would have an uncertainty of 5 watts, yet this is the order of the wind loss for the test plates.

Fortunately, the error in radiation can be considered a systematic one, since the lamp radiation is controlled at a constant value, and the ambient and surface temperatures do not vary greatly during a test. By plotting wind heat loss versus wind speed, the resulting straight line will not pass through the origin due to an offset caused by this systematic error. This offset can then be subtracted out so that the measured heat loss curve passes through the origin just as the calculated heat loss curve does.

Figure 4-42 shows a plot of the theoretical and measured values of wind heat loss with the measured values having been corrected for this systematic offset. A suction mass flow rate of $.02 \text{ kg}/(\text{m}^2\text{-s})$ was chosen for this test. A low suction value increases the magnitude of the heat loss term. Going lower than about $.02$, however, results in an increasingly significant error in the outlet suction air temperature due to heat losses in the test box.

WIND HEAT LOSS

FABRIC ABSORBER, $G = 0.02 \text{ KG/M}^2\text{-S}$

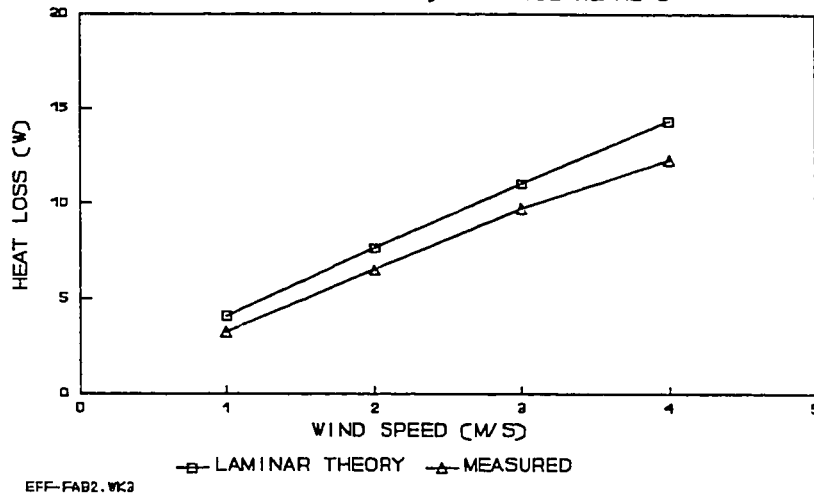
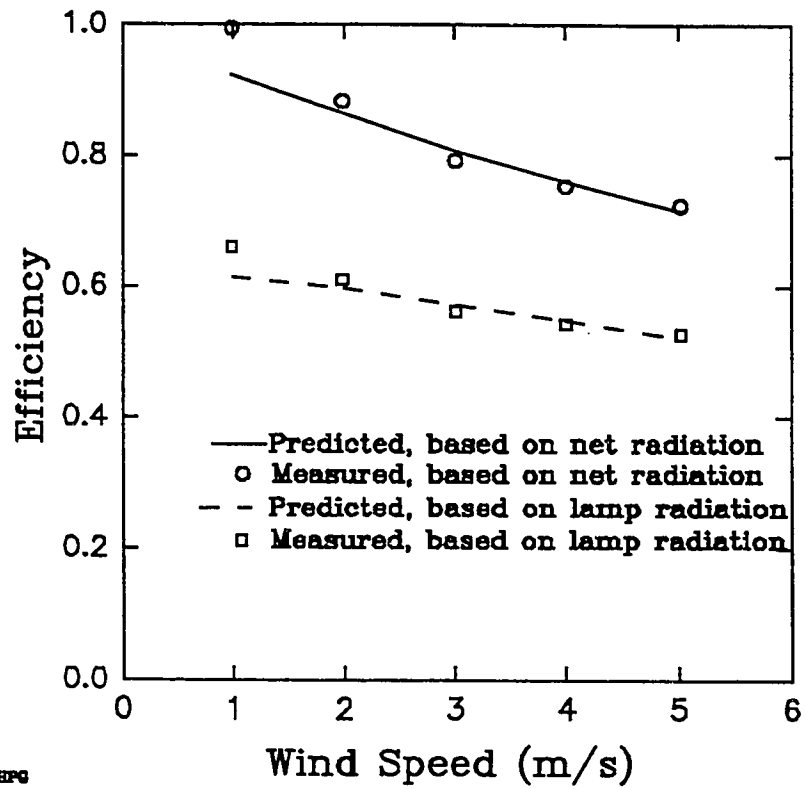


Figure 4-42. Heat loss vs. wind speed for black fabric absorber.

The agreement between the measured heat loss (corrected as described above) and that predicted from laminar asymptotic theory is quite good. Additional testing is needed to provide a higher confidence level. Because infrared images of the black fabric indicated some spottiness in the surface temperature (due probably to non-uniformities in the porosity), absorbers with a more uniform porosity will be sought for additional testing.

Figure 4-43 shows the effects of wind heat loss from a perforated plate, plotted in terms of collector efficiency as a function of wind speed for plate 6 at a suction mass flow rate of $0.02 \text{ kg}/(\text{m}^2\text{-s})$. The lines show the theoretical predictions from laminar asymptotic suction theory (which assumes a homogeneous suction surface) but based on the measured surface temperatures. The data points show experimentally measured efficiency values. Efficiency is defined as the energy picked up by the suction air divided by either the net incoming and outgoing (short wave and long wave) radiation on the absorber (upper curve) or the incoming short-wave radiation from the lamps (lower curve). No systematic correction was made here, and the error can be seen in the low wind speed data. As wind speed increases, efficiency drops due to loss to the wind. The theory predicts the actual efficiency for this perforated plate quite well. Preliminary tests on plates with a larger hole pitch show wind losses somewhat greater than the predictions. Detailed testing is planned for the other plates to determine the effect of geometry on wind heat loss.



27706.HPG

Figure 4-43. Collector efficiency vs. wind speed for plate 6.

5. CONCLUSIONS, SUMMARY, AND FUTURE WORK

5.1 Conclusions and Application of Results

A transpired collector performance model was presented in Chapter 2. To use this model, the designer must know the heat exchange effectiveness of the absorber. In Chapter 3 numerical simulations showed that most of the heat transfer occurs on the front surface and demonstrated that a heat transfer coefficient based on the log mean temperature difference provides the best means for developing the effectiveness. Numerical simulations also provided insight into the heat transfer that occurs in the hole and on the back surface and also revealed the impact of wind. Factorial experiments revealed that mass suction flow rate, hole pitch, hole diameter, and wind speed are key factors in determining the amount of heat transfer. Plate thickness and plate orientation are of minor significance. Detailed heat transfer measurements were made on a series of test plates of .794 mm (1/32 in.) thickness (the thickness used commercially) and oriented vertically (the typical application). Results without wind and at three different wind speeds were determined, and an overall correlation able to predict heat exchange effectiveness to better than $\pm 10\%$ was developed. A pressure drop correlation was also developed so that the designer can ensure uniform flow across the absorber and

determine fan power. Finally, wind heat loss measurements were taken to verify the theoretical prediction that in a large collector this is a minor loss term.

It is straightforward to determine heat exchange effectiveness from the Nusselt number correlations obtained in this report. The effectiveness can be written as:

$$e_{HX} = 1 - e^{-NTU} \quad (5-1)$$

where

$$NTU = \frac{UA}{GA'C_p} = \frac{A}{A'} \frac{U}{GC_p} \quad (5-2)$$

Since A is the plate surface area minus the hole area and A' is the total frontal area (including holes), the ratio A/A' can be expressed in terms of the porosity, $\sigma = .907 (D/P)^2$, as:

$$\frac{A}{A'} = 1 - \sigma \quad (5-3)$$

Noting that the overall heat transfer coefficient, U, can be expressed in terms of the Nusselt number as:

$$U = \frac{k}{D} Nu_D \quad (5-4)$$

these can be combined to obtain the effectiveness as:

$$e_{HX} = 1 - \exp\left[\frac{\sigma - 1}{GC_p} \frac{k}{D} Nu_D\right] \quad (5-5)$$

Nu_D correlations are given in Chapter 4 in terms of the hole pitch, P , the hole diameter, D , and the hole Reynolds number, Re_D , which is defined as:

$$Re_D = \frac{G D}{\mu} = 1.1025 \frac{GP^2}{\mu D} \quad (5-6)$$

The designer can conservatively use the zero wind correlation, or he can choose a design wind speed and a corresponding correlation, or use the overall correlation that includes wind speed. If using the separate wind speed correlations, since these correlations are not non-dimensional in wind speed, the designer should be careful to multiply his design wind speed by his average expected air density divided by the average density for the tests reported here, 0.96 kg/m^3 .

In determining pressure drop across the absorber, the designer should use the correlation for non-dimensional pressure drop given in Chapter 4:

$$\zeta = 6.82 \left(\frac{1-\sigma}{\sigma}\right)^2 Re_D^{-.236} \quad (5-7)$$

The pressure drop is then:

$$\Delta P = \frac{1}{2} \rho V^2 \zeta \quad (5-8)$$

where V = approaching face velocity = G/ρ .

5.2 Summary

This study experimentally developed correlations for heat exchange effectiveness with and without wind applicable to perforated plates used for transpired solar collector applications, thereby providing designers with a tool needed to predict and optimize thermal performance. A pressure drop correlation was also developed which will allow designers to provide for sufficient flow uniformity while minimizing fan power. Numerical simulation results provide information on where the heat transfer occurs for air flow through perforated plates, and infrared thermography provided visualization of heat transfer on the most important portion of the plate, the front surface. Preliminary experimental verification was provided for laminar asymptotic suction layer theory applied to wind heat loss for such plates.

The following is a list of the specific new contributions from this study:

- A correlation was developed for normal flow heat exchange effectiveness for perforated plates in the porosity and suction flow rate range of interest for transpired solar collectors.

- Separate correlations for heat exchange effectiveness were developed for three different wind speeds, and an overall correlation for arbitrary wind speed was developed. The latter can predict heat exchange effectiveness to within $\pm 10\%$ over the range of plate geometries, suction mass flow rate, and wind speed of interest.
- Using an axisymmetric FLUENT model, the proportion of heat transfer on the front surface, hole, and back surface were determined, thereby quantitatively determining the dominance of front surface heat transfer.
- It was shown that a front surface heat transfer correlation based only on pitch can be used to predict front surface heat transfer.
- It was shown that the Sieder-Tate pipe entrance flow correlation overestimates hole heat transfer.
- Infrared thermography was used to show the effect of wind on front surface heat transfer, and the effect of the orientation of the hole grid with respect to wind direction was shown visually.
- It was shown experimentally that in comparing the two major grid directions with respect to wind, one results in significantly higher heat exchange effectiveness than the other.
- It was shown experimentally that for the parameters of interest for transpired solar collectors, the heat

exchange effectiveness of a vertical plate is only slightly higher than for a horizontal plate, thus demonstrating the dominance of forced convection.

- A pressure drop correlation for low Reynolds number flows through low porosity plates was developed which is significantly more accurate and easier to use than previously available results.
- A new type of aspirated temperature probe employing a porous matrix was developed which shows promise for applications in which high aspiration rates can not be used.
- A transient radiation instrument was developed which can determine the net long-wave and short-wave radiation flux on a test surface in a single measurement.
- A computer program was developed for designing a lamp array. An array of 16 lamps designed from runs of this program demonstrated flux levels of up to 1200 W/m^2 on a 30 cm x 50 cm target with a spatial uniformity of better than $\pm 2\%$.
- The wind heat loss theory developed by Kutscher, Christensen, and Barker (1991a) was verified by experimental results on a fabric absorber.

5.3 Future Work

The heat exchange effectiveness correlations developed in this report do not include any effect of flow up the

back of the absorber, because it is expected to be small, and any effect would depend on the depth and height of the plenum. This term is expected to be small for a number of reasons as follows: the driving temperature difference is small; the heat transfer coefficients for air flow in a channel are low and the velocity increase up the wall is expected to laminarize the flow; and the back of the absorber is an injection surface which should thicken the boundary layer. In addition, preliminary tests in the laboratory and on a large outdoor test wall indicated very little temperature rise up the wall. Nevertheless, some further study of this issue is desirable, since in very tall vertical absorbers, the effect could become important.

In briefly examining wind loss experimentally, it was found that for a perforated absorber, the heat loss may be somewhat greater than asymptotic boundary layer theory would suggest at large hole pitches. It would be useful to examine wind heat loss as a function of hole size and spacing and compare results; this work is now underway at NREL.

A three dimensional version of FLUENT with boundary-fitted coordinates became available only at the end of this study, and preliminary results were included to provide physical insight into the cross-flow phenomenon. NREL has recently obtained a work station that will provide the ability to run FLUENT with larger numbers of nodes and at

greater speed. The 3-D FLUENT model will be used to examine the effects of wind on heat transfer at the surface and in the hole and will also be used to examine the edge heat loss. Hot wire anemometry will also be used to examine the boundary layer, and the results will be compared to the FLUENT model.

Infrared thermography of large walls in the field has revealed problems with flow uniformity. At NREL a 23.8 m² (256 ft²) adjustable test wall with a variable depth plenum was built. This is currently being used to investigate flow uniformity issues and the first version of a detailed computer model of flow uniformity has been written. The model utilizes the pressure drop correlation presented in this report to calculate the local pressure drops across the wall and the heat exchange effectiveness correlation to determine temperature distributions needed for calculating the thermal buoyancy term.

BIBLIOGRAPHY

Andrews, G.E. and F. Bazdidi-Tehrani, "Small Diameter Film Cooling Hole Heat Transfer: The Influence of the Number of Holes," ASME paper No. 89-GT-7, presented at the American Society of Mechanical Engineers Gas Turbine and Aeroengine Congress and Exposition, June 4-8, 1989, Toronto, Canada.

Arens, E. A. and P. B. Williams, "The Effect of Wind on Energy Consumption in Buildings," Energy and Buildings, Vol. 1, May 1977, pp. 77-84.

Arpaci, V. S. and P. S. Larsen, Convection Heat Transfer, Prentice-Hall, Inc., Englewood Cliffs, New Jersey, 1984, Chapter 4, pp. 160-169.

Batchelor, G. K., An Introduction to Fluid Dynamics, Cambridge University Press, Cambridge, England, 1967.

Bejan, A., Convection Heat Transfer, John Wiley & Sons, New York, 1984, Chapter 4, pp. 114-122.

Box, G. E., W. G. Hunter, and J. S. Hunter, Statistics for Experimenters, John Wiley & Sons, New York, 1978.

Burmeister, L. C., Convective Heat Transfer, John Wiley & Sons, New York, 1983.

Cain, C. L., Heat Transfer and Friction Factor Design Data for All-Metal Compact Heat Exchangers, Air Force Wright Aeronautical Labs, Wright-Patterson Air Force Base, Ohio, March 1989.

Chau, K. V. and S. M. Henderson, "Performance of a Matrix Solar Collector for Heating Air," Transactions of the ASAE, 1977, pp. 558-561.

Currie, I. G., Fundamental Mechanics of Fluids, Mc-Graw Hill, New York, 1974.

Davenport, A. G., and H. Y. L. Hui, External and Internal Wind Pressures on Cladding of Buildings, Boundary Layer Wind Tunnel Laboratory, The University of Western Ontario, London, Ontario, BLWT-820133, 1982.

Dutton, R. A., "The Effects of Distributed Suction on the Development of Turbulent Boundary Layers," Aeronautical Research Council Technical Report, R. & M. No. 3155, London, England, 1960.

El-Wakil, M. M., Nuclear Heat Transport, International Textbook Company, Scranton, Pennsylvania, 1971.

Gregory, N., "Research on Suction Surfaces for Laminar Flow," pp. 942 and 953 in Lachmann, G. V. (editor), Boundary Layer and Flow Control -- Its Principles and Application, Vol. 2, Pergamon Press Ltd., London, England, 1961.

Hausen, H., Z. VDI Beih. Verahrenstech, 4, 91, 1943.

Hubbell, R. H. and C. L. Cain, "New Heat Transfer and Friction Factor Design Data for Perforated Plate Heat Exchangers," Advances in Cryogenic Engineering, V. 33, pp. 383-390, Plenum Publishing Company, New York, 1988.

Idelchik, I. E., Handbook of Hydraulic Resistance, Hemisphere Publishing Company, New York, 1986.

Iglisch, R., "Exact Calculation of Laminar Boundary Layer in Longitudinal Flow Over a Flat Plate with Homogeneous Suction," Technical Memorandum No. 1205, National Advisory Committee for Aeronautics, Washington, D.C., 1944.

Incropera, F. P., and D. P. DeWitt, Fundamentals of Heat and Mass Transfer, John Wiley & Sons, New York, 1985.

Kays, W. M. and M. E. Crawford, Convective Heat and Mass Transfer, McGraw-Hill Book Company, New York, 1980, Chapters 10 and 12.

Kumada, M., M. Hirata, and N. Kasagi, "Studies of Full-Coverage Film Cooling Part 2: Measurement of Local Heat Transfer Coefficient," ASME Paper 81-GT-38, presented at American Society of Mechanical Engineers Gas Turbine Conference and Products Show, March 9-12, 1981, Houston, Texas.

Kutscher, C. F., C. B. Christensen, and G. M. Barker (1991a), "Unglazed Transpired Solar Collectors: Heat Loss Theory," Solar Engineering 1991. Proceedings of the 12th Annual ASME International Solar Energy Conference, American Society of Mechanical Engineers. Also accepted for publication in the Journal of Solar Energy Engineering.

Kutscher, C. F., C. B. Christensen, and G. M. Barker (1991b), "Unglazed Transpired Solar Collectors: An Analytical Model and Test Results," Proceedings of the Biennial Congress of the International Solar Energy Society, August 1991, pg. 1245.

Kutscher, C. F. and C. B. Christensen, "Unglazed Transpired Solar Collectors," Advances in Solar Energy: An Annual Review of Research and Development, Volume 7, edited by K. W. Boer, American Solar Energy Society, 1992.

Lachmann, G. V. (editor), Boundary Layer and Flow Control - Its Principles and Application, 2 Volumes, Pergamon Press Ltd., London, England, 1961.

Loehrke, R. I. and H. M. Nagib, "Control of Free-Stream Turbulence by Means of Honeycombs: A Balance Between Suppression and Generation," Journal of Fluids Engineering, Volume 98, September 1976, pp. 342-353.

Maddaus, A. D. and J. R. Shanebrook, "The Three-Dimensional Laminar Asymptotic Boundary Layer with Suction," Journal of Engineering Mathematics, Volume 17, 1983, pp. 73-91.

McCormick, D. C., F. L. Test, and R. C. Lessman, "The Effect of Free-Stream Turbulence on Heat Transfer from a Rectangular Prism," Journal of Heat Transfer, Vol. 106, May 1984, pp. 268-275.

Moffat, R. J. and W. M. Kays, "A Review of Turbulent-Boundary-Layer Research at Stanford, 1958-1983," Advances in Heat Transfer, Volume 16, Academic Press, Orlando, Florida, 1984.

Murakami, S., "Numerical Simulation of Turbulent Flowfield Around Cubic Model: Current Status and Applications of $k-\epsilon$ Model and LES," Journal of Wind Engineering and Industrial Aerodynamics, 33 (1990), pp. 139-152.

Panton, R. L., Incompressible Flow, John Wiley & Sons, New York, 1984.

Roache, P., Computational Fluid Dynamics, Hermosa Publishers, 1984, Albuquerque, New Mexico.

Rotta, J. C., "Control of Turbulent Boundary Layers by Uniform Injection and Suction of Fluid," The Seventh Congress of the International Council of the Aeronautical Sciences, Rome, Italy, Sept. 14-18, 1970.

Schlichting, H., Boundary Layer Theory, Seventh Edition, McGraw-Hill Book Company, New York, 1979, Chapter XIV, pp. 383-389.

Schulz, H., "Das Solarzelt (The Solar Tent)," report published by Landtechnik Weihenstephan der TU, Munich, Federal Republic of Germany, 1988.

Sparrow, E. M. and M. Carranco Ortiz, "Heat Transfer Coefficients for the Upstream Face of a Perforated Plate Positioned Normal to an Oncoming Flow," International Journal of Heat and Mass Transfer, Vol. 25, No. 1, 1982, pp. 127-135.

Sparrow, E. M., J. W. Ramsey, and E. A. Mass, "Effect of Finite Width on Heat Transfer and Fluid Flow About an Inclined Rectangular Plate," Journal of Heat Transfer, Vol. 101, May 1979, pp. 199-204.

Sparrow, E. M., W. Q. Tao, and D. D. Radtke, "Heat Transfer at an Array of Co-Planar Slat-Like Surfaces Oriented Normal to a Forced Convection Flow," International Journal of Heat and Mass Transfer, Vol. 26, No. 1, 1983, pp.33-40.

Test, F. L., R. C. Lessman, and A. Johary, "Heat Transfer During Wind Flow over Rectangular Bodies in the Natural Environment," Journal of Heat Transfer, Vol. 103, May 1981, pp. 262-267.

Verrolet, E., et al., "Turbulent Boundary Layer with Suction and Heating to the Wall," Heat and Mass Transfer in Boundary Layers, Volume 1, Pergamon Press, Oxford and New York, 1972, pp. 157-168.

Wieneke, F., "Solardach Absorber," Patent No. 29 29 219, Federal Republic of Germany, 1981.

Wuest, W., "Survey of Calculation Methods of Laminar Boundary Layers with Suction in Incompressible Flow," pg. 772 in Lachmann, G. V. (editor), Boundary Layer and Flow Control -Its Principles and Application, Vol. 2, Pergamon Press Ltd., London, England, 1961.

APPENDIX A. UNCERTAINTY ANALYSIS

A.1 Heat Exchange Effectiveness

Heat exchange effectiveness was determined by direct measurement of ambient, surface, and outlet temperatures as follows:

$$e_{HX} = \frac{T_o - T_{amb}}{T_s - T_{amb}} \quad (A-1)$$

The uncertainty in effectiveness, e_e , be it systematic (bias) or random error, can be expressed as:

$$e_e = \left[\left(e_{T_o} \frac{\partial e_{HX}}{\partial T_o} \right)^2 + \left(e_{T_{amb}} \frac{\partial e_{HX}}{\partial T_{amb}} \right)^2 + \left(e_{T_s} \frac{\partial e_{HX}}{\partial T_s} \right)^2 \right]^{.5} \quad (A-2)$$

or,

$$e_e = \left[\left(e_{T_o} \frac{1}{T_s - T_{amb}} \right)^2 + \left(e_{T_{amb}} \frac{T_o - T_{amb}}{(T_s - T_{amb})^2} \right)^2 + \left(e_{T_s} \left[-\frac{1}{T_s - T_{amb}} + \frac{T_o - T_{amb}}{(T_s - T_{amb})^2} \right] \right)^2 \right] \quad (A-3)$$

To determine the uncertainty, one must know the error in each temperature and the delta T's. Separately estimating the systematic and random errors in the temperature measurements is difficult. Random error can be reduced by taking the average of many data points. The effectiveness measurements reported here were each the

average of at least 100 data points. The remaining random error can be expected to appear in any lack of repeatability. Repeatability was determined by repeating the experiment totally from scratch several times. The repeatability error observed in this way was better than ± 0.015 .

In estimating systematic error, the thermistor error is taken to be $\pm 0.15^{\circ}\text{C}$, including sensor and data acquisition errors. (Lead wires were chosen of sufficient gauge that lead wire resistance was negligible compared with the thermistor resistance. Also, the current supplied to the thermistors, 61 μamps , was chosen to limit self-heating error to less than 0.05°C .) The more difficult quantity to estimate is the systematic error due to installation. Both ambient and outlet thermistors were radiation shielded and aspirated. The surface thermistor was attached to the back surface with high thermal conductivity epoxy and the leads were attached to the surface for over 5 centimeters. The surface temperature was also checked against an infrared camera. However, some uncertainty is involved with the actual location, especially in the case of the ambient temperature in zero wind tests. The following are estimates of the systematic error in each temperature based on experiments with varying their positions. These are believed to be conservative:

$$\begin{aligned}
e_{T_s} &= \pm .3K \\
e_{T_o} &= \pm .4K \\
e_{T_a} &= \pm .5K
\end{aligned}
\tag{A-4}$$

To calculate the error in effectiveness, the ΔT s must be known. Rather than calculate the errors for example values of ΔT s, it is much more useful to relate the effectiveness and ΔT s via a model and then determine the error in effectiveness as a function of effectiveness itself. A simple estimated exponential model of effectiveness was used at the start of this project to allow a rough assessment of alternative experimental techniques. (This showed that the direct temperature measurement could be expected to have a higher accuracy than other methods for effectiveness values above about .5.) At the conclusion of the data analysis, with a correlation for heat exchange effectiveness as a function of suction flow rate and plate geometry, it is possible to calculate (within the accuracy of the estimates for individual temperature measurement error) the actual error of any measured effectiveness value on any plate.

Linearizing the radiation loss from the test plate, an energy balance yields:

$$GC_p e_{HX} (T_s - T_{amb}) = Q_s - h_r (T_s - T_{amb})
\tag{A-5}$$

where Q_s is the incoming short-wave (lamp) radiation, h_r is the radiative heat transfer coefficient, $\epsilon\sigma_{SB}(T_s+T_{amb})(T_s^2+T_{amb}^2)$

Re-arranging:

$$T_s - T_{amb} = \frac{Q_s}{h_r + GC_p e_{HX}} \quad (A-6)$$

This provides one of the ΔT s in terms of heat exchange effectiveness if G can be expressed in terms of the effectiveness. To do that the experimental correlation for zero wind is used:

$$Nu_D = 2.748 \left(\frac{P}{D} \right)^{-1.208} Re_D^{.4295} \quad (A-7)$$

Rewriting this in terms of the heat transfer coefficient, U , yields:

$$U = 2.866 k \mu^{-.4295} P^{-.3490} D^{-.2215} G^{.4295} \quad (A-8)$$

Recall that the effectiveness is:

$$e_{HX} = 1 - e^{-\frac{UA}{GA/C_p}} \quad (A-9)$$

where

$$\frac{A}{A'} = 1 - \sigma \quad (\text{A-10})$$

Plugging in the expression for U and solving for G in terms of effectiveness, yields:

$$G = [-.3489 \text{ k}^{-1} \mu^{.4295} C_p^{.3490} D^{.2215} (1 - \sigma)^{-1} \ln(1 - e_{HX})]^{-1.753} \quad (\text{A-11})$$

Substituting this into the expression for $T_s - T_{amb}$ gives this ΔT in terms of only effectiveness, h_r , and known physical and geometric parameters. The other ΔT needed to determine uncertainty, $T_o - T_{amb}$, is simply $\epsilon_{HX}(T_s - T_{amb})$.

Because h_r does not vary greatly over the range of temperatures of interest, it is reasonably accurate to base it on an average value assuming, say, that $T_{amb} = 300\text{K}$ and $T_s = 325\text{K}$. However, greater accuracy can be obtained by iteratively recalculating h_r (using the above as an initial guess) after the ΔT s are determined until convergence is obtained. Because of the small variation of h_r , this converges rapidly. This iterative method was used in a Lotus 1-2-3 spreadsheet program to calculate the error in effectiveness as a function of effectiveness for any plate geometry. Using the values above for systematic error in the individual temperature measurements yields an overall systematic error. To obtain the total error in effectiveness, a root sum square of the calculated

systematic error and the estimate of 0.015 for the overall random error is used:

$$e_{HX} = [e_b^2 + (.015)^2]^{1/2}$$

This contribution was included in the spreadsheet model. A similar analysis was used to determine the uncertainty in effectiveness for two other measurement methods: energy balance and transient. Plots of uncertainty in effectiveness versus effectiveness for the three different methods are shown in **Figure A-1** (Figure 4-8, repeated) for plate 16, a plate which is fairly well centered in the geometric space of interest. Note that for effectiveness values greater than .45, the uncertainty in the direct temperature method is 6% or less and is especially good at the higher effectiveness values.

One additional point should be made. Not included in this analysis is the fact that at very low suction flow rates ($G = .01 \text{ kg/m}^2\text{-s}$ and less), conduction loss in the test box (and perhaps also natural convection in the box) caused the outlet temperature to read too low. Thus even the direct method exhibits an increase in uncertainty at very high effectiveness values. (The highest effectiveness value measured for any plate was 0.92 meaning, conservatively, that the maximum error at an actual effectiveness value of 1 is 8%.) Although data were taken at G values of 0.01 and lower, these proved to be outliers in the curve fits. (Data points for $G = .01 \text{ kg/m}^2\text{-s}$ deviated

only slightly from the fit.) For maximum accuracy, the correlations were based only on data for G values of 0.02 and higher. Thus for the data included in the correlations, the uncertainty analysis presented here is valid.

UNCERTAINTY ANALYSIS

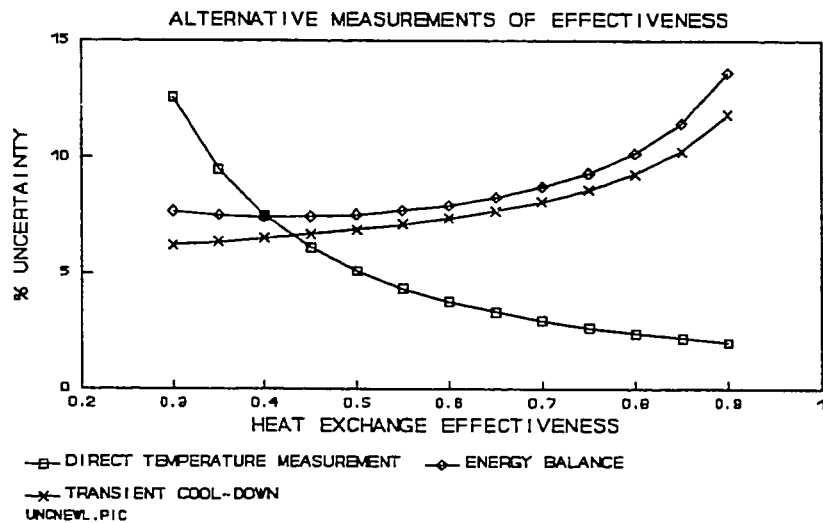


Figure A-1 (Figure 4-8 repeated). Percent uncertainty in effectiveness measurement vs. effectiveness for three different measurement methods -- plate 16.

A.2 Pressure Drop

The expression for non-dimensional pressure drop is:

$$\zeta = \frac{\Delta P}{\frac{1}{2} \rho V^2} = 2 \Delta P \rho^{-1} V^{-2} \quad (\text{A-12})$$

The error is:

$$e_{\zeta} = \left[(e_{\Delta P} \frac{\partial \zeta}{\partial \Delta P})^2 + (e_{\rho} \frac{\partial \zeta}{\partial \rho})^2 + (e_V \frac{\partial \zeta}{\partial V})^2 \right]^{1/2} \quad (\text{A-13})$$

Now since this is a product of terms, it is easily shown that the fractional error can be written as:

$$\frac{e_{\zeta}}{\zeta} = \left[\left(\frac{e_{\Delta P}}{\Delta P} \right)^2 + \left(\frac{e_{\rho}}{\rho} \right)^2 + \left(2 \frac{e_V}{V} \right)^2 \right]^{1/2} \quad (\text{A-14})$$

The three terms in brackets on the right-hand-side of the equation are fractional uncertainties in each of the component variables. Each of the latter two terms can be estimated directly. Thus for the determination of air density and suction velocity:

$$e_{\rho}/\rho = 0.01 \quad (1 \text{ percent of value})$$

$$e_V/V = 0.015 \quad (1.5 \text{ percent of reading})$$

However, the pressure drop cannot be estimated in terms of percent of reading. The pressure was measured with a Dwyer point gauge manometer readable to ± 0.001 inches of water. The percent uncertainty in pressure

reading is a function of the pressure reading. The accuracy of the pressure reading is:

$$e_{\Delta P} = .001 \text{ in. H}_2\text{O} = .25 \text{ Pa}$$

Now while it is not possible to come up with a fixed fractional uncertainty in ζ , it can be expressed as a function of ζ . To do this ΔP must be expressed in terms of ζ which can be done via the correlation:

$$\zeta = 6.818 \left(\frac{1-\sigma}{\sigma} \right)^2 \text{Re}_D^{-.2360} \quad (\text{A-15})$$

Rearranging this to obtain V in terms of ζ , and writing ΔP in terms of ζ :

$$V = 3408 \mu \rho^{-1} \sigma \left(\frac{1-\sigma}{\sigma} \right)^{8.475} D^{-1} \zeta^{-4.237} \quad (\text{A-16})$$

and

$$\begin{aligned} \Delta P &= \frac{1}{2} \rho V^2 \zeta \\ &= 5.805 \times 10^6 \mu^2 \rho^{-1} \sigma^2 \left(\frac{1-\sigma}{\sigma} \right)^{16.95} D^{-2} \zeta^{-7.474} \end{aligned} \quad (\text{A-17})$$

Plugging this expression for ΔP , along with the fractional uncertainties in ρ and V , into the equation for e_ζ/ζ yields the fractional uncertainty in ζ . This was done in the form of a Lotus 1-2-3 spreadsheet for the various

plates. The spreadsheet includes in the root sum square an additional fractional error of 3% to account for random error based on the observed repeatability of the pressure drop runs. A typical result, namely for plate 16, is shown in **Figure A-2**. This shows uncertainties to be in the range of 4% to 5%. Note that the uncertainty increases with increasing ζ . This is because ζ increases with decreasing V . Thus for a given plate, an increase in ζ results from a decrease in V , and the uncertainty rises because the fixed error in ΔP becomes more significant at the lower velocities and accompanying lower pressure drops.

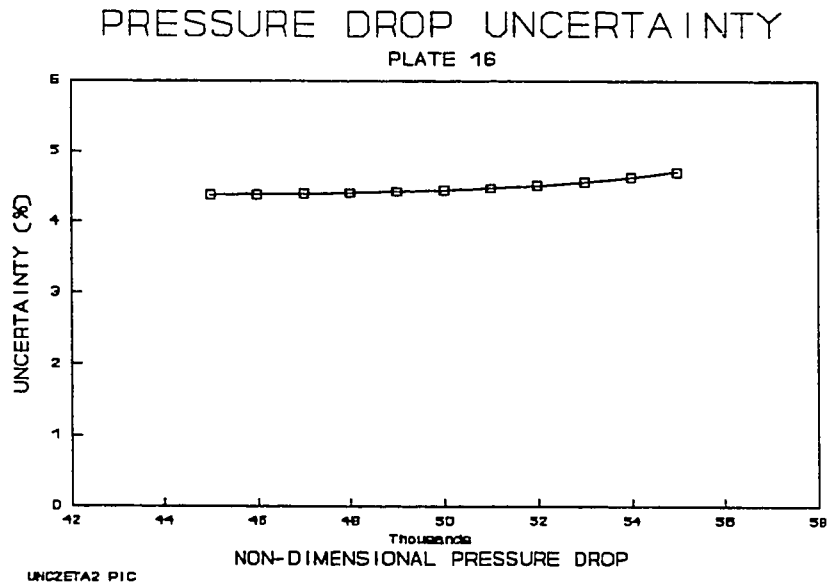


Figure A-2. Percent uncertainty in non-dimensional pressure drop vs. non-dimensional pressure drop for plate 16.

APPENDIX B. FLUX DISTRIBUTION MODEL

Flux Distribution from Lamps

General Electric supplies lamp distribution curves in terms of thousands of candelas vs. degrees off beam.

1 candela = 1 lumen per steradian of solid angle
So the manufacturer's graph gives lumens/steradian vs. angle θ , where θ is the angle between the measurement point and the lamp centerline.

Consider first a lamp pointed normal to the target:

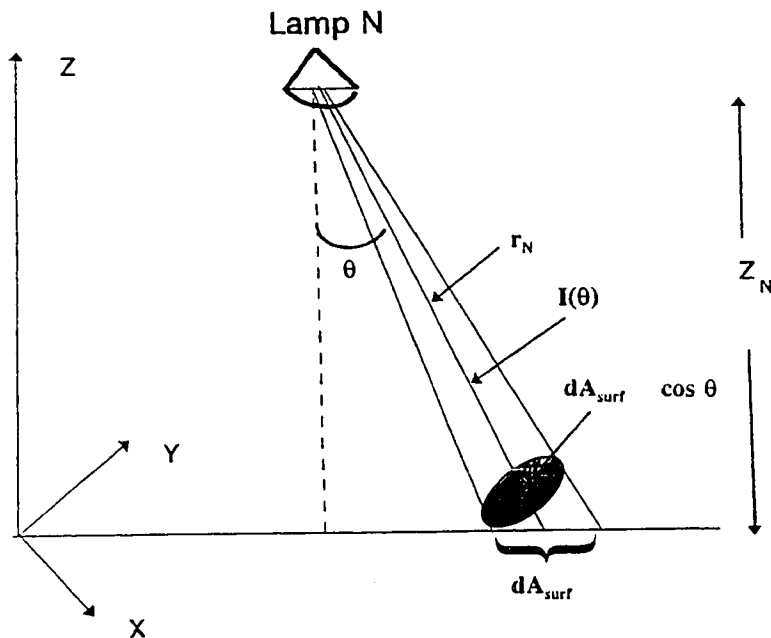


Figure B-1. Geometry for lamp pointing normal to target.

Let $d\omega$ = solid angle subtended by surface element dA_{surf} .

$$d\omega = \frac{dA_{\text{surf}} \cos \theta}{r^2}$$

The power on surface is:

$$P = I\omega = I(\theta) \frac{dA_{\text{surf}} \cos \theta}{r^2}$$

$$\text{Flux on surface is: } dQ'' = \frac{P}{dA_{\text{surf}}} = \frac{I(\theta) \cos \theta}{r^2}$$

$$\text{But } \theta = \cos^{-1} \frac{z_n}{r}$$

$$\text{So } dQ'' = \frac{I(\theta_n) z_n}{r_n^3}$$

$$\text{where } r_n = \sqrt{(x-x_n)^2 + (y-y_n)^2 + z_n^2} \quad (\text{B-1})$$

$$\text{and } \theta_n = \cos^{-1} \frac{z_n}{r_n}$$

(The target plane is at $z = 0$.)

To get $I_n(\theta)$ in watts/steradian instead of lumens/steradian, a pyranometer reading is taken, and the

distribution curve is scaled, i.e., a correction factor is applied to the entire curve. (This assumes that all wavelengths follow the same distribution curve.)

To obtain the flux at the surface due to the lamp, dQ'' is calculated at each target grid point. This is then repeated for each lamp and summed to get the total flux.

Arbitrary Lamp Angles

For arbitrary lamp angles, the center beam does not coincide with the target normal. It is no longer possible to use the same variable, θ , to correspond both to the angle between the center beam and surface element and the angle between the lamp-to-surface element vector and surface normal. The symbol θ is still used for the former but now the latter angle is $\kappa \neq \theta$.

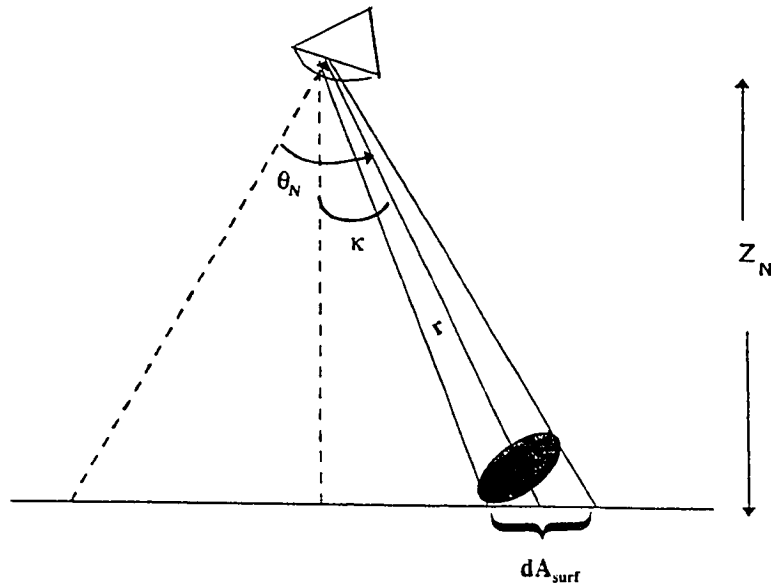


Figure B-2. Geometry for arbitrary lamp angles.

$$\text{Now } d\omega = \frac{dA_{surf} \cos \kappa}{r^2}$$

$$P = I \omega = I (\theta) \frac{dA_{surf} \cos \kappa}{r^2}$$

$$dQ'' = \frac{P}{dA_{surf}} = \frac{I(\theta) \cos \kappa}{r^2}$$

As before $\cos \kappa = \frac{z_n}{r}$

$$\therefore dQ'' = \frac{I(\theta_n) z_n}{r^3} \quad (B-2)$$

This is the same formula as before but now θ_n is different.

How is θ_n determined?

Consider the 2 vectors:

$\vec{v}_b =$ vector defining lamp center beam

$\vec{v}_r =$ vector along r (lamp-to-surface element)

Since

$$\vec{v}_b \cdot \vec{v}_r = |\vec{v}_b| |\vec{v}_r| \cos \theta_n,$$

$$\theta_n = \cos^{-1} \frac{\vec{v}_b \cdot \vec{v}_r}{|\vec{v}_b| |\vec{v}_r|}$$

Now $\vec{v}_r = (x-x_L) \hat{i} + (y-y_L) \hat{j} + (z-z_L) \hat{k}$

Where (x, y, z) = coordinates of surface element

(x_L, y_L, z_L) = coordinates of lamp

If the lamp center beam points at angles:

α from + x-axis

β from + y-axis

γ from + z-axis

then its aiming vector can be written in terms of its direction cosines:

$$\vec{v}_r = \cos \alpha \hat{i} + \cos \beta \hat{j} + \cos \gamma \hat{k}$$

This is a unit vector as $\cos^2 \alpha + \cos^2 \beta + \cos^2 \gamma = 1$

$$\text{So, } \theta_n = \cos^{-1} \frac{\cos \alpha (x - x_L) + \cos \beta (y - y_L) + \cos \gamma (z - z_L)}{(1) [(x - x_L)^2 + (y - y_L)^2 + \cos \gamma (z - z_L)^2]^{1/2}}$$

$$\text{or } \theta_n = \cos^{-1} \frac{\cos \alpha (x - x_L) + \cos \beta (y - y_L) + \cos \gamma (-z_L)}{r} \quad (\text{B-3})$$

Note that if lamp points straight down, $\alpha = 90^\circ$, $\beta = 90^\circ$,

$\gamma = 180^\circ$ and the above reduces to $\theta_n = \cos^{-1} \frac{z_L}{r}$ as before.

Summary of Solution Procedure

- Input lamp locations and angles
- For each lamp and each point in target plane:
 - calculate r from equation (B-1)
 - calculate θ_n from equation (B-3)
 - calculate dQ'' from equation (B-2)
- Sum fluxes for all lamps

Lamp Distribution Curve

- Use GE curves. Sample program shown uses 500R/3FL
- Curve is normalized to a peak of 1.0 and then curve fit. The best polynomial fit is:

$$I(\theta) = 1.00 + .00197 \theta - 7.668 \times 10^{-4} \theta^2 + 1.0930 \times 10^{-5} \theta^3 - 4.465 \times 10^{-8} \theta^4$$

$$0 \leq \theta \leq 100^\circ$$

For $\theta > 100^\circ$, set $I(\theta) = 0.0$

Pyranometer readings show that peak fluxes go as $\frac{1}{r^2}$ with

r measured from near front edge of lamp.

For example, data for a 500R/3FL bulb is:

<u>r (m)</u>	<u>Q (w/m²)</u>
.63	80.
.73	280.
.84	213.
.94	167.
1.04	136.

For the center beam, $Q'' = \frac{I \cos(0^\circ)}{r^2}$

$$I_p = Q'' r^2$$

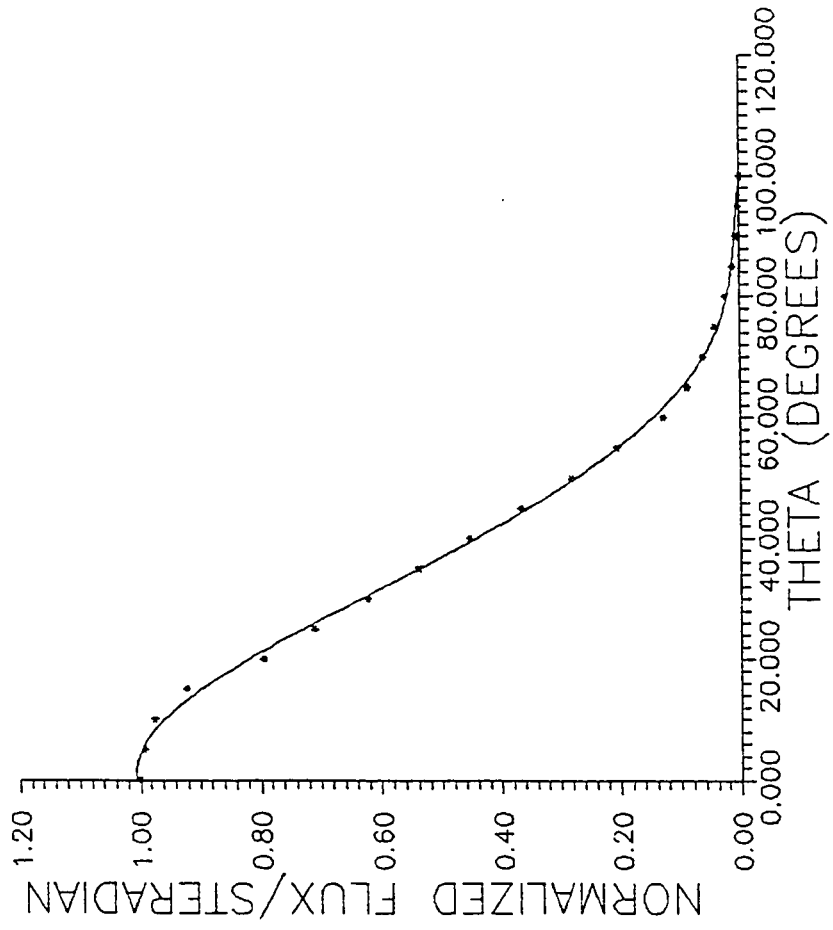
@ $r = 1.04\text{m}$,

$$I_p = 136 \frac{\text{W}}{\text{m}^2} \times (1.04\text{m})^2 = 147 \text{ W/steradian}$$

The polynomial for I is multiplied by 147 to get W/steradian.

A FORTRAN 77 (Lahey 4.0) program and sample data file and output are attached.

4TH ORDER POLYNOMIAL FIT
TO LAMP DISTRIBUTION CURVE
GE 500R/3FL



Program Listing

PROGRAM FLUXMAPG

```

*****
* THIS PROGRAM CALCULATES THE FLUX DISTRIBUTION ON A *
* PLANE IRRADIATED BY LAMPS AND ALLOWS LAMP TILTS. *
* THE DISTRIBUTION CURVE FOR THE LAMP IS KNOWN AND *
* IS CONTAINED IN A SUBROUTINE. LAMP LOCATIONS AND *
* TILTS ARE CONTAINED IN AN INPUT DATA FILE. *
* WRITTEN BY C. F. KUTSCHER, JULY 21, 1991 *
*****
*
* INPUT DATA FILE INSTRUCTIONS: *
* EACH LINE SHOULD CONTAIN THE THREE LAMP LOCATION *
* COORDINATES AND THE THREE LAMP ANGLES: *
* XL,YL,ZL,ALPHA,BETA,GAMMA *
* FOR EXAMPLE: *
* -0.25,0.50,1.5,90.0,123.69,146.31 *
* COORDINATE SYSTEM IS RIGHT-HANDED AND ORIGIN, (0,0,0), *
* IS LOCATED AT CENTER OF TARGET. *
* BE CAREFUL THAT EACH ANGLE IS RELATIVE TO POSITIVE AXIS*
* CHECK THAT THE SUM OF THE THREE DIRECTION COSINES IS 1.*
* LAST LINE OF DATA FILE MUST BE: *
* 999.,999.,999.,999.,999.,999. *
*
* OUTPUT DATA FILE: *
* AN OUTPUT FILE IS PRINTED OUT AND WRITTEN TO FILENAME *
* 'FLUXMAP.DAT' TO ALLOW CONTOUR MAPS TO BE MADE WITH A *
* PROGRAM LIKE GRAPHOR. THERE ARE THREE ITEMS ON EACH *
* LINE: X-COORDINATE ON TARGET (M), Y-COORDINATE ON *
* TARGET (M), FLUX AT THAT POINT (W/M2) *
*
*****
*
* VARIABLE DEFINITIONS *
*
* ALPHA (K) = ANGLE BETW. LAMP & POSITIVE X-AXIS (DEG)*
* BETA(K) = ANGLE BETW. LAMP & POSITIVE Y-AXIS (DEG)*
* COSAA = COSALF(K) IN SUBROUTINE LAMP *
* COSALF(K) = DIRECTION COSINE FOR LAMP ANGLE ALPHA *
* COSBB = COSBET(K) IN SUBROUTINE LAMP *
* COSCC = COSGAM(K) IN SUBROUTINE LAMP *
* COSBET(K) = DIRECTION COSINE FOR LAMP ANGLE BETA *
* COSGAM(K) = DIRECTION COSINE FOR LAMP ANGLE GAMMA *
* DEL = SIZE OF TARGET GRID ELEMENT (M) *
* DUM = INTERMEDIATE DUMMY VARIABLE IN SUB. LAMP*
* DUM2 = INTERMEDIATE DUMMY VARIABLE IN SUB. LAMP*
* GAMMA(K) = ANGLE BETW. LAMP & POSITIVE Z-AXIS (DEG)*
* I = INTEGER GRID COUNT IN X-DIRECTION *
* J = INTEGER GRID COUNT IN Y-DIRECTION *
* K = INDEX USED TO COUNT LAMPS *
* NX = INTEGER NUMBER OF X GRID LINES *
* NY = INTEGER NUMBER OF Y GRID LINES *
* NLAMPS = INTEGER NUMBER OF LAMPS *
* PERCO = VARIATION OF MAX. FLUX ABOVE AVERAGE (%) *
* PERCU = VARIATION OF MIN. FLUX BELOW AVERAGE (%) *
* R = DISTANCE BETW. LAMP & TARGET ELEMENT (M)*
* THETA = ANGLE BETW. LAMP CENTER BEAM AND R LINE *
* TL = TARGET LENGTH IN X-DIRECTION (M) *
* TW = TARGET LENGTH IN Y-DIRECTION (M) *

```

```

* Q(I,J)      = FLUX ON TARGET DUE TO GIVEN LAMP (W/M2) *
* QT(I,J)    = ACCUMULATED FLUX DUE TO ALL LAMPS (W/M2) *
* QTMAX      = MAXIMUM SURFACE FLUX (W/M2) *
* QTMIN      = MINIMUM SURFACE FLUX (W/M2) *
* QTSUM      = SUM OF FLUX AT ALL GRID POINTS (W/M2) *
* QTAVG      = AVERAGE SURFACE FLUX (W/M2) *
* XL(K)      = X-COORDINATE OF LAMP (M) *
* XXL       = XL(K) IN LAMP SUBROUTINE (M) *
* XMAX       = X-COORDINATE OF MAXIMUM TARGET FLUX (M) *
* XMIN       = X-COORDINATE OF MINIMUM TARGET FLUX (M) *
* YL(K)      = Y-COORDINATE OF LAMP (M) *
* YYL       = YL(K) IN LAMP SUBROUTINE (M) *
* YMAX       = Y-COORDINATE OF MAXIMUM TARGET FLUX (M) *
* YMIN       = Y-COORDINATE OF MINIMUM TARGET FLUX (M) *
* ZL(K)      = Z-COORDINATE OF LAMP (M) *
* ZZL       = ZL(K) IN LAMP SUBROUTINE (M) *
*

```

```

*****

```

```

COMMON X(200),Y(200),Q(200,200),NX,NY
DIMENSION QT(200,200)
DIMENSION XL(100),YL(100),ZL(100)
DIMENSION ALPHA(100),BETA(100),GAMMA(100)
DIMENSION COSALF(100),COSBET(100),COSGAM(100)
CHARACTER FNAME*20
PRINT *, 'ENTER TARGET LENGTH X (M) '
READ *, TL
PRINT *, 'ENTER TARGET WIDTH Y (M) '
READ *, TW
PRINT *, 'ENTER SIZE OF GRID ELEMENT (M) '
READ *, DEL
PRINT *, 'ENTER INPUT FILENAME '
READ, FNAME

C
C OPEN AND READ INPUT FILE
C
OPEN (UNIT=1, FILE=FNAME,STATUS='OLD')
K = 0
20 K = K+1
READ(1,*) XL(K),YL(K),ZL(K),ALPHA(K),BETA(K),GAMMA(K)

C
C CONVERT TILTS FROM DEGREES TO RADIANS AND COMPUTE
C DIRECTION COSINES
C
ALPHA(K) = .017453*ALPHA(K)
BETA(K) = .017453*BETA(K)
GAMMA(K) = .017453*GAMMA(K)
COSALF(K) = COS(ALPHA(K))
COSBET(K) = COS(BETA(K))
COSGAM(K) = COS(GAMMA(K))
IF(XL(K).LT.998) GOTO 20
NLAMPS = K

C
C SET UP GRID IN TARGET PLANE
C
X0 = -TL/2.
Y0 = -TW/2.
NX = TL/DEL + 1.001
NY = TW/DEL + 1.001
DO 30 I = 1,NX

```

```

30   X(I) = X0 + (I-1)*DEL
    DO 40 J = 1, NY
40   Y(J) = Y0 + (J-1)*DEL
C
C   INITIALIZE FLUX ARRAY
C
    DO 60 I = 1, NX
    DO 50 J = 1, NY
      QT(I,J) = 0.0
50   CONTINUE
60   CONTINUE
C
C   OBTAIN FLUX DISTRIBUTION ON TARGET FOR EACH LAMP
C
    DO 90 K = 1, NLAMPS
      CALL LAMP(XL(K), YL(K), ZL(K), COSALF(K),
1     COSBET(K), COSGAM(K))
      DO 80 I = 1, NX
      DO 70 J = 1, NY
        QT(I,J) = QT(I,J) + Q(I,J)
70   CONTINUE
80   CONTINUE
90   CONTINUE
C
C   WRITE AND PRINT OUTPUT AND FIND MAX AND MIN VALUES
C
    PRINT
    PRINT, '      X (M) ', '      Y (M) ', 'FLUX (W/M2)'
    OPEN (UNIT=7, FILE='FLUXMAP.DAT', STATUS='UNKNOWN')
9000  FORMAT (1X, 5X, F5.2, 6X, F5.2, 3X, F8.2)
      QTMIN = QT(1,1)
      QTMAX = QT(1,1)
      XMIN = X(1)
      YMIN = Y(1)
      XMAX = X(1)
      YMAX = Y(1)
      QTSUM = 0.0
      DO 110 I = 1, NX
      DO 100 J = 1, NY
        WRITE (7,9000) X(I), Y(J), QT(I,J)
        PRINT 9000, X(I), Y(J), QT(I,J)
        IF (QT(I,J).GT.QTMAX) THEN
          QTMAX = QT(I,J)
          XMAX = X(I)
          YMAX = Y(J)
        ENDIF
        IF (QT(I,J).LT.QTMIN) THEN
          QTMIN = QT(I,J)
          XMIN = X(I)
          YMIN = Y(I)
        ENDIF
        QTSUM = QTSUM + QT(I,J)
100  CONTINUE
110  CONTINUE
C
C   CALCULATE AVERAGE FLUX AND PERCENT VARIATIONS
C
      QTAVG = QTSUM/(NX*NY)
      PERCO = 100.*(QTMAX-QTAVG)/QTAVG

```

```

      PERCU = 100.*(QTAVG-QTMIN)/QTAVG
C
C   PRINT OUT STATISTICAL RESULTS
C
      PRINT
      PRINT, 'AVERAGE FLUX ON TARGET = ',QTAVG,' W/M2'
      PRINT, 'MAX VALUE IS ', PERCO, ' % ABOVE AVERAGE'
      PRINT, 'MAX OCCURS AT X = ',XMAX,' Y = ',YMAX
      PRINT, 'MIN VALUE IS ', PERCU, ' % BELOW AVERAGE'
      PRINT, 'MIN OCCURS AT X = ',XMIN,' Y = ',YMIN
      END
*****
* SUBROUTINE TO CALCULATE FLUX DISTRIBUTION ON TARGET *
* DUE TO A SINGLE LAMP *
*****
      SUBROUTINE LAMP(XXL,YYL,ZZL,COSAA,COSBB,COSCC)
      COMMON X(200),Y(200),Q(200,200),NX,NY
      DO 210 I = 1,NX
      DO 200 J = 1,NY
C
C   CALCULATE DISTANCE R BETWEEN LAMP AND SURFACE ELEMENT
C
      R = ((X(I)-XXL)**2.+(Y(J)-YYL)**2.+ZZL**2.)**.5
C
C   CALCULATE ANGLE THETA BETWEEN LAMP CENTER BEAM AND LINE
C   BETWEEN LAMP & CENTER BEAM
C
      DUM = COSAA*(X(I)-XXL)+COSBB*
1      (Y(J)-YYL)+COSCC*(-ZZL)
      DUM2 = DUM/R
      THETA = 57.2958*ACOS(DUM2)
      IF(THETA.LT.100.) THEN
C
C   POLYNOMIAL CURVE FIT FOR LAMP DISTRIBUTION
C
      Q(I,J) = 147.*(1.0+.00197*THETA-7.668E-
1      4*THETA**2.+1.0930E-5*THETA**3.-
2      4.465E-8*THETA**4.)
C
C   CALCULATE FLUX ON SURFACE ELEMENT
C
      Q(I,J) = Q(I,J)*ZZL/R**3.
      ELSE
C
C   IF OUTSIDE RANGE OF POLYNOMIAL CURVE FIT SET FLUX TO
C   ZERO
C
      Q(I,J) = 0.00
      ENDIF
200 CONTINUE
210 CONTINUE
      RETURN
      END

```

Example Input Data File

```
.30,.173,.9,90.0,90.0,180.0  
-.30,.173,.9,90.0,90.0,180.0  
.30,-.173,.9,90.0,90.0,180.0  
-.30,-.173,.9,90.0,90.0,180.0  
0.20,0.346,.9,90.0,90.0,180.0  
0.20,-0.346,.9,90.0,90.0,180.0  
-0.20,0.346,.9,90.0,90.0,180.0  
-0.20,-0.346,.9,90.0,90.0,180.0  
0.10,0.519,.9,90.0,90.0,180.0  
0.10,-0.519,.9,90.0,90.0,180.0  
-0.10,0.519,.9,90.0,90.0,180.0  
-0.10,-0.519,.9,90.0,90.0,180.0  
0.30,0.519,.9,90.0,90.0,180.0  
0.30,-0.519,.9,90.0,90.0,180.0  
-0.30,0.519,.9,90.0,90.0,180.0  
-0.30,-0.519,.9,90.0,90.0,180.0  
999.,999.,999.,999.,999.,999.
```

fluxg2n

ENTER TARGET LENGTH X (M) .32

ENTER TARGET WIDTH Y (M) .52

ENTER SIZE OF GRID ELEMENT (M) .04

ENTER INPUT FILENAME trial10v.dat

X (M)	Y (M)	FLUX (W/M2)
-0.16	-0.26	1347.08
-0.16	-0.22	1351.78
-0.16	-0.18	1353.41
-0.16	-0.14	1353.12
-0.16	-0.10	1351.93
-0.16	-0.06	1350.65
-0.16	-0.02	1349.86
-0.16	0.02	1349.86
-0.16	0.06	1350.65
-0.16	0.10	1351.94
-0.16	0.14	1353.13
-0.16	0.18	1353.42
-0.16	0.22	1351.78
-0.16	0.26	1347.09
-0.12	-0.26	1372.50
-0.12	-0.22	1376.68
-0.12	-0.18	1377.83
-0.12	-0.14	1377.09
-0.12	-0.10	1375.53
-0.12	-0.06	1373.98
-0.12	-0.02	1373.05
-0.12	0.02	1373.05
-0.12	0.06	1373.98
-0.12	0.10	1375.53
-0.12	0.14	1377.10
-0.12	0.18	1377.83
-0.12	0.22	1376.69
-0.12	0.26	1372.52
-0.08	-0.26	1390.58
-0.08	-0.22	1394.36
-0.08	-0.18	1395.13
-0.08	-0.14	1394.07
-0.08	-0.10	1392.23
-0.08	-0.06	1390.49
-0.08	-0.02	1389.46
-0.08	0.02	1389.47
-0.08	0.06	1390.50
-0.08	0.10	1392.24
-0.08	0.14	1394.07
-0.08	0.18	1395.14
-0.08	0.22	1394.37
-0.08	0.26	1390.59
-0.04	-0.26	1401.37
-0.04	-0.22	1404.91
-0.04	-0.18	1405.45
-0.04	-0.14	1404.18
-0.04	-0.10	1402.18
-0.04	-0.06	1400.33

-0.04	-0.02	1399.24
-0.04	0.02	1399.24
-0.04	0.06	1400.33
-0.04	0.10	1402.18
-0.04	0.14	1404.19
-0.04	0.18	1405.46
-0.04	0.22	1404.92
-0.04	0.26	1401.39
0.00	-0.26	1404.96
0.00	-0.22	1408.42
0.00	-0.18	1408.88
0.00	-0.14	1407.54
0.00	-0.10	1405.49
0.00	-0.06	1403.59
0.00	-0.02	1402.49
0.00	0.02	1402.49
0.00	0.06	1403.60
0.00	0.10	1405.49
0.00	0.14	1407.55
0.00	0.18	1408.88
0.00	0.22	1408.43
0.00	0.26	1404.97
0.04	-0.26	1401.38
0.04	-0.22	1404.92
0.04	-0.18	1405.46
0.04	-0.14	1404.19
0.04	-0.10	1402.19
0.04	-0.06	1400.33
0.04	-0.02	1399.25
0.04	0.02	1399.25
0.04	0.06	1400.33
0.04	0.10	1402.19
0.04	0.14	1404.19
0.04	0.18	1405.46
0.04	0.22	1404.93
0.04	0.26	1401.39
0.08	-0.26	1390.59
0.08	-0.22	1394.38
0.08	-0.18	1395.15
0.08	-0.14	1394.08
0.08	-0.10	1392.24
0.08	-0.06	1390.51
0.08	-0.02	1389.48
0.08	0.02	1389.48
0.08	0.06	1390.51
0.08	0.10	1392.25
0.08	0.14	1394.09
0.08	0.18	1395.15
0.08	0.22	1394.38
0.08	0.26	1390.61
0.12	-0.26	1372.52
0.12	-0.22	1376.70
0.12	-0.18	1377.84
0.12	-0.14	1377.11
0.12	-0.10	1375.55
0.12	-0.06	1374.00
0.12	-0.02	1373.07
0.12	0.02	1373.07
0.12	0.06	1374.00
0.12	0.10	1375.55

0.12	0.14	1377.12
0.12	0.18	1377.85
0.12	0.22	1376.71
0.12	0.26	1372.53
0.16	-0.26	1347.10
0.16	-0.22	1351.80
0.16	-0.18	1353.43
0.16	-0.14	1353.15
0.16	-0.10	1351.96
0.16	-0.06	1350.68
0.16	-0.02	1349.88
0.16	0.02	1349.89
0.16	0.06	1350.68
0.16	0.10	1351.96
0.16	0.14	1353.15
0.16	0.18	1353.44
0.16	0.22	1351.81
0.16	0.26	1347.12

AVERAGE FLUX ON TARGET = 1383.16 W/M2
 MAX VALUE IS 1.85998 % ABOVE AVERAGE
 MAX OCCURS AT X = 0.000000 Y = 0.180000
 MIN VALUE IS 2.60841 % BELOW AVERAGE
 MIN OCCURS AT X = -0.160000 Y = -0.260000